Efficient, Low-Cost Organic-Inorganic Hybrid Solar Cells via Materials, Interface, and Device Structure Design

Leize Zhu

A dissertation

submitted in partial fulfillment of the

requirements for the degree of

Doctor of Philosophy

University of Washington

2015

Reading Committee:

Qiuming Yu, Chair

Stuart B. Adler

Hong Ma

Program Authorized to Offer Degree:

Chemical Engineering

University of Washington

Abstract

Efficient, Low-Cost Organic-Inorganic Hybrid Solar Cells via Materials, Interface, and Device Structure Design

Leize Zhu

Chair of the Supervisory Committee:
Professor Qiuming Yu
Department of Chemical Engineering

The concept of the inter-mixing of donor-acceptor materials in a single layer revolutionized the solar cell technology. The commonly used materials are lack of strong absorption in the near-infrared region. Pyrite FeS_2 is a promising material because of its high absorption in the range of 300-1100 nm. In addition, it is abundant, non-toxic and has long term stability as well as the extraordinary electrical properties. Pyrite FeS_2 hierarchical microparticles consisting of cubic crystals with defined {100} faceted textures were synthesized using a hydrothermal method with the presence of ethylenediamine and polyvinylpyrrolidone. Short, branched, and chromosome-like pyrite FeS_2 rods with a diameter of 10 nm and a length of 20-30 nm as well as quasi-cubic NC agglomerates with a size of 200 nm were obtained by hot injection methods. The growth of anisotropic iron pyrite nanocrystals (NCs) follows the oriented attachment mechanism at the

early growth stage of the hot injection synthesis followed by Ostwald ripening mechanism as time progresses.

In the fabrication of inverted organic-inorganic hybrid solar cells with pyrite NCs, we realize an effective hole transport layer (HTL) improves the performance of the solar cells and provides additional protection against water and oxygen. The HTL serves as a selective contact by extracting holes while concurrently blocking electrons, thereby reducing dark (leakage) current and enhancing the open circuit voltage (V_{OC}), short circuit current (J_{SC}), and fill factor (FF). The inverted hybrid CdSe -polymer solar cells with the poly (3, 4-ethylenedioxythiophene)-poly (styrenesulfonate) (PEDOT:PSS)/MoO_3 dual HTLs showed superior performance over those with a single HTL of PEDOT:PSS or MoO_3. The enhancement in electron transport in the active layer, the improvement in hole extraction at active layer/anode interface as well as a prevention of leakage current account for the enhancement in the efficiency of the solar cells with dual HTLs.

In order to achieve an efficient charge separation and correlates the film morphology and grain size with the device performance. A two-step solution process with thermal plus solvent vapor-assisted thermal annealing was developed for the fabrication of binary Pb-Sn triiodine perovskite films. This was an effective method to make films with large and smooth grains. Using this new process to control and manipulate film morphology, grain size, and especially the distribution of metal cations in binary metal perovskite layers, opens an avenue to grow perovskite materials with desired properties to enhance device performance.

TABLE OF CONTENTS

LIST OF FIGURES v
LIST OF SCHEMES xvi
LIST OF TABLES xvii
Chapter 1 INTRODUCTION 1
1.1 Overview 1
1.2 Bulk Heterojunction (BHJ) Solar Cells 3
1.3 Inverted BHJ Solar Cells: Device Parameters, Architecture, and Operation Principles 3
1.3.1 Device Parameters 3
1.3.2 Device Architecture and Operation Principles 5
1.4 Strategies to Improve the Efficiency of BHJ Solar Cells 7
1.5 Earth-Abundant Solar Absorber 7
1.5.1 Synthesis of Pyrite FeS_2 Materials 8
1.5.2 Growth Mechanism of Nanocrystals (NCs) 9
1.6 Emerging Organic-Inorganic Halide Perovskite Solar Cells 11
1.7 Objectives and Goals 12
Chapter 2 HYDROTHERMAL SYNTHESIS AND CHARACTERIZATION OF PYRITE FES2 HIERARCHICAL PARTICLES 14
2.1 Introduction 14
2.2 Experimental Section 16
2.2.1 Materials for the Synthesis of Pyrite FeS_2 Hierarchical Particles 16
2.2.2 Hydrothermal Synthesis of Pyrite FeS_2 Hierarchical Particles 16
2.2.3 Characterization of Pyrite FeS_2 Hierarchical Particles 16
2.3 Results and Discussion 17
2.3.1 Pyrite FeS_2 Hierarchical Particles 17
2.3.2 Role of PVP in the Synthesis 19

2.3.3 Role of En in the Synthesis 25
2.4 Conclusions 31
Chapter 3 HOT INJECTION SYNTHESIS, CHARACTERIZATION OF PYRITE NCS FOR ORGANIC-INORGANIC HYBRID SOLAR CELLS 32
3.1 Introduction 32
3.2 Experimental Section 34
3.2.1 Materials for the Synthesis of Pyrite FeS_2 NCs 34
3.2.2 Hot injection Synthesis of Pyrite FeS_2 NCs 34
3.2.3 Characterizations of Pyrite FeS_2 NCs 36
3.3 Results and Discussion 37
3.3.1 Short Pyrite FeS_2 NRs and Chromosome-Like Rods 37
3.3.2 Solvents on the Morphology of Pyrite FeS_2 NCs 42
3.3.3 Additives on the Morphology of Pyrite FeS_2 NCs 44
3.3.4 S:Fe Ratio and Reaction Temperature on the Phase Purity 47
3.3.5 Discussions on the Growth Mechanism 48
3.4 Conclusions 50
Chapter 4 ANISOTROPIC GROWTH OF IRON PYRITE FES2 NCS VIA ORIENTED ATTACHMENT 51
4.1 Introduction 51
4.2 Experimental Section 52
4.2.1 Materials for Anisotropic Growth of Pyrite FeS_2 NCs 52
4.2.2 Synthesis of Pyrite FeS_2 NCs 52
4.2.3 Characterization of Anisotropic Pyrite FeS_2 NCs 53
4.3 Results and Discussion 54
4.3.1 Time-Dependent Crystallinity, Morphology, and Size of the NCs 54
4.3.2 Plane to Plane Attachment 59
4.3.3 Point to Point Attachment 67
4.3.4 Solvents on the Morphology of Pyrite FeS_2 NCs 70
4.4 Conclusions 73

Chapter 5 DUAL HOLE TRANSPORT LAYER FOR INVERTED POLYMER-CDSE QDS HYBRID SOLAR CELLS 74
5.1 Introduction 74
5.2 Device Theory 77
5.2.1 Equivalent Circuit 77
5.2.2 Simple Shockley Model 78
5.2.3 Improved Shockley Model Using Space-Charge Approach 79
5.2.4 Space Charge Limited Current 79
5.3 Experimental Section 80
5.3.1 Materials for CdSe QDs and NRs Synthesis and Device Fabrication 80
5.3.2 CdSe QD and NRs Synthesis and Ligand Exchange 81
5.3.3 Device Fabrication 81
5.3.4 Characterization of CdSe QDs and Device Testing 82
5.4 Results and discussion 83
5.4.1 Synthesis and Characterization of CdSe QDs and NRs 83
5.4.2 UV-Vis and PL of the CdSe QDs:P3HT films 86
5.4.3 Electron and Hole Mobilities 87
5.4.4 Influence of HTLs on the Solar Cell Performance 90
5.4.5 Dependence of Device Parameters on the Performance of Solar Cells 97
5.4.6 Study of the CdSe QDs: PTB7-F20 Hybrid Films 98
5.4.7 Inverted CdSe QDs + NRs: PTB7-F20 Hybrid Solar Cells 100
5.5 Conclusions 102
Chapter 6 SOLVENT VAPOR-ASSISTED THERMAL ANNEALING FOR THE HIGH-PERFORMANCE PLANAR CH3NH3SNXPB1-XI3 PEROVSKITE SOLAR CELLS 103
6.1 Introduction 103
6.2 Experimental Section 107
6.2.1 Materials and Synthesis of MAI 107
6.2.2 Perovskite Film Fabrication and Characterization 107
6.2.3 Device Fabrication and PV Performance Measurement 109

6.3 Results and Discussions 110
6.3.1 Fabrication and Characterization of Metal Iodide ($Sn_xPb_{1-x}I_2$) Films 110
6.3.2 Fabrication and Characterization of $CH_3NH_3Sn_xPb_{1-x}I_3$ Films 113
6.3.3 Device Performance of $CH_3NH_3Sn_xPb_{1-x}I_3$ Solar Cells 121
6.4 Conclusion 129
Chapter 7 CONCLUSIONS AND OUTLOOK 130
7.1 Conclusions 130
7.2 Outlook 131
Appendix A SOLVOTHERMAL SYNTHESIS AND CHARACTERIZATION OF IRON SULFIDE MATERIALS 134
A.1 Introduction 134
A.2 Experimental Section 136
A.2.1 Materials for the Synthesis of Iron Sulfide Materials 136
A.2.2 Solvothermal Synthesis of Iron Sulfide Materials 137
A.2.3 Characterizations of Iron Sulfide Materials 138
A.3 Results and Discussion 138
A.3.1 Concentration, S:Fe Ratio, and Iron Source on the Morphology of Iron Sulfide Materials 138
A.3.2 Reaction Temperature on the Morphology of Iron Sulfide Materials 141
A.3.3 Composition of Iron Sulfide Materials 142
A.4 Conclusions 146
References 148
Appendix B ABBREVIATION I

LIST OF FIGURES

Figure 1.1 The record efficiency of the typical solar cells certified by National Renewable Energy Laboratory (NREL) (Data were extracted from ref.[39]) 2

Figure 1.2 A typical J-V characteristics of solar cells under illumination. 4

Figure 1.3 Typical device structure of conventional and inverted BHJ solar cells. Inset: An illustration to show charge separation, recombination, and transportation processes in a BHJ layer. Dark brown region is the donor phase and black region is the acceptor phase. HTL: hole tansport layer; ETL: electron transport layer. 5

Figure 1.4 The crystalline structure of commonly observed iron sulfide materials including mackinawite FeS_{1-x}, troilite FeS, pyrrhotite $Fe_{1-x}S$, greigite Fe_3S_4, marcasite FeS_2, and pyrite FeS_2. 9

Figure 1.5 Device configurations of planar perovskite solar cells: (A) Conventional device architecture; (B) Inverted device architecture causes electrons and holes to exit the device in the opposite direction. 12

Figure 2.1 The SEM images (A and B) and XRD pattern (C) of the pyrite FeS_2 hierarchical particles synthesized in an ethylenediamine aqueous solution (2.2 mL of en : 17.0 mL of water) containing 0.6 g of PVP at 200°C for 24 h. Raman spectra (D) show naturally occurring pyrite (I) and synthesized pyrite FeS_2 hierarchical microparticles (II). 18

Figure 2.2 The SEM images of the products synthesized in an ethylenediamine aqueous solution (2.2 mL of en : 17 mL of water) containing 0.3 g (A), 1.2 g (B), and 2.4 g (C) of PVP at 200°C for 24 h. Arrows in (B) and (C) indicate the amorphous iron sulfide plates. The insets show the typical morphology of the microparticles. The XRD patterns are the products with 0.3 g (I), 1.2 g (II), and 2.4 g (III) of PVP. The XRD peaks of marcasite FeS_2 are marked as "+" and magnetite Fe_3O_4 as "#". 20

Figure 2.3 The atomic structures of the pyrite (100) surface terminated in layers A, B, and C. Side- and top-view are shown in the top and bottom rows, respectively. Blue balls are iron atoms and yellow balls are sulfur atoms. In the top-view, the dangling bonds are terminated by hydrogen atoms in red. For easy visualization, the top two and three layers are displayed in the top-view of layers A, B, and C, respectively. 22
Figure 2.4 The atomic structures of the pyrite (111) surface terminating in layers A and B. The side- and top-view are shown in the top and bottom rows, respectively. Blue balls are iron atoms and yellow balls are sulfur atoms. In the top-view, the dangling bonds are terminated by hydrogen atoms in red color. Only the top two layers are shown in the top-view. 23
Figure 2.5 Side-view of (111) surface terminated in layers C, D, and E. Blue balls are iron atoms and yellow balls are sulfur atoms. Based on the analysis of the atomic structures of different terminating layers of (100) and (111) surfaces, the (111) surface terminated in Layer A could be the most energetically favorable surface to bind PVP because all the outmost surface atoms are iron which have three dangling bonds and all sulfur atoms are in the sub-surface and are coordinatively saturated. Therefore, during the crystal growth, the oxygen atoms on PVP could bind to the iron atoms at the {111} surfaces and the growth would be along the <100> directions, resulting in the {100} facets. By taking a closer look at the product synthesized in the solution containing 0.6 g of PVP, it was found that about 7% of the total products (by counting 200 particles) were either the single {100} facetted cubes with truncated {111} corners or the connected two cubes with well-defined {100} facets (Figure 2.6). Small pitches formed by the {111} facets were observed at the <100> edges and the {111} facets of single and dual particles in Figure 5. While the dominated facets are {100}, small amount of {111} facets can also be observed at the hierarchical microspheres (Figure 2.1A, B). All these experimental results supported the hypothesis that the {100} facetted cubic textures at the hierarchical microparticles could be due to the structure-direction effect caused by PVP in the reaction mixtures. Based on the above analysis, a possible mechanism is proposed as shown in Scheme

2.2. The binding of PVP on {111} facets leads to the aggregation of cubic-like crystals and subsequently the formation of pyrite FeS_2 hierarchical microparticles. . 24
Figure 2.6 The SEM images of one truncated pyrite cube with the {100} and {111} facets (A) and two connected pyrite cubes with the defined {100} facets (B). Small pitches formed by the {111} facets are also observed. Particles with these morphologies were about 7% of the total products determined by counting 200 particles in an SEM image. 25
Figure 2.7 The SEM images of the products synthesized in an ethylenediamine aqueous solution with the volume ratio of en to water of 1 mL/18.2 mL (A), 2.2 mL/17 mL (B), 4.2 mL/15 mL (C), and 6.2 mL/13 mL (D) without the presence of PVP at 200°C for 24 h. Insets are the typical morphology of particles in the products. (E) The XRD patterns of I, II, III, and IV correspond to the products of (A), (B), (C), and (D), respectively. The XRD peaks of marcasite FeS_2 are marked as "+". 27
Figure 2.8 The area ratio of the XRD peaks of the marcarsite (110) plane (2θ at 25.9°) and the pyrite (111) plane (2θ at 28.4°) versus the volume of en added in the reaction. 28
Figure 2.9 SEM images of the products synthesized in the solutions with the volume ratio of en to water of 0.2 mL/19 mL (A) and 0 mL/19.2 mL (B) without the presence of PVP at 200ºC for 24 h. The XRD patterns of I and II are for the products shown in (A) and (B), respectively. The XRD peaks of marcasite FeS_2 are marked as "+" and pyrite FeS_2 are marked as "*". The arrow indicates the peak due to other impurity. En is a strong chelating agent and can form complexes with metal ions. En can coordinate with Fe^{2+} ions to form complex $[Fe(en)_2]^{2+}$ ions.[82] It was also reported that sulfur powder can react with en to generate a greenish solution due to the reversible nucleophilic attack of the S_8 rings by en. As a result, octathioamine [NH_2-$(CH_2)_2$-HN-S_8^-] is formed. Octathioamine can further degenerate to polythioamines [NH_2-$(CH_2)_2$-HN-S_y^-] ($y < 8$).[139, 140] Assuming no degeneration of octathioamine [NH_2-$(CH_2)_2$-HN-S_8^-] ($y = 8$), a total of 0.00346 mol of en (i.e. 0.231 mL) should be consumed to form $[Fe(en)_2]^{2+}$ and [NH_2-$(CH_2)_2$-HN-S_8^-] by taking into account that 0.0984 g (3.08 mmol) of S and 0.3057 g (1.54 mmol) of $FeCl_2 \cdot 4H_2O$ were used.

When the volume of en was less than 0.231 mL, excess Fe^{2+} ions and sulfur powder cannot form the complexes with en, which might affect the dispersion, nucleation, and reaction of Fe^{2+} ions with sulfur. This may be the reason why other impurities formed besides the pyrite and marcasite phases when no en or 0.2 mL of en was added in the reaction solution. 28

Figure 2.10 Figure 2.11 The SEM images of the hierarchical microspheres synthesized using $FeCl_3 \cdot 6H_2O$ (a) and $FeSO_4 \cdot 7H_2O$ (b) as iron reagents in an ethylenediamine aqueous solution (2.2 mL of en:17 mL of water) containing 0.6 g of PVP at 200°C for 24 h. (c) The XRD patterns show the products synthesized with $FeCl_3 \cdot 6H_2O$(I) and $FeSO_4 \cdot 7H_2O$(II). The XRD peaks of marcasite FeS_2 are marked as "+" and magnetite Fe_3O_4 as "#". 30

Figure 3.1 (A) XRD patterns and (B) Raman spectra of NC-ODA and NC-OLA showing the pure pyrite phase. (C and D) Size distribution of NC-ODA and NC-OLA pyrite NCs dispersed in chloroform determined by DLS. 38

Figure 3.2 (A) UV-Vis-NIR spectra of NC-ODA and NC-OLA. (B and C) Plots of $(\alpha h\nu)^n$ vs. $h\nu$ with n = 1/2 (blue line) and 2 (red line) for obtaining the indirect bandgap and the first and second direct transitions. (D) The indirect bandgap of pyrite NCs plotted against the radius of NCs based on Eqn. 4.1 40

Figure 3.3 (A and B) TEM and (C and D) STEM images of NC-ODA (A and C) and NC-OLA (B and D) pyrite NCs. 42

Figure 3.4 (A and C) TEM images of the pyrite NCs synthesized by using OLA as the solvent to dissolve both sulfur and iron agents and the concentrations of the reactants were noted as 2C. (B and D) TEM and (E) HRTEM images of the pyrite NCs synthesized by using OLA as the solvent but the concentrations of the reactants were noted as 1C. (F) Raman spectra of the synthesized pyrite NCs with the reactant concentrations of 1C and 2C, respectively. 44

Figure 3.5 (A and B) The TEM images and (C) the hydrodynamic size distribution of the pyrite NCs synthesized by using ODA and TOPO to dissolve the iron source and DPE to dissolve sulfur. (D) The XRD patterns of the products synthesized by using OLA and

TOPO to dissolve the iron source compared to using ODA and TOPO. Sulfur powder was dissolved with DPE and the concentrations of the reactants were 2C for both reactions. 46
Figure 3.6 (A) The XRD patterns of the products using OLA plus TOPO and OLA plus Diol to dissolve $FeCl_2 \cdot 4H_2O$, respectively. Sulfur powder was dissolved in OLA for both reactions. (B) The TEM image of the quasi-cubic NC agglomerates synthesized by using OLA plus TOPO to dissolve $FeCl_2 \cdot 4H_2O$. (C) The SEM image of the quasi-cubic NC agglomerates synthesized by using OLA plus Diol to dissolve $FeCl_2 \cdot 4H_2O$. 46
Figure 3.7 (A) XRD patterns of the products synthesized under the same conditions as those for NC-ODA but with lower molar ratio of sulfur to iron from 6: 1 to 4: 1 and 2: 1, respectively. The XRD peaks belong to pyrite FeS_2, greigite Fe_3S_4, and pyrrhotite $Fe_{1-x}S$ and are marked as P, G, and Pht, respectively. (B) XRD patterns of the products synthesized under the same conditions as those for NC-ODA but at 250 and 120°C, respectively. (C and D) TEM images of the products synthesized with the molar ratio of sulfur to iron as 4: 1 and 2:1, respectively. The pyrrhotite $Fe_{1-x}S$ phase NCs are shown as the hexagonal plates indicated by the white arrows for example..... 47
Figure 4.1 (A) XRD and (B-I) DLS results and TEM images of the products reacted after the injection of the sulfur precursor in DPE to the iron precursor in ODA at 120°C for 30 min and at 220°C for 5, 10, 20, and 30 min and 2, 4, and 12 h, respectively. 54
Figure 4.2 A representative point EDX spectrum under the STEM mode on a mackinawite nanosheet obtained at 120°C for 30 min. 55
Figure 4.3 HRTEM images of iron pyrite NCs as spherical-like monomers (A, B) and formed via OA of two (C, D) and multiple (E, F) monomers along with their FFT images. Facets and planes are indicated by the dotted lines. The scale bar is 5 nm. 59
Figure 4.4 The atomic structures of the pyrite FeS_2 (001) surface with three different terminations. Side- and top-view are shown in the top and bottom rows, respectively. Blue balls are iron atoms and yellow balls are sulfur atoms. The unit cell is indicated

by the green dotted line. In the top-view, the dangling bonds are terminated by hydrogen atoms in red. Only the top two layers are shown in the top-view..... 62
Figure 4.5 The atomic structures of the pyrite FeS_2 (210) surface with six different terminations. Side- and top-view are shown in the top and bottom rows, respectively. Blue balls are iron atoms and yellow balls are sulfur atoms. The unit cell is indicated by the green dotted line. In the top-view, the dangling bonds are terminated by hydrogen atoms in red. Only the top two layers are shown in the top-view. 63
Figure 4.6 The atomic structures of the pyrite FeS_2 (111) surface with five different terminations. The side- and top-view are shown in the top and bottom rows, respectively. Blue balls are iron atoms and yellow balls are sulfur atoms. The unit cell is indicated by the green dotted line. In the top-view, the dangling bonds are terminated by hydrogen atoms in red color. Only the top two layers are shown in the top-view. Only the top two layers are shown in the top-view. 64
Figure 4.7 (A-D) HRTEM images and the corresponding FFT patterns of pyrite iron disulfide NCs formed by possible point-contact and interparticle growth of orientated attachment. The direction of the long axis is indicated by the white arrows. Zone axis for each HRTEM image is indicated. Scale bars are 5 nm. 68
Figure 4.8 (A-C) HRTEM images and FFT patterns of faceted pyrite iron disulfide NCs formed by the reaction of iron precursor in ODA and sulfur precursor in DPE at 220°C for 12 h. Facets are highlighted by dotted lines. Scale bars are 5 nm. 69
Figure 4.9 (A) and (B) The TEM images and (C) the corresponding XRD results of iron pyrite NCs synthesized by the reaction of iron precursor in OLA and sulfur precursor in DPE at 220ºC for 2 and 4 h, respectively. 70
Figure 4.10 (A and B) HRTEM images and FFT patterns of the typical iron pyrite NCs synthesized by the injection of the sulfur precursor in DPE to the iron precursor in OLA and the reaction at 220°C for 4 h. Scale bars are 5 nm..... 71
Figure 4.11 HRTEM images and FFT patterns of the complicated iron pyrite NCs formed by the injection of the sulfur precursor in DPE to the iron precursor in OLA and the reaction at 220°C for 4 h. Scale bars are 5 nm. 72

Figure 5.1 Diagram of an equivalent circuit of a solar cell. 78
Figure 5.2 (A) UV-Vis absorption spectra and (B) PL spectra of CdSe QDs synthesized by reacting at 280°C for 2-30 min. The size of CdSe QDs was calculated from the wavelength of the first excitonic absorption peak of the UV-Vis spectra. 84
Figure 5.3 (A) UV-Vis absorption spectra and (B) PL spectra of CdSe NRs synthesized by reacting at 250°C for 1-30 min. 84
Figure 5.4 The XRD result of the product after 2 min's reaction at 250°C. (B) and (C) The TEM and HRTEM image of the same sample. (D) The TEM image of CdSe NRs synthesized by reacting at 250°C for 30 min. 86
Figure 5.5 (A) UV-Vis absorption spectra and (B) PL spectra of pure P3HT film and the hybrid CdSe QDs:P3HT films with 60 wt%, 80 wt%, and 85 wt% of CdSe QDs. Blend films of almost similar thickness (ca. 100 nm) for all CdSe QDs:P3HT ratios were spin-coated on ITO coated glass with a 36 nm ZnO NPs layer to eliminate the influence of the film thickness. 86
Figure 5.6 (A) and (B) Schematics of a hole-only and an electron-only device, respectively. (C) and (D) The dark J-V characteristics of a hole-only and an electron-only device, respectively. The solid lines are fit to the SCLC regions using Eq. 6.8. The active layers in hole-only and electron-only devices are composed of 85 wt% of CdSe QDs and P3HT. 88
Figure 5.7 (A) A TEM image of CdSe QDs synthesized with the average size of 6.3 ± 0.2 nm. (B) Schematic of an inverted OIHSC with CdSe QDs:P3HT as the active layer. (C) Typical J-V characteristics of the inverted devices under 1 sun AM 1.5G solar illumination. (D) EQE as a function of the wavelength of those inverted solar cells. Devices were fabricated with a structure of ITO/ZnO/85 wt% CdSe QDs:P3HT/HTL/Ag. A MoO_3 only, a PEDOT:PSS only, or a PEDOT:PSS/MoO_3 were used as the HTL. The thickness of PEDOT:PSS and MoO_3 are 40 and 10 nm, respectively. 89
Figure 5.8 Typical J-V characteristics of the inverted devices under 1 sun AM 1.5G solar illumination. Devices were fabricated with a structure of ITO/ZnO/80 wt% CdSe

QDs:P3HT/HTLs/Ag. A MoO_3 only, a PEDOT:PSS only, or a PEDOT:PSS/MoO_3 were used as the HTL. The thickness of PEDOT:PSS and MoO_3 are 40 and 10 nm, respectively. 91
Figure 5.9 The energy band diagrams of the materials used in the inverted hybrid CdSe QDs:P3HT solar cells. The energies (in eV) are all referenced from the vacuum level. 93
Figure 5.10 AFM images of 85 wt% (A) and 80 wt% (B) CdSe QDs:P3HT films on ZnO coated ITO glass. 94
Figure 5.11 Typical semilog scale J-V plots of inverted CdSe QDs:P3HT solar cells in the dark. Devices were fabricated with a structure of ITO/ZnO/85 wt% CdSe QDs:P3HT/HTL/Ag. A MoO_3 only, a PEDOT:PSS only, or a PEDOT:PSS/MoO_3 were used as the HTLs. The thickness of PEDOT:PSS and MoO_3 are 40 and 10 nm, respectively. 95
Figure 5.12 (A) V_{OC} and FF as a function of logarithmic scaled light intensity. A fit of V_{OC} and logarithmic light intensity to the simple Shockley equation is shown. Ideality factor (n) is determined to be 2.2. (B) J_{SC} and PCE as a function of light intensity in a double logarithmic scale. A fit of J_{SC} and light intensity (I) to the relationship of $J_{SC} \propto I^{\alpha}$ with $\alpha = 1.43$ is shown. Devices were fabricated with a structure of ITO/ZnO/85 wt% CdSe QDs:P3HT/ PEDOT:PSS/MoO_3/Ag. The thickness of PEDOT:PSS and MoO_3 are 40 and 10 nm, respectively. 97
Figure 5.13 (A) UV-Vis absorption spectra and (B) PL spectra of pure PTB7-F20 film and the hybrid CdSe QDs:PTB7-F20 films with 60 wt% and 85 wt% of CdSe QDs. Blend films of almost similar thickness (ca. 100 nm) for all CdSe QDs:PTB7-F20 ratios were spin-coated on ITO coated glass with a 36 nm ZnO NPs layer to eliminate the influence of the film thickness. 99
Figure 5.14 Typical J-V characteristics of the inverted CdSe:PTB7-F20 solar cells under AM 1.5G 1 sun illumination. Devices were fabricated with a structure of ITO/ZnO/85 wt% CdSe:PTB7-F20/PEDOT:PSS/MoO_3/Ag. CdSe QDs or a CdSe QDs + CdSe

NRs (weight ratio = 2:1) were used as the acceptors. The thickness of PEDOT:PSS and MoO_3 are 40 and 10 nm, respectively. 101
Figure 6.1 Schematics of a two-step solution-process method to prepare the $CH_3NH_3Sn_xPb_{1-x}I_3$ layers. The $CH_3NH_3Sn_xPb_{1-x}I_3$ polycrystalline films were obtained by only-thermal annealing or thermal annealing plus DMF or DMSO solvent vapor-assisted thermal annealing. The chemical structures of DMF and DMSO solvents are also shown... 108
Figure 6.2 (A) XRD patterns of the PbI_2, $Sn_{0.1}Pb_{0.9}I_2$, and $Sn_{0.25}Pb_{0.75}I_2$ films. The peaks belong to ITO are labeled by asterisk. (B-D) SEM images of PbI_2, $Sn_{0.1}Pb_{0.9}I_2$, and $Sn_{0.25}Pb_{0.75}I_2$ films, respectively..... 110
Figure 6.3 The first frame (2θ from 10° to 40°) and the second frame (2θ from 40° to 70°) of 2D X-ray diffraction patterns of the PbI_2 (A and B), $Sn_{0.1}Pb_{0.9}I_2$ (C and D), and $Sn_{0.25}Pb_{0.75}I_2$ (E and F) films. The scale of 2θ increases from right to left. 111
Figure 6.4 XRD patterns of the $CH_3NH_3PbI_3$, $CH_3NH_3Sn_{0.1}Pb_{0.9}I_3$, and $CH_3NH_3Sn_{0.25}Pb_{0.75}I_3$ films. The perovskite layers were prepared with the only-thermal annealing (A), or the thermal plus DMF (B) or DMSO (C) vapor-assisted thermal annealing. 113
Figure 6.5 The first frame (2θ from 10° to 40°) and the second frame (2θ from 40° to 70°) of 2D X-ray diffraction patterns of the $CH_3NH_3PbI_3$ (A and B), $CH_3NH_3Sn_{0.1}Pb_{0.9}I_3$ (C and D), and $CH_3NH_3Sn_{0.25}Pb_{0.75}I_3$ (E and F) films prepared via only-thermal annealing. The scale of 2θ increases from right to left..... 115
Figure 6.6 SEM images and grain size distributions of the $CH_3NH_3PbI_3$ (A, B, C, and D), $CH_3NH_3Sn_{0.1}Pb_{0.9}I_3$ (E, F, G, and H), and $CH_3NH_3Sn_{0.25}Pb_{0.75}I_3$ (I, J, K, and L) films. The perovskite layers were prepared with the only-thermal annealing, or thermal annealing plus DMF or DMSO vapor-assisted thermal annealing. 116
Figure 6.7 Cross-sectional SEM images of the $CH_3NH_3PbI_3$, $CH_3NH_3Sn_{0.1}Pb_{0.9}I_3$, and $CH_3NH_3Sn_{0.25}Pb_{0.75}I_3$ films. The perovskite layers were prepared with the only-thermal annealing (A, D, and G), or the DMF (B, E, and H) or DMSO (C, F, and I) vapor-assisted thermal annealing. 117
Figure 6.8 Schematics of the possible bond breaking of Sn-I (or Pb-I) in $CH_3NH_3Sn_xPb_{1-x}I_3$ perovskite grains via DMSO attacking during the thermal plus DMSO vapor-assisted

thermal annealing process, leading to large, flat grains and the redistribution of Pb and Sn in grains. 120
Figure 6.9 (A) Device configuration of a planar $CH_3NH_3Sn_xPb_{1-x}I_3$ perovskite solar cell. (B) Energy diagram for materials involved in the solar cells. (C) Typical J-V characteristics and (D) EQE spectra of $CH_3NH_3Sn_xPb_{1-x}I_3$ (X = 0, 0.1, and 0.25) perovskite solar cells under 1 sun AM 1.5G solar illumination with the perovskite layers prepared via only-thermal and thermal plus DMSO vapor-assisted annealing. 121
Figure 6.10 Typical J-V characteristics of $CH_3NH_3Sn_xPb_{1-x}I_3$ (x = 0, 0.10, and 0.25) perovskite solar cells under 1 sun AM 1.5G solar illumination. The perovskite layers were prepared with the thermal plus DMF vapor-assisted thermal annealing. 125
Figure 6.11 (A) Energy diagram for materials involved in the planar perovskite solar cells. (B) Typical J-V characteristics of $CH_3NH_3Sn_xPb_{1-x}I_3$ (x = 0.5, 0.9, and 1.0) perovskite solar cells under 1 sun AM 1.5G solar illumination. The perovskite layers were prepared via the only-thermal annealing. 126
Figure 6.12 XRD patterns of the $CH_3NH_3Sn_{0.5}Pb_{0.5}I_3$ (A), $CH_3NH_3Sn_{0.75}Pb_{0.25}I_3$ (B), and $CH_3NH_3SnI_3$ (C) films prepared by the two-step solution-process followed by the only-thermal annealing. Additional peaks at 26.4° and 32.2° marked in red arrows are ascribed to the oxidized Sn^{4+} in the form of $(CH_3NH_3)_2SnI_6$ crystal. 128
Figure 7.1 The SEM images of iron sulfide materials synthesized by reacting $Fe(NO_3)_3{\cdot}9H_2O$ with thiourea at 180°C for 12 h in en. The concentration of $Fe(NO_3)_3{\cdot}9H_2O$ in the reactor is (A) 0.005 mol/l, (B) 0.03 mol/l, (C) 0.04 mol/l, and (D) 0.08 mol/l. Fe:S ratio was kept as 1:4. 139
Figure 7.2 The SEM images of iron sulfide materials synthesized by reacting $Fe(NO_3)_3{\cdot}9H_2O$ with thiourea at 180°C for 12 h in en. The concentration of $Fe(NO_3)_3{\cdot}9H_2O$ in the reactor was kept as 0.005 mol/l. Fe:S ratio was (A) 1:4 and (B) 1:6, respectively. (C) Bundles were formed after drying sample-7 at room temperature. 140
Figure 7.3 The SEM images of iron sulfide materials synthesized by reacting (A) $FeCl_3{\cdot}6H_2O$ or (B) $FeCl_2{\cdot}4H_2O$ with thiourea at 180°C for 12 h in en. The concentration of

$FeCl_3 \cdot 6H_2O$ or $FeCl_2 \cdot 4H_2O$ in the reactor was kept as 0.005 mol/l. Fe:S ratio was 1:4. (C) and (D) are the typical SEM images for wire and plates. A layered structure was observed for both morphologies. 141

Figure 7.4 The SEM images of synthesized (A) wires, (B) rods and (C) plates. The red crosses indicate the spots where the EDS were performed. The Fe:S atomic ratio of the spot shown in figures is found to be 1:1.36, 1:1.53, and 1:1.12 for nanowires, NRs and plates. 141

Figure 7.5 The SEM images of iron sulfide materials synthesized by reacting $Fe(NO_3)_3 \cdot 9H_2O$ with thiourea at (A) 180°C, (B) 195°C, and (C) 210°C for 12 h in en. The concentration of $Fe(NO_3)_3 \cdot 9H_2O$ in the reactor was kept as 0.005 mol/l. Fe:S ratio was 1:4. 142

Figure 7.6 (A) Survey scan and (B) XPS S_{2p} spectrum of sample-3 synthesized by reacting $Fe(NO_3)_3 \cdot 9H_2O$ with thiourea at 180°C for 12 h in en. The concentration of $Fe(NO_3)_3 \cdot 9H_2O$ in the reactor is 0.04 mol/l and Fe:S ratio was kept as 1:4. (C) Survey scan and (D) XPS S_{2p} spectrum of a naturally occurring pyrite sample..... 143

Figure 7.7 The TEM images of synthesized iron sulfide (A) wires, (B) rods and (C) plates.(D) Bubbles indicated by white arrows were generated when the electron beam is focused on the sample. (E) Voids were clearly observed in the samples heated with electron beams. (F) A HRTEM image shows the synthesized wires were amorphous. 144

Figure 7.8 The STEM images of synthesized iron sulfide (A) wires with square cross section and (B) core-shell wires. 145

Figure 7.9 The SEM images of iron sulfide (A) wires and (B) plates annealed at 700°C for 30 min under the protection of nitrogen. (C) The XRD and (D) TGA results of sample-3(I) and sample-8 (II). TGA result of a naturally occurring pyrite sample was used as a contrast. 146

LIST OF SCHEMES

Scheme 1.1 Illustrations of NC growth controlled by OR mechanism and OA mechanism. An attachment occurs at a planar interface of two particles sharing the common crystallographic facets or via a "point contact" along an energy favorite crystallographic direction followed by the subsequent inter-particle growth..... 10

Scheme 2.1 Structures of en and PVP. 19

Scheme 2.2 Illustration of a possible mechanism for the formation of pyrite FeS_2 hierarchical microparticles..... 25

Scheme 4.1 (A) Illustration of the nucleation of pyrite iron disulfide within the pre-formed mackinawite crystalline nanosheets and the growth of NCs through OA in the early stage (0-20 min) at 220°C and (B) Illustration of the isolation of individual larger NCs from NC clusters and the growth of the faceted anisotropic NCs through OR with the proceeding of reaction (30-120 min). 57

Scheme 4.2 (A) Illustration of an orientated attachment via sharing the common crystallographic facets at a planar interface and (B) Illustration of an orientated attachment via a "point contact" along an energy favorite crystallographic direction followed by the subsequent interparticle growth. 57

Scheme 4.3 Illustrations of the attachment through (A) (001)-2S and (001)-Fe and (B) (210)-2S and (210)-Fe planes. Dotted red lines indicate the positions where the bonds are formed through the OA. 66

Scheme 5.1 An illustration of the morphology dependence of (A) CdSe QDs + CdSe NRs:PTB7-F20 film and (B) CdSe QDs + CdSe NRs:P3HT film on the substrate coated with ZnO layer. The percolation pathways were marked as white lines in the illustrations. Electrons were collected by the cathode through a ZnO layer. 98

LIST OF TABLES

Table 2.1 Summary of the (100) and (111) surfaces of pyrite FeS_2 terminated in different layers. X: the outmost surface atoms; N_{Fe} and N_S: the number of dangling bonds of iron and sulfur atoms, respectively. 21

Table 3.1 Summary of the reaction conditions and the phase and morphology of the products. . 35

Table 4.1 Summary of the (001), (210), and (111) surfaces of pyrite FeS_2 terminated in different layers. X: the outmost surface atoms; N_{Fe} and N_S: the number of dangling bonds of iron and sulfur atoms, respectively. The surface free energies of each terminated layer are estimated at the two fixed changes in sulfur chemical potential ($\Delta\mu_s$ = -0.3 and -0.8) in Figure 7 of ref. [164] to represent the S-rich and S-lean conditions, respectively. 61

Table 5.1 Summary of the performance parameters of inverted hybrid CdSe QDs:P3HT solar cells under AM 1.5G 1 sun illumination. Devices were fabricated with a structure of ITO/ZnO/85 wt% CdSe QDs:P3HT/HTL/Ag. A MoO_3 only, a PEDOT:PSS only, or a PEDOT:PSS/MoO_3 were used as the HTL. The thickness of PEDOT:PSS and MoO_3 are 40 and 10 nm, respectively. 90

Table 5.2 Summary of the performance parameters of inverted hybrid CdSe QDs:P3HT solar cells under AM 1.5G 1 sun illumination. Devices were fabricated with a structure of ITO/ZnO/80 wt% CdSe QDs:P3HT/HTLs/Ag. A MoO_3 only, a PEDOT:PSS only, or a PEDOT:PSS/MoO_3 were used as the HTLs. The thickness of PEDOT:PSS and MoO_3 are 40 and 10 nm, respectively. 92

Table 5.3 Summary of the performance parameters of inverted CdSe:PTB7-F20 solar cells under AM 1.5G 1 sun illumination. Devices were fabricated with a structure of ITO/ZnO/85 wt% CdSe:PTB7-F20/PEDOT:PSS/MoO_3/Ag. CdSe QDs or a CdSe QDs + CdSe NRs (weight ratio = 2:1) were used as the acceptors. The thickness of PEDOT:PSS and MoO_3 are 40 and 10 nm, respectively. 102

Table 6.1 PV performance parameters of the $CH_3NH_3Sn_xPb_{1-x}I_3$ (x = 0, 0.1, and 0.25) perovskite solar cells under 1 sun AM 1.5G solar illumination. The $CH_3NH_3Sn_xPb_{1-x}I_3$ perovskite films were prepared via the only-thermal annealing or the thermal plus DMSO vapor-assisted thermal annealing. 122
Table 6.2 PV performance parameters of the $CH_3NH_3Sn_xPb_{1-x}I_3$ (x = 0, 0.1, and 0.25) perovskite solar cells under 1 sun AM 1.5G solar illumination. The $CH_3NH_3Sn_xPb_{1-x}I_3$ perovskite films were prepared via the thermal plus DMF vapor-assisted thermal annealing. 125
Table 6.3 PV performance parameters of the $CH_3NH_3Sn_xPb_{1-x}I_3$ (x = 0.5, 0.9, and 1.0) perovskite solar cells under 1 sun AM 1.5G solar illumination. The $CH_3NH_3Sn_xPb_{1-x}I_3$ perovskite films were prepared via the only-thermal annealing process. 127
Table 7.1 Summary of the reaction conditions and morphology of the major products. 137

ACKNOWLEDGEMENTS

It seems long, five years' graduate study in University of Washington is actually very short in one's life. There are many people that I owe much gratitude to. First and foremost, I would like to thank my advisor Prof. Qiuming Yu for her guidance, encouragements, patience, and generous support to conduct research in the emerging solar cells. I could feel her passion for photovoltaics from day one when I met her. I really appreciate her patience when my progress doesn't go well. She is always willing to help you even when she is very, very busy. I am also grateful to her for the great opportunities to interact with several "big names" in this field at international conferences.

I would like to thank Prof. Stuart B. Adler, Prof. Fumio S. Ohuchi, Prof. Guozhong Cao, and Prof. Hong Ma for their time to serve on my supervisory committee. Their comments and suggestions on my general exam are very constructive and inspiring. I cannot make huge improvements without their critical reviews.

Many thanks go to all previous and present members of Dr. Yu's group for their help and support in one way or another, especially, Dr. Beau J. Richardson, Fang Sun, John Bae, Dr. Jiajie Xu, Jessica Tanumihardja, Brian Yuh, Ahmed Alamer, Stefan Schoen, Monica Esopi, and David Galvan. It was a great pleasure and a lot of fun to work with them. I also would like to express my gratitude to staffs such as, Scott Braswell, Dr. Alec Pakhomov, and Dr. Paul Wallace in UW NanoTech User Facility.

This research would not have been possible without the financial support provided by the American Chemical Society Petroleum Research Funds (ACS PRF), the National Science Foundation (NSF), the Defense Threat Reduction Agency (DTRA), the University of Washington (UW) faculty start-up funds, and the UW site of the National Nanotechnology Infrastructure Network (NNIN) supported by the National Science Foundation (NSF).

Finally, I would like to acknowledge the support of my family and my friends throughout the pursuit of my Ph.D. Thanks to everyone.

DEDICATION

To my parents and to my beloved Cindy J. H.

Chapter 1 INTRODUCTION

1.1 Overview

With industrial development and population growth in recent decades, global energy demand for conventional energy resources such as coal, petroleum, and natural gas has been rapidly increased. To date, over 80% of energy consumption is from non-renewable fossil fuels, which causes the environmental pollution and global-warming issues.[1] As the resources of global energy are diminishing, the search for the potential use of renewable energy such as hydro, wind, tide, solar, and geothermal energy sources becomes crucial. Among them, solar energy is the most prominent resource to alternate fossil fuels due to the abundant energy origin from the sun.[2-7]

Solar energy is divided into two different types as thermal and photovoltaic (PV) energy. Solar thermal energy systems absorb the sunlight as a heat source and utilize the heat to generate electricity. While, PV cells harvest the solar energy as a direct conversion procedure generating electrical charge carriers and thus PV cells have the advantages over solar thermal energy systems with scalable installation, the ability to work under diffuse light, and the excellent compatibility for distributed application.[7]

PV technology has gone through three stages. The first generation solar cell is based on crystalline silicon and polycrystalline silicon. Since the first practical fabrication of solar cell from a silicon p-n junction, silicon solar cells are currently leading in PV cells market with the power conversion efficiency (PCE) in the range of 18-28%[8] (Figure 1.1). However, purity as high as 99.9999% of silicon is often required to enhance charge transport and reduce charge recombination caused by defects.[9] In order to efficiently absorb sunlight, typically 300 μm silicon active layer is employed.[10] This makes silicon solar cells expensive. One approach to reduce manufacture costs with the trade-off of reduced efficiency is to produce thin film solar cells based on copper indium gallium selenide (CIGS),[11-13] copper zinc tin sulfide selenide (CZTSSe),[14, 15] CdTe,[16, 17] and amorphous Si.[18] These are so-called second generation solar cells. During the past decades, great efforts were made to reduce the cost and improve the PCE of CIGS, CZTSSe, CdTe, and amorphous Si solar cells. PCE as high as 23.3%, 12.6%, 20.4%, and 13.4% are achieved for CIGS, CZTSSe, CdTe, and amorphous Si solar cells (Figure 1.1). Technologies based

on CIGS, CZTSSe, and CdTe are operational but not fully successful and is facing difficulties in large-scale production.[19] The target of the development of third generation solar cells is to adopt cheaper deposition technology, utilize new device concepts such as hot carrier collection,[20, 21] intermediate bands,[22, 23] heterojunction cells,[24, 25] tandem cells,[26, 27] and dye-sensitized solar cells (DSSC),[28, 29] and the development of solar cells using low cost materials such as pyrite FeS_2,[30-33] In_2S_3,[34, 35] and perovskites ($CH_3NH_3PbX_3$, X=halogen).[36-38]

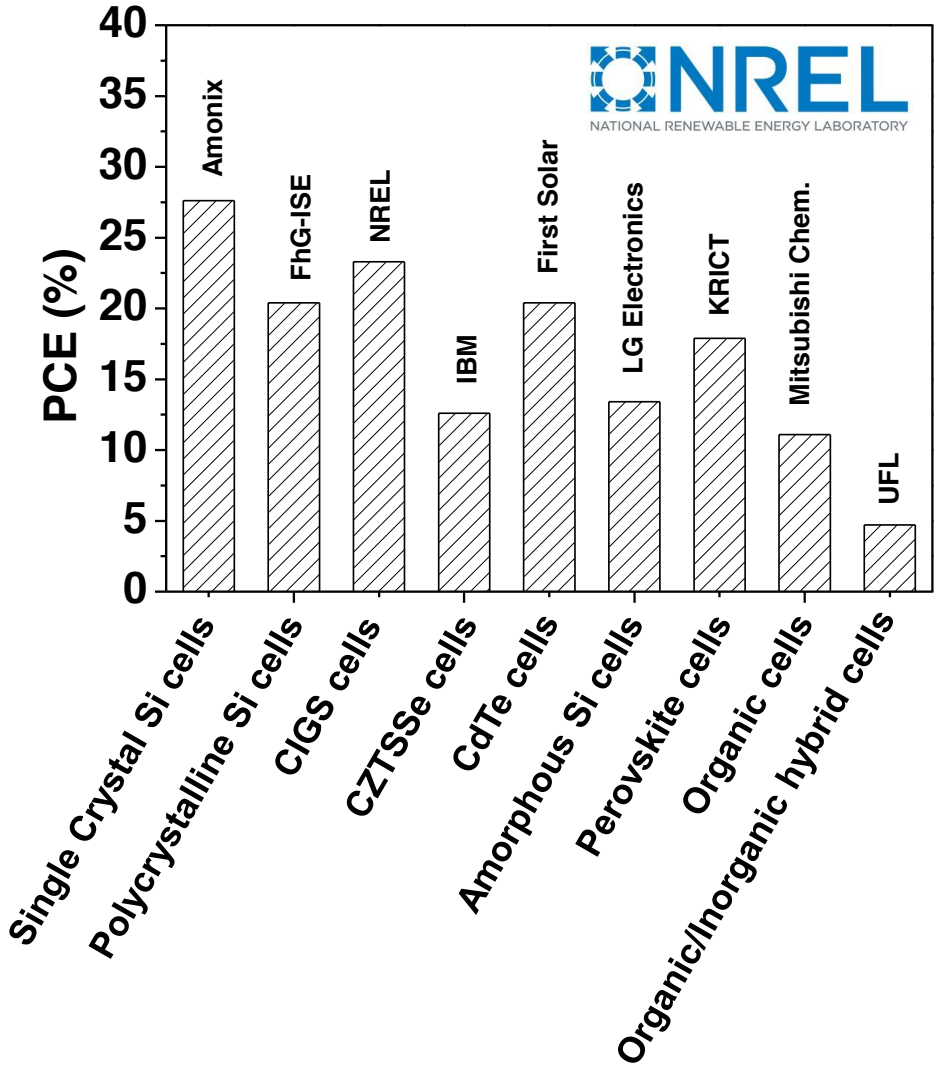

Figure 1.1 The record efficiency of the typical solar cells certified by National Renewable Energy Laboratory (NREL) (Data were extracted from ref.[39]).

1.2 Bulk Heterojunction (BHJ) Solar Cells

The inter-mixing of donor-acceptor materials in a single layer revolutionized the PV technology. The BHJ structure offers a high density of heterojunction interfaces in the device, and the structure can be easily prepared by solution or vacuum deposition techniques. Generally, a BHJ solar cell is composed by two components, donor and acceptor. Conjugated polymer and fullerene derivatives are used as the electron donors and acceptors, respectively. Until now, a record PCE as high as 11.1% is achieved by Mitsubishi Chemical Corporation[40] (Figure 1.1). Although fullerene derivatives, including [6, 6]-phenyl C_{61}-butyric acid methyl ester ($PC_{61}BM$) and [6, 6]-phenyl C_{71}-butyric acid methyl ester ($PC_{71}BM$), have many advantages such as a deep-lying lowest unoccupied molecular orbital (LUMO) (-3.8~-4.2 eV),[41] reversible reduction with ability to accept up to six electrons,[42] ultra-fast three-dimensional charge transfer,[43] and high electron mobility,[44] they are lack of strong absorption in the solar spectrum region and suffer from poor photochemical stability in air. Thus, the development of new non-fullerene acceptor materials such as CdSe quantum dots (QDs) and non-toxic and environmental stable FeS_2 nanocrystals (NCs) which have a strong absorption in the solar spectrum is an important goal for the BHJ solar cell research.

1.3 Inverted BHJ Solar Cells: Device Parameters, Architecture, and Operation Principles

1.3.1 Device Parameters

Solar cells are characterized under standard simulated illumination (AM 1.5G spectrum, 25°C). The main parameters that are used to characterize the performance of a solar cell are the open-circuit voltage (V_{OC}), the short-circuit current density (Jsc), the fill factor (FF), the peak power (P_{max}), and the external quantum efficiency (EQE). These parameters are determined from the illuminated current density-voltage (J-V) characteristic as illustrated in Figure 1.3.

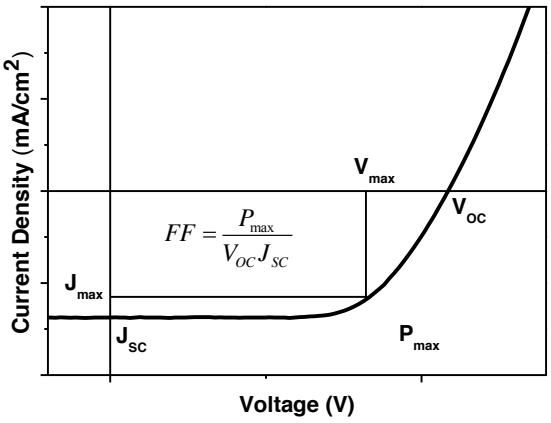

Figure 1.2 A typical J-V characteristics of solar cells under illumination.

The V_{OC} is the maximum voltage a solar cell can provide to an external circuit and is defined as the voltage at zero current (Figure 1.3). The empirically expression is given by the equation:

$$V_{oc} = e^{-1} \times (\left| E_{HOMO}{}^{donor} \right| - \left| E_{LUMO}{}^{acceptor} \right| - 0.3 \text{ eV}) \quad (1.1)$$

Where e is the elementary charge, E is the energy level, and 0.3 eV is an empirical value for efficient charge separation. Thus, a donor polymer with a lower HOMO level and an acceptor inorganic semiconductor with higher LUMO will give a higher V_{OC}. J_{SC} is the current through the solar cell when the voltage across the solar cell is zero (Figure 1.3). J_{SC} is affected by bandgap of acceptor polymer, carrier mobility of donor and acceptor, intermolecular interaction between polymer chains, interface between inorganic semiconductor, and polymer and molecular chain packing. P_{max} is a product of V_{max}, the voltage at maximum power and J_{max}, the current at maximum power. The FF is defined as the ratio between the maximum obtainable power and the product of J_{SC} and V_{OC} (Figure 1.3). It is affected by many factors, including charge carrier mobility and balance, interface recombination, series and shunt resistances, film morphology, and miscibility between the donor and acceptor.

The PCE of solar cells, which gives the standard value to evaluate the device performances, is determined from these parameters as:

$$PCE = \frac{p_{\max}}{P_i} = \frac{V_{\max} \times J_{\max}}{P_i} = FF \frac{V_{OC} \times J_{SC}}{P_i} \quad (1.2)$$

Where P_i is the power of incident light.

The EQE as a function of wavelength (λ) is the ratio between the collected photon generated charges and the number of incident photons, ultimately being the product of four efficiencies (η): absorption (A), exciton diffusion (ED), charge separation (CS), and charge collection (CC):

$$EQE(\lambda) = \eta_A(\lambda) \times \eta_{ED}(\lambda) \times \eta_{CS}(\lambda) \times \eta_{CC}(\lambda) \quad (1.3)$$

1.3.2 Device Architecture and Operation Principles

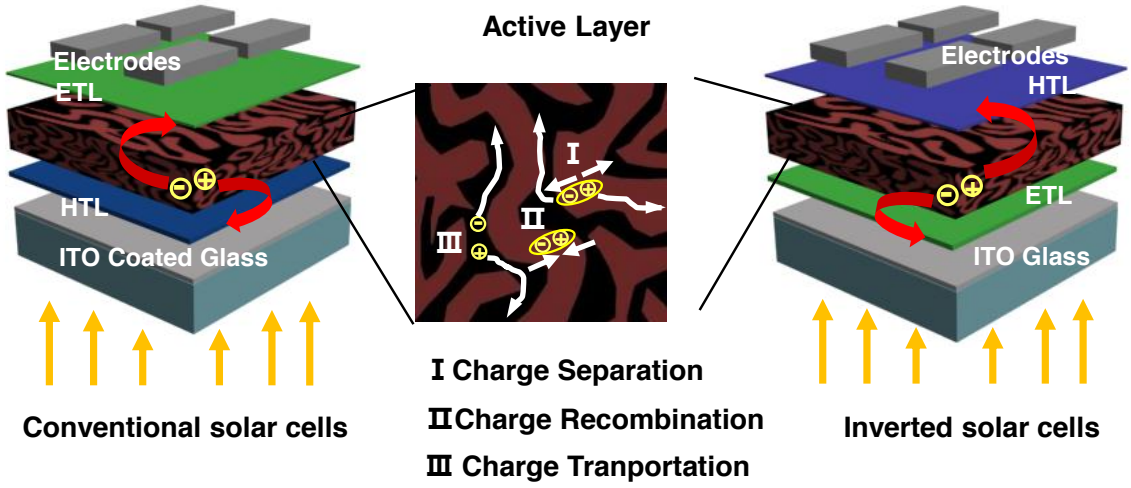

Figure 1.3 Typical device structure of conventional and inverted BHJ solar cells. Inset: An illustration to show charge separation, recombination, and transportation processes in a BHJ layer. Dark brown region is the donor phase and black region is the acceptor phase. HTL: hole tansport layer; ETL: electron transport layer.

Hybrid BHJ solar cells were fabricated either in a conventional or inverted configuration as shown in Figure 1.4. In a conventional hybrid solar cell, the incident light enters through an anode and undergoes several processes: Partial of the light is reflected from the glass surface and most of the light is absorbed in a photoactive layer. The rest of the light transmits through the cell. Reflection and transmission of sunlight do not

contribute to the generation of electrical power and is considered as losses. The absorbed photons in both donor and acceptor generate excitons, which are electron-hole pairs. Those excitons diffuse to organic-inorganic interface during their lifetime. With the help of a build-in electrical field by p-n junction at the interface, excitons are dissociated into the holes and electrons (Figure 1.4 inset I). Next, those charge carriers should overcome the charge recombination (Figure 1.4 inset II) to be transported to their respective electrodes (Figure 1.4 inset III) to generate an external current. Holes are transported toward the anode at the bottom through the donor materials. A HTL is required between the active layer and the anode to block the transfer of electrons to the anode and facilitate hole extraction. Electrons are transported to the cathode at the top via the acceptor materials. An ETL is deposited between the active layer and cathode to prevent the transfer of holes to the cathode. However, these devices are unstable because indium may diffuse into the polymer and thus degrade the performance of polymer solar cells (PSCs). Prolonged exposure of the device in air can cause oxidation of the top electrode and degradation of the active layer. In addition, direct deposition of metal onto the active layer may lead to metal diffusion into the film adversely affecting its semiconducting properties. Thus, inverted hybrid BHJ solar cells with a typical structure of indium tin oxide (ITO)/ETL/BHJ/HTL/Ag or Au were developed to alleviate these issues. In these devices, ITO is used as the cathode. An ETL (e.g. ZnO) is placed on top of ITO to selectively extract electrons to the cathode. Because of this layer, the leakage current in the devices is greatly reduced and the diffusion of indium into the active layer is also prevented. HTL (e.g. poly (3, 4-ethylenedioxythiophene)-poly (styrenesulfonate) (PEDOT:PSS)) is inserted between the active layer and anode. Air-stable high-work-function metals, typically, Ag or Au, were used as the anode. The anode, such as Ag (or Au), which can be formed using coating or printing technology from Ag (or Au) pastes, to simplify and lower the cost of manufacturing.[45, 46]

A HTL serves as a selective contact by extracting holes while concurrently blocking electrons, thereby reducing dark (leakage) current and enhancing the V_{OC}, J_{SC}, and FF. The HTL is inserted between anode and active layer in a hybrid BHJ solar cell. For materials used as HTL, their work functions need to be large enough so that the Fermi levels of HTL

match the HOMO levels of PV polymers, which will help to form ohmic contact with the BHJ layer to improve the V_{OC} and charge-collecting ability of solar cells.[47] Usually, PEDOT:PSS was used as the hole transport layer due to its broad applicability, ease of use, and availability.[31, 48, 49] A high work function of PEDOT:PSS (-4.8~-5.2 eV) helps the anode to form ohmic contact with the BHJ layer to improve the V_{OC} and charge-collecting ability of solar cells.[47] However, PEDOT:PSS suffers from several drawbacks including large electrical and microstructural inhomogeneities,[50] poor electron blocking property,[51] and the tendency of eroding the electrodes.[52, 53] Various transition metal oxides such as nickel oxide (NiO),[54, 55] molybdenum oxide (MoO_3),[47, 56] vanadium oxide (V_2O_5),[57, 58] and tungsten oxide (WO_3)[59] were developed to use as an alternative HTL to PEDOT:PSS. Among these, MoO_3 is one of the most promising materials because of its nontoxic nature, the very deep-lying electronic states, and strongly n-doped by oxygen vacancies.[60, 61] MoO_3 was incorporated into devices either through vacuum deposition[62] or solution based processing such as spin-coating, brush painting, or spray coating. Inverted devices fabricated using MoO_3 as HTL consistently show higher power conversion efficiency than conventional devices using PEDOT:PSS as the bottom electrode interlayer.[63, 64]

1.4 Strategies to Improve the Efficiency of BHJ Solar Cells

In order to improve the efficiency of a BHJ solar cell, the first strategy is to enhance the sunlight absorption. Most of the photovoltaic materials are lack of the absorption in the near infrared region (Wavelength > 800 nm). This part of energy accounts for 40% of the total solar energy. The synthesis of photovoltaic materials with a high absorption coefficient (>10^5 cm^{-1}) especially with the near infrared absorption is one of the solutions to maximize the solar energy harvest. With the enhanced absorption, more photons will be trapped in the active layer. This leads to the increased number of excitons and thus results in higher carrier concentrations. A higher carrier concentration means an increased photocurrent in the fabricated solar cells if electrons and holes are effectively collected at the cathode and anode, respectively.

1.5 Earth-Abundant Solar Absorber

Iron is the fourth abundance element among all the elements in the earth crust, and it is the least expensive metallic element to extract from nature. More than 25 years ago, pyrite

FeS_2 was proposed to use in solar cells.[65] Pyrite FeS_2 are among candidates such as CuS_2, Zn_3P_2, and amorphous Si etc. that could achieve production costs lower than crystalline silicon at 0.039¢/W and produce equal or greater electricity versus crystalline silicon.[66] Compared to other semiconductors which contain toxic substances such as Cd, Te, Ga, In, or Se, pyrite FeS_2 is more attractive for mass production with least pollution to the environment. In addition to the abundance and nontoxicity features of pyrite FeS_2 materials, an absorption coefficient 3.3×10^5 cm^{-1} in the wavelength between 300 and 750 nm[67] provides a unique opportunity among inorganic materials such as $CuInSe_2$, $CuInS_2$, CdTe, and GaAs to use least materials to capture most of the incident solar radiation. For example, only a very thin pyrite FeS_2 absorber layer (< 0.1 μm) can harvest as much sunlight as > 200 μm for single-crystal Si absorber.[68] Besides its exceptional optical properties, pyrite FeS_2 has an indirect and direct band gap at 0.95 and 1.03 eV, respectively. The LUMO and highest occupied molecular orbital (HOMO) of pyrite FeS_2 are determined to be -3.9 eV and -5.6 eV,[31] respectively. Single pyrite crystals are commonly observed to be n-type, which indicates pyrite FeS_2 could be an environmentally stable non-fullerene acceptor with strong absorption in the solar spectrum region.

1.5.1 Synthesis of Pyrite FeS_2 Materials

Iron sulfide system contains a number of phases, such as mackinawite FeS_{1-x}, troilite FeS, pyrrhotite $Fe_{1-x}S$, greigite Fe_3S_4, marcasite FeS_2, and pyrite FeS_2. The crystals structure of these phases are shown in Figure 1.2. Among them, pyrite FeS_2 has a cubic structure with the space group of Pa3 and the lattice constant of 5.418 Å, in which the Fe atoms are octahedrally coordinated by six S atoms, while the S atoms are tetrahedrally coordinated to three Fe atoms and one S atom (Figure 1.2). The Fe atoms are situates at all corners and face center positions, and <111>-oriented S-S dimers are at the center and midpoints of the twelve edges of the unit cell. In solar cell applications, even trace amount of impure phase will cause the low V_{OC} observed in the previous work.[67, 69, 70] Thus, the synthesis of pure pyrite FeS_2 is very crucial for the application of this material in solar cells. Pure pyrite FeS_2 materials are synthesized through high temperature approaches including sulfurization of iron films or iron oxide films,[71-73] reactive sputtering,[74] and spray pyrolysis.[75] Because the segregation of iron and sulfur species is unavoidable at elevated

temperatures, the stoichiometry and phase of the deposited film could be changed, especially at film surfaces, which significantly affects the device performance.[67] Low temperature solution based methods such as hot injection or hydro/solvothermal process were developed to synthesize this material. Hot injection method is typically for the synthesis of pyrite nanoparticles with sizes below 100 nm.[76-79] Hydro/solvothermal process is employed for the synthesis of pyrite particles with the size ranging from 100 nm to several micrometers.[67, 80-83]

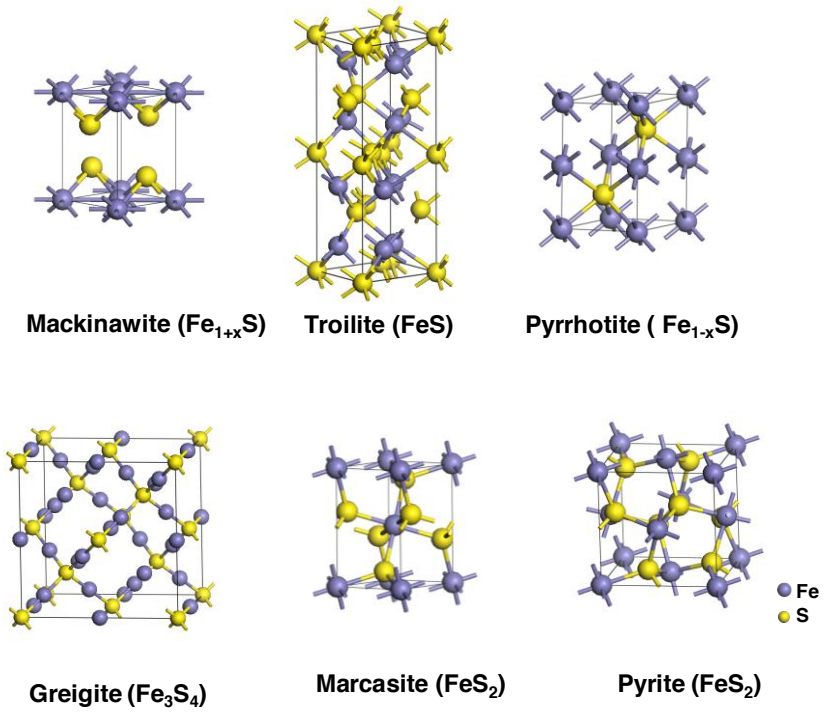

Figure 1.4 The crystalline structure of commonly observed iron sulfide materials including mackinawite FeS_{1-x}, troilite FeS, pyrrhotite $Fe_{1-x}S$, greigite Fe_3S_4, marcasite FeS_2, and pyrite FeS_2.

1.5.2 Growth Mechanism of Nanocrystals (NCs)

The classical Ostwald ripening (OR) crystal growth mechanism is widely used to explain the crystal growth of NCs. It interprets as the larger particles grow at the expense of the smaller particles, driven by a decrease of surface energy (Scheme 1.1). Growth of NCs is mainly controlled by the dissolution of small particles into ions, the diffusion of ions, the property of solvent, and the interface between large particle and solvent. Recently,

in order to explain the growth of particles with exotic shapes such as nanosheets,[84] highly branched, zigzag and helical nanowires, and nanorings,[85-87] a new crystal growth mechanism called "oriented attachment (OA)" is proposed. This mechanism is based on the spontaneous self-organization of adjacent NCs into a single solid particle that share a common crystallographic orientation (Scheme 1.1). The growth of particles undergoes approaching, reorientation, replacing ligand, and attachment. A strong and stable surface adsorption of surfactants or solvent could direct and mediate these processes. NC growth via the OA mechanism generally leads to the formation of anisotropic NCs and sometimes creates defects, such as line and plane defects as well as dislocation along the attachment planes. The driving force of the OA mechanism can be ascribed to an interaction of permanent or temporary electric (or magnetic) dipole movements. The intrinsic crystal lattice, the presence of polar facets, and anisotropic shape of a neutral nanoparticle all can lead to a dipole in the NC.[88]

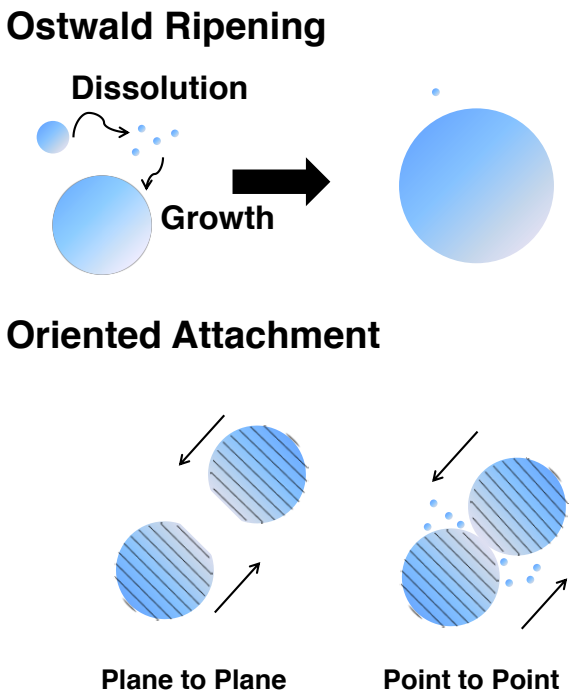

Scheme 1.1 Illustrations of NC growth controlled by OR mechanism and OA mechanism. An attachment occurs at a planar interface of two particles sharing the common crystallographic facets or via a "point contact" along an energy favorite crystallographic direction followed by the subsequent inter-particle growth.

1.6 Emerging Organic-Inorganic Halide Perovskite Solar Cells

In a conventional organic-inorganic hybrid solar cells, charge separation happens at the interface between inorganic nanocrystals and organic polymer. Because of the low permittivity of the organic thin films, the exciton binding energy is high in the active layer. Meanwhile, the size of an inorganic nanocrystal is much larger than that of a polymer chain. All these lead to inefficient charge separation in the conventional organic-inorganic hybrid solar cells. The application of the recently developed material, organic-inorganic halide perovskite, is one of choices to address this issue. Organic-inorganic halide perovskite is a class of materials with the general chemical formula of AMX_3, where M is a small divalent metal ions (e.g., Pb^{2+}, Sn^{2+}, and Ge^{2+}), X is an anion from the halide series (F^-, Cl^-, Br^-, and I^-), and A is a large organic cation and typically restricted to methylammonium (MA, $CH_3NH_3^+$), ethylammonium (EA, $CH_3CH_2NH_3^+$),[89, 90] tetramethylammonium (TMA, $(CH_3)_4N^+$),[91] and formamidinium (FA, $NH_2CH_2{=}NH_2^+$).[92-98] Organic-inorganic halide perovskite materials are promising for PV applications because they have the extraordinary electronic properties of the hybrid organic-inorganic halide perovskites including tunable bandgap,[95, 99] high panchromatic absorption,[100] long carrier diffusion length,[101, 102] and excellent ambipolar charge transport properties.[103]

Since the first report of organolead halide perovskites ($CH_3NH_3PbI_3$ and $CH_3NH_3PbBr_3$) as visible-light sensitizers in photoelectrochemical cells,[104] great progresses have been made to use organometal halide perovkites for PV applications[36-38, 95, 105-109] and the certified PCE has rocketed to 20.1%.[63] In a typical cell shown in Figure 1.5A, $CH_3NH_3PbI_{3-x}Cl_x$ was sandwiched between a n-type compact layer composed by TiO_2 and p-type hole transporter, 2, 2', 7, 7'-tetrakis-(N, N-di-p-methoxyphenylamine) 9, 9'-spirobifluorene (Spiro-OMeTAD) (including lithium bis(trifluoromethylsyfonyl) imide salt and tert-butylpyridine as additives). $CH_3NH_3PbI_{3-x}Cl_x$ was deposited either through vapor deposition or via solution processing. The generated electrons travel through the n-type compact layer and are collected by the cathode. At the same time, the generated holes flow through the p-type electron blocker to the anode. Planar perovskite solar cells were also fabricated in an inverted structure[110-113] as shown in Figure 1.5B. The p-type hole transporter PEDOT:PSS layer is spun on top of ITO coated glass and followed by the fabrication of perovskite layer. $PC_{61}BM$ is commonly used as the n-type electron

transporter. The generated electrons and holes exit devices in the opposite direction compared to those in the conventional structure.

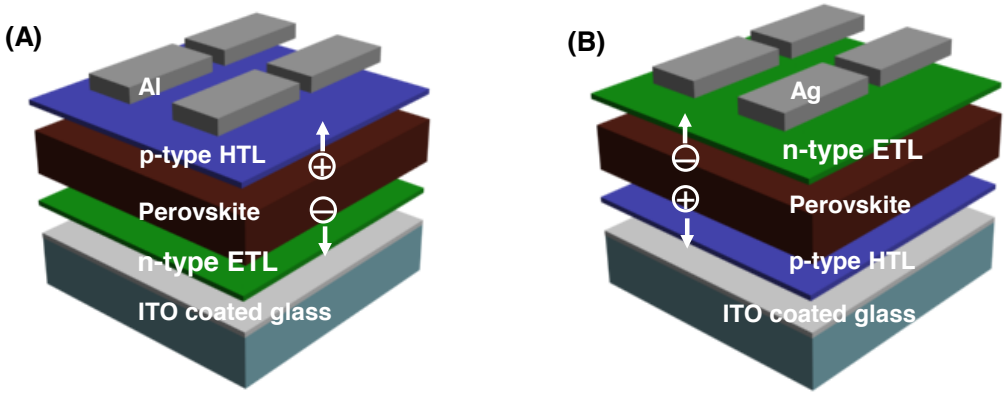

Figure 1.5 Device configurations of planar perovskite solar cells: (A) Conventional device architecture; (B) Inverted device architecture causes electrons and holes to exit the device in the opposite direction.

1.7 Objectives and Goals

The primary goal of this research is to develop the next generation low cost, efficient organic-inorganic hybrid solar cells with the consideration of materials, interface, and device structure. The objectives of this research focus on addressing several issues in this field:

1. Synthesize, characterize, and control the morphology of a non-toxic semiconductors from 10 nm to 4-5 μm to enhance the sunlight absorption;
2. Understand the growth mechanism of the developed semiconductor;
3. Optimize the HTL for an inverted organic-inorganic hybrid solar cell to achieve high efficiency;
4. Realize the fabrication of organic-inorganic hybrid solar cells and correlate the materials composition of the absorber with the solar cell performance.

Pyrite FeS_2 materials were synthesized via low temperature solution based methods including hydro/solvothermal synthesis and hot injection method. Techniques such as scanning electron microscopy (SEM), transmission electron microscopy (TEM), X-ray photoelectron spectroscopy (XPS), thermal gravimetric analysis (TGA), dynamic light scattering (DLS), powder X-ray diffraction (XRD), and Raman spectroscopy were used to

study the size, morphologies, compositions, and crystal structure of the obtained materials. A detailed study of NCs using high resolution transmission electron microscopy (HRTEM) was performed to understand the growth mechanism of pyrite FeS_2 materials. An understanding of the synthesized structure correlating with the surface and crystal structure of pyrite was investigated using the surface structure of {100}, {111}, and {210} facets constructed in Materials Studio. The obtained knowledge will help us to understand the growth mechanism and the possible means to better control the phase and morphologies of synthetic pyrite FeS_2 materials for PV applications. Inverted hybrid solar cells with three types of HTLs including PEDOT:PSS, MoO_3, and PEDOT:PSS/MoO_3 were fabricated to explore the effects of HTLs on the performance of inverted hybrid solar cells. The results obtained in this study are applicable to other inverted hybrid solar cells to achieve better efficiency. Moreover, molecular level organic-inorganic halide perovskite is used in the active layer to replace conventional organic-inorganic hybrid system. A two-step solution process with thermal plus solvent vapor-assisted thermal annealing was developed and demonstrated that it was an effective method to make binary Pb-Sn triiodine perovskite films with large and smooth grains. Using this new process to control and manipulate film morphology, grain size, and especially the distribution of metal cations in binary metal perovskite layers, opens an avenue to grow perovskite materials with desired properties to enhance device performance.

Chapter 2 HYDROTHERMAL SYNTHESIS AND CHARACTERIZATION OF PYRITE FES2 HIERARCHICAL PARTICLES

2.1 Introduction

The search for inorganic semiconductors with large absorption coefficient (>10^5 cm^{-1}) covering the whole sunlight spectrum is important for the development of the next generation organic-inorganic solar cells because the charge generation process in a solar cell is strongly dependent on the light absorption. Metal chalcogenides with defined morphology is of particular interest because of the strong size and shape dependence of their physical properties.[114-116] Among the family of metal sulfides, iron sulfides have attracted much interest not only because the iron sulfide system contains a number of phases, such as mackinawite $Fe_{1+x}S$, pyrrhotite $Fe_{1-x}S$, smythite Fe_9S_{11}, greigite Fe_3S_4, troilite FeS, cubic FeS FeSc, pyrite FeS_2, and marcasite FeS_2,[117] but also because of their broad applications in optical[118] and magnetic devices[119] and high capacity lithium batteries.[120]

Nontoxic and abundant pyrite iron disulfide FeS_2 has interesting electronic properties: an indirect and direct band gap at 0.95 and 1.03 eV, respectively,[67] and a high capacity (exceeding 890 mAh/g);[121] and excellent optical properties: high absorption coefficient (3.3 x 10^5 cm^{-1}) for the energy spectrum of wavelength values (λ) between 300 and 750 nm.[67] It has been explored for applications in PV devices, photoeletrochemical solar cells, cathode material for lithium batteries, and a depolarizer anode for hydrogen production.[118, 121-123] Pyrite thin films were prepared using several high temperature approaches including sulfurization of iron films or iron oxide films,[71-73] reactive sputtering,[74] and spray pyrolysis.[75] Because the segregation of iron and sulfur species is unavoidable at elevated temperatures, the stoichiometry and material phase of the deposited film could be changed, especially at film surfaces, which could significantly influence the device performance.[67] Thus, low temperature methods like hot injection and hydro/solvothermal processes have been explored recently to synthesize pyrite particles for the solution processed, low-cost, flexible large-area devices.[76-78, 80, 81, 124] Pyrite nanoparticles with sizes below 100 nm were typically synthesized via a hot injection method by injecting a sulfur source into a heated

iron source with one or two capping agents and reacting at 220°C for 2-3 h.[76-78] It was reported that larger sized pyrite particles were synthesized via the hydro/solvothermal process in an autoclave at temperatures around 180°C for about 6-24 h.[80-82] By thermally decomposing a single iron-sulfur complex via a hydrothermal process, cubic pyrite particles with {100} facets were obtained with the size ranging from 150 nm[125] to 500 nm.[126] Both pyrite cubes with the {100} facets and octahedrons with the {111} facets were synthesized by using surfactants and controlling the pH value of the reaction solutions.[127, 128] Recently, it was also demonstrated that monodispersed pyrite microspherolites can be obtained via a microwave-assisted hydrothermal process in the presence of polyvinylpyrrolidone (PVP).[124]

Despite the recent advancement of hydro/solvothermal routes to the synthesis of pyrite particles, synthesis of monodispersed hierarchical pyrite particles with specific facets using a simple yet effective method is still not achieved. Control of pyrite particles with specific facets is of particular importance because the surface structures and the dangling bonds of the surface atoms could affect the adsorption of molecules[129] and, thus, could significantly influence the charge separation at the pyrite and polymer interfaces in a hybrid solar cell and the intercalation of lithium ions into pyrite particles in a lithium battery. In addition, the oxidation process of pyrite particles strongly depends on the exposed surface facets of the particles, which could potentially affect the stability and life time of PV devices.

In this chapter, we report a hydrothermal method for the preparation of pyrite hierarchical microparticles in an ethylenediamine (en) aqueous solution using ferrous chloride tetrahydrate and sulfur powder as the precursors and PVP as both a phase regulator and a surface capping agent. Pyrite FeS_2 hierarchical microparticles consisting of cubic-like crystals with {100} facetted textures were obtained. The roles of PVP and en in the synthesis are discussed based on the atomic structure of pyrite (100) and (111) surfaces and the molecular interactions with the precursors. The effects of the oxidation state of iron and the species of the anions on the crystalline structure and morphology of the products were also studied.

2.2 Experimental Section

2.2.1 Materials for the Synthesis of Pyrite FeS_2 Hierarchical Particles

En (≥99.5%) was obtained from Fluka. $FeCl_2 \cdot 4H_2O$ (99.99%), $FeSO_4 \cdot 7H_2O$ (≥99 %), sulfur powder (99.98%), and PVP （M.W. = 1,300,000 determined by light scattering) were purchased from Sigma-Aldrich. $FeCl_3 \cdot 6H_2O$ (ACS, 97.0-102.0%) was obtained from Alfa Aesar. Millipore water was self-made using a Millipore Simplicity Ultrapure Water System. All chemicals were used as received without further purification.

2.2.2 Hydrothermal Synthesis of Pyrite FeS_2 Hierarchical Particles

In a typical reaction, 0.0984 g (3.08 mmol) of sulfur powder was dissolved in 2.2 mL of en under constant stirring to form a homogeneous, greenish solution. Then, 0.6 g (4.62 x 10^{-4} mmol) of PVP dissolved in 17.0 mL of water and 0.3057 g (1.54 mmol) of ferrous chloride tetrahydrate ($FeCl_2 \cdot 4H_2O$) were added in sequence under vigorous stirring. The mixture was stirred vigorously for 30 min before sealed in a 25 mL teflon-lined stainless steel autoclave. The autoclave was placed in a muffle oven and maintained at 200°C. After being reacted for 24 h, the autoclave was taken out of the oven and cooled to the room temperature. The greenish supernatant was discarded and the precipitates were redispersed in ethanol and collected by centrifuging at 4400 rpm for 18 min. The supernatant was discarded. The precipitates were redispersed in Millipore water and collected by centrifuging. The washing procedures were repeated for three times in order to remove residues of reactants, polymers, and any side products. The resultant products were dried in a vacuum oven at 70°C overnight. The molar ratio of iron to sulfur was kept at 1:2 for all reactions. The amount of PVP was varied from 0 to 2.4 g. While the total volume of the aqueous solutions was 19.2 mL, the volume of en was changed from 0 to 6.2 mL. Other iron reagents, $FeCl_3 \cdot 6H_2O$ and $FeSO_4 \cdot 7H_2O$, were also used in the synthesis.

2.2.3 Characterization of Pyrite FeS_2 Hierarchical Particles

The morphology and elemental composition of the products were characterized using SEM and energy-dispersive X-ray spectroscopy (EDS) (FEI Sirion SEM), respectively. The SEM samples were prepared by dropping the particle solution on a silicon chip and being dried in air. XRD measurement was carried out on a GADDS D8 Discover diffractometer (Bruker) using Cu Kα radiation (λ = 1.5419 Å). Three frames with 100

seconds/frame were obtained for each sample. Scan angle 2θ begins at 30 degrees with a frame width of 25 degrees. Data were processed using the EVA package provided by Bruker Axs. Raman spectra of the products were acquired using a Renishaw InVia Raman spectrometer attached to a Leica DMLM upright microscope. A 100x (0.75 N.A.) objective was used to focus the 514 nm laser onto the microparticles and to collect the back scattered light from the microparticles. The illuminated sample areas were about 3 μm^2 with the power of 1.5 mW. All spectra were collected for 10 accumulations with 10 s exposure time for each scan. Samples for XRD and Raman spectroscopy measurements were prepared by dusting the vacuum dried samples on a double-sided tape attached to a glass slide. Surface and crystal structures were built using Materials Studio 5.0 with the lattice parameters obtained from the literature.[130]

2.3 Results and Discussion

2.3.1 Pyrite FeS_2 Hierarchical Particles

Figure 2.1A and B show the SEM images of the hierarchical microparticles synthesized in an en aqueous solution (2.2 mL of en and 17.0 mL of water) containing 0.6 g of PVP at 200°C for 24 h. The average size of the microparticles is 4.5 ± 0.7 μm estimated from the SEM images. The hierarchical morphology of these microparticles composed of smaller nanoparticles dominated with {100} facets can be seen in the higher magnification SEM image (Figure 2.1B). Selected area EDS analysis indicates that the microparticles have a molar ratio of iron to sulfur as 1:2.01, consistent with the stoichiometric composition of pyrite FeS_2. The pyrite crystalline structure was confirmed by the powder XRD analysis. Figure 2.1C clearly shows that the product has a pure pyrite phase (compared to JSPDS File No. 42-1340). The strong and sharp diffraction peaks imply the high crystallinity of the microparticles. Raman vibrational spectroscopy was also employed to verify the phase purity of the microparticles. Figure 2.1D shows the Raman spectra of the synthesized microparticles and the sample of natural pyrite under the illumination of a 514 nm laser. Two strong peaks at 340 and 376 cm^{-1} belong to the E_g and A_g modes and a weak peak at 425 cm^{-1} belongs to the T_g mode.

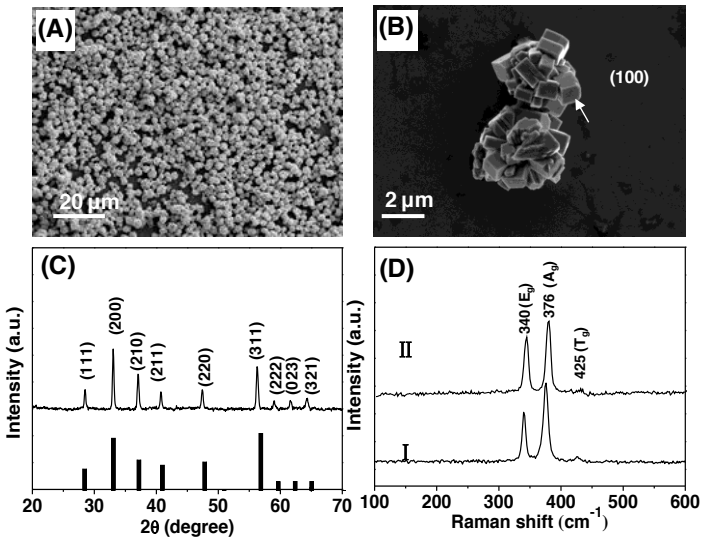

Figure 2.1 The SEM images (A and B) and XRD pattern (C) of the pyrite FeS_2 hierarchical particles synthesized in an ethylenediamine aqueous solution (2.2 mL of en : 17.0 mL of water) containing 0.6 g of PVP at 200°C for 24 h. Raman spectra (D) show naturally occurring pyrite (I) and synthesized pyrite FeS_2 hierarchical microparticles (II).

Because the symmetry of the pyrite structure is the non-symmorphic space group Pa3 (point group T_h^6), there are five Raman active modes ($A_g + E_g + 3T_g$). The A_g mode is mainly due to the stretching of S_2 dumb-bells which are in-phase throughout the crystal. The E_g mode is attributed to the displacements of S atom perpendicular to the dumb-bells axes and the phonon is a vibration. The T_g mode is triply degenerated. Its frequency is very near the A_g mode.[131] Here, only one T_g mode was observed at 425 cm^{-1} and the other two modes could be buried in the A_g mode at 376 cm^{-1}.

The structure of en and PVP used in this study are shown in Scheme 2.1. En contains two amine groups that have a strong chelating ability to bind to a variety of metals. PVP is a water-soluble polymer made from the monomer N-vinylpyrrolidone. Each repeating unit contains a five-member ring as the side chain. Nitrogen in the five-member ring has one lone electron pair (LEP). Oxygen has two LEPs. These LEPs on PVP can not only be given away in a reaction but also be coordinated with metal atoms. Therefore, PVP has been commonly used as a reduction or a structure-direction agent to control the crystalline phase and morphology of NCs.[132, 133]

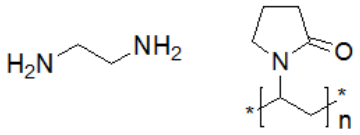

Scheme 2.1 Structures of en and PVP.

2.3.2 Role of PVP in the Synthesis

In order to study the effects of PVP on the synthesis of pyrite hierarchical microparticles with controlled faceted textures, the amount of PVP added to the reaction mixture was varied while the reaction temperature and time, the concentrations of iron and sulfur reagents, and the volume of en remained the same. When the reaction mixture contained low amount of PVP, e.g., 0.3 g, microparticles with poor-defined facets were obtained (Figure 2.2A). The XRD pattern shows that the dominated crystalline phase of the microparticles is pyrite and a trace amount of Fe_3O_4 and marcarsite phases was also observed (Figure 2.2D-I). As the amount of PVP was increased to 1.2 and 2.4 g, hierarchical microparticles with {100} facetted cubic textures were obtained (Figure 2.2B, C). The XRD patterns indicate that the products have a pyrite phase with trace amount of marcarsite and no other detectable impurity phases (Figure 2.2D-II, III). It appears that the products synthesized with the larger amount of PVP contain more defined {100} facets (Figure 2.2B, C). A new morphology of plates was observed in the products synthesized in the solution containing 1.2 and 2.4 g of PVP (Figure 2.2B, C). More plates were formed in the reaction with 2.4 g of PVP than that with 1.2 g of PVP. The elemental composition of the plates was analyzed using point and area EDS by scanning the electron beam only on the plates. An average ratio of Fe:S = 1:1.12 was obtained, indicating a sulfur deficient product. Since there is no other impurity peaks except marcasite appeared in the XRD patterns of these two products, the plates could be one amorphous phase of sulfur deficient product. According to the Huggins[134] and Wilke-Chang[135] equations that describe the species diffusion in a mixture, the diffusion of iron and sulfur ions could be slowed down due to the increased viscosity of the reaction solution caused by the larger amount of the heavy PVP polymer used in this study (PVP M.W. = 1,300,000). In addition, the larger amount of PVP could bind to more iron ions and inhibit the attachment of sulfur dimers,

resulting in the sulfur deficient products. Similar phenomenon was also observed in the previous synthesis of pyrite particles.[128]

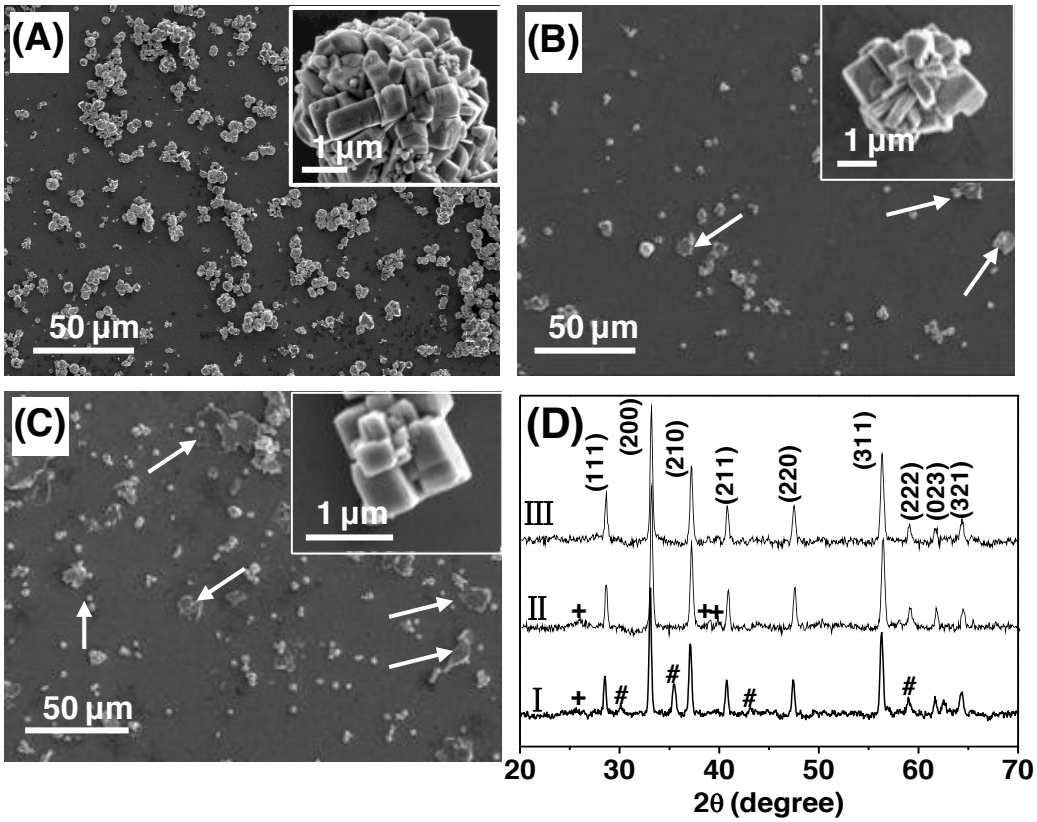

Figure 2.2 The SEM images of the products synthesized in an ethylenediamine aqueous solution (2.2 mL of en : 17 mL of water) containing 0.3 g (A), 1.2 g (B), and 2.4 g (C) of PVP at 200°C for 24 h. Arrows in (B) and (C) indicate the amorphous iron sulfide plates. The insets show the typical morphology of the microparticles. The XRD patterns are the products with 0.3 g (I), 1.2 g (II), and 2.4 g (III) of PVP. The XRD peaks of marcasite FeS_2 are marked as "+" and magnetite Fe_3O_4 as "#".

Table 2.1 Summary of the (100) and (111) surfaces of pyrite FeS_2 terminated in different layers. X: the outmost surface atoms; N_{Fe} and N_S: the number of dangling bonds of iron and sulfur atoms, respectively.

Layer	**X**	**N_{Fe}**	**N_S**	**Layer**	**X**	**N_{Fe}**	**N_S**
(100)				**(111)**			
A	Fe	3	1	**A**	Fe	3	0
B	S	1	1	**B**	S, Fe	2, 3	1
C	S	0	3, 1	**C**	S	1	2

Apparently, PVP plays two roles in the synthesis of pyrite hierarchical microparticles, reduction agent and structure-direction surfactant. The iron oxide crystals were observed in the product synthesized with a low PVP concentration but were not present in the products with higher PVP concentrations. It is generally accepted that the formation of specific crystalline facets of synthesized crystals is due to the favorable binding of surfactants to specific crystalline surfaces preventing the growth from this direction while promoting the crystal growth in other energetically and kinetically favorable directions. The LEP at the nitrogen atom of PVP can shift to the oxygen atom resulting in the negatively charged oxygen atom[128] which can bind to a positively charged iron ion. The (100) and (111) surfaces are the most stable facets of crystalline pyrite FeS_2[136, 137] and are the facets commonly observed in natural and synthesized pyrite crystals.[67, 138]

For (100) and (111) surfaces of pyrite FeS_2, there are three and nine ways, respectively, to form the surface terminated with different surface atoms and structures. Table 2.1 summarizes the atoms and the number of dangling bonds of iron and sulfur atoms at (100) and (111) surfaces in three and five different termination layers. The other four ways to terminate the (111) surface have the same surface atoms and number of dangling bonds as those in the Layers B, C, D, and E but different dangling bond orientations and thus are not listed in Table 2.1.

For (100) surface, the side- and top-view of the atomic structures of Layers A, B, and C are shown in Figure 2.3. The dangling bonds in the top-view are terminated with hydrogen atoms labelled in red. For the (100) surface terminated with Layer A, the outmost iron atoms have three dangling bonds with two types of orientations. The iron atoms are connected by sharing two sulfur atoms. Each sulfur atom has one dangling bond which orientates in two directions as well. Because each surface iron atom has three dangling bonds, the oxygen atoms on PVP could bind to those iron atoms. However, the neighboring sulfur atoms with one dangling bond could weaken or interfere with the binding of oxygen to iron. For the (100) surface terminated with Layer B, both the outmost sulfur atoms and the sub-surface iron atoms have one dangling bond as shown with the red balls of the terminating hydrogen atoms. The dangling bond of iron and that of sulfur are orientated toward each other, which making the binding of PVP energy unfavorable. The third way of terminating the (100) surface only has sulfur atoms at the outmost and sub-surface with one or three dangling bonds. Therefore, this surface is highly negatively charged and does not bind to PVP.

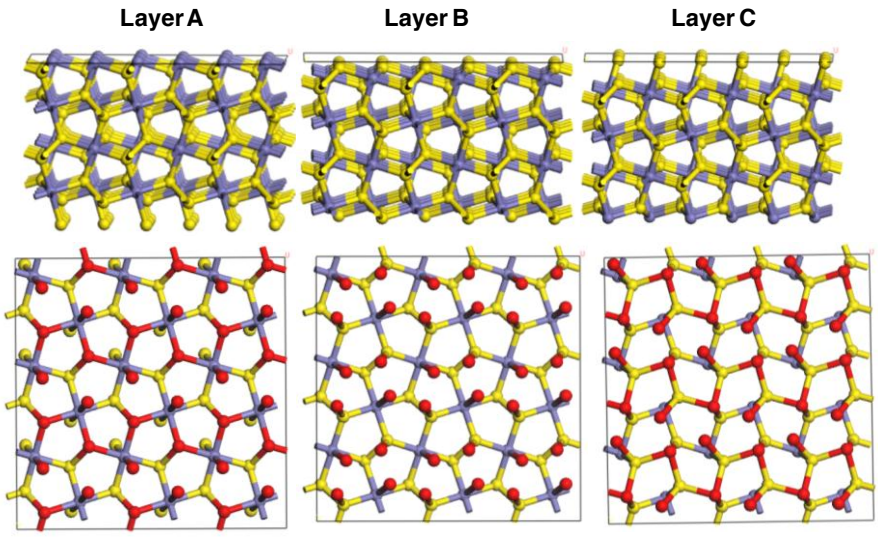

Figure 2.3 The atomic structures of the pyrite (100) surface terminated in layers A, B, and C. Side- and top-view are shown in the top and bottom rows, respectively. Blue balls are iron atoms and yellow balls are sulfur atoms. In the top-view, the dangling bonds are terminated by hydrogen atoms in red. For easy visualization, the top two and three layers are displayed in the top-view of layers A, B, and C, respectively.

The same analysis can also be applied to the (111) surface with different terminating layers. The side- and top-view of the atomic structures of Layers A and B for (111) surface are shown in Figure 2.4. For the (111) surface terminated with Layer A, iron atoms are the outmost surface atoms and each of them has three dangling bonds which are terminated with hydrogen atoms labelled in red balls. There are four different orientations of surface iron atoms. All sub-surface sulfur atoms have four coordinates and no dangling bonds. Obviously, the oxygen atoms on PVP are much easier to interact with iron atoms on this (111) surface than on Layer A of (100) surface. For the (111) surface terminated with Layer B, sulfur atoms with one dangling bond are the outmost surface atoms. Each of these sulfur atoms bonds to three sub-surface iron atoms. All sub-surface iron atoms have two dangling bonds and three different orientations. This (111) surface should have less tendency to bind the oxygen atoms on PVP than Layer A (111) surface. For the (111) surface terminated with Layers C, D, and E, the outmost surface atoms are sulfur and the side-view of these terminations are sown in Figure 2.5. Similar to the (100) surface terminated in Layer C, these (111) surfaces are not energy favorable for binding PVP.

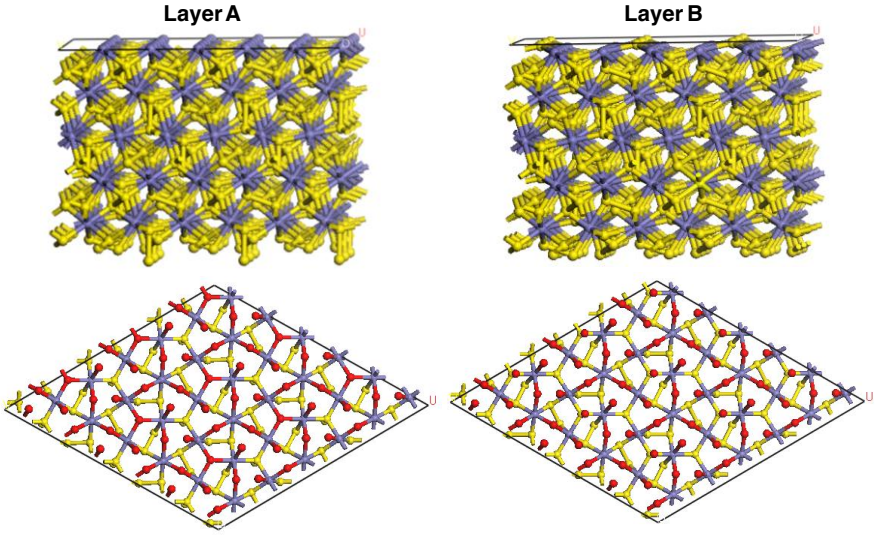

Figure 2.4 The atomic structures of the pyrite (111) surface terminating in layers A and B. The side- and top-view are shown in the top and bottom rows, respectively. Blue balls are iron atoms and yellow balls are sulfur atoms. In the top-view, the dangling bonds are terminated by hydrogen atoms in red color. Only the top two layers are shown in the top-view.

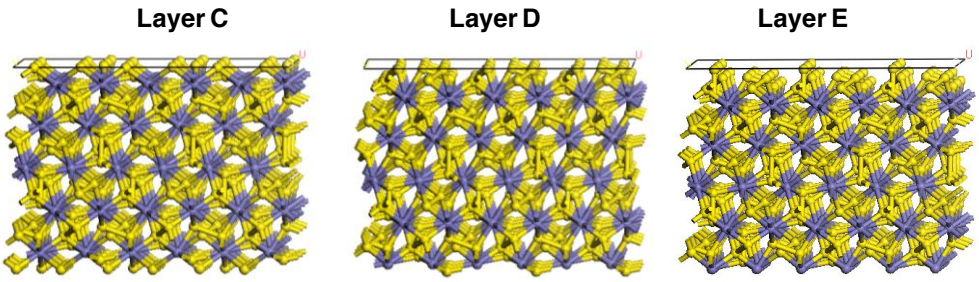

Figure 2.5 Side-view of (111) surface terminated in layers C, D, and E. Blue balls are iron atoms and yellow balls are sulfur atoms.

Based on the analysis of the atomic structures of different terminating layers of (100) and (111) surfaces, the (111) surface terminated in Layer A could be the most energetically favorable surface to bind PVP because all the outmost surface atoms are iron which have three dangling bonds and all sulfur atoms are in the sub-surface and are coordinatively saturated. Therefore, during the crystal growth, the oxygen atoms on PVP could bind to the iron atoms at the {111} surfaces and the growth would be along the <100> directions, resulting in the {100} facets. By taking a closer look at the product synthesized in the solution containing 0.6 g of PVP, it was found that about 7% of the total products (by counting 200 particles) were either the single {100} facetted cubes with truncated {111} corners or the connected two cubes with well-defined {100} facets (Figure 2.6). Small pitches formed by the {111} facets were observed at the <100> edges and the {111} facets of single and dual particles in Figure 5. While the dominated facets are {100}, small amount of {111} facets can also be observed at the hierarchical microspheres (Figure 2.1A, B). All these experimental results supported the hypothesis that the {100} facetted cubic textures at the hierarchical microparticles could be due to the structure-direction effect caused by PVP in the reaction mixtures. Based on the above analysis, a possible mechanism is proposed as shown in Scheme 2.2. The binding of PVP on {111} facets leads to the aggregation of cubic-like crystals and subsequently the formation of pyrite FeS_2 hierarchical microparticles.

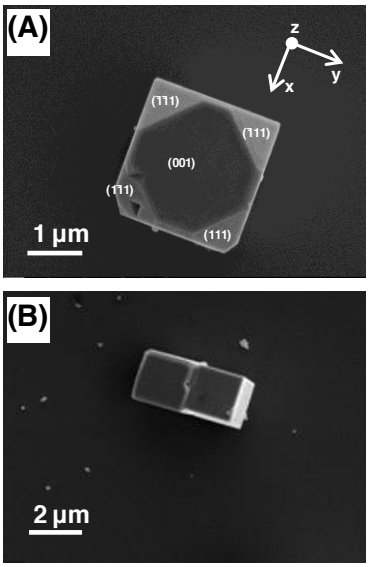

Figure 2.6 The SEM images of one truncated pyrite cube with the {100} and {111} facets (A) and two connected pyrite cubes with the defined {100} facets (B). Small pitches formed by the {111} facets are also observed. Particles with these morphologies were about 7% of the total products determined by counting 200 particles in an SEM image.

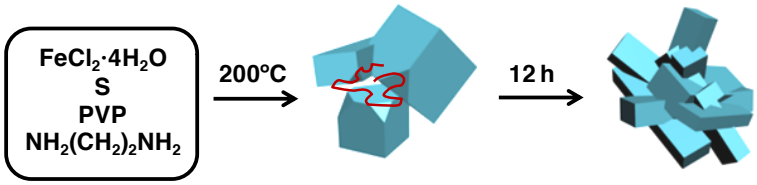

Scheme 2.2 Illustration of a possible mechanism for the formation of pyrite FeS_2 hierarchical microparticles.

2.3.3 Role of En in the Synthesis

In order to understand the role of en in the synthesis of hierarchical microparticles, the reactions were conducted by using different concentrations of en while PVP was not used and the other parameters remained the same. Figure 2.7A shows that the microparticles synthesized using 1.0 mL of en and 18.2 mL of water have no crystalline facets. The XRD pattern shows the peaks of the pyrite phase are weak and broad, indicating the poor crystallinity (Figure 2.7E-I). The peaks of the marcasite phase were clearly observed in the XRD pattern. As the volume of en was increased to 2.2 mL, some facets can be seen on the microparticles (Figure 2.7B) and the peaks of the pyrite phase were stronger and sharper

while the peaks of the marcasite phase were weaker as shown in the XRD pattern (Figure 2.7E-II). This reaction was taken at the same condition as that of the product shown in Figure 2.1 except that the PVP was not used. Clearly, PVP plays a critical role in the formation of the {100} facets on the hierarchical microparticles. Moreover, PVP also plays an important role in the formation of pure pyrite phase of the microparticles. Further increasing the volume of en to 4.2 and 6.2 mL, more facets were formed on the microparticles (Figure 2.7C, D). The peaks of the pyrite phase were stronger and sharper for 4.2 mL of en but weaker and broader for 6.2 mL of en. The products still have the phase of marcasite FeS_2 as shown in the XRD patterns (Figure 2.7E-III, IV). The area ratio of the peaks at $2\theta = 25.9^{\circ}$ of marcasite (110) and 28.4° of pyrite (111) versus the volume of en used in the reaction was plotted and shown in Figure 2.8. It shows that the lowest amount of marcasite was obtained in the product synthesized using 2.2 mL of en. The reactions were conducted with even lower volume of en and even without the addition of en.

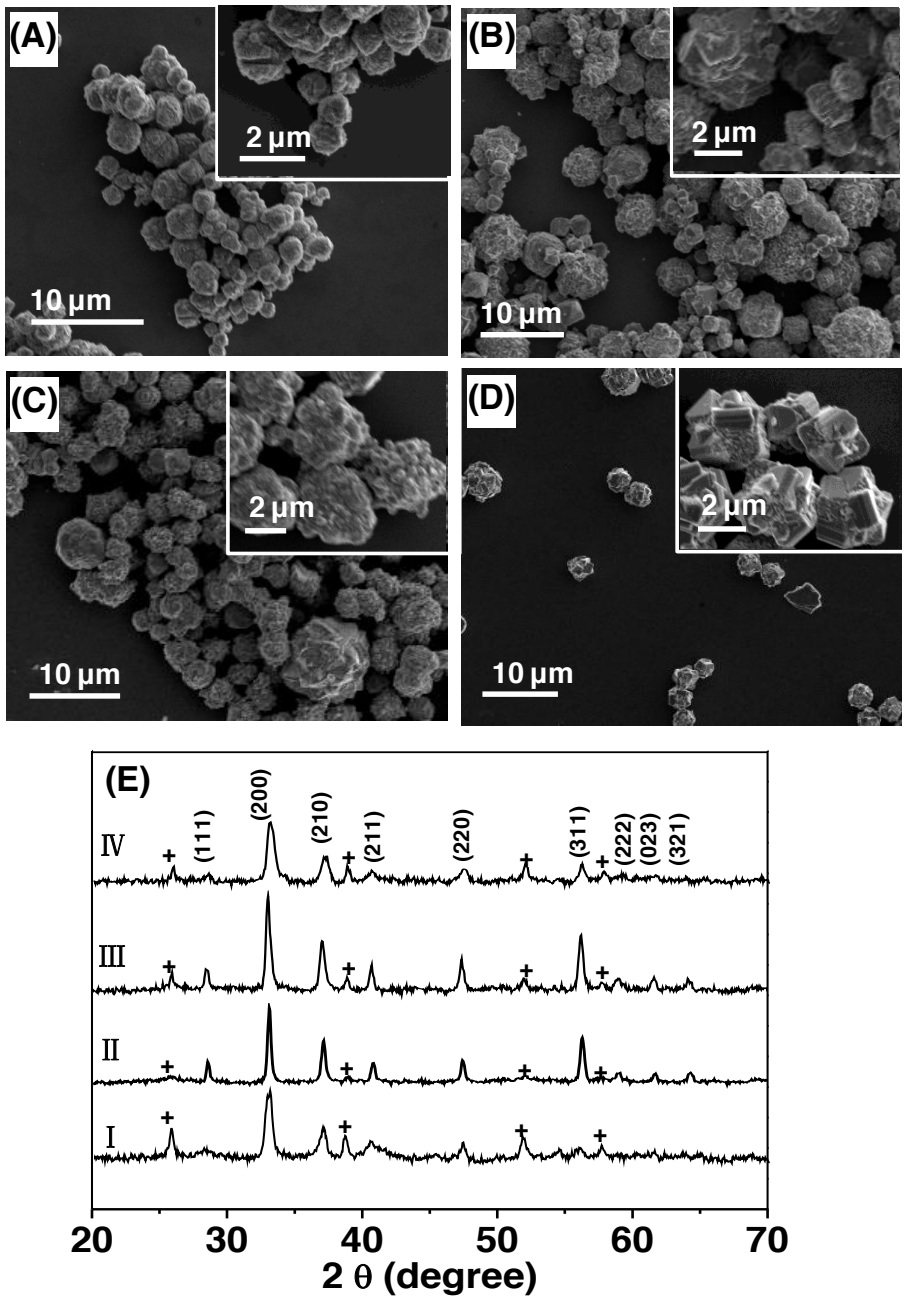

Figure 2.7 The SEM images of the products synthesized in an ethylenediamine aqueous solution with the volume ratio of en to water of 1 mL/18.2 mL (A), 2.2 mL/17 mL (B), 4.2 mL/15 mL (C), and 6.2 mL/13 mL (D) without the presence of PVP at 200°C for 24 h. Insets are the typical morphology of particles in the products. (E) The XRD patterns of I, II, III, and IV correspond to the products of (A), (B), (C), and (D), respectively. The XRD peaks of marcasite FeS_2 are marked as "+".

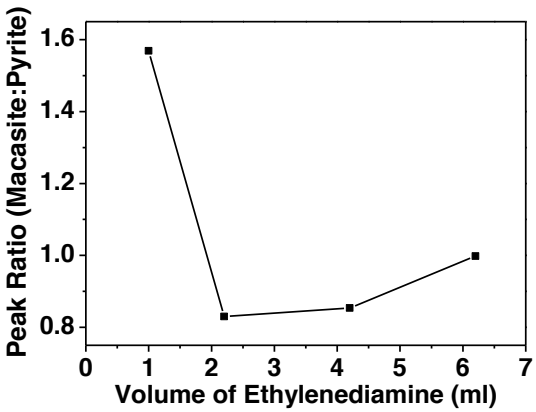

Figure 2.8 The area ratio of the XRD peaks of the marcarsite (110) plane (2θ at 25.9°) and the pyrite (111) plane (2θ at 28.4°) versus the volume of en added in the reaction.

The product synthesized with the en volume of 0.2 mL has the morphology of microparticles without facets (Figure 2.9A) and the XRD pattern indicates that both pyrite and marcasite FeS_2 and a trace amount of other phase impurity were in the product (Figure 2.9C-I). It was found that the product synthesized without the addition of en formed big chunks (Figure 2.9B). No microparticles were observed and more impurity phases existed in the product (Figure 2.9C- II).

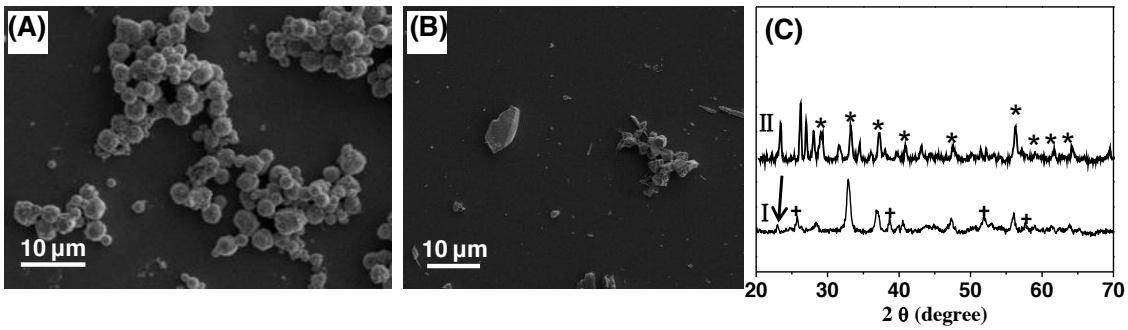

Figure 2.9 SEM images of the products synthesized in the solutions with the volume ratio of en to water of 0.2 mL/19 mL (A) and 0 mL/19.2 mL (B) without the presence of PVP at 200ºC for 24 h. The XRD patterns of I and II are for the products shown in (A) and (B), respectively. The XRD peaks of marcasite FeS_2 are marked as "+" and pyrite FeS_2 are marked as "*". The arrow indicates the peak due to other impurity.

En is a strong chelating agent and can form complexes with metal ions. En can

coordinate with Fe^{2+} ions to form complex $[Fe\ (en)_2]^{2+}$ ions.[82] It was also reported that sulfur powder can react with en to generate a greenish solution due to the reversible nucleophilic attack of the S_8 rings by en. As a result, octathioamine $[NH_2\text{-}(CH_2)_2\text{-}HN\text{-}S_8^-]$ is formed. Octathioamine can further degenerate to polythioamines $[NH_2\text{-}(CH_2)_2\text{-}HN\text{-}S_y^-]$ $(y < 8)$.[139, 140] Assuming no degeneration of octathioamine $[NH_2\text{-}(CH_2)_2\text{-}HN\text{-}S_8^-]$ $(y = 8)$, a total of 0.00346 mol of en (i.e. 0.231 mL) should be consumed to form $[Fe\ (en)_2]^{2+}$ and $[NH_2\text{-}(CH_2)_2\text{-}HN\text{-}S_8^-]$ by taking into account that 0.0984 g (3.08 mmol) of S and 0.3057 g (1.54 mmol) of $FeCl_2{\cdot}4H_2O$ were used. When the volume of en was less than 0.231 mL, excess Fe^{2+} ions and sulfur powder cannot form the complexes with en, which might affect the dispersion, nucleation, and reaction of Fe^{2+} ions with sulfur. This may be the reason why other impurities formed besides the pyrite and marcasite phases when no en or 0.2 mL of en was added in the reaction solution.

Pyrite and marcasite are two polymorphs of naturally occurring iron disulfide FeS_2. The cubic pyrite form (Figure 1.2, space group Pa3) is by far the most abundant of the iron disulfides.[130] The Fe atoms are octahedrally coordinated to six sulfur atoms and are at the corners and face centers of the cubic unit cell, while the sulfur atoms are tetrahedrally coordinated to three iron atoms and one sulfur atom. The axes of the S_2 dumb-bells are aligned along the four equivalent <111> directions. The orthorhombic marcasite form (Figure 1.2, space group Pnnm) is the less abundant polymorph. The coordination environments of Fe and S atoms in marcasite are very similar to those in pyrite while the difference between the two structures is found in the linking of Fe-centered octahedra. The difference in the free energy of formation between the two polymorphs is very low, with pyrite being 0.04 eV/FeS_2 more stable than marcasite at 298.15K.[141] The fact that the co-existence of the marcasite phase in the products synthesized without the addition of PVP indicates that the structure-direction agent PVP not only guides the formation of the {100} faceted textures on the hierarchical microparticles but also directs the crystal growth toward the pyrite phase.

Other iron sources were also used in the synthesis in order to investigate the effects of the oxidation state of Fe ions and the anions on the phase and morphology of the products. When replacing $FeCl_2{\cdot}4H_2O$ with $FeCl_3{\cdot}6H_2O$ while keeping all other conditions the same, microparticles with poorly defined textures were obtained as shown in Figure 2.10A.

Although the microparticles have a good pyrite crystalline structure demonstrated by the strong and sharp pyrite peaks in the XRD pattern, they also contain impurities of Fe_3O_4 and other phases (Figure 2.10C-I). The higher oxidation state of Fe^{3+} compared to Fe^{2+} could be the reason causing more iron oxides in the microparticles despite the presence of PVP. When $FeSO_4 \cdot 7H_2O$ was used as the iron reagent, microparticles with a slightly better facetted morphology were formed (Figure 2.10B). Again, while the good pyrite crystalline structure was formed in the microparticles, the impurity of marcasite phase without the impurities of the oxide and other phases was observed in the product (Figure 2.10C-II). Clearly, the anion of the iron reagent also plays a critical role in the formation of the pure pyrite phase. The effect of the anions on the crystalline structures and morphologies was also observed in the synthesis of CdS and CdSe NCs.[142]

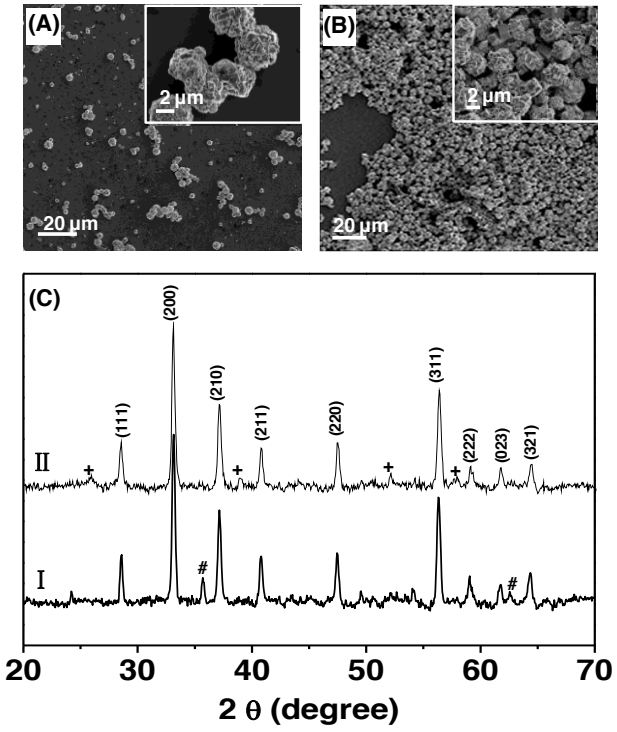

Figure 2.10 Figure 2.11 The SEM images of the hierarchical microspheres synthesized using $FeCl_3 \cdot 6H_2O$ (a) and $FeSO_4 \cdot 7H_2O$ (b) as iron reagents in an ethylenediamine aqueous solution (2.2 mL of en:17 mL of water) containing 0.6 g of PVP at 200°C for 24 h. (c) The XRD patterns show the products synthesized with $FeCl_3 \cdot 6H_2O$(I) and $FeSO_4 \cdot 7H_2O$(II). The XRD peaks of marcasite FeS_2 are marked as "+" and magnetite Fe_3O_4 as "#".

2.4 Conclusions

In summary, we have successfully synthesized pyrite hierarchical microparticles consisting of cubic-like crystals with well-defined {100} facetted cubic textures using a simple hydrothermal method with the presence of en and PVP. While en plays a role of chelating with Fe^{2+} and reacts with S_8 of sulfur powder to help with dispersion and nucleation besides the role of reducing agent, PVP acts as both a phase regulator due to its reducing ability and a surface capping agent for directing the formation of a specifically facetted morphology. The atomic structures and dangling bonds at the (100) and (111) surfaces of pyrite with different termination layers lead to different binding capacities and energies of PVP on the surfaces, which results in the growing of crystals along the [100] direction due to the favorable binding of PVP on {111} surfaces. The facts that by using Fe^{3+} and changing the anions from Cl^- to SO_4^{2-} make microparticles containing oxide and marcasite phases, respectively, indicate that the oxidation state of iron ions and the species of anions also play critical roles in the crystalline structure and morphology of microparticles. The mechanisms discussed in this paper may provide new insights to the synthesis of pyrite materials and help to better understand the formation of pyrite phase and the control of morphology. The hierarchical microparticles with the dominated {100} facets could be used as a model system to investigate the ion intercalation and polymer-pyrite interactions in the lithium battery and hybrid PV devices. The pyrite hierarchical microparticles could also be used as a new semiconductor ink for solution processing PV devices and photodetectors as well as cathode materials for lithium battery.

Chapter 3 HOT INJECTION SYNTHESIS, CHARACTERIZATION OF PYRITE NCS FOR ORGANIC-INORGANIC HYBRID SOLAR CELLS

3.1 Introduction

Although phase pure pyrite FeS_2 micro-size materials are able to be synthesized by hydrothermal method in an autoclave, the synthesized materials are too big for organic-inorganic hybrid solar cells because the typical thickness of an active layer is a few hundred nanometers. Large particles can penetrate the film, connect two electrodes, and short the fabricated solar cells. In a hydrothermal synthesis, inhomogeneous nucleation happens accompanied by the fast growth of the crystals. Eventually, large particles formed in the reactions. With a homogeneous mixture and fast nucleation of the seeds, the synthesized particles are expected to be smaller. Based on our previous understanding of pyrite FeS_2 materials, we further investigated the synthesis of pyrite FeS_2 materials by using hot injection method.

The synthesis of 10-20 nm spherical pyrite NCs using the hot injection method was first demonstrated by Law's group.[76] Pyrite NCs were obtained by injecting the sulfur diphenyl ether (DPE) solution into the iron chloride ($FeCl_2$) octadecylamine (ODA) complex at 220°C and keeping the reaction at 220°C for 3 h. Ren's group modified this procedure by varying the injection temperature and adding a second injection of the $FeCl_2$-ODA complex but keeping the reaction at 220°C for 90 min.[79] Pyrite NCs with spherical, popcorn-like, and cubic shapes were obtained with the size of ~30 to ~220 nm. They also used different iron agents and found that thin and thick two dimensional sheets were formed when iron(II) acetylacetonate ($Fe(acac)_2$) and iron(0) pentacarbonyl ($Fe(CO)_5$) were used, respectively. Oleyamine (OLA) was reported as the solvent to dissolve both iron source and sulfur source.[77] Pyrite nanodendrites and clusters of nanocubes were formed with a high (four times the low concentration) and a low concentration of the reactant, respectively, by the reaction between a sulfur OLA solution and an $FeCl_2$-OLA solution at 220°C for 20 min. Additional surface capping agents or co-solvents, such as 1, 2-hexadecanediol (Diol),[143] trioctylphosphine oxide (TOPO),[144] en,[145] or 1-hexadecanesulfonate[146] were added in the reaction solution to achieve better surface

passivation or to direct the formation of specific morphologies. Well dispersed pyrite NCs were synthesized by injecting an OLA solution of sulfur into an OLA solution of $FeCl_2$ with Diol as an additional capping agent.[143] The solar cell constructed by using these NCs showed extended red light harvesting. Pyrite cubic-like NCs (~60-200 nm) synthesized by injecting an OLA solution of sulfur into an OLA solution of $FeCl_2$ with TOPO demonstrated high air stability, which was attributed to the possible formation of O-Fe and P-S bonds between TOPO and pyrite NC surfaces to prevent oxidation.[144] Recently, pyrite nanocubes with {100} facets and < 50 nm size were successfully synthesized via a procedure including the high temperature (250°C) nucleation in the solvent of hexadecylamine and a S:Fe molar ratio of 6:1 followed by two steps of crystal growth at 200°C in the co-solvent of hexadecylamine and OLA and a reduced S:Fe molar ratio of 2.05.[147] A strategy of using an uncommon ligand, 1-hexadecanesulfonate, also demonstrated the success in growing cubic pyrite NCs.[146] Despite the recent progress in the synthesis of pyrite NCs, thorough investigations are required in order to understand the reaction mechanisms and key parameters in determining the phase purity and morphology of pyrite NCs.

In this chapter, we demonstrated that short, branched, and chromosome-like nanorods (NRs) versus quasi-cubic NC agglomerations can be synthesized by carefully controlling the reaction conditions including solvent, reactant concentration, and capping agent. We further varied the molar ratio of sulfur to iron and the reaction temperature and showed that the phase of the synthesized products was significantly influenced by these two parameters. Our experimental results suggest that these parameters affected the generation of H_2S gas produced by sulfur and amine which played a critical role in the phase of final products. The present study shed light on the growth mechanism and the possible means to control the morphology of pyrite NCs. Pyrite NCs with different morphology and surface passivation can be used as model systems for the study of crystalline structures and surface chemical and structural properties on the electronic and optical properties of pyrite NCs in order to improve the physical properties of pyrite NCs for efficient PV conversion.

3.2 Experimental Section

3.2.1 Materials for the Synthesis of Pyrite FeS_2 NCs

All chemicals were used as received. $FeCl_2 \cdot 4H_2O$ (99.99%), Chloroform (≥99.8%), TOPO (99%), and sulfur powder (99.98%) were purchased from Sigma-Aldrich, while OLA (80-90%), ODA (90%), and DPE (99%) were obtained from Acros. Ethanol (200 Proof, 100%) was obtained from Decon Labs, Inc and Diol (>98.0% (GC)) was purchased from TCI America.

3.2.2 Hot injection Synthesis of Pyrite FeS_2 NCs

All synthesis conditions are listed in Table 4.1. The typical reaction was carried out as following. $FeCl_2 \cdot 4H_2O$ (0.2010 g, 1.0 mmol) was mixed with ODA (10.0 g, 37.1 mmol) (or OLA (8.1 g, 10.0 mL, 30.4 mmol)) to form Fe-ODA (or Fe-OLA) complex under the condition of degassing with N_2 for 1 h at 120°C in a three-neck flask. In a separate tube, an injection solution consisting of sulfur (0.1922 g, 6.0 mmol) in DPE (5.4 g, 5 mL) was degassed with N_2 at 70°C for 1 h. The molar ratio of sulfur to iron was 6:1. The injection solution was added to the iron source solution using a syringe and the reaction mixture was kept at 120°C for 30 min. The temperature of the reaction solution was then raised to 220°C under nitrogen atmosphere for 2 h. The reaction was terminated by removing the heating mantle and allowing the reaction solution cool naturally. Once the temperature fell below 100°C, 5 mL of chloroform was injected into the solution to prevent ODA from solidifying. The product was separated from the reaction mixture by precipitation using ethanol. The precipitate was further purified by washing with chloroform/ethanol mixtures (1:9/volume:volume). Subsequent addition of chloroform followed by centrifugation at 4400 rpm for 5 min removed the large NCs and any residuals of side products from the product suspension. The redispersion and precipitation were repeated for three times.

For the synthesis using OLA to dissolve sulfur, 0.2010 g (1.0 mmol) $FeCl_2 \cdot 4H_2O$ was dissolved in 10.0 mL OLA and the injection solution consisted of 0.1922 g (6.0 mmol) sulfur powder in 5.0 mL OLA. Reduced concentration, i.e. 0.1005 g (0.5 mmol) $FeCl_2 \cdot 4H_2O$ in 10.0 mL OLA and 0.0961 g (3.0 mmol) sulfur powder in 5.0 mL OLA, was also applied to the synthesis. The other procedures and conditions were kept the same as aforementioned.

For the synthesis with an additive, 1.1599 g of TOPO or 0.1290 g of Diol was added to ODA (10.0 g, 37.1 mmol) (or OLA(8.1 g, 10.0 mL, 30.4 mmol)) to dissolve $FeCl_2 \cdot 4H_2O$ and the mixture was degassed with N_2 at 120°C for 1 h in a three-neck flask before the Table 3.1 Summary of the reaction conditions and the phase and morphology of the products.

Solvents for $FeCl_2 \cdot 4H_2O$	**Solvents for sulfur**	**S:Fe[a]**	**Temperature[b] (°C)**	**Concentration[c]**	**Phase**	**Morphology of major product**
ODA	DPE	6:1	220	2C	Pyrite	Short rods
OLA	DPE	6:1	220	2C	Pyrite	Chromosome-like rods
OLA	OLA	6:1	220	2C	Pyrite	Mixed spherical, short and curved rods
OLA	OLA	6:1	220	1C	Pyrite	Quasi-cubic NC agglomerates
ODA + TOPO	DPE	6:1	220	2C	Pyrite	Faceted NCs
OLA + TOPO	DPE	6:1	220	2C	Greigite + pyrite	—
OLA + TOPO	OLA	6:1	220	2C	Pyrite	Quasi-cubic NC agglomerates
OLA + Diol	OLA	6:1	220	2C	Pyrite	Quasi-cubic NC agglomerates
ODA	DPE	4:1	220	2C	Pyrite + greigite	~100-200 nm Crystals
ODA	DPE	2:1	220	2C	Pyrite + pyrrhotite	NCs + hexagonal plates
ODA	DPE	6:1	250	2C	Pyrite + greigite	—
ODA	DPE	6:1	120	2C	Amorphous	—
ODA	DPE	6:1	220	2C	Pyrite	Short rods

a Molar ratio. *b* Reaction temperature. *c* 2C refers to 0.2010 g (1.0 mmol) $FeCl_2 \cdot 4H_2O$ in 10.0 g (37.1 mmol) ODA or 8.1 g (10.0 mL) OLA.

injection of the sulfur solution. The rest of the synthesis and purification steps were the same as aforementioned.

Reactions were also conducted at the following conditions. The molar ratio of sulfur to iron was reduced to 4:1 and 2:1 (sulfur (0.1281 g, 4.0 mmol): $FeCl_2 \cdot 4H_2O$ (0.2010 g, 1.0 mmol) and sulfur (0.0641 g, 2.0 mmol): $FeCl_2 \cdot 4H_2O$ (0.2010 g, 1.0 mmol)). The concentration of sulfur and iron sources was reduced by half. The reaction was conducted at 120 and 250°C.

3.2.3 Characterizations of Pyrite FeS_2 NCs

TEM and STEM images were acquired using FEI Tecnai G2 F20 TEM operating at an accelerating voltage of 200 kV. Spot size 9 was applied for STEM measurement and a HAADF detector was used to collect images. The samples for TEM/STEM analysis were prepared by drop casting a dilute solution of NCs in chloroform onto ultrathin carbon-coated copper grids. Fast fourier transform (FFT) images were generated by ImageJ 1.45 S. XRD measurement was carried out on a GADDS D8 Discover diffractometer (Bruker) using Cu Kα radiation (λ = 1.5419 Å). Three frames with 100 seconds/frame were obtained for each sample. Scan angle 2θ begins at 30 degrees with a frame width of 25 degrees. Data were processed using the EVA package provided by Bruker Axs. Raman spectra of the products were acquired using a Renishaw InVia Raman spectrometer attached to a Leica DMLM upright microscope. A 100x (0.75 N.A.) objective lens was used to focus the 514 nm laser onto the particles and to collect the back scattered light from the particles. The illuminated sample area was about 3 μm^2 with the power of 1.5 mW. All spectra were collected for 10 accumulations with 10 s exposure time for each scan. Samples for XRD and Raman spectroscopy measurements were prepared by dusting the vacuum dried particles on a double-sided tape attached to a glass slide. UV-Vis-NIR optical absorption measurements of the samples were performed on a Varian Cary 5000 UV-Vis-NIR spectrophotometer. The hydrodynamic size of the particles was analyzed with a DLS particle sizer (Nano ZS, Zetasizer Nano, Malvern). Purified pyrite NCs dissolved in chloroform were used for UV-Vis-NIR and DLS measurements.

3.3 Results and Discussion

3.3.1 Short Pyrite FeS_2 NRs and Chromosome-Like Rods

Following the typical reaction conditions, ODA and OLA were used to dissolve $FeCl_2 \cdot 4H_2O$ and to form the iron precursor, respectively, and sulfur powder was dissolved in DPE. The as-synthesized NCs are denoted as NC-ODA and NC-OLA. The phase purity of NC-ODA and NC-OLA was determined using powder XRD and Raman spectroscopy. All the XRD peaks (Figure 4.1A) can be assigned to pure cubic pyrite phase of FeS_2 with a lattice constant of a = 5.416 Å (compared to JSPDS File No. 42-1340). No other iron-sulfur related phases, such as marcasite FeS_2, pyrrhotite $Fe_{1-x}S$, troilite FeS, or greigite Fe_3S_4 were observed. Raman spectroscopy provides the phonon vibrational modes of crystalline materials, which is very sensitive to their phase and composition, and therefore, was also applied to confirm the phase purity of NC-ODA and NC-OLA. Figure 4.1B shows Raman peaks at 340, 376, and 425 cm^{-1} for both products that match well with the reported values for the E_g, A_g, and T_g modes of pyrite FeS_2,[131] respectively, indicating the high phase purity of the products. The full width at half maximum (FWHM) of the XRD and Raman peaks of NC-ODA are narrower than those of NC-OLA, indicating better crystallinity of NC-ODA.

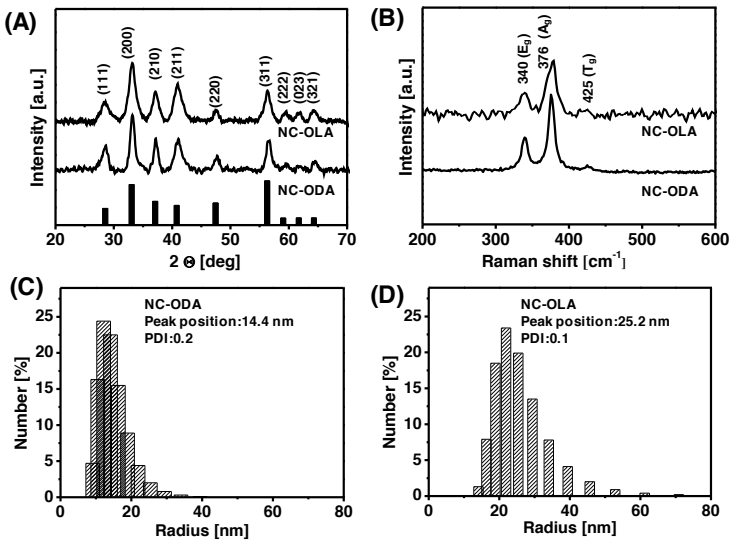

Figure 3.1 (A) XRD patterns and (B) Raman spectra of NC-ODA and NC-OLA showing the pure pyrite phase. (C and D) Size distribution of NC-ODA and NC-OLA pyrite NCs dispersed in chloroform determined by DLS.

The hydrodynamic radius of NC-ODA and NC-OLA was determined using DLS by dispersing NCs in chloroform. The radius of a nonspherical particle is determined as the radius of a sphere that has the same translational diffusion speed as the spherical particle. Figures 4.1C and 4.1D show the peak positions of the NC radii are 14.4 and 25.2 nm for NC-ODA and NC-OLA, respectively. NC-OLA has a broader size distribution than NC-ODA. To utilize these NCs for solution processable device fabrication, it is desired that they can be well suspended in different organic solvents. The DLS results show that the as-synthesized NC-ODA pyrite NCs in chlorobenzene (CB), tolunene, and hexane have similar peak positions and size distributions as those in chloroform but an additional large aggregation around 100-200 nm in pyridine.

The optical property of NC-ODA and NC-OLA dispersed in chloroform was investigated by UV-Vis-NIR spectroscopy. The synthesized pyrite NCs have the absorption extended to near infrared region (> 900 nm) as shown in the UV-Vis-NIR absorption spectra (Figure 4.2A). The indirect bandgap and the first and secondary direct transitions were estimated by plotting $(\alpha h\nu)^n$ versus $h\nu$ with n = ½ and 2, respectively (Figures 4.2B and 4.2C). The indirect bandgap was obtained as 1.24 and 1.16 eV for NC-

ODA and NC-OLA, respectively. The first and secondary direct transitions were 2.24 and 2.94 eV for NC-ODA and 1.97 and 2.90 eV for NC-OLA. We noticed that the indirect bandgap of pyrite NCs was larger compared to that of bulk pyrite. This phenomenon was also observed by several other groups.[143, 147-149] The size dependence of the bandgap of semiconductor NCs has been observed in other semiconductor materials and the lowest electronic transition can be related to the size of the semiconductor NCs using the following equation:[150]

$$E_g^{NC}(R)=E_g^{bulk}+\frac{h^2\pi^2}{2R^2}\left[\frac{1}{m_e^*}+\frac{1}{m_h^*}\right] \quad (4.1)$$

Where, $E_{g\ bulk}$ is the bulk bandgap, R is the radius of the NCs, h is Plank's constant 6.63 x 10^{-34} J·s, and m_h* and m_e* are the effective hole and electron mass, respectively. For pyrite, $E_{g\ bulk}$ = 0.95 eV, m_h* = 2.2m_e and m_e* = 0.25m_e are obtained from the literature.[151]

The calculated indirect bandgap as a function of NC radius is plotted in Figure 4.2D. The bandgap exponentially decays with the increase of the NC radius. The calculated indirect bandgaps are 1.27 and 1.05 eV for NCs with R = 14.4 and 25.2 nm, which are the average sizes of NC-ODA and NC-OLA determined by DLS, respectively. The small errors between the calculated and experimental values of the indirect bandgap may be caused by the non-spherical feature of the NCs. The first and second direct transitions have been previously studied experimentally by analyzing band-edge absorption of cubic pyrite NCs[147] and theoretically from density functional theory (DFT) calculations.[152] Our estimated values of the first direct transition of both NC-ODA and NC-OLA pyrite NCs are close to those determined experimentally (1.9 eV)[147] and theoretically (2.1 eV).[152] The values of the secondary direct transition of both pyrite NCs are close to the experimental value (3.0 eV)[147] but smaller than the theoretical value (3.5 eV).[152] This difference in the secondary direct transition is ascribed to the ambiguity of the proper level of absorption in this energy region.[147]

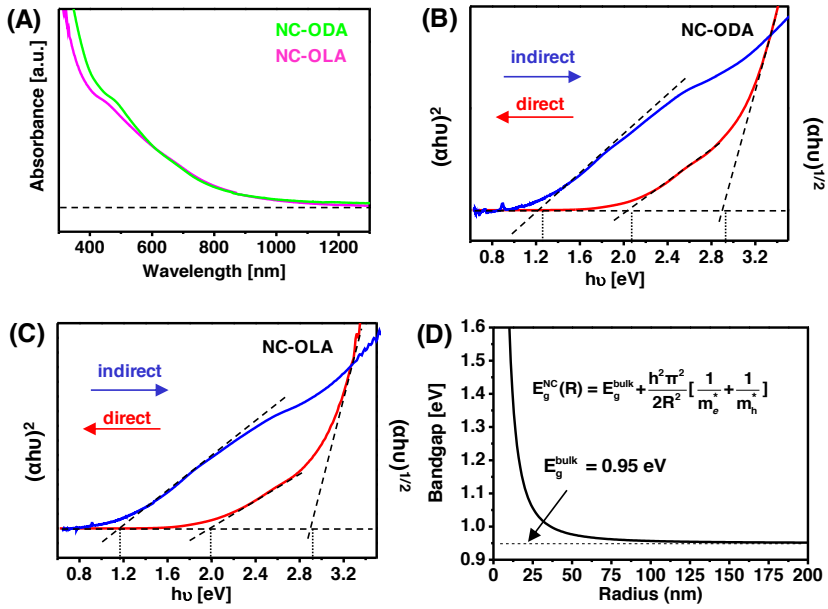

Figure 3.2 (A) UV-Vis-NIR spectra of NC-ODA and NC-OLA. (B and C) Plots of $(\alpha h\nu)^n$ vs. hν with n = 1/2 (blue line) and 2 (red line) for obtaining the indirect bandgap and the first and second direct transitions. (D) The indirect bandgap of pyrite NCs plotted against the radius of NCs based on Eqn. 4.1.

The morphology of NC-ODA and NC-OLA pyrite NCs were examined using TEM and STEM. Figure 4.3A shows the TEM image of NC-ODA pyrite NCs which are dominated by short rods (~8 nm in diameter and ~20 nm in length) and rods with kinks and branches (~8 nm in diameter and ~30 nm in length). Compared to the previous synthesis,[76] we doubled the concentration of both iron and sulfur reagents while keeping the S:Fe molar ratio the same, i.e. 6:1. More anisotropic NCs were obtained by using a higher concentration of reactants after reaction for 2 h. The elongation of NCs induced by increasing concentration of reactants has also been observed in the synthesis of CdSe NCs.[153] The anisotropic growth of CdSe along a kinetically favorable crystalline direction is promoted by the high local reactant concentration. The rod-type pyrite NCs were also observed in the products of NC-OLA as shown in the TEM image of Figure 4.3B. However, the NC-OLA pyrite NCs are mainly curved and chromosome-like rods with smaller diameters. By counting 200 NCs, the average branch diameter of NC-OLA is about 2-3 nm

smaller than that of NC-ODA. STEM images (Figures 4.3C and 4.3D) also show the difference between these two types of pyrite NCs. The NC-ODA pyrite NCs are separated, individual NRs, while the NC-OLA pyrite NCs are branched, chromosome-like NRs and form clusters. The morphologic difference of NC-ODA and NC-OLA may be caused by the different passivation density and orientation of ODA and OLA on the NC surface as well as the different interaction between aliphatic chains during the course of the growth. Both OLA and ODA have an 18 carbon chain but OLA has a double bond in the middle of the chain and has a cis configuration. A single OLA chain occupies a larger steric space than a single ODA chain. Both OLA and ODA bind iron atoms via the N-Fe interaction. The rotation of the octahedrons formed by the six bonds of each iron atom at the corners and the face centers of the cubic unit cell (Figure 1.2) makes it energetically unfavorable to passivate the same number of iron atoms with OLA compared to ODA. The packing of OLA on the NC surface was thus not expected to be strong, well ordered, or dense enough. The high-energy or poorly covered facets then favor an OA,[77, 154] Meanwhile, after injection of the sulfur source and increasing of the temperature to 220ºC, a higher concentration of H_2S caused by the vulcanization process[155, 156] between sulfur and the double bond of OLA could also favor the growth of branched structures.[157] Thus, using OLA as a solvent leads to the growth of pyrite NCs with more branches, chromosome-like shapes and poorer crystallinity compared to NCs synthesized using ODA as a solvent.

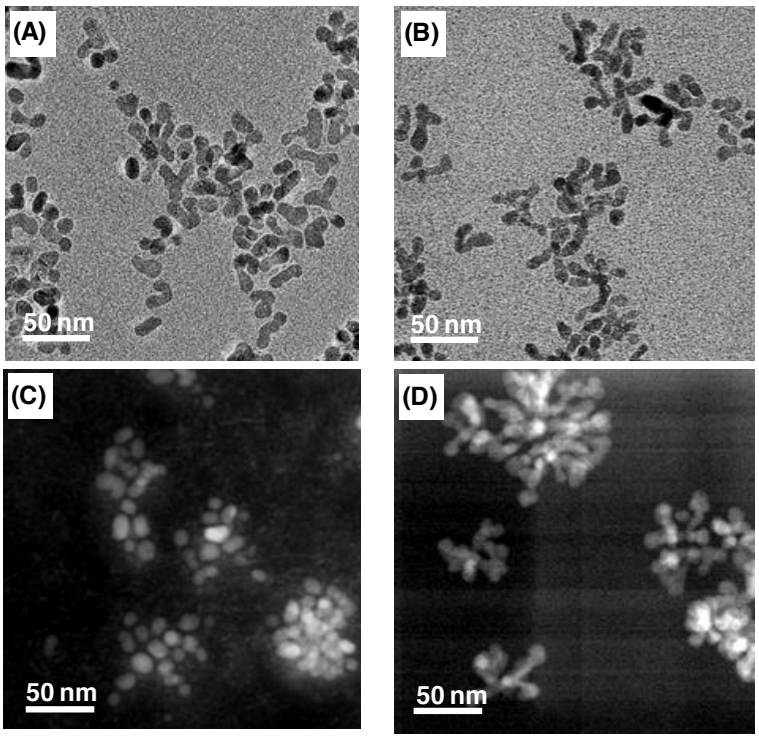

Figure 3.3 (A and B) TEM and (C and D) STEM images of NC-ODA (A and C) and NC-OLA (B and D) pyrite NCs.

3.3.2 Solvents on the Morphology of Pyrite FeS_2 NCs

In the synthesis of pyrite NCs using $FeCl_2 \cdot 4H_2O$ and sulfur powder with the hot injection method, both DPE and OLA have been used to dissolve sulfur powder.[76, 77, 79] We investigated the effect of the solvent used to dissolve sulfur on the morphology of pyrite NCs. We conducted the experiment by using OLA to dissolve both sulfur and iron agents. While keeping the molar ratio of sulfur to iron 6:1, the concentrations were 6 mmol sulfur powder in 5.0 mL OLA and 1.0 mmol $FeCl_2 \cdot 4H_2O$ in 10.0 mL OLA. These concentrations are the same as those for the synthesis of NC-ODA and NC-OLA but doubled compared to those reported in the previous works.[76, 77, 143, 144] The product is noted as 2C. Unlike the curved and chromosome-like NRs of NC-OLA pyrite NCs shown in Figures 4.3B and 4.3D, the TEM images in Figures 4.4A and 4.4C show that the product has smaller size with mixed spherical and short and curved-rod-like shapes. The crystal structure of the product is pure pyrite as shown by the selected area electron diffraction (SAED) patterns in the inset of Figure 4.4A. We also investigated the concentration effect. We reduced the

concentrations of the reactants to half, i.e., 3 mmol sulfur in 5.0 mL OLA and 0.5 mmol $FeCl_2 \cdot 4H_2O$ in 10.0 mL OLA. The product is noted as 1C. The TEM images in Figures 4.4B and 4.4D show quasi-cubic NC agglomerations formed by the attachment of single cube-like NCs. The SAED pattern in the inset of Figure 4.4B shows the product is pure pyrite. The HRTEM image in Figure 4.4E shows the fringe spacing of a single cubic NC in the quasi-cubic NC agglomerations is 2.7 Å, matching the distance between the (100) planes of pyrite FeS_2. Figure 4.4E also shows that one edge of the NC is parallel to the (100) plane. The phase purity of the products synthesized using high and low concentrations of the reactants was further confirmed by Raman spectroscopy shown in Figure 4.4F. One reason for the production of the quasi-cubic NC agglomerations with well-defined {100} facets could be ascribed to the generation of local sulfur-lean spots when the concentration is halved.[158] Using OLA to dissolve iron and sulfur agents was reported before.[77] Although the iron source was stirred at 100°C and the reaction took place at 220°C for 20 min, which were different from our procedures, similar quasi-cubic NC agglomerations and nanodendrites with elongated hyperbranches were obtained when the concentrations of the reactants were close to 1C and 4C, respectively, and the S:Fe molar ratio was kept as 6:1. This trend is in concord with our observations that higher concentration leads to elongated NCs with branches.

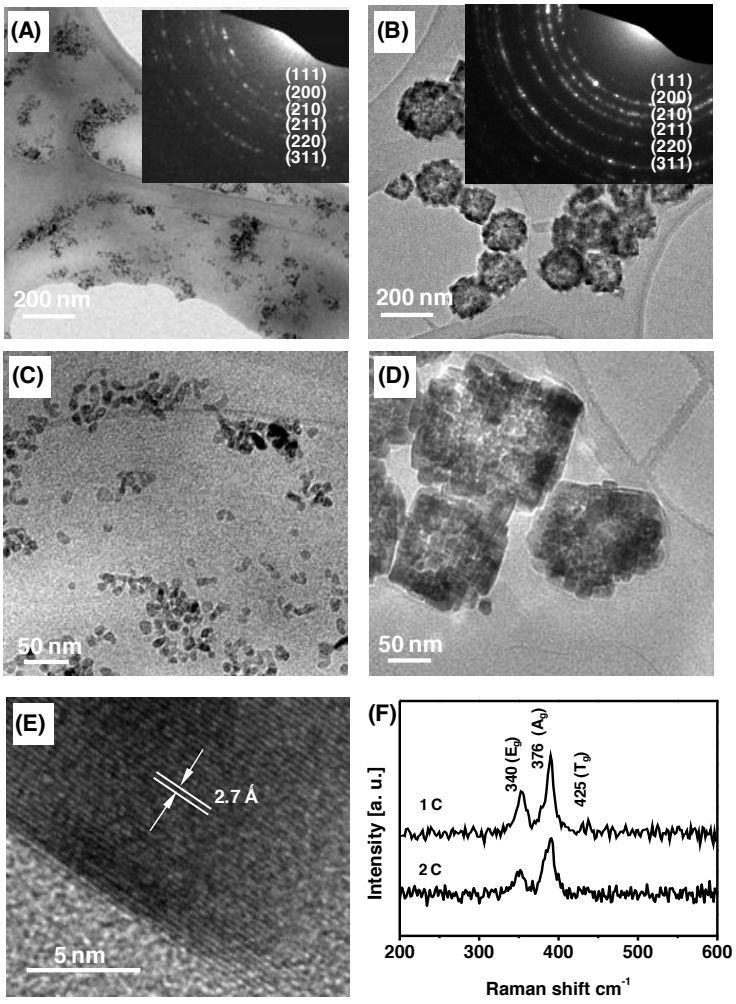

Figure 3.4 (A and C) TEM images of the pyrite NCs synthesized by using OLA as the solvent to dissolve both sulfur and iron agents and the concentrations of the reactants were noted as 2C. (B and D) TEM and (E) HRTEM images of the pyrite NCs synthesized by using OLA as the solvent but the concentrations of the reactants were noted as 1C. (F) Raman spectra of the synthesized pyrite NCs with the reactant concentrations of 1C and 2C, respectively.

3.3.3 Additives on the Morphology of Pyrite FeS_2 NCs

While ODA and OLA not only function as a solvent but also a capping agent to iron atoms via the interaction between Fe and N, we added additional capping agent in the reaction to investigate their effects on both morphology and phase purity of the products. The results are summarized in Table 4.1. When TOPO was added to the iron ODA solution

while all the other conditions were the same as for the synthesis of NC-ODA, the TEM images show a similar morphology but with more facets (Figures 4.5A and 4.5B) compared to NC-ODA (Figure 4.3A). The peak position and size distribution of the radius of the NCs determined by DLS is 14.4 nm with a polydispersity index (PDI) of 0.2 (Figure 4.5C) which is close to the size of NC-ODA without TOPO (14.4 nm with a PDI of 0.2, Figure 4.1C). The product was pure pyrite phase determined by XRD (Figure 4.5D). We investigated the chemical states of the iron and sulfur atoms at the surface of these NCs using XPS and found more oxidized iron compared to those without adding TOPO.[159] This leads to the rise of the conduction band energy from -4.5 to -3.9 eV. These pyrite NCs were blended with P3HT and $PC_{61}BM$ to make the inverted BHJ solar cells which showed enhanced photocurrent and high air stability.[159] While all the reaction conditions were the same, simply changing the solvent from ODA to OLA to dissolve the iron agent, the dominating phase in the product was greigite Fe_3S_4 with only a trace amount of pyrite phase as shown in Figure 4.5D. Product with pure pyrite can be restored by replacing DPE with OLA to dissolve sulfur while keeping OLA plus TOPO or Diol as the solvent to dissolve the iron source (Figure 4.6A). The products appear to have better crystallinity indicated by the narrower XRD peaks, which is mainly due to the relatively large (60-200 nm) quasi-cubic NC agglomerations (Figures 4.6B and 4.6C). The possible mechanisms will be discussed later.

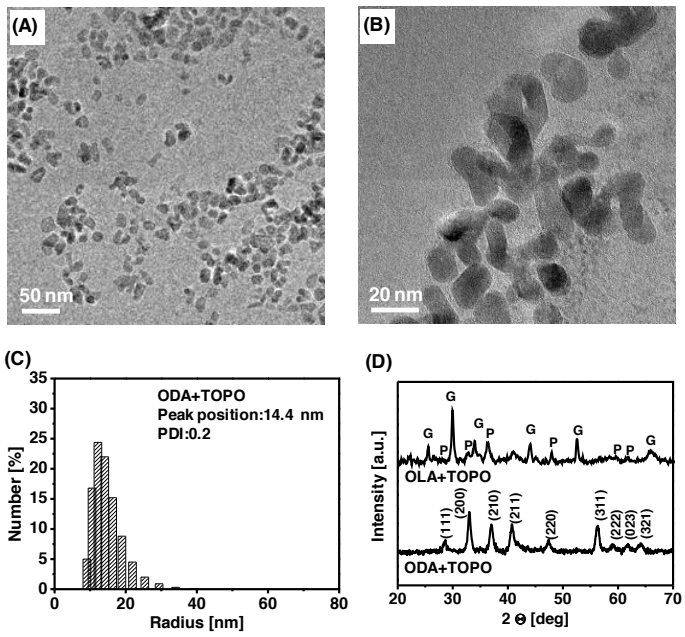

Figure 3.5 (A and B) The TEM images and (C) the hydrodynamic size distribution of the pyrite NCs synthesized by using ODA and TOPO to dissolve the iron source and DPE to dissolve sulfur. (D) The XRD patterns of the products synthesized by using OLA and TOPO to dissolve the iron source compared to using ODA and TOPO. Sulfur powder was dissolved with DPE and the concentrations of the reactants were 2C for both reactions.

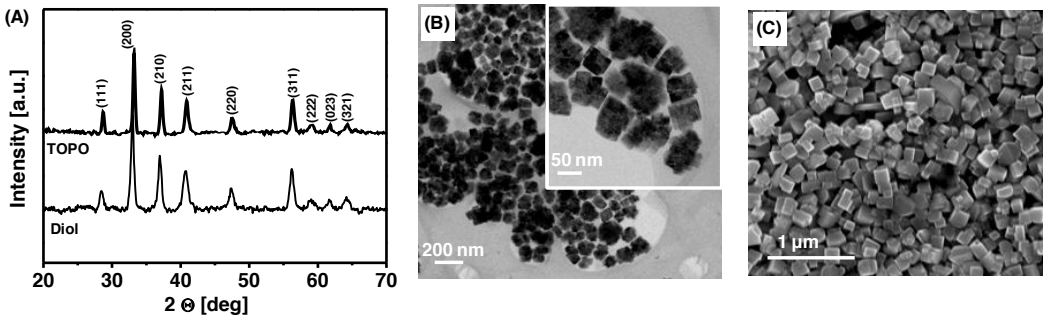

Figure 3.6 (A) The XRD patterns of the products using OLA plus TOPO and OLA plus Diol to dissolve $FeCl_2 \cdot 4H_2O$, respectively. Sulfur powder was dissolved in OLA for both reactions. (B) The TEM image of the quasi-cubic NC agglomerates synthesized by using OLA plus TOPO to dissolve $FeCl_2 \cdot 4H_2O$. (C) The SEM image of the quasi-cubic NC agglomerates synthesized by using OLA plus Diol to dissolve $FeCl_2 \cdot 4H_2O$.

3.3.4 S:Fe Ratio and Reaction Temperature on the Phase Purity

We then investigated the reaction conditions that influence the phase purity. We first varied the molar ratio of sulfur to iron. With the same reaction conditions as the synthesis of NC-ODA but by reducing the molar ratio of sulfur to iron from 6:1 to 4:1, the XRD pattern in Figure 4.7A shows that a trace amount of the greigite Fe_3S_4 phase exists in the product besides the pyrite phase. The narrower XRD peaks are due to larger crystals (~300-500 nm) (Figure 4.7C). Further reducing this ratio to 2:1, the XRD pattern in Figure 4.7A shows that only the greigite Fe_3S_4 and pyrrhotite $Fe_{1-x}S$ phases are in the product and no pyrite phase.

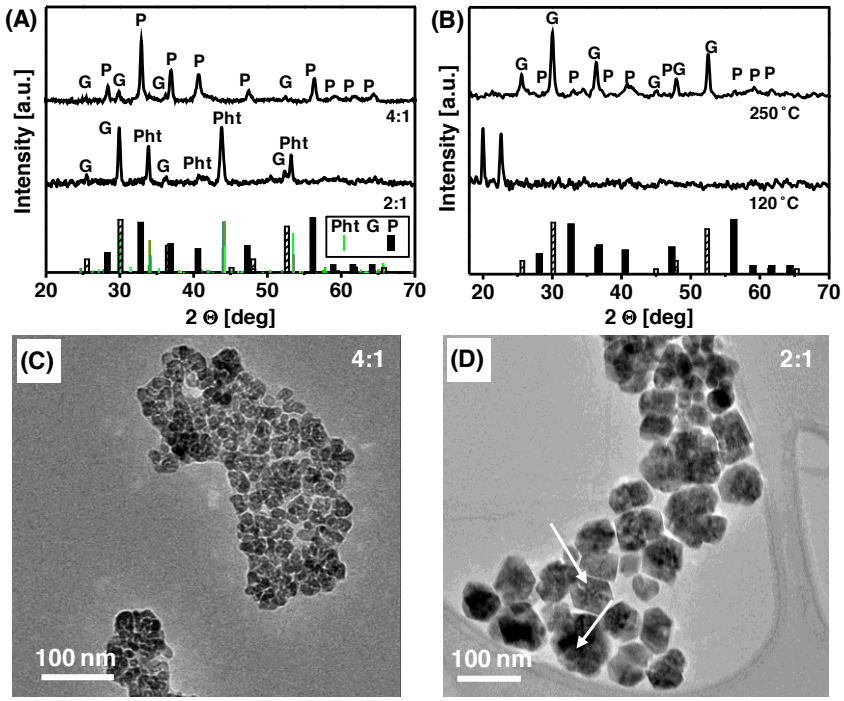

Figure 3.7 (A) XRD patterns of the products synthesized under the same conditions as those for NC-ODA but with lower molar ratio of sulfur to iron from 6: 1 to 4: 1 and 2: 1, respectively. The XRD peaks belong to pyrite FeS_2, greigite Fe_3S_4, and pyrrhotite $Fe_{1-x}S$ and are marked as P, G, and Pht, respectively. (B) XRD patterns of the products synthesized under the same conditions as those for NC-ODA but at 250 and 120°C, respectively. (C and D) TEM images of the products synthesized with the molar ratio of sulfur to iron as 4: 1 and 2:1, respectively. The pyrrhotite $Fe_{1-x}S$ phase NCs are shown as the hexagonal plates indicated by the white arrows for example.

The TEM image in Figure 4.7D shows some ~100 nm hexagonal plates in the product, which could be the pyrrhotite phase NCs.[160-163] It appears that excess sulfur in the reactants with a molar ratio of sulfur to iron of 6:1 is necessary to ensure product with the pure pyrite phase. Next, we investigated the effect of reaction temperature on phase purity. We conducted the experiments using the same conditions as those for the synthesis of NC-ODA but increased and lowered the reaction temperature from 220 to 250°C and 120°C, respectively. The XRD pattern in Figure 7B shows that the product synthesized at the higher reaction temperature of 250°C for 2 h has the greigite Fe_3S_4 crystalline phase with a trace amount of pyrite. The product synthesized at the lower reaction temperature of 120°C for 2 h shows no strong peaks between the 2θ of 25 to 65°. Two peaks at lower angle of the XRD pattern may be due to the complex formed between $FeCl_2$ and ODA.[117]

3.3.5 Discussions on the Growth Mechanism

All of the synthesis conditions and the phase and morphology of the products are summarized in Table 4.1. Sulfur powder dispersed in long chain primary alkylamines, such as OLA, has been widely used as a sulfur precursor in the synthesis of metal sulfide using the hot injection method.[164-166] A recent study showed that the reaction between sulfur powder and OLA could undergo four different reaction pathways, each of which produced H_2S and other byproducts.[167] It was found that alkylammonium polysulfides were the main product in the injection solution, which was typically prepared by mixing sulfur and OLA at a low temperature (< 80°C). Upon injecting into the hot metal precursor solutions and heating to NC growth temperatures, H_2S was liberated and other byproducts were formed. Under appropriate conditions, H_2S combines with the metal precursor to form metal sulfide NCs. Here, in our typical reactions, we used the non-amine solvent DPE to dissolve sulfur powder. It was reported that elemental sulfur can cleave DPE to benzene, thiophenol and phenol and generate H_2S but this takes place at 450°C.[168] Therefore, sulfur powder may be just dissolved in DPE at 70°C. When the sulfur-DPE solution was injected into the iron-ODA or OLA solution and the mixture was kept stirring for 30 min at 120°C, the reaction between sulfur and amine (and sulfur and the double bond of OLA[156]) could happen. A similar reaction mechanism[167] could be followed when the temperature was raised to 220°C. Therefore, having an adequate amount of H_2S in the reaction solution plays a crucial role

in the formation of pyrite phase. When the molar ratio of sulfur to iron was 4:1, less H_2S was generated and thus sulfur deficient product, Fe_3S_4, was produced in addition to pyrite phase. By further reducing this ratio to 2:1, the lack of H_2S impeded the formation of pyrite iron disulfide and thus only greigite Fe_3S_4 and pyrrhotite $Fe_{1-x}S$ were produced (Figure 4.7A).

Since the amount of H_2S in the reaction solution can also be affected by the reaction temperature as observed in the previous studies for CdS[156] and CdSe,[155] it is expected that the phase purity of the products could be affected by the reaction temperature. A higher reaction temperature (e.g. 250°C) could cause the escape of H_2S gas. This might be the reason for the final product consisting of the greigite phase with a trace amount of the pyrite phase (Figure 4.7B). On the other hand, if the reaction temperature is too low (e.g., 120°C), the reaction could remain at the stage of the formation of alkylammonium polysulfides. The incompletion of the amine and sulfur reaction could result in no or less generation of H_2S gas, and thus no crystalline phase in the product (Figure 4.7B).

Adding TOPO into the reaction of $FeCl_2{\cdot}4H_2O$ in ODA and sulfur in DPE has a different effect on the phase purity of the product as compared to adding TOPO into the reaction of $FeCl_2{\cdot}4H_2O$ in OLA and sulfur in DPE. Pure pyrite phase was obtained for ODA but greigite with trace pyrite for OLA (Table 4.1). This could be due to several factors taking place, such as the double bond in OLA causes the slower rate of nucleophilic attack on S_8 rings; the vulcanization process between sulfur and the double bond of OLA which is similar to the behavior observed in sulfur with 1-octadecence (ODE)[156] and selenium with ODE;[155] and steric hindering of TOPO and OLA. As a result, less H_2S is generated. When DPE was replaced by OLA to dissolve sulfur, alkylammonium polysulfides have been formed in the injection solution. After injecting the sulfur OLA solution to the iron precursor solution and subsequently raising the temperature to 220°C, enough H_2S was generated[155, 156, 167] to ensure the formation of pure pyrite phase in the product. Therefore, the additional capping agent (TOPO or Diol) mainly affects the morphology of the pyrite NCs but not the phase purity of the product.

3.4 Conclusions

In summary, we systematically studied the morphology and phase purity of pyrite NCs synthesized via the hot injection method by varying the reaction conditions and local chemical environment. High reactant concentrations or dissolving sulfur in OLA led to the growth of elongated NCs (short, branched, and chromosome-like rods) resulting from the fast growth of the kinetically favorable direction and possible OA of high energy facets. Quasi-cubic NC agglomerations were obtained when the reactant concentration was reduced or additional capping agent (TOPO or Diol) was added in the reactions where both iron and sulfur reagents were dissolved in OLA. The molar ratio of iron to sulfur and the reaction temperature were identified as two key parameters controlling the crystalline phase of the synthesized products. A mechanism involving the generation and amount of H_2S in the reaction solution can successfully explain the phase of products synthesized under different conditions. The as-synthesized pyrite NCs have absorption up to the NIR region and exhibit a slightly larger indirect bandgap than that of bulk pyrite. The present study demonstrated that the synthesis of pyrite NCs with controlled size, shape, and surface states is feasible. The phase and morphology-controlled pyrite NCs make it possible to further study the optical and electronic properties of pyrite NCs and to develop pyrite NC based PV devices for sustainable energy.

Chapter 4 ANISOTROPIC GROWTH OF IRON PYRITE FES2 NCS VIA ORIENTED ATTACHMENT

4.1 Introduction

In the previous chapter, pyrite FeS_2 nanocrystals were synthesized by using hot injection with varied reaction conditions. The shape, crystallinity, and phase purity were systematically studied. The anisotropic growth of pyrite FeS_2 nanocrystals were identified as oriented attachment. As we know, during the OA growth process, adjacent NCs spontaneously self-organize in such a way that they share a common crystallographic orientation and then form bonds among the opposite facets to reduce the total surface energy. The coherence generally leads to the formation of anisotropic NCs with abrupt edges. It sometimes also creates defects, such as misfit dislocations along the attachment planes. The anisotropic morphology and defects in NCs may create interstates or quantum wells along certain directions, providing unique electronic properties.[169-173] Defects could also act as an intrinsic dopant for semiconductor materials[174] or an alternative pathway of carrier transportation[175] and thus open a possibility to improve the performance of devices. Indeed, the OA growth of pyrite NCs have been observed in the previous reports.[47, 76, 176] The doughnut-like pyrite iron disulfide NCs were considered to be formed due to the fusion of several smaller, irregularly shaped pyrite NCs via the OA growth.[76] Dendritic or cubic pyrite iron disulfide NCs were generated by adjusting the concentration of iron precursor dissolved in oleylamine that in fact, controls the nucleus concentration and the growth kinetics.[47] The formation of pyrite iron disulfide nanodendrites was speculated to the attachment of several near-spherical NCs with a common crystalline orientation driven by the dipole moment of each NC. Thin pyrite iron disulfide nanosheets were also observed in the hot injection synthesis.[176] The formation was interpreted by the in-plane attachment of pyrite seeds with {110}-rich surfaces. Although the OA growth phenomena have been observed in the previous studies, there is still lack of fundamental investigation on how the attachment occurs, what driving force dominates, along what crystalline planes or directions the attachment occurs, and what other factors affect the OA process.

In this chapter, we studied the growth of anisotropic pyrite iron disulfide NCs by characterizing the crystalline structure as well as size and morphology of the products at

different growth stages using TEM, XRD, and DLS techniques. We analyzed the HRTEM images of pyrite iron disulfide NCs. Combined with the study of the atomic structure and the surface energy of different cleaved facets, a possible attachment mechanism is proposed. The influence of solvent (or surfactant) on the OA growth of anisotropic pyrite iron disulfide NCs was also investigated.

4.2 Experimental Section

4.2.1 Materials for Anisotropic Growth of Pyrite FeS_2 NCs

All chemicals were used as received. $FeCl_2 \cdot 4H_2O$ (99.99%), chloroform (≥ 99.8%), and sulfur powder (99.98%) were purchased from Sigma-Aldrich, while oleylamine (OLA, 80-90%), ODA (90%), and DPE (99%) were obtained from Acros. Ethanol (200 Proof, 100%) was obtained from Decon Labs, Inc.

4.2.2 Synthesis of Pyrite FeS_2 NCs

The typical reaction was carried out as following. $FeCl_2 \cdot 4H_2O$ (0.2010 g, 1.0 mmol) was mixed with ODA (10.0 g, 37.1 mmol) to form Fe-ODA complex under the condition of degassing with N_2 for 1 h at 120°C in a three-neck flask. In a separate tube, an injection solution consisting of sulfur (0.1922 g, 6.0 mmol) in DPE (5.4 g, 5 mL) was degassed with N_2 at 70°C for 1 h. The molar ratio of sulfur to iron was 6:1. The injection solution was added to the iron source solution using a syringe and the reaction mixture was kept at 120°C for 30 min and then raised to 220°C under nitrogen atmosphere. A 0.5 ml aliquot of solution was taken out of the reactor by using a syringe after the injection of 30 min at 120°C and at the different time periods between 5 min to 12 h after the temperature was increased to 220°C. The aliquot was transferred to a tube and a 0.5 mL of chloroform was injected to prevent ODA from solidifying. The products were separated from the reaction mixture by precipitation using 3 ml ethanol and centrifugation at 4400 rpm for 5 min. The precipitates were further washed by re-dispersing the precipitate through adding 1 ml chloroform, precipitating by adding 3 ml ethanol, and separating by centrifugation at 4400 rpm for 5 min. The washing steps were repeated for three times.

For the synthesis using OLA to dissolve $FeCl_2 \cdot 4H_2O$, $FeCl_2 \cdot 4H_2O$ (0.2010 g,1.0 mmol) was dissolved in 10.0 mL OLA (8.1 g, 30.4 mmol) and the injection solution consisted of

sulfur powder (0.1922 g, 6.0 mmol) in DPE (5.4g, 5.0 mL). Reactants were taken out at 2 and 4 h after the reaction temperature was raised to 220°C. The other procedures and conditions were kept the same as aforementioned.

4.2.3 Characterization of Anisotropic Pyrite FeS_2 NCs

TEM and HRTEM images were acquired on an FEI Tecnai G2 F20 TEM system operating at an accelerating voltage of 200 kV. The system can perform scanning TEM (STEM) and is equipped with an EDX detector. Samples for TEM analysis were prepared by drop casting a dilute solution of NCs in chloroform onto 300 mesh ultrathin Lacey Formvar/carbon-coated copper grids and allowing the solvent to evaporate at room temperature. FFT images were generated by ImageJ 1.45 S. The measurement of XRD was carried out on a Bruker GADDS D8 Discover diffractometer using Cu Kα radiation (λ = 1.5419 Å). Three frames with 100 s/frame were obtained for each sample. Scan angle 2θ begins at 30° with a frame width of 25°. Data were processed using the EVA package provided by Bruker Axs. Samples for XRD measurements were prepared by dusting the vacuum dried NCs on a double-sided tape attached to a glass slide. The hydrodynamic size of NCs was analyzed with a DLS particle sizer (Nano ZS, Zetasizer Nano, Malvern). Samples for DLS experiments were the purified pyrite iron disulfide NCs dissolved in chloroform.

4.3 Results and Discussion

4.3.1 Time-Dependent Crystallinity, Morphology, and Size of the NCs

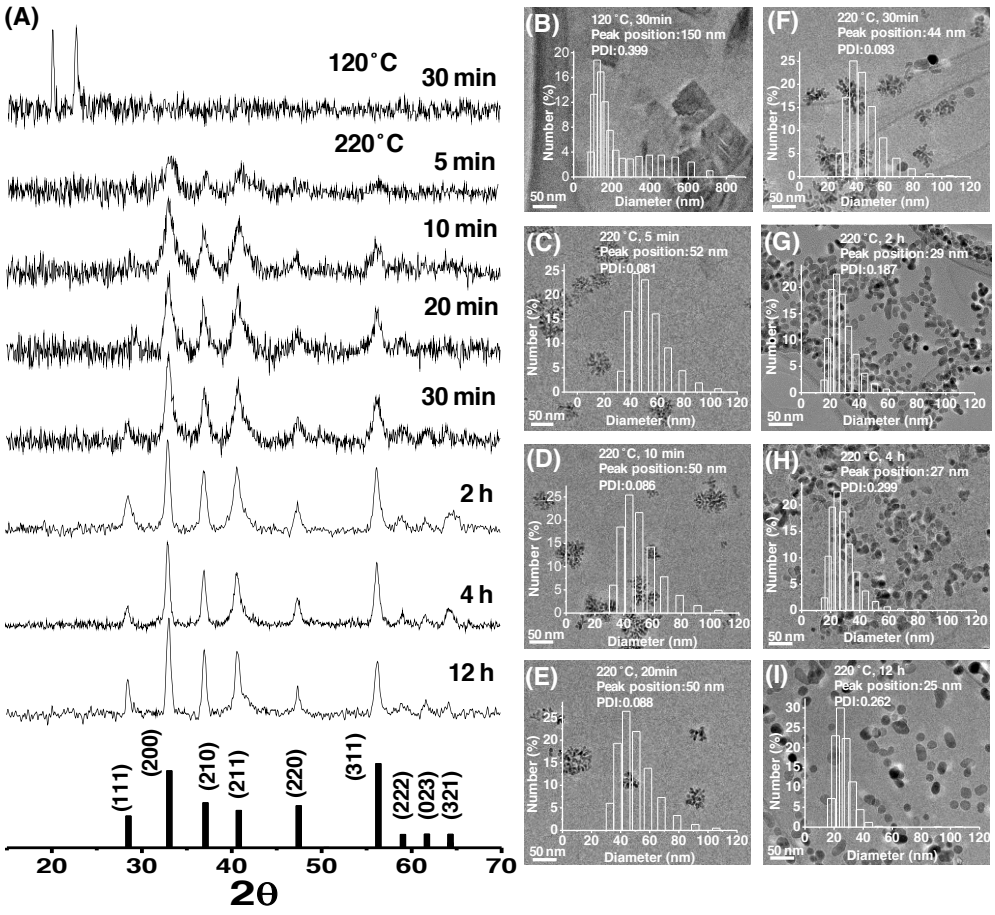

Figure 4.1 (A) XRD and (B-I) DLS results and TEM images of the products reacted after the injection of the sulfur precursor in DPE to the iron precursor in ODA at 120°C for 30 min and at 220°C for 5, 10, 20, and 30 min and 2, 4, and 12 h, respectively.

In order to understand the formation of anisotropic pyrite iron disulfide NCs, we first investigated the time-dependent crystallinity, morphology, and size of the NCs synthesized by the injection of a sulfur precursor in DPE solution to an iron precursor in ODA solution. An aliquot of solution was taken out of the reaction solution after the injection of the sulfur precursor solution into the iron precursor solution at 120°C for 30 min and at the different time periods between 5 min to 12 h after the increasing of the temperature to 220°C. The crystallinity and morphology of the products were studied using XRD and TEM,

respectively. To obtain better statistics on particle size distribution, the particle size was also measured using DLS in addition to the estimation from the TEM images. Figure 5.1A shows the XRD patterns of the products collected at different reaction conditions and the corresponding TEM images and DLS results are shown in Figures 5.1B-1I. For the sample collected after the injection at 120°C for 30 min, two diffraction peaks at low angles of 19.9 and 22.6º were observed. These two peaks are ascribed to the spacing of the (111) and (112) planes of mackinawite crystal (FeS_{1-x} with $0 < x < 0.07$), i.e., 4.5 and 3.9 Å, respectively.[177] The TEM image in Figure 5.1B shows the product is mainly cubic nanosheets with the size ~70-200 nm. The elemental composition of the nanosheets was analyzed using point energy dispersive X-ray spectrometer (EDX) under the STEM mode. The average atomic Fe:S ratio was determined to be 1:0.94 through the measurement of five spots on the nanosheets. A typical EDX spectrum is shown in Figure 5.2. The DLS result shows the particle size distribution centered around 150 nm, which is concord with the TEM result. The morphology of mackinawite crystal was also cubic sheets as reported in the previous study.[177] Therefore, cubic mackinawite $FeS_{0.94}$ phase iron sulfide nanosheets were formed during the reaction at the low temperature.

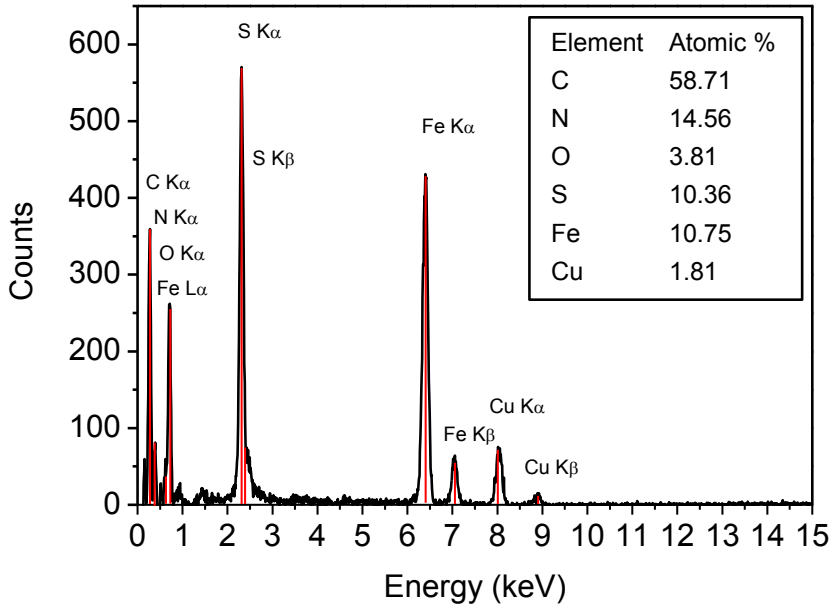

Figure 4.2 A representative point EDX spectrum under the STEM mode on a mackinawite nanosheet obtained at 120°C for 30 min.

When the reaction temperature was raised to 220°C, pure pyrite phase was formed even at the reaction for 5 min, indicated by the (200), (210), (211), and (311) of the diffraction peaks of pyrite iron disulfide in Figure 5.1A. The TEM image in Figure 5.1C shows elongated and twisted small NCs with the diameter of ~8 nm and the length of ~20 nm within the cubic matrices and each of these matrices has the side of ~50 nm. The DLS result also shows the particle size distribution centered around 50 nm. The XRD and TEM results indicate that when the temperature was raised to 220°C, the nucleation and growth of pyrite iron disulfide took place immediately within the pre-formed crystalline mackinawite nanosheets. The elongated and twisted rod-like NCs formed in such a short time could be the results of OA among adjacent small primary monomer seeds along the high surface energy facets in order to reduce the total surface energy of primary monomer seeds. The XRD patterns show better crystallinity of the products obtained after 10 and 20 min reactions. The morphology and size of NCs, however, show almost no change and NCs are still clustered in the similar size matrices (Figure 5.1D and 5.1E).

One key difference between NCs grown via the OR and the OA mechanisms is the dependence of particle size and the number of particles on growth time. Via the OR mechanism, large particles grow larger at the expense of smaller particles, resulting in particle size increase but particle number decrease as time progresses. Via the OA mechanism, the particles attach to create a more stable particle, and then usually cease the size and number of particles for a certain period of time. This is the behavior exhibited in the growth of 5-20 min as shown in Figure 5.1C-5.1E, and thus the growth of pyrite iron disulfide NCs in this period of time is mainly via the OA mechanism. The pre-formed mackinawite crystalline nanosheets at the low temperature provides the templates for nucleation. When the temperature was suddenly raised to 220°C, nucleation bust occurred within the nanosheets. The template effect could make adjacent nuclei orientate along some common crystallographic directions, and thus easily attached to each other with minimum re-orientation or diffusion as illustrated in Scheme 5.1A. At the initial stage of OA, some nuclei or monomers may have large area facets so they can join at the planar interface and form bonds (Scheme 5.2A). For those without large area facets, they

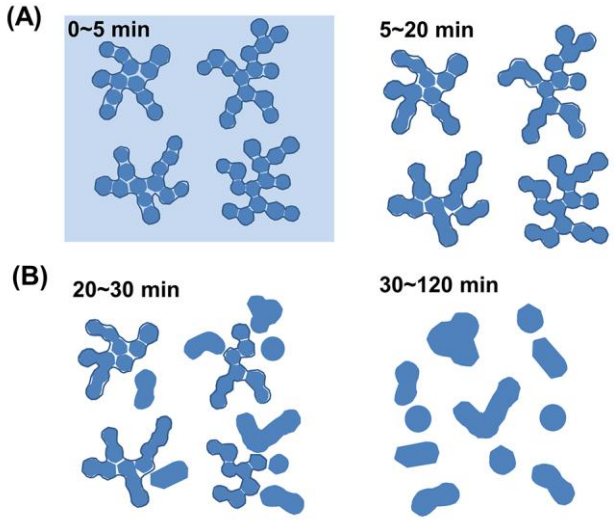

Scheme 4.1 (A) Illustration of the nucleation of pyrite iron disulfide within the pre-formed mackinawite crystalline nanosheets and the growth of NCs through OA in the early stage (0-20 min) at 220°C and (B) Illustration of the isolation of individual larger NCs from NC clusters and the growth of the faceted anisotropic NCs through OR with the proceeding of reaction (30-120 min).

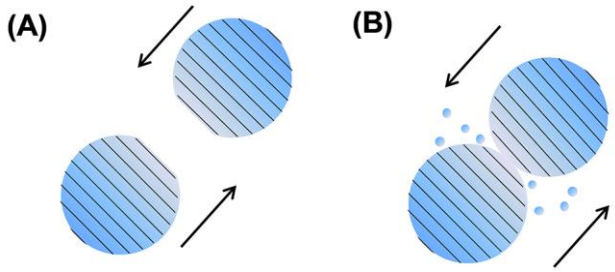

Scheme 4.2 (A) Illustration of an orientated attachment via sharing the common crystallographic facets at a planar interface and (B) Illustration of an orientated attachment via a "point contact" along an energy favorite crystallographic direction followed by the subsequent interparticle growth.

may orientate along an energy favorite crystallographic direction, approached to each other to form a "point contact", and then molecules diffused and attached to the lattice positions to fill the gap (Scheme 5.2B). Therefore, crystallinity became better as time progressed from 5 to 20 min as shown in the XRD patterns in Figure 5.1A.

The change of morphology is shown in the TEM image taken from the product after the reaction of 30 min at 220°C (Figure 5.1E). While most NCs are still in clusters, they grow into more round-like or fat rod-like NCs than thin rod-like NCs observed in the shorter time reactions, indicating OR growth becomes more important than OA growth. Some smaller particles are consumed in the growth of large particles, resulting in the decrease of the number of NCs in clusters as well as the shrink of cluster size from ~50 to ~44 nm as shown in the DLS results (Figures 5.1B-5.1E). After the reaction for 2 h, the crystallinity of the product is even better (Figure 5.1A) and more dispersed individual anisotropic NCs are observed in the TEM image (Figure 5.1F). The DLS result confirms more dispersed particles with a peak around 29 nm. The growth of NCs in this period of time is illustrated in Scheme 5.1B. No dramatic morphology change is shown in the TEM image (Figure 5.1H) after the reaction for 4 h except that the NCs are slightly more isotropic. This trend was also observed in the previous studies.[76] Further increasing the reaction time to 12 h, NCs grow into faceted particles and the particle size is more uniform indicated by the narrow size distribution of the DLS result (Figure 5.1I).

4.3.2 Plane to Plane Attachment

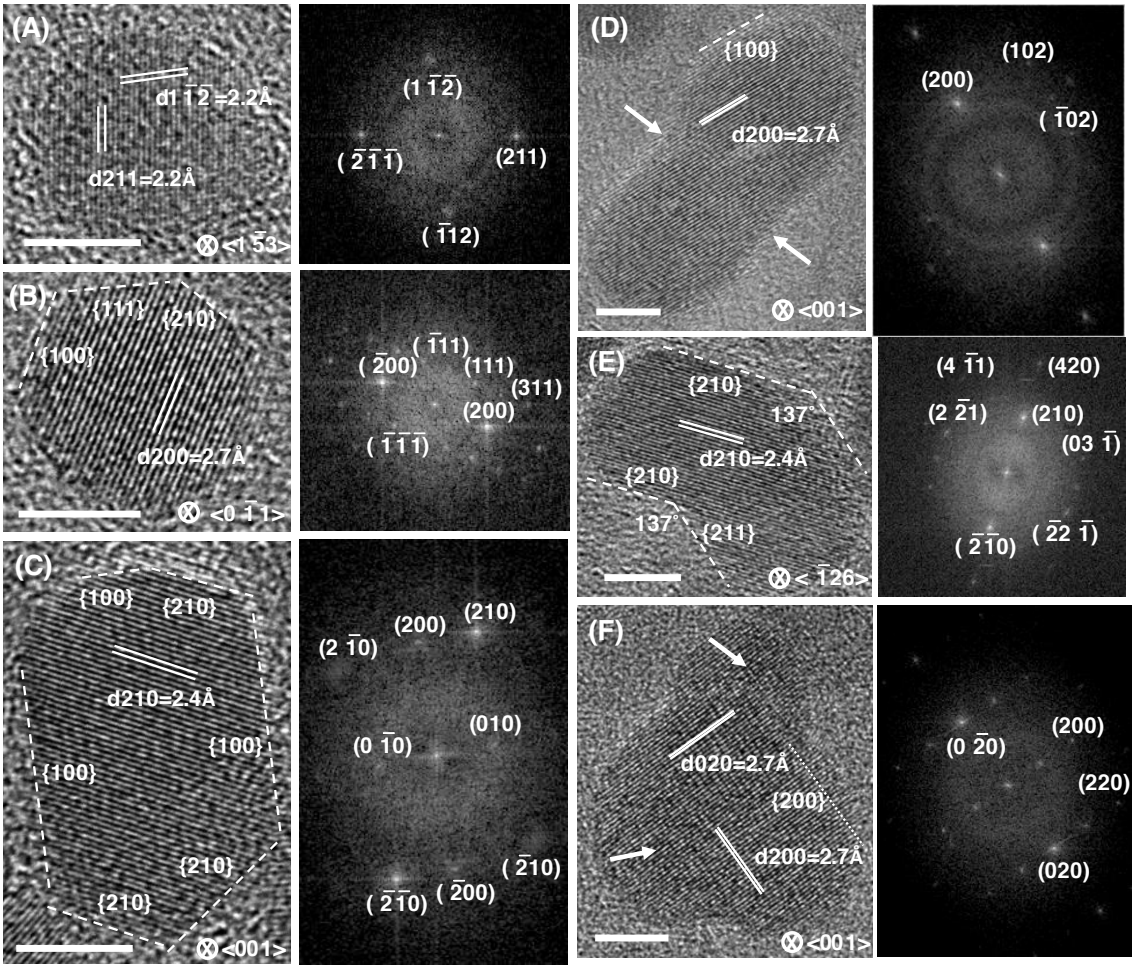

Figure 4.3 HRTEM images of iron pyrite NCs as spherical-like monomers (A, B) and formed via OA of two (C, D) and multiple (E, F) monomers along with their FFT images. Facets and planes are indicated by the dotted lines. The scale bar is 5 nm.

HRTEM images were taken in order to identify the crystallographic planes and orientations where the attachment occurs. Since attachment takes place rapidly at the initial stage, it is difficult to take high quality HRTEM images. We took HRTEM images of pyrite iron disulfide NCs synthesized at 220°C for 2 h. Under this condition, the NCs grown via OA can still be identified and the crystallographic planes and facets can also be well resolved. As shown in Figure 5.1G, the NCs exist in a variety of morphologies such as spherical-like monomers, rod-like dimers, kinked trimmers, and even branched structures. Figures 5.2A and 5.2B show the HRTEM images of two monomers with the size of ~9.4

nm. All the fringes are indexed according to the generated FFT patterns. Two sets of the parallel fringes with the distance of 2.2 Å are shown in Figure 5.2A, which corresponds to the lattice spacing of the {211} planes of pyrite iron disulfide crystals. One set of the parallel fringes with the distance of 2.7 Å is shown in Figure 5.2B, which matches the lattice distance of the {200} planes of pyrite iron disulfide crystals. Figure 5.2B also shows that the monomer has the {111}, {100}, and {210} facets.

The HRTEM image in Figure 5.2C shows a rod-like single crystalline NC with the parallel fringe distance 2.4 Å, corresponding to the lattice spacing of the {210} planes of pyrite iron disulfide crystals. The long axis of the rod is along the <100> direction. The rod is bounded with the {100} and {210} facets and the partial curvature at one end could be due to the several step defects at one {100} facet, which are commonly observed in {100} facet of pyrite NCs.[178-180] Another rod-like single crystalline NC, shown in Figure 5.2D, has a different morphology with different sizes at the two ends and a slightly narrowed middle part. The long axis direction is identified as <210> direction. The step defects at {100} facets makes the two ends more round-like. Figure 5.2E shows a single crystalline NR with a 137° kink formed between the {210} and {211} planes. Parallel fringes with the distance 2.4 Å, which corresponds to the lattice spacing of the {210} planes, cross the kinked interplane smoothly without any defect. The abrupt edge is a typical morphology resulted from the OA growth. Similarly, Figure 5.2F shows a triangular-like NC also with the abrupt edges. This NC could be formed by the attachment of two monomers from the top and the bottom right corner to the NR. Again, parallel fringes corresponding to the {200} planes extend smoothly across the interplanes.

For OA growth, the adjacent NCs undergo a self-organization process to orientate each other with a common crystalline direction and then form bonds between the opposite facets. The driving force of the self-organization process can be ascribed to the interaction of the permanent or temporary electric dipole moments carried by NCs. The presence of polar facets due to nonstoichiometric surfaces as well as the anisotropic shape of a neutral NC all can lead to a dipole in the NC.[88] As shown in Figures 5.2A-5.2F, {100}, {210}, and {111} facets are mostly observed in the HRTEM images of pyrite iron disulfide NCs. There are three, six and five different terminations for the (001), (210), and (111)

Table 4.1 Summary of the (001), (210), and (111) surfaces of pyrite FeS_2 terminated in different layers. X: the outmost surface atoms; N_{Fe} and N_S: the number of dangling bonds of iron and sulfur atoms, respectively. The surface free energies of each terminated layer are estimated at the two fixed changes in sulfur chemical potential ($\Delta\mu_s$ = -0.3 and -0.8) in Figure 7 of ref. [158] to represent the S-rich and S-lean conditions, respectively.

Layer	**X**	**N_{Fe}**	**N_S**	**Energy (J/m^2) $\Delta\mu_s$ = -0.3**	**Energy (J/m^2) $\Delta\mu_s$ = -0.8**
(001)					
(001)-Fe	**Fe**	**3**	**1**	2.72	**2.16**
(001)-S	S	1	1	1.22	1.22
(001)-2S	**S**	**0**	**3, 1**	1.41	**2.01**
(210)					
(210)-Fe	**Fe**	**2, 3**	**1, 2**	2.32	**2.02**
(210)-2S	**S**	**2**	**2, 3**	1.81	**2.05**
(210)-S	S	1, 2	1, 2	1.60	1.60
(210)-Fe’	Fe	1, 3	1	1.97	1.65
(210)-2S’	S, Fe	1	1, 2	1.01	1.23
(210)-S’	S, Fe	2	1	1.52	1.52
(111)					
(111)-Fe	Fe	3	0	-	-
(111)-S	S, Fe	2, 3	1	2.56	2.16
(111)-2S	S	1	2	1.44	1.44
(111)-3S	S	0	1, 2	0.88	1.39
(111)-4S	S	0	1, 2, 3	1.23	1.92

surfaces, respectively, which are summarized in Table 5.1. The atomic structures of different terminations are provided in Figures 5.4-5.6. The surface unit cell of the (001) plane is a square as shown in Figure 5.4. The termination of the (001)-Fe contains Fe atoms only in the topmost layer while the other two terminations of the (001)-S and (001)-2S each contain S atoms in the topmost layer. The surface unit

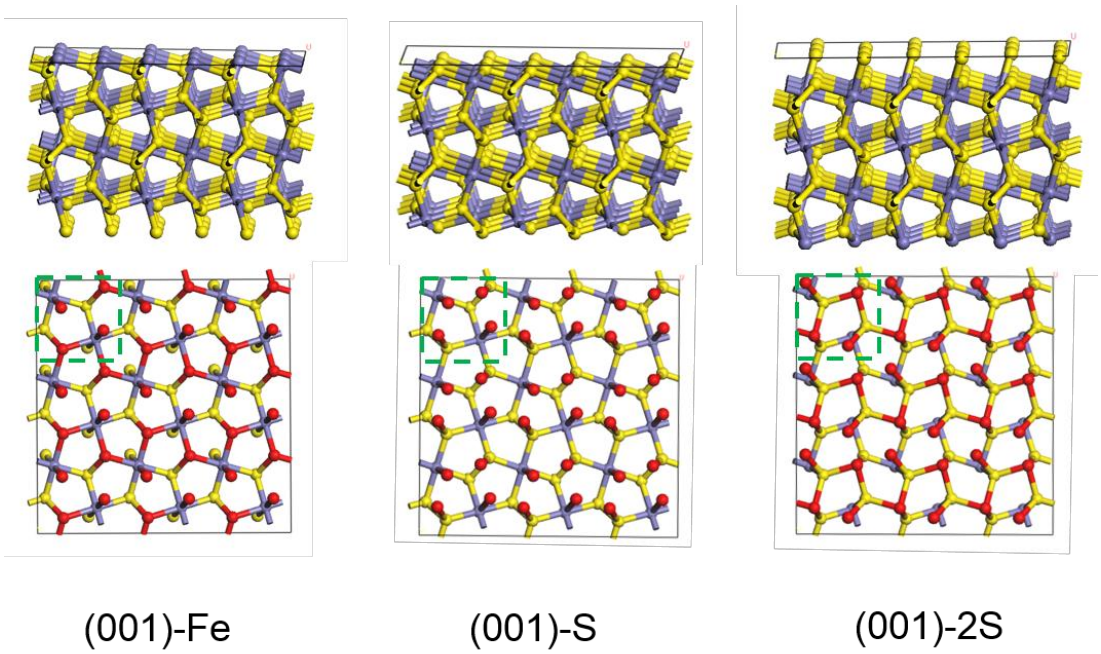

Figure 4.4 The atomic structures of the pyrite FeS_2 (001) surface with three different terminations. Side- and top-view are shown in the top and bottom rows, respectively. Blue balls are iron atoms and yellow balls are sulfur atoms. The unit cell is indicated by the green dotted line. In the top-view, the dangling bonds are terminated by hydrogen atoms in red. Only the top two layers are shown in the top-view.

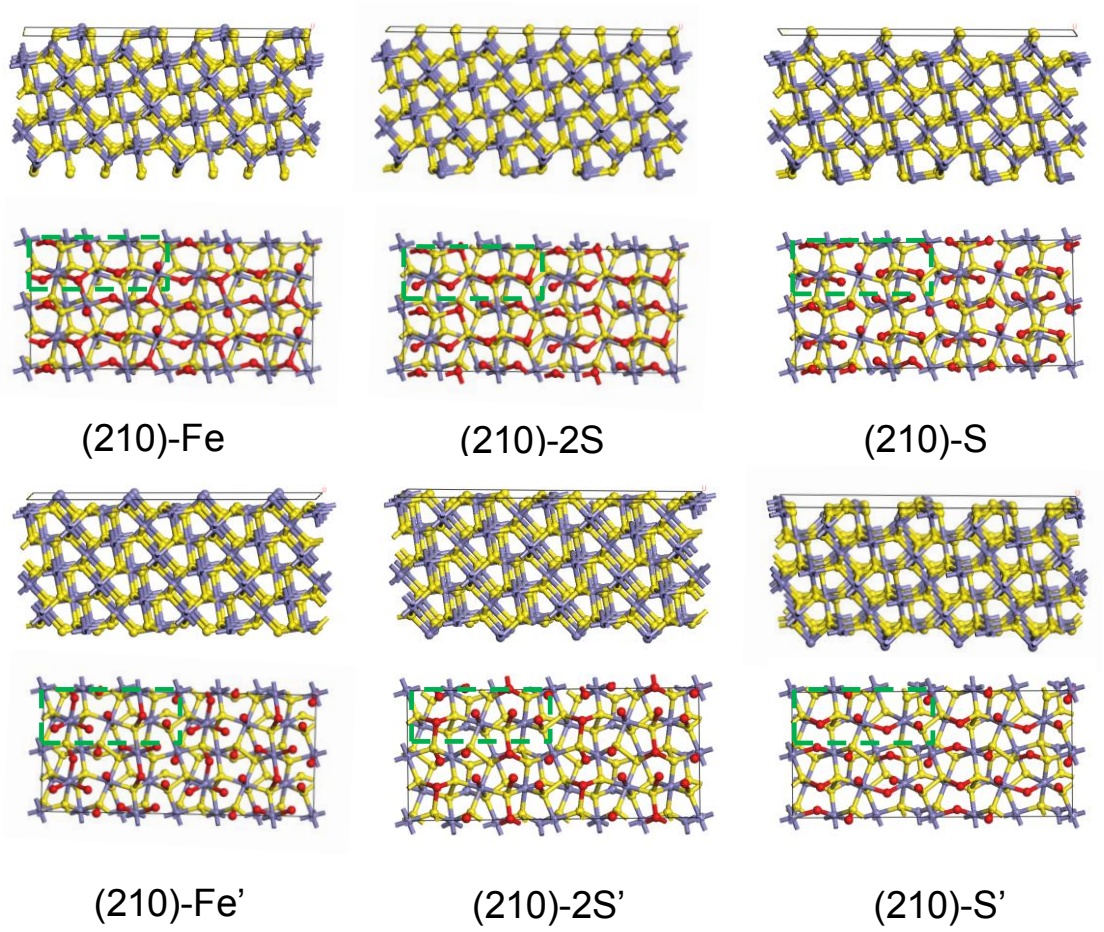

Figure 4.5 The atomic structures of the pyrite FeS_2 (210) surface with six different terminations. Side- and top-view are shown in the top and bottom rows, respectively. Blue balls are iron atoms and yellow balls are sulfur atoms. The unit cell is indicated by the green dotted line. In the top-view, the dangling bonds are terminated by hydrogen atoms in red. Only the top two layers are shown in the top-view.

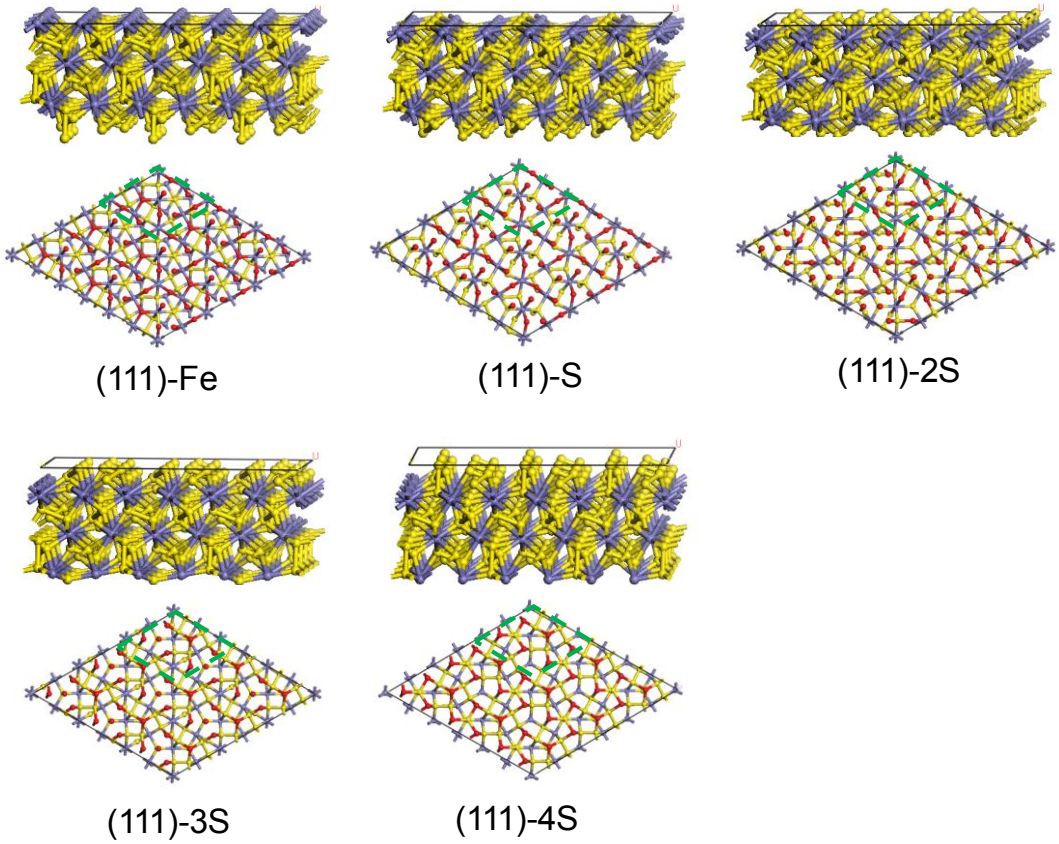

Figure 4.6 The atomic structures of the pyrite FeS_2 (111) surface with five different terminations. The side- and top-view are shown in the top and bottom rows, respectively. Blue balls are iron atoms and yellow balls are sulfur atoms. The unit cell is indicated by the green dotted line. In the top-view, the dangling bonds are terminated by hydrogen atoms in red color. Only the top two layers are shown in the top-view. Only the top two layers are shown in the top-view.

cell of the (210) plane is rectangular as shown in Figure 5.5. The (210)-Fe and (210)-Fe' planes are terminated by Fe, the (210)-2S and (210)-S planes are terminated by S, and the (210)-2S' and (210)-S' planes each contains both Fe and S atoms at the topmost layer. The surface unit cell of the (111) plane is hexagonal as shown in Figure 5.6. The (111)-2S, (111)-3S, and (111)-4S planes all are terminated with S atoms, while the (111)-Fe plane is terminated with Fe atoms and the (111)-S contains both Fe and S atoms in the topmost layer. The number of dangling bonds of each termination is summarized in Table 5.1. The dangling bonds are terminated with H atom shown in red balls in Figures 5.4-5.6. Among

these cutting facets, the (001)-S, (111)-2S, (210)-S, and (210)-S' planes are stoichiometric and thus are nonpolar. These facets may not be involved in the process of directly forming bonds between the opposite facets. The (001)-2S, (210)-2S, (111)-3S, (111)-4S, and (210)-2S' planes contain excess sulfur atoms while the (001)-Fe, (111)-S, (210)-Fe, and (210)-Fe' have excess iron atoms. When the NCs are terminated with these facets, the dipole moment created by the polar facets could be the driving force to move and rotate adjacent NCs to facing each other with shared common crystallographic directions. Surface energy also plays an important role in the OA process. The facets with high surface energy have high probability to form bonds between the opposite facets shared the common crystallographic directions. Surface energy of the stoichiometric terminations with the surface expose to vacuum has been calculated using DFT and the trend of (001)-S < (111)-2S < (210)-S was obtained.[158, 181] Recently, surface free energy of all terminations of (001), (210), (111), and (011) surfaces in equilibrium of arbitrary sulfur environment was calculated using DFT in combination of a thermodynamic description of the surfaces.[158] It was found that with the increase of the sulfur chemical potential the surface free energy remains constant for all stoichiometric planes, decreases for all planes with extra S atoms, and increases for all planes with extra Fe atoms. In the calculations, the S-lean condition is defined as the low-limit of S chemical potential ($\Delta\mu_S$ = -0.9) at which sulfide decomposes into Fe and S atoms while the S-rich condition is defined as $\Delta\mu_S$ = 0 at which S gas condenses completely on the surface. The similar trend for surface free energy of (001)-S, (111)-2S, and (210)-S surfaces was obtained using this method although the values are slight higher than those reported previously. Since the nucleation and initial growth of pyrite iron disulfide NCs occur in the pre-formed mackinawite $FeS_{0.94}$ crystalline nanosheets as shown in Figure 1B, we consider the local S environment is more like S-lean. We summarized the surface free energy at $\Delta\mu_S$ = -0.3 and -0.8 to represent the S-rich and S-lean conditions, respectively, for all types of terminations of (001), (210), and (111) in Table 1. Among all the 14 cleaved facets, the (001)-Fe, (210)-2S, (210)-Fe, and (001)-2S are four facets with high surface free energy under the S-lean condition (Table 5.1). As shown in Scheme 5.3, seamless, direct bonding could be formed by the attachment of (001)-Fe and (001)-2S as well as (210)-Fe and (210)-2S. Therefore, abrupt structure changes at {100} (Figure 5.2F) and {210} (Figures 5.2D and 5.2E) facets

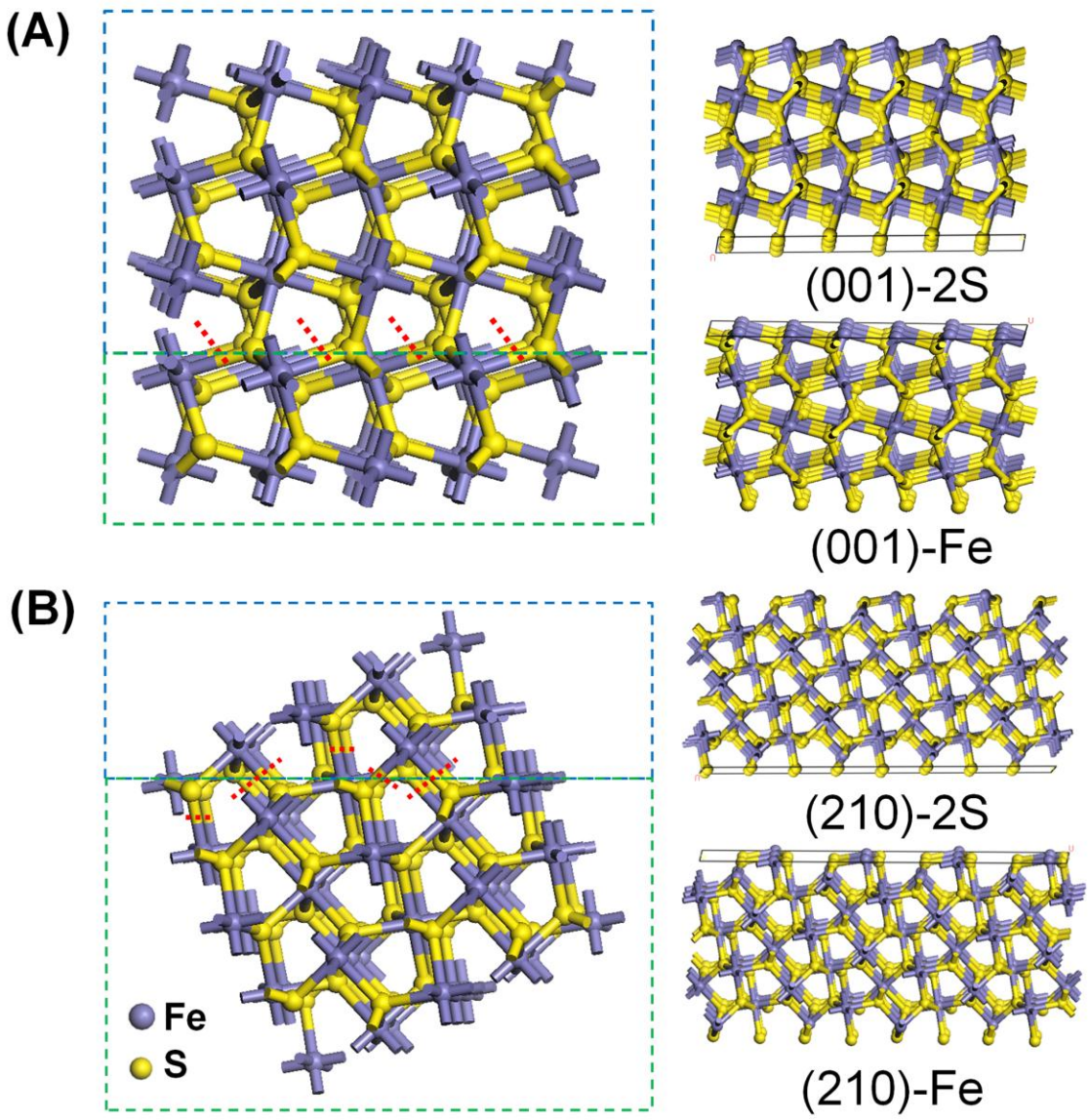

Scheme 4.3 Illustrations of the attachment through (A) (001)-2S and (001)-Fe and (B) (210)-2S and (210)-Fe planes. Dotted red lines indicate the positions where the bonds are formed through the OA.

are observed, resulting from the attachment between the {100} opposite facets and the {210} opposite facets. No attachment through the {111} facets is observed because the high energy {111} facets are all terminated by sulfur and no Fe-S bond can be formed by the collision. The locally S-lean condition at the early growth stage can also inferred from the morphology. The theoretical Wulff shapes for FeS_2 at the S-lean and S-rich limits were

constructed based on the facets that have low surface free energy at each limit.[158] At the S-lean conditions ($\Delta\mu_S$ between -0.9 and -0.75), pyrite FeS_2 tends to appear as a cubic-like crystal dominated by the {100} facets at the faces with truncated {111} and {210} planes. In contrast, at the S-rich conditions ($\Delta\mu_S$ between -0.5 and 0), pyrite FeS_2 tends to appear as an octahedron-like crystal mainly enclosed by the {111} facets with the minority of the {210} facets at the apexes of the octahedron. Since all the monomers observed under TEM (Figures 5.2A and 5.2B) are symmetrical, spherical and no octahedron-like crystals are observed, local S-lean condition in nanosheets accounts for the generation of symmetrical, spherical NCs at the early stage of NC growth.

4.3.3 Point to Point Attachment

In addition to the attachment of two planes at a planar interface, OA growth could take place by filling the gap between two monomers orientated along the common crystallographic direction, forming a dumbbell-like NC (Scheme 5.2B). Figure 5.7A shows a dumbbell-like NC with a narrow region between two monomers, where the same crystallographic fringes are observed as those of the two end monomers and no defects exist between the interfaces of the narrow part and the monomers. This type of OA growth was also observed in the previous studies of TiO_2,[182] ZnS,[183] PbSe,[85] and FeS_2 NCs.[176] More complex-shaped pyrite FeS_2 NCs were formed by joining adjacent particles in a sideway through the inter-particle growth when the opposite planes of high surface energy facets were close. Figure 5.7B shows the coalescence of two dimers probably via filling the gap between two dimers merged through a “point contact” at (210) plane, forming a curve-shaped NC without any defects at the interfaces. Figure 5.7C shows a branch-shaped NC that could be formed by joining a kinked NC, similar to that in Figure 5.2E, and a rod-like NC, similar to that in Figure 5.2D. The kinked and the rod-like particles could self-organize to make them orientated along the common crystallographic direction. Then,

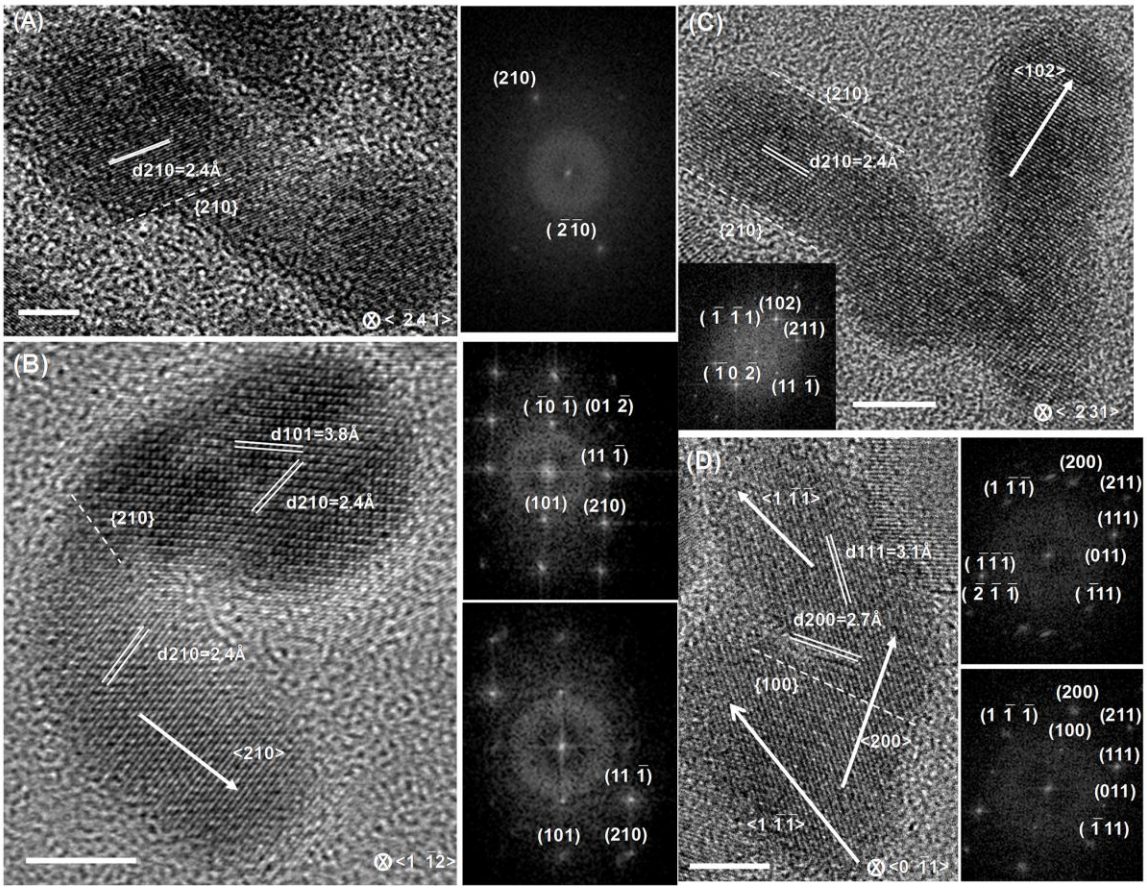

Figure 4.7 (A-D) HRTEM images and the corresponding FFT patterns of pyrite iron disulfide NCs formed by possible point-contact and interparticle growth of orientated attachment. The direction of the long axis is indicated by the white arrows. Zone axis for each HRTEM image is indicated. Scale bars are 5 nm.

precursors diffuse into the gap area and form chemical bonds from the surfaces of each particle. Full coordination is eventually reached, resulting in a defect-less branch-shaped NC. Figure 5.7D shows the side-attachment of two rod-like NCs. While part of the interface has been fully grown into defect-less lattice, about two thirds of the interfaces are still not healed. As time progresses, this part could be completely filled without defects or could form dislocation or twin defects.

After the reaction for 12 h, clear facetted NCs are observed in Figure 5.1I. HRTEM images of three typical facetted NCs are shown in Figure 5.8. Figure 5.8A shows a NC bounded by the {100} and {210} facets. Figure 5.8B shows an elongated NC with the tip

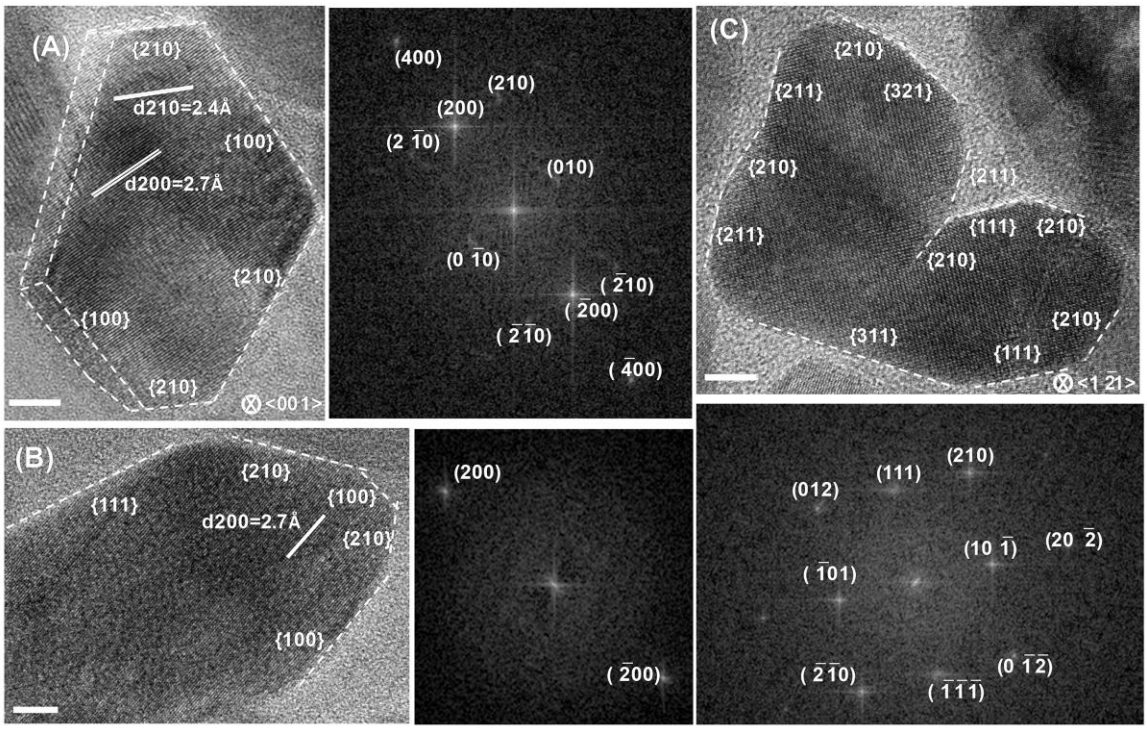

Figure 4.8 (A-C) HRTEM images and FFT patterns of faceted pyrite iron disulfide NCs formed by the reaction of iron precursor in ODA and sulfur precursor in DPE at 220°C for 12 h. Facets are highlighted by dotted lines. Scale bars are 5 nm.

bounded by the {100} and {210} facets and the side enclosed by {111} facets. Figure 5.8C clearly shows a NC formed via OA growth with well-defined {100}, {111}, and {210} facets. However, an un-fused part is shown along the {210} facets between two particles. Compared to the NCs formed at the reactions of 2 and 4 h, the edges are more flat and

sharp and the {100}, {111}, and {210} facets are the major facets observed in the products of the reaction for 12 h.

4.3.4 Solvents on the Morphology of Pyrite FeS_2 NCs

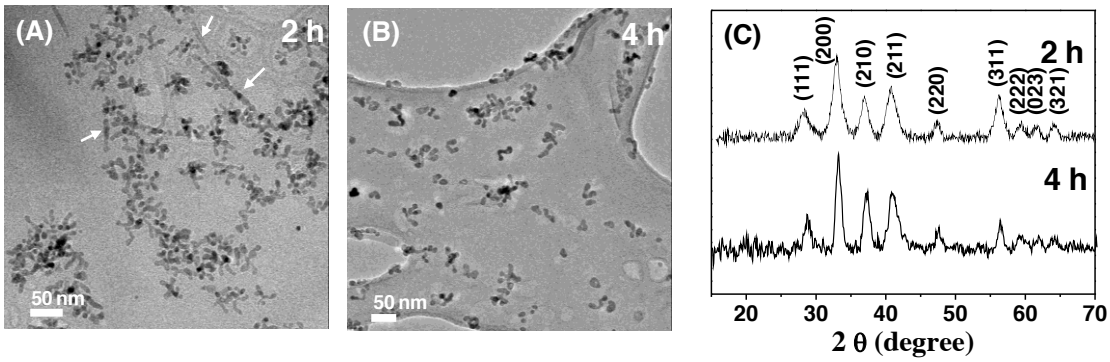

Figure 4.9 (A) and (B) The TEM images and (C) the corresponding XRD results of iron pyrite NCs synthesized by the reaction of iron precursor in OLA and sulfur precursor in DPE at 220ºC for 2 and 4 h, respectively.

Similar to ODA, OLA is another long-chain primary alkylamine but it has a double bond in the middle of the molecule. OLA can play multiple roles, not only a solvent but also a surfactant that can form a bond via the amine group with surface atoms as well as a reducing agent because of the unsaturated double bond and amine group. Therefore, OLA has been widely used in the synthesis of a variety of semiconductor NCs in order to control morphology and size.[184] In this work, we investigated how OLA affects the OA growth and thus the morphology of pyrite FeS_2 NCs. Figure 5.9A shows that pyrite FeS_2 NCs tend to have more thin-branched shapes synthesized using OLA instead of ODA to dissolve the iron precursor at the same reaction conditions, i.e., 220°C for 2 h. "Zigzag" pyrite nanowires are also observed as indicated by white arrows. A longer reaction time to 4 h leads to NCs with mixed morphologies, including dots and shorter, fatter branched rods as shown in Figure 5.9B.

The HRTEM image in Figure 5.10A shows two particles that each could have been formed via OA growth attach via a point-contact or two small {210} facets. NCs with a Π-shape are also commonly observed in the products. Figure 5.10B shows that the two branches with the <210> direction as the long axis are attached to the side of a rod through

the (210) plane. For some complicated structures shown in Figure 5.11, branches are always stretched out along the <210> direction and are attached to other NC through the {210} facet.

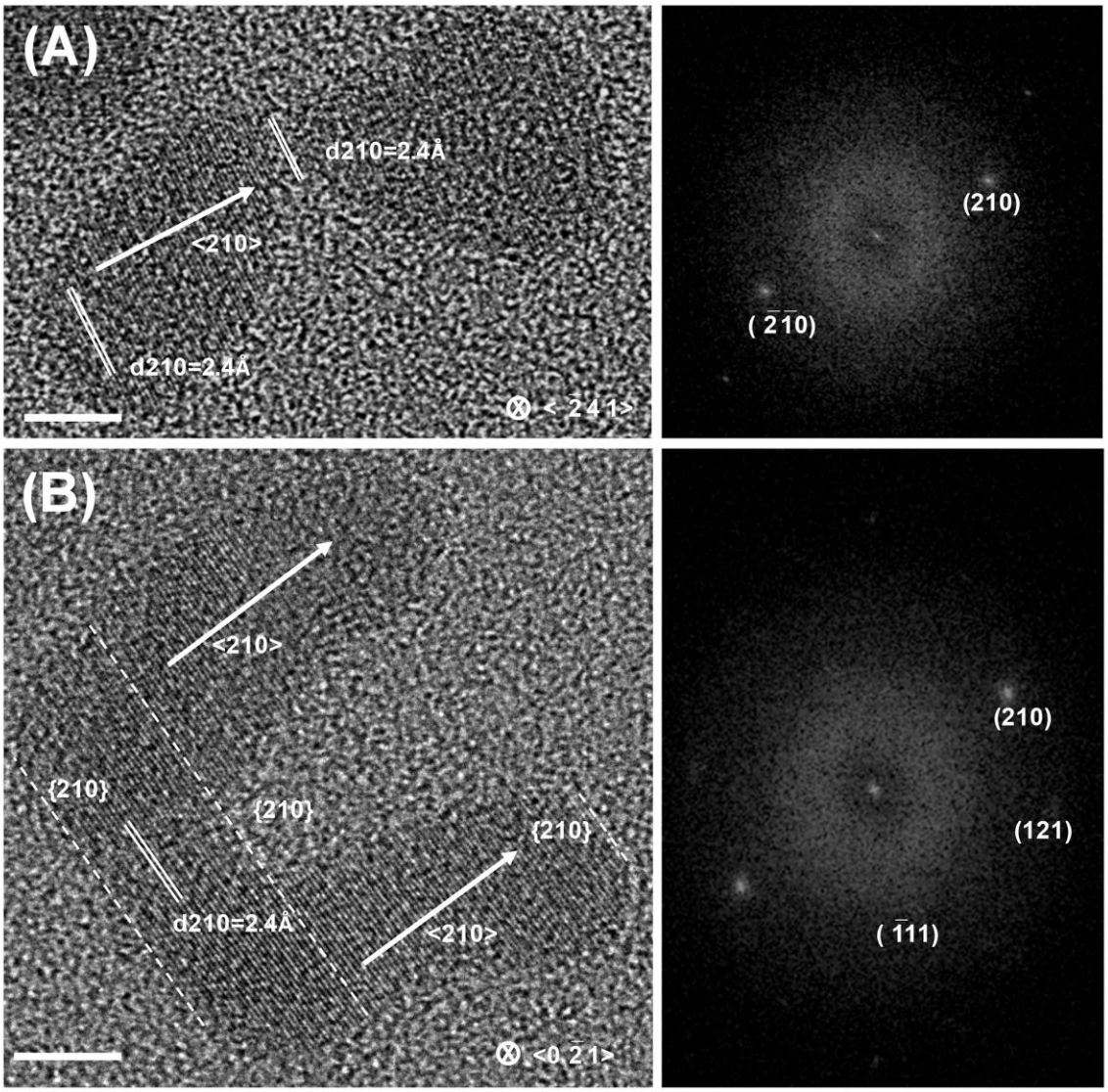

Figure 4.10 (A and B) HRTEM images and FFT patterns of the typical iron pyrite NCs synthesized by the injection of the sulfur precursor in DPE to the iron precursor in OLA and the reaction at 220°C for 4 h. Scale bars are 5 nm.

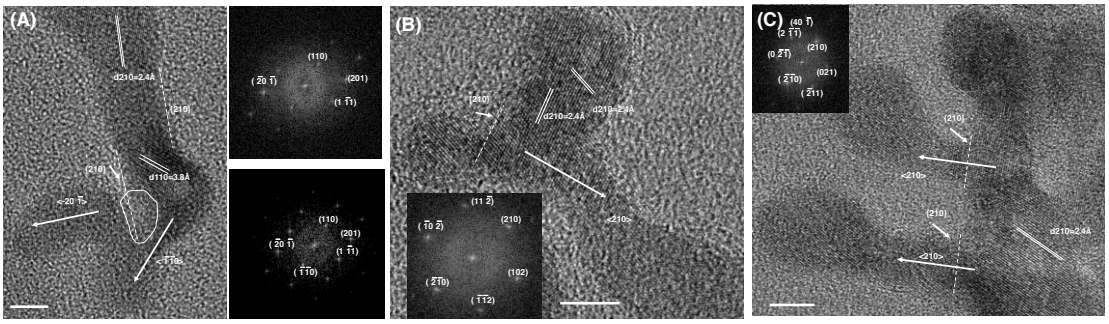

Figure 4.11 HRTEM images and FFT patterns of the complicated iron pyrite NCs formed by the injection of the sulfur precursor in DPE to the iron precursor in OLA and the reaction at 220°C for 4 h. Scale bars are 5 nm.

As discussed above, using OLA as a solvent leads to the growth of pyrite NCs with more branches, chromosome-like shapes compared to NCs synthesized using ODA as a solvent. The different passivation density and orientation of ODA and OLA on the NC surface as well as the different interaction between aliphatic chains during the course of the growth may account for this morphologic difference. After injection of the sulfur source and increasing of the temperature to 220°C, a higher concentration of H_2S caused by the vulcanization process[155, 156] between sulfur and the double bond of OLA could favor the growth of branched structures. OLA has a double bond in the middle of the chain and has a cis configuration compared to ODA that also has an 18-carbon chain. A single OLA chain occupies a larger steric space than a single ODA chain. Both OLA and ODA bind iron atoms via the N-Fe interaction. The rotation of the octahedrons formed by the six bonds of each iron atom at the corners and the face centers of the cubic unit cell makes it energetically unfavorable to passivate the same number of iron atoms with OLA compared to ODA. The packing of OLA on the NC surface was thus not expected to be strong, well ordered, or dense enough. The high-energy or poorly covered facets then favor an OA.[47, 176] Meanwhile, a preferential attachment along <210> is observed for the NC synthesized in OLA and DPE (Figures 5.10A, 5.10B and 5.6). Although there is a little difference between the total energy of the (001)-Fe and (001)-2S pair and (210)-Fe and (210)-2S pair in vacuum under sulfur rich condition (Table 5.1), the weak, disordered, sparse packing of OLA on the surface of NCs may raise the total energy of (210)-Fe and (210)-2S pair and

thus a preferential attachment along <210> is observed for the NC synthesized in OLA and DPE.

4.4 Conclusions

In summary, we have investigated the morphology and crystalline structure of pyrite FeS_2 NCs synthesized using hot injection. The formation of anisotropic pyrite FeS_2 NCs involves a nucleation burst and an orientated attachment process at the early growth stage as supported by the results of time-dependent XRD, TEM, and DLS. The pre-formed mackinawite nanosheets at low temperature provide templates for nucleation burst in a sulfur-lean local condition. The attachment appears to be either through the formation of bonds between the opposite facets sharing the common crystallographic direction or through a "point contact" followed by inter-particle growth. The analysis of HRTEM images combined with surface free energy of different terminations of the (001), (210), and (111) planes suggests that the orientated attachment most likely occurs between the (001)-Fe and (001)-2S as well as the (210)-Fe and (210)-S facets, which have high surface free energy under the sulfur-lean conditions. OR crystal growth becomes more important than orientated attachment growth after the reaction for 30 min, resulting in facetted, more isotropic NCs. Solvent or surfactant has a pronounced effect on NC morphology. Using oleylamine to replace ODA as the solvent for the iron precursor, complex, branch-shaped NCs are formed via orientated attachment of multiple NCs along the <210> direction. This study sheds the light to the understanding of the growth of anisotropic pyrite FeS_2 NCs and the evolution of their morphologies. The knowledge provides a mean to control the morphology of pyrite FeS_2 NCs in order to achieve desired optical and electrical properties for the development of efficient, low-cost, and environmental benign solar cells.

Chapter 5 DUAL HOLE TRANSPORT LAYER FOR INVERTED POLYMER-CDSE QDS HYBRID SOLAR CELLS

5.1 Introduction

In the previous chapters, an earth abundant, non-toxic semiconductor pyrite FeS_2 were successfully developed. The size and morphologies were able to be controlled from 10 nm to 4-5 μm. The synthesized pyrite FeS_2 nanocrystals show the absorption up to 1100 nm and a high absorption coefficient covering the visible light region. However, once the synthesized pyrite FeS_2 nanocrystals were incorporated to polymer solar cells composed by P3HT and $PC_{61}BM$. The fabricated devices always show very low efficiency (< 3%)[159]. One of the issues leads to low efficiency is that the surface morphology of the spin-coated organic-inorganic hybrid film is very rough when the weight ratio of pyrite FeS_2 nanocrystals exceeds 3.9%[159]. This will cause the incomplete coverage of interfacial layers between the electrodes and the active layer. Thus, to explore an effective interfacial layer is very important for an efficient organic-inorganic hybrid solar cells (OIHSCs). In order to simplify the study of the hole transport layers and reduce the effects of material quality on the device performance, CdSe QDs or NRs were used. In the following section, we summarized the current research on OIHSCs.

OIHSCs are attractive for the PV research community as an alternative to all-organic solar cells. OIHSCs combine the advantages of the tunable band gap[185] and facilitated charge transport[3] enabled by inorganic semiconductor QDs or NRs and the flexibility, light weight, and low-cost fabrication offered by conjugated semiconductor polymers.[186] They typically adopt a BHJ structure with the inter-mixing of polymers as an acceptor and inorganic semiconductors as a donor in a single active layer. Polymers such as P3HT,[3, 31, 187] poly [2, 6-(4, 4-bis(2-ethylhexyl)-4H-cyclopenta[2, 1-b:3, 4-b0]-dithiophene)-alt-4, 7-(2, 1, 3-benzothiadiazole)] (PCPDTBT),[188-190] poly [2-methoxy-5-(2-ethylhexyloxy)-1, 4-phenylenevinylene] (MEH-PPV),[191, 192] and poly ({4, 8-bis[(2-ethylhexyl)oxy]benzo[1, 2-b:4, 5-b′]dithiophene-2, 6-diyl}{3-fluoro-2-[(2-ethylhexyl)carbonyl]thieno[3, 4-b]thiophenediyl}) (PTB7)[193] and their derivatives are commonly used as the donor. The acceptors are the inorganic semiconductors such as CdSe,[3, 194] CdS,[195, 196] and PbS[197] QDs

or NRs. These inorganic semiconductors offer enhanced absorption in the solar spectrum region and generate extra excitons in addition to the polymer part. The nanoscale phase separation creates a high density of donor/acceptor interfaces to enable exciton dissociation and the subsequent charge transportation in the donor and acceptor domains.[198]

OIHSCs are typically fabricated with a conventional device configuration of ITO/hole transport layer (HTL)/BHJ/Al, where ITO acts as the bottom hole-collecting anode and a low work function metal (e.g., Al) as the top electron-collecting cathode. PEDOT:PSS is used as HTL due to its broad applicability, ease of use, and availability.[31, 48, 49] The active layer is a mixture of inorganic semiconductor QDs or NRs and polymers. Until now, the highest PCE of 3.64 % was achieved by using a blend of CdSe QDs and NRs as the donor and P3HT as the acceptor with a conventional configuration.[194] However, OIHSCs with a conventional configuration are unstable because indium is able to diffuse into the polymer layer and thus degrade the performance of OIHSCs.[199] In addition, prolonged exposure of conventional configuration devices to air and moisture can cause the oxidation of the top electrode as well as the degradation of the active layer.[200] Finally, direct deposition of metal onto the active layer may lead to either metal diffusion into the film or metal reaction with the polymer, and thus adversely affecting the semiconducting properties of the polymer.[201, 202]

Regarding these issues raised by adopting a conventional structure, an inverted device configuration was developed with a typical structure of ITO/ETL/BHJ/HTL/Ag. In these devices, an air-stable high work function metal (e.g., Ag or Au) is placed on top as the anode while the bottom ITO is used as the cathode. An ETL (e.g., ZnO) is inserted between the ITO and the active layer to selectively extract electrons to the cathode. The presence of an ETL greatly reduces the leakage current in the devices and prevents the diffusion of indium into the active layer. An HTL is inserted between the active layer and the anode to selectively extract holes while concurrently block electrons, thereby further reducing the dark (leakage) current and increasing the V_{OC}. The high work function of PEDOT:PSS (4.8-5.2 eV) is typically used as the HTL. PEDOT:PSS helps the anode to form ohmic contact with the BHJ active layer to improve the V_{OC} and charge-collecting ability of solar cells.[47] However, PEDOT:PSS suffers from several drawbacks including large electrical and microstructural inhomogeneities,[50] poor electron blocking property,[51] and the tendency

of eroding the electrodes.[52, 53] Various transition metal oxides such as nickel oxide (NiO),[54, 55] molybdenum oxide (MoO_3),[47, 56] vanadium oxide (V_2O_5),[57, 58] and tungsten oxide (WO_3)[59] were developed to use as an alternative HTL to PEDOT:PSS. Among these, MoO_3 is one of the most promising materials because of its nontoxic nature, the very deep-lying electronic states, and strongly n-doped by oxygen vacancies.[60, 61] Inverted devices fabricated using MoO_3 as the HTL consistently show higher PCE than conventional devices using PEDOT:PSS as the bottom electrode interlayer.[63, 64] Despite the inverted configuration has been extensively used in fabricating all-organic solar cells, only a few works have been reported regarding the OIHSCs with an inverted structure. An inverted binary OIHSC was fabricated by using CdSe NRs as the acceptor and P3HT as the donor. CdSe NRs arrays were deposited on TiO_2 coated ITO glass.[203] The interstitial spaces between the NRs were infiltrated with P3HT, and the devices were completed with an Au top electrode. The best power conversion efficiency was achieved at 1.38% under 100 mW cm^{-2} of AM 1.5G illumination. Inverted ternary OIHSCs were developed to improve the binary polymer solar cells. Inverted hybrid solar cells based on pyrite FeS_2 NCs in P3HT:PC_{61}BM were fabricated[204] with a structure of ITO/ZnO/P3HT:PC_{61}BM:FeS_2/PEDOT:PSS/Ag. The devices showed enhanced photocurrent and great air-stability after aging 28 days exposed in air. Solar cells with a structure of ITO/TiO_2/PCDTBT:PC_{61}BM:CdSe QDs/MoO_3/Ag were constructed. By the incorporation CdSe QDs into binary PCDTBT:PC_{61}BM polymer solar cells, the inverted devices showed the enhancement of V_{OC}, J_{SC}, and FF, and thus improved PCE of 6.94%.[205] Very recently, a MoO_3:PEDOT:PSS hybrid ink was developed by mixing MoO_3 nanoparticles with PEDOT:PSS and deployed as the HTL in the inverted organic solar cells with P3HT:PCBM and PTB7:PCBM active layers. The inverted organic solar cells with the hybrid HTL achieved comparable PCEs as those using the thermally evaporated MoO_3 HTL when the thickness of MoO_3 is greater than 20 nm. The solution processability along with the less thickness dependence of device performance makes this HTL hybrid ink more compatible with roll-to-roll printing process[206].

In this chapter, we fabricated inverted hybrid CdSe-polymer solar cells with a structure of ITO/ZnO/CdSe:polymer/HTL/Ag. Two widely used conjugated semiconducting polymers P3HT and PTB7 were blended with CdSe QDs, or NRs or QDs + NRs to form

the hybrid BHJ layers. First, three types of HTLs including two single HTLs, PEDOT:PSS and MoO_3, and a dual HTLs, PEDOT:PSS/MoO_3, were inserted between the active layer of CdSe QDs:P3HT and the top anode. Different from the previous work using the mixture of MoO_3:PEDOT:PSS as a hybrid ink for HTL[206], we spin-coated a layer of PEDOT:PSS first and then thermally evaporated a layer of MoO_3, which serves as a dual HTL. The performance of the fabricated inverted hybrid solar cells was evaluated. Hole mobility and electron mobility were obtained by applying the space-charge-limited-current (SCLC) method to the hole-only and electron-only devices with the same hybrid active layer, respectively. EQE measurements were performed in order to understand photon absorption and charge carriers generation process. An improved Shockley model using space-charge approach was applied to fit the dark J-V curves to obtain the shunt resistance (R_{sh}) and series resistance (R_S), which were added to understand the different performance observed in the devices using three types of HTLs. The enhancement in the efficiency of the fabricated solar cell was ascribed to an improved electron blocking at active layer/anode interface as well as a prevention of leakage current. By adopting the inverted structure and using the dual HTLs, the resistive losses of CdSe:P3HT hybrid system at high illumination power are effectively prevented. The further study showed the dual HTLs was applicable to CdSe:PTB7-F20 solar cells. An efficiency as high as 2.35% was reached by inverted hybrid CdSe-PTB7-F20 solar cells with a structure of ITO/ZnO/CdSe QDs + NRs:PTB7-F20/HTL/Ag.

5.2 Device Theory

The theory used in this chapter to model the device is summarized below:

5.2.1 Equivalent Circuit

Device physics of solar cells can be illustrated by using a simple equivalent electric circuit as a diode in series with a resistor (the series resistor), and in parallel with a constant photocurrent source, a capacitor, and another resistor (the shunt resistor) (Figure 6.1). In a steady state measurement, the capacitance is neglectable. Both the series resistance and the shunt resistance determine the shape of J-V curve. A low series resistance means that high currents will flow through the cell at low applied voltages. This is reflected as a high slope of J-V curve at V_{OC}. A low shunt resistance means there are pinholes presented in the active

layer or connected pathways between two electrodes[207] or the imperfect coverage of HTL. A reduced shunt resistance results in a steeper slope in the J-V curve under reversed bias and a reduced FF. Contributions to the series resistance include contact resistances between the electrodes and the semiconductors as well as the bulk resistance of the blend in the PV device. To obtain a high FF for efficient power conversion, a series resistance approaching zero and a shunt resistance approaching infinity is desirable.

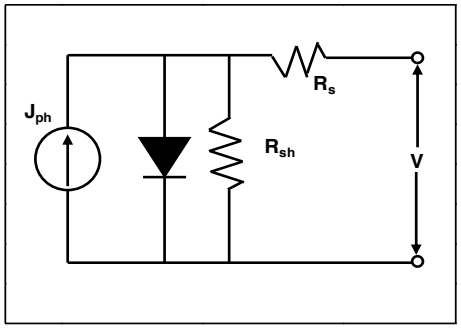

Figure 5.1 Diagram of an equivalent circuit of a solar cell.

5.2.2 Simple Shockley Model

Mathematical model for a solar cell with one ohmic and one Schottky contact is represented by the relationship:

$$J = J_0[\exp(\frac{e(V - JR_s)}{nK_BT}) - 1] + \frac{V - JR_s}{R_{sh}} - J_{ph} \qquad (6.1)$$

Where J is the current density, V is the applied voltage, J_0 is the reverse bias saturation current density, J_{ph} is the photocurrent, e is the elementary charge, R_s is the series resistance, n is the diode ideality factor, k_B is Boltzmann's constant (1.38×10^{-23} J/K), T is temperature, and R_{sh} is the shunt resistance. From this equation, we can derive the equation for J_{SC}, Voc, and FF.

For an ideal solar cell with R_s approaching 0, R_{sh} approaching ∞, equation is approximated by:

$$J = J_0[\exp(\frac{eV}{nK_BT}) - 1] - J_{ph} \tag{6.2}$$

At V= 0, Jsc is the cell current density,

$$J_{sc} \approx -J_{ph}(V = 0) \tag{6.3}$$

At J = 0, by solving equation Eqn. 6.1, Voc is determined as:

$$V_{oc} = \frac{nK_BT}{e} \ln(\frac{J_{sc}}{J_s} + 1)(J = 0) \tag{6.4}$$

5.2.3 Improved Shockley Model Using Space-Charge Approach

If the charge carrier mobilities are low, space-charge effects become important at higher electric fields because there is a high current level resulting from injection of charges. A modified Shockley model which incorporates the decrease in electric field due to space charge is used to model the OIHSCs:

$$J = \frac{R_{sh}}{1/AS + R_{sh}}(J_0\{e^{[\frac{e(V-V_b)}{nK_BT}]} - 1\} + \frac{V}{SR_{sh}}) \tag{6.5}$$

Where S is the area of the device. The term V_b accounts for both series resistance and space charge as follows,

$$J = AV_b + BV_b^2,\ V_b = \frac{-A + \sqrt{A^2 + 4JB}}{2B} \text{ with } A = \frac{1}{SR_s},\ B = \frac{9}{8d^3}\mu\varepsilon\Theta \tag{6.6}$$

B accounts for the trap density Θ, and the carrier mobility μ in a thin film with contact area S, thickness d, and permittivity ε. This model can also be used to describe NC-polymer devices for NCs of various diameters and aspect ratios.

5.2.4 Space Charge Limited Current

Energy-conversion devices such as solar cells and light emitting diodes rely on carrier injection, whose uncompensated charge and the concomitant push-back electrostatic fields

give rise to SCLC. In the absence of any trapping effects the current density is given by the Mott-Gurney Law:

$$J = \frac{9}{8}\mu\varepsilon\varepsilon_0\frac{V^2}{L^3} \tag{6.7}$$

Where L is the active layer thickness, μ is the mobility, ε is the relative permittivity, ε_0 is the permittivity of free space.

In the presence of a strong electric field, the effective depth of a trap is reduced. Subsequetly, the proportion of carriers which are free is increased. Frenkel effect[208] becomes prominent, which gives a modified Mott-Gurney Law:

$$J = \frac{9}{8}\mu\varepsilon\varepsilon_0\frac{V^2}{L^3}\exp(\frac{0.89\beta}{\sqrt{L}}\sqrt{V}) \tag{6.8}$$

Where β is the field-activation factor; J is the current density; V is the applied voltage; L is the active layer thickness; μ is the mobility; ε is the relative permittivity; ε_0 is the permittivity of free space and β is the field-activation factor

5.3 Experimental Section

5.3.1 Materials for CdSe QDs and NRs Synthesis and Device Fabrication

Cadmium oxide (CdO, ≥99.99%), selenium powder (Se, 99.99%), TOPO (99%), oleic acid (≥99.0%), and zinc oxide nanoparticle (ZnO NP) dispersion (50 wt% in H_2O and the particle size < 100 nm determined using DLS) were purchased from Sigma-Aldrich. Trioctylphosphine (TOP, 97%) and n-tetradecylphosphonic acid (TDPA, 97%) were obtained from Strem Chemicals Inc. P3HT (4002-E) was purchased from Rieke Metals, Inc. Poly(thienothiophene-co-benzodithiophenes)7-F20 (PTB7-F20) was obtained from 1-Material, Inc. PEDOT:PSS (Clevios P VP AI4083) was obtained from H.C. Starck and filtered through a 0.22 μm nylon filter before use. MoO_3 powder (99.9995%) was purchased from Alfa Aesar. Ag pallets (99.99%) and ITO coated glass were obtained from R.D. Mathis and Colorado Concept Coatings LLC, respectively.

5.3.2 CdSe QD and NRs Synthesis and Ligand Exchange

CdSe QDs were synthesized by the hot injection method.[196] Briefly, CdO (0.5 mmol), oleic acid (10.0 mmol), and TOPO (2.5 mmol) were mixed and heated to 280°C under the N_2 protection. In a separate airtight tube, 0.5 mmol of Se was dissolved in 1.5 ml of TOP to form a TOP-Se solution at 150°C. Subsequently, 1.5 ml of TOP-Se solution was swiftly injected into the three-neck flask using a glass syringe. After the injection, the temperature was maintained at 280°C for 2 to 30 min in order to obtain CdSe QDs with the size from 4.0 to 7.4 nm. The reaction was quenched by adding 5 ml toluene. CdSe QDs were purified by washing with toluene and being precipitated in methanol for three cycles. QDs were ligand exchanged with pyridine overnight at 60°C. The ligand exchanged QDs were then precipitated by adding hexane, separated by centrifugation at 6000 rpm for 2 min, and re-dispersed in 1.0 ml pyridine:CB (1:20 vol/vol).

CdSe NRs were synthesized according to the reported protocol[187] with a few modifications. Typically, CdO (0.4 mmol), TDPA (1.1 mmol), and TOPO (10.6 mmol) were mixed and heated to 300°C under the N_2 protection to dissolve CdO in the TDPA/TOPO solution. After an optically clear solution was obtained, it was heated up to 320°C. In a separate airtight tube, 0.5 mmol of Se was dissolved in 4.0 ml of TOP to form the injection solution at 150°C. This solution was injected into the reaction flask at 320°C by using a 5-ml glass syringe. After the injection, the temperature of the reaction mixture dropped down and was kept at 250°C for the growth. The reaction was stopped at 30 min by removing the heating mantle. The purification and ligand exchange procedures of CdSe NRs were the same as those of CdSe QDs.

5.3.3 Device Fabrication

Inverted OIHSCs were fabricated on ITO coated glass substrates with a sheet resistance = 10 Ω sq^{-1}. The substrates used for all devices were first cleaned by several ultrasonication steps in soapy deionized (DI) water, DI water, acetone, and isopropanol, each for 15 min. The cleaned substrates were treated with oxygen plasma for 30 s prior to depositing any films. The substrates were first spin-coated with a 5.22 wt% ZnO NP dispersion at 3000 rpm for 30 s. After being baked in air at 120°C for 10 min, the substrates were transferred to a nitrogen glovebox for the spin coating of CdSe-polymer layers. The CdSe-polymer

solutions were prepared by dissolving CdSe QDs or NRs and P3HT or PTB7-F20 in pyridine:CB (1:20 vol/vol) to a total concentration of 30 mg ml^{-1}. The weight ratio of CdSe QDs in the mixture was 80 or 85 wt%. The weight ratio of QDs to NRs was 2:1 for the devices containing the mixture of CdSe QDs + NRs:PTB7. The CdSe-polymer layers were fabricated by spin-coating of CdSe-polymer solutions at 1000 rpm for 30 s, followed by being baked at 150°C for 10 min. Three types of HTLs were inserted between the active layer and the top Ag anode. The 40 nm PEDOT:PSS layer was fabricated by spin-coating of a dilute PEDOT:PSS solution at 5000 rpm and being baked at 120°C for 10 min. The 10 nm MoO_3 layer was fabricated by thermal evaporation. The dual HTLs of 40 nm PEDOT:PSS/10 nm MoO_3 was fabricated by spin-coating of a dilute PEDOT:PSS solution and thermal deposition of the MoO_3 layer. Finally, a 100 nm Ag layer was thermally evaporated through a shadow mask to make four electrodes each with an area of 10 mm^2. The background pressure was kept below 10^{-6} Torr during the deposition.

The electron-only devices were fabricated with a structure of 100 nm Al/85 wt% CdSe QDs:P3HT/100 nm Al. A 100 nm thick Al was thermally evaporated onto a glass substrate and then the CdSe QDs:P3HT solution was spin-coated on the Al-covered substrate followed by the deposition of a 100 nm thick Al layer. The area for those electron-only devices was 10 mm^2. Similarly, the hole-only devices were fabricated for the measurement of hole mobility in the hybrid thin film with a structure of ITO/40 nm PEDOT:PSS/85 wt% CdSe QDs:P3HT/100 nm Au. A layer of 40 nm PEDOT:PSS was spin-coated on an ITO coated glass substrate and baked at 105°C for 20 min, followed by spin-coating of the active layer. Finally, a 100 nm Au was deposited onto the active layer.

5.3.4 Characterization of CdSe QDs and Device Testing

UV-Vis spectra of CdSe QDs and NRs in toluene were acquired using a Varian Cary 5000 UV-Vis-NIR spectrophotometer from the wavelength of 450 to 750 nm. Photoluminescence (PL) spectra of the same solutions were recorded by Perkin Elmer LS-50B Fluorimeter with an excitation wavelength of 450 nm. TEM images were acquired using a FEI Tecnai G2 F20 TEM operating at an accelerating voltage of 200 kV. The samples for TEM analysis were prepared by drop casting a dilute solution of NCs in chloroform onto ultrathin carbon-coated copper grids. The film thickness was measured

using an Alpha-Step 500 profilometer (KLA-Tencor, San Jose, CA). The illuminated J-V curves were recorded in a glove box under nitrogen atmosphere using a Keithley 2400 source meter unit. The measurements were performed under AM1.5 illumination condition at an intensity of 100 mW/cm^2. The light intensity was calibrated to 100 mW/cm^2 using a calibrated silicon solar cell that had been previously standardized at the National Renewable Energy Laboratory. The J-V curves of the hole-only and the electron-only devices were measured using the same set-up under dark. EQE spectra were gathered in air using an Oriel Xenon lamp (450 W) with an AM 1.5 filter, a monochromator (Oriel Cornerstone 130 1/8 m), a chopper with a frequency of 100 Hz, a lock-in amplifier (SR830, Stanford Research Corp), and a Si-based diode (J115711-1-Si detector) for calibration.

5.4 Results and discussion

5.4.1 Synthesis and Characterization of CdSe QDs and NRs

Inorganic semiconductor QDs or NRs in OIHSCs absorb sunlight to generate electron-hole pairs. The connected inorganic semiconductor phase serves as a pathway to transport electrons. The size of CdSe QDs not only affects the light absorption but also the efficiency of electron transfer and the mixing uniformity with polymers. It was reported that CdSe QDs with the size of 6.5±0.5 nm blended with P3HT generated a PCE of 1.7±0.1% for the devices with a conventional configuration.[188] Larger size CdSe QDs of 8-10 nm induced the aggregation of QDs in the mixtures, which causes a poor electrical contact between the active layer and the electrodes and poor reproducibility of device performance.[209] CdSe QDs with the size below 6 nm resulted in large hopping distances among QDs in the active layer, leading to insufficient percolation pathway for the electron transport. As a result, a small J_{SC} was commonly observed in those devices.[210]

Therefore, CdSe QDs with the size around 6-7 nm were synthesized. The reaction time was controlled from 2 to 30 min at 280°C and the UV-Vis and PL spectra of the synthesized CdSe QDs were measured. The first excitonic absorption peak shifts from 604 to 654 nm as shown in the UV-Vis spectra in Figure 6.2A. The corresponding PL emission changes from 619 to 660 nm with the excitation wavelength of 450 nm (Figure 6.2B). The diameter of the synthesized CdSe QDs was estimated by using the empirical fitting function that correlates the diameter of CdSe QDs to the wavelength of the first excitonic absorption

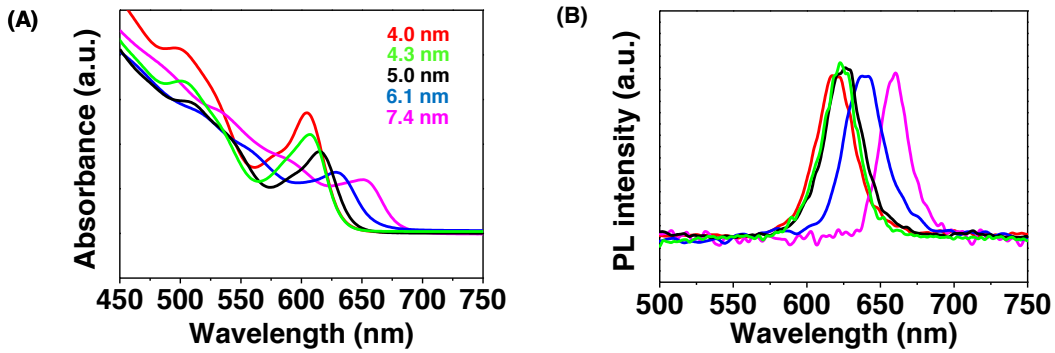

Figure 5.2 (A) UV-Vis absorption spectra and (B) PL spectra of CdSe QDs synthesized by reacting at 280°C for 2-30 min. The size of CdSe QDs was calculated from the wavelength of the first excitonic absorption peak of the UV-Vis spectra.

peak[211] and the values of 4.0, 4.3 5.0, 6.1, and 7.4 nm were obtained. The morphology and the size of synthesized CdSe QDs were also studied using TEM. Figure 6.5A shows a TEM image of CdSe QDs synthesized by reacting at 280°C for 5 min. The QDs are spherical particles and the average diameter is 6.3±0.2 nm calculated by counting 200 particles, which is in a good agreement with the value of 6.1 nm determined from the empirical fitting equation.[211] These CdSe QDs were used to fabricate all the devices reported in this work.

After the injection of selenium solution into the three-necked flask, the color of the mixture changed from colorless to yellowish in about 1 min. The UV-Vis absorption and PL spectra of CdSe NRs varying with growth time are shown in Figure 6.11. The

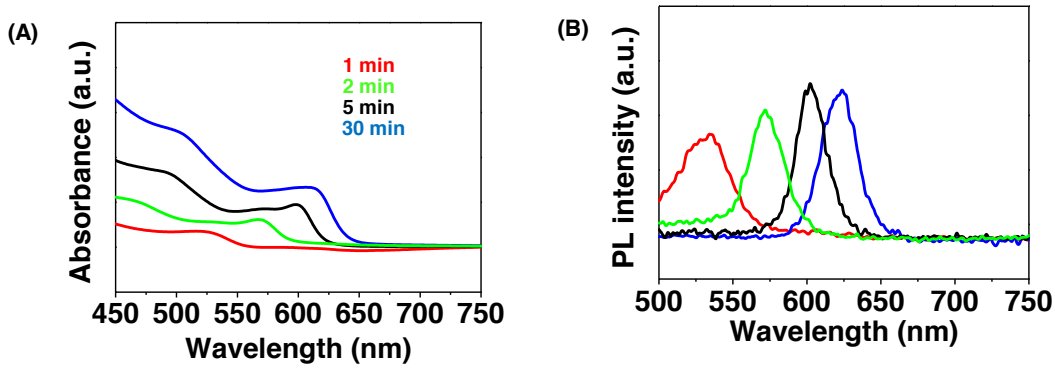

Figure 5.3 (A) UV-Vis absorption spectra and (B) PL spectra of CdSe NRs synthesized by reacting at 250°C for 1-30 min.

wavelengths of the first exciton absorption peak in UV-Vis spectra and PL emission peak are at 524 nm and 531 nm for CdSe NRs synthesized at 1 min's reaction (Figure 6.11A). These peaks in UV-Vis spectra and PL spectra red shift to longer wavelength when the reaction time is increased. The wavelength of the first exciton absorption peak in UV-Vis spectra was at 613 nm and that of PL emission peak was at 623 nm after 30 min's reaction. Samples with 2 min and 30 min's reaction were studied by TEM. The results are shown in Figure 6.12.

The product after 2 min's reaction has a pure wurtzite phase (compared to JSPDS File No. 42-1340) as demonstrated by XRD characterization (Figure 6.12A). CdSe short rods along with CdSe QDs were the major products when the reaction was kept at 250°C for 2 min (Figure 6.12B). A parallel fringe with the distance of 3.3 Å is shown in Figure 6.12C, which matches the lattice distance of the {110} planes of wurtzite CdSe crystals. The average aspect ratio of these CdSe NRs is calculated to be 1:3 by counting 200 NRs. The NRs grow along long axis and reach the aspect ratio of 1:8 after 30 min's reaction at 250°C (Figure 6.12D). These NRs with the aspect ratio of 1:8 were blended with 6.1 nm CdSe QDs and PTB7-F20 to fabricate inverted hybrid solar cells.

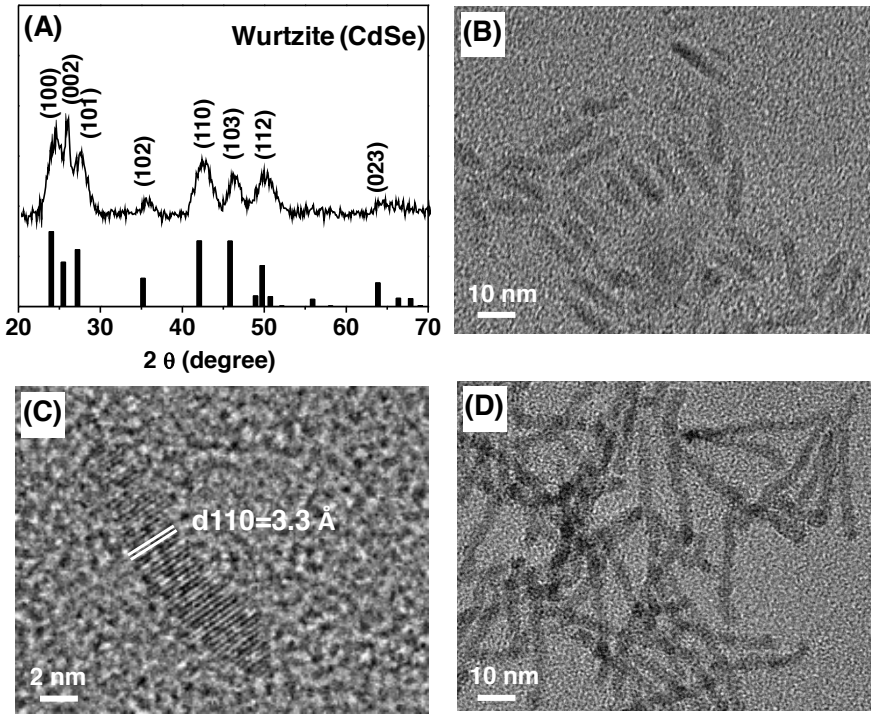

Figure 5.4 The XRD result of the product after 2 min's reaction at 250°C. (B) and (C) The TEM and HRTEM image of the same sample. (D) The TEM image of CdSe NRs synthesized by reacting at 250°C for 30 min.

5.4.2 UV-Vis and PL of the CdSe QDs:P3HT films

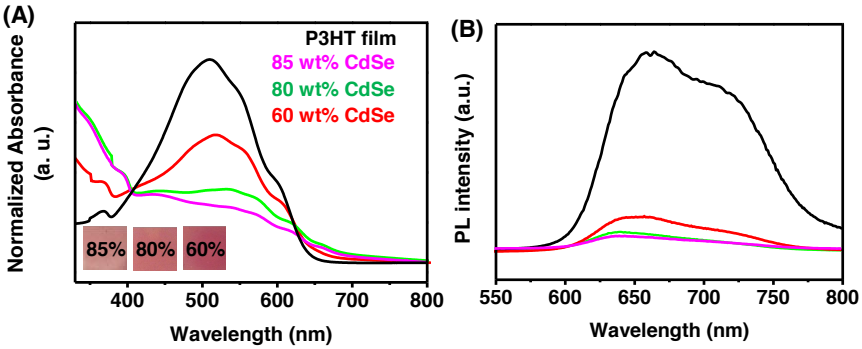

Figure 5.5 (A) UV-Vis absorption spectra and (B) PL spectra of pure P3HT film and the hybrid CdSe QDs:P3HT films with 60 wt%, 80 wt%, and 85 wt% of CdSe QDs. Blend films of almost similar thickness (ca. 100 nm) for all CdSe QDs:P3HT ratios were spin-coated on ITO coated glass with a 36 nm ZnO NPs layer to eliminate the influence of the film thickness.

Pure P3HT film and the hybrid CdSe QDs:P3HT films with 60 wt%, 80 wt%, and 85 wt% of CdSe ODs were studied by UV-Vis and PL spectroscopy at the room temperature outside glove box. Figure 6.3A shows the UV-Vis absorption spectra of the hybrid films. In order to eliminate the influence of the film thickness, blend films of almost similar thickness (ca. 100 nm) for all CdSe QDs:P3HT ratios were spin-coated on ITO coated glass with a 36 nm ZnO NPs layer. The pure P3HT film exhibits an absorption maximum at 520nm and pronounced shoulders at 550 and 600 nm, in good agreement with P3HT spectra reported elsewhere.[212-214] The shoulders are indicative of the structural order in the P3HT film, i.e., the formation of lamellae of π-stacked polymer chains. The blend film show a tail extending out to 700 nm as well as significant absorption at wavelengths shorter than 350 nm. These features that lie outside the primary absorption band of P3HT indicate the presence of CdSe QDs. The shoulder at 600nm is still present in the UV-Vis spectrum of CdSe QDs:P3HT films, meaning that the P3HT phase still has ordered domains in the blend.

To investigate the effect of CdSe QDs on the photophysical properties of the CdSe:P3HT blend, the PL of P3HT has been investigated for films with different amounts of CdSe QDs. The PL intensity of the films has decreased with the addition of CdSe QDs (Figure 6.3B). As expected, the PL quenching becomes more efficient by increasing the amount of CdSe QDs. Up to 90% of the emission of the P3HT is quenched by the addition of 80 wt% of CdSe QDs. Further increasing the weight ratio of CdSe QDs to 85 wt% shows little impact on the PL quenching.

5.4.3 Electron and Hole Mobilities

The transport properties of electrons and holes in the active layer significantly affect the performance of the fabricated solar cells. In an efficient solar cell, high electron and hole mobility is preferred because this means charge carriers can be transported to the respective electrodes quickly, which suppresses current losses via recombination. The hole-only and electron-only devices were constructed in order to obtain the electron and hole mobility in the active layer. The structures of ITO/PEDOT:PSS/85 wt% CdSe QDs:P3HT/Au (Figure 6.4A) and Al/85 wt% CdSe QDs:P3HT/Al (Figure 6.4B) were adopted for the hole-only and electron-only devices, respectively. The work functions of

Au and Al are -5.2 and -4.3 eV, respectively. The mobility can be obtained by fitting the part of the dark J-V curve under the high forward bias, the so-called SCLC regime, where the build-in voltage created by space-charge becomes significant at high electric fields. The J–V curves of the hole-only and electron-only devices were measured in dark (Figs. 6.4C and 6.4D). The SCLC regimes were fitted to Mott-Gurney's Law including Frenkel effect.[208] (Eqn. 6.8)

Hole mobility was determined to be 1.8×10^{-6} $cm^2(V \cdot s)^{-1}$ which concords very well with the reported value of 2.6×10^{-6} $cm^2(V \cdot s)^{-1}$.[215] Electron mobility was determined to be 1.1×10^{-3} $cm^2(V \cdot s)^{-1}$, which is faster than the literature values that are in the range of 10^{-4} to 10^{-6} $cm^2(V \cdot s)^{-1}$.[209, 216] A higher electron mobility indicates shorter interparticle separation[217] and thus more percolation pathways are created in the film for the electron transport. This could be resulted from the high CdSe QD loading (85 wt%) in the active layer.

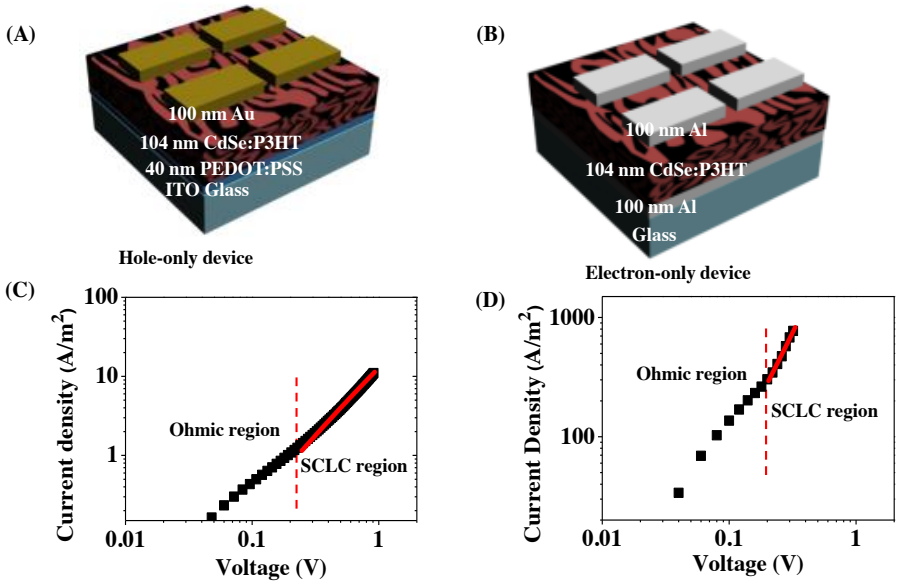

Figure 5.6 (A) and (B) Schematics of a hole-only and an electron-only device, respectively. (C) and (D) The dark J-V characteristics of a hole-only and an electron-only device, respectively. The solid lines are fit to the SCLC regions using Eq. 6.8. The active layers in hole-only and electron-only devices are composed of 85 wt% of CdSe QDs and P3HT.

Hole mobility was determined to be 1.81×10^{-6} $cm^2(V \cdot s)^{-1}$ which concords very well with the reported value of 2.6×10^{-6} $cm^2(V \cdot s)^{-1}$.[215] Electron mobility was determined to be 1.05×10^{-3} $cm^2(V \cdot s)^{-1}$, which is faster than the literature values that are in the range of 10^{-4} $cm^2(V \cdot s)^{-1}$ to 10^{-6} $cm^2(V \cdot s)^{-1}$.[209, 216] A higher electron mobility indicates shorter interparticle separation[217] and thus more percolation pathways are created in the film for the electron transport. Devices with high electron mobility require an effective HTL to block the transfer of electrons to the anode and thus prevent the recombination of charge carriers at the interface of the active layer and anode.

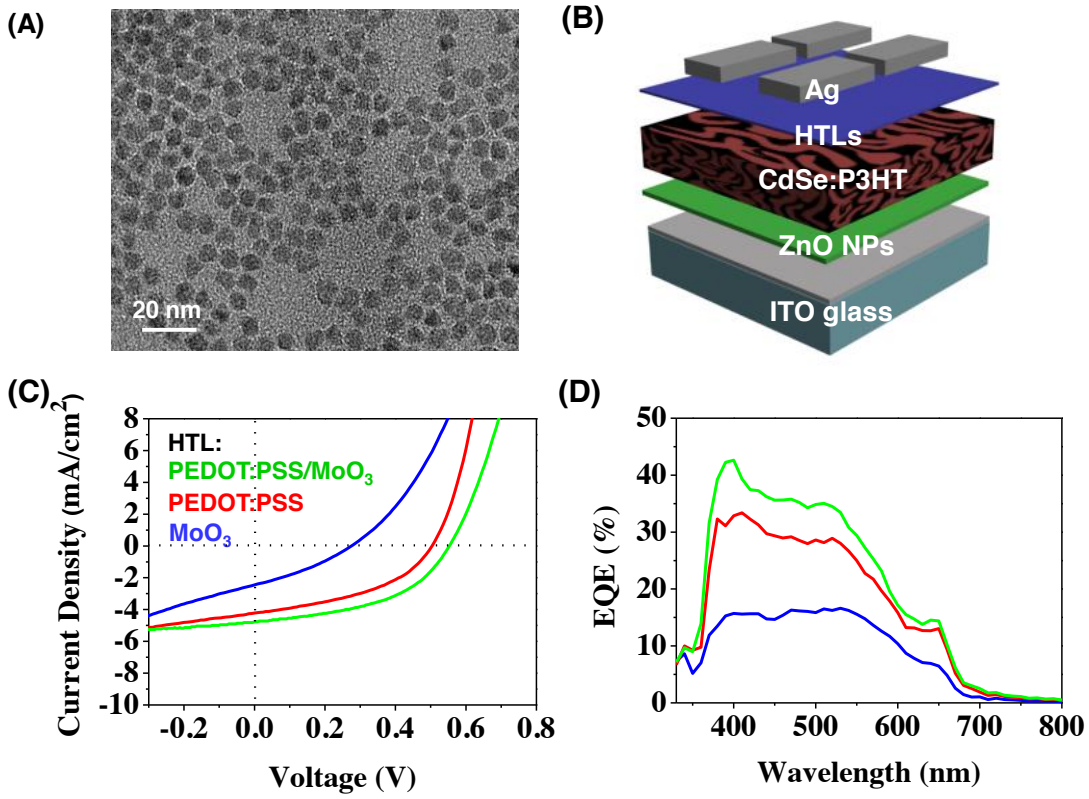

Figure 5.7 (A) A TEM image of CdSe QDs synthesized with the average size of 6.3 ± 0.2 nm. (B) Schematic of an inverted OIHSC with CdSe QDs:P3HT as the active layer. (C) Typical J-V characteristics of the inverted devices under 1 sun AM 1.5G solar illumination. (D) EQE as a function of the wavelength of those inverted solar cells. Devices were fabricated with a structure of ITO/ZnO/85 wt% CdSe QDs:P3HT/HTL/Ag. A MoO_3 only, a PEDOT:PSS only, or a PEDOT:PSS/MoO_3 were used as the HTL. The thickness of PEDOT:PSS and MoO_3 are 40 and 10 nm, respectively.

5.4.4 Influence of HTLs on the Solar Cell Performance

Table 5.1 Summary of the performance parameters of inverted hybrid CdSe QDs:P3HT solar cells under AM 1.5G 1 sun illumination. Devices were fabricated with a structure of ITO/ZnO/85 wt% CdSe QDs:P3HT/HTL/Ag. A MoO_3 only, a PEDOT:PSS only, or a PEDOT:PSS/MoO_3 were used as the HTL. The thickness of PEDOT:PSS and MoO_3 are 40 and 10 nm, respectively.

HTLs	**V_{OC} (V)**	**J_{SC} (mA/cm^2)**	**FF (%)**	**PCE (%)**	**PCE_{max} (%)**	**Rs (Ω)**	**Rsh (Ω)**
PEDOT:PSS/ MoO_3	0.55±0.02	4.96±0.13	47.6±2.4	1.37±0.23	1.53	3.45	29705.6
PEDOT:PSS	0.50±0.01	4.22±0.23	43.2±2.5	0.85±0.06	0.88	2.05	27005.4
MoO_3	0.28±0.05	2.45±0.32	31.9±3.3	0.22±0.23	0.41	3.07	2396.9

The inverted hybrid CdSe-polymer solar cells were first made with the active layer of CdSe QDs:P3HT and the architecture is shown in Figure 6.5B. The ZnO NP layer with a thickness of 36±3 nm was used as the ETL. An HTL was inserted between the Ag anode and the active layer. Three types of HTL: 40 nm PEDOT:PSS, 10 nm MoO_3, and 40 nm PEDOT:PSS/10 nm MoO_3, were investigated. The device performance is summarized in Table 6.1. Figure 6.5C shows the typical J-V characteristics of the fabricated devices under 1 sun (= 100 mW/cm^2) AM1.5 G simulated solar illumination. For the devices containing 85 wt% CdSe QDs with the single HTL of MoO_3, a J_{SC} of 2.45±0.32 mA/cm^2, a V_{OC} of 0.28±0.05 V, and a FF of 31.9±3.3% were obtained, which leads to an overall PCE of 0.22±0.23%. Using PEDOT:PSS as the single HTL greatly improved the J_{SC}, V_{OC}, and FF of the devices to the values of 4.22±0.23 mA/cm^2, 0.50±0.01 V, and 43.2±2.5%, respectively, leading to an overall PCE of 0.85±0.06%. The device performance was further improved by the deposition of 10 nm MoO_3 on top of the spin-coated PEDOT:PSS. A PCE as high as 1.37±0.23% was achieved because of the further increase in J_{SC}, V_{OC},

and FF. This PCE of the inverted hybrid BHJ solar cells with the dual HTLs is comparable to the PCE of the conventional hybrid solar cells containing the active layer of P3HT and CdSe QDs, where the QDs were also ligand exchanged with pyridine.[210, 218] The devices with the active layers containing 80 wt% of CdSe QDs exhibited a worse performance than those with 85 wt% of CdSe QDs and the same HTL as shown in Table 6.2 and Figure 6.6. The inferior performance of the devices with a lower weight ratio of CdSe QDs in the active layer is ascribed to the increased hopping distances between the QDs in the active layer, thereby forming insufficient percolation pathways for the electron transportation.[219, 220] The effect of different HTLs on the performance of the devices with 80 wt% CdSe QDs follows the same trend as those with 85 wt% CdSe QDs. The PCEs of the devices are 0.18±0.19%, 0.74±0.01%, and 0.94±0.18% for the devices with MoO_3, PEDOT:PSS, and < PEDOT:PSS/MoO_3 as the HTL, respectively.

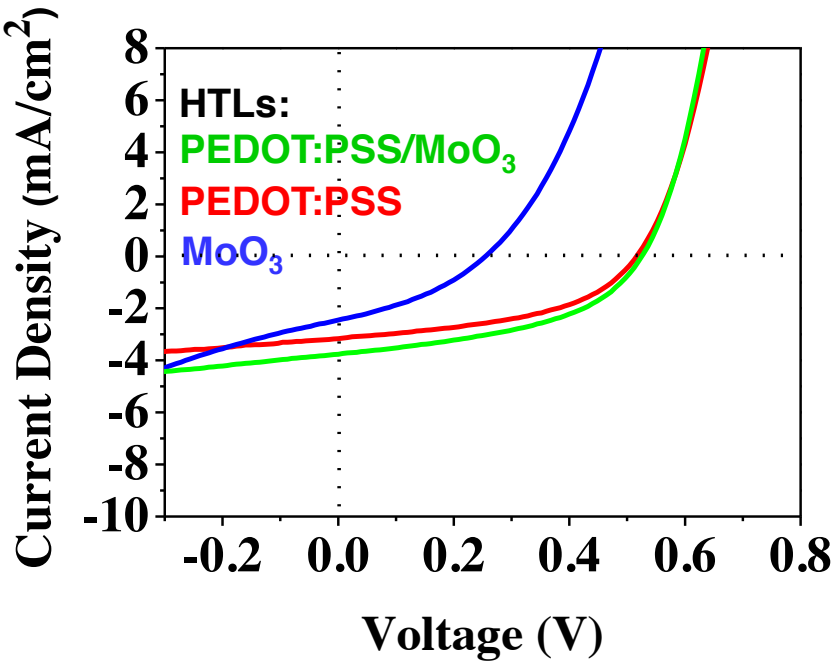

Figure 5.8 Typical J-V characteristics of the inverted devices under 1 sun AM 1.5G solar illumination. Devices were fabricated with a structure of ITO/ZnO/80 wt% CdSe QDs:P3HT/HTLs/Ag. A MoO_3 only, a PEDOT:PSS only, or a PEDOT:PSS/MoO_3 were used as the HTL. The thickness of PEDOT:PSS and MoO_3 are 40 and 10 nm, respectively.

Table 5.2 Summary of the performance parameters of inverted hybrid CdSe QDs:P3HT solar cells under AM 1.5G 1 sun illumination. Devices were fabricated with a structure of ITO/ZnO/80 wt% CdSe QDs:P3HT/HTLs/Ag. A MoO_3 only, a PEDOT:PSS only, or a PEDOT:PSS/MoO_3 were used as the HTLs. The thickness of PEDOT:PSS and MoO_3 are 40 and 10 nm, respectively.

HTL	**V_{OC} (V)**	**J_{SC} (mA/cm^2)**	**FF (%)**	**PCE (%)**	**PCE_{max} (%)**	**Rs (Ω)**	**Rsh (Ω)**
PEDOT:PSS/ MoO_3	0.53±0.01	3.66±0.11	45.4±1.2	0.94±0.18	1.07	4.67	26764.3
PEDOT:PSS	0.52±0.00	3.16±0.18	46.8±1.6	0.74±0.01	0.75	2.18	25512.7
MoO_3	0.21±0.04	2.62±0.29	31.9±2.8	0.18±0.19	0.34	0.40	1522.5

EQE measurements of devices with 85 wt% CdSe QDs in the BHJ layer and PEDOT:PSS, MoO_3, or PEDOT:PSS/MoO_3 as the HTL were performed in order to understand photon absorption and charge carrier generation process. As can be seen from Figure 6.5D, the EQE curves correlate well with the absorption of P3HT since most of the photo-generated charge carriers are created in P3HT. By comparing the absorption spectrum of 6.1 nm CdSe QDs (Figure 6.2A) with the EQE spectrum (Figure 6.5D), one can clearly see that the shoulder around 650 nm is due to the photon-generated charge carriers from CdSe QDs. By integrating the area underneath the EQE curves from the wavelength of 330 to 800 nm, the J_{SC} were determined to be 2.41, 4.15, and 4.83 mA/cm^2 for the devices with MoO_3, PEDOT:PSS, or PEDOT:PSS/MoO_3 as the HTL. The calculated J_{SC}'s concord very well with those determined from the J-V measurements (Table 6.1).

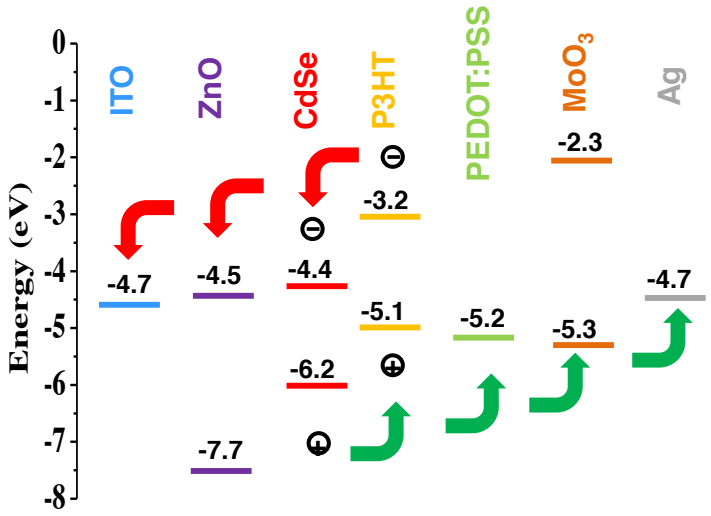

Figure 5.9 The energy band diagrams of the materials used in the inverted hybrid CdSe QDs:P3HT solar cells. The energies (in eV) are all referenced from the vacuum level.

In order to understand the effect of different HTLs on the device performance, we first compared the energy levels of the materials used to fabricate the devices. The energy band diagram of the materials involved in the inverted hybrid devices is displayed in Figure 6.7. The band gap of the 6.1 nm CdSe QDs is estimated to be 1.8 eV from the first absorption onset of the UV-Vis spectrum.[221] The conduction and valence band edges (E_{CB} and E_{VB}) are derived to be -4.4 and -6.2 eV, respectively, by considering the quantum confinement effect.[222] The E_{CB} of MoO_3 (-2.3 eV) is higher than that of the 6.1 nm CdSe QDs (-4.4 eV). Thus, the introduction of a MoO_3 layer prevents the transfer of electrons from the active layer to the anode. Meanwhile, the lower E_{VB} of MoO_3 (-5.3 eV) compared to the HOMO of P3HT (-5.1 eV) creates a small barrier for hole extraction. For PEDOT:PSS, a slightly higher work function of -5.2 eV could be beneficial for the hole extraction but it does not have the ability to block electrons. Surface roughness of the active layer and the coverage of the HTL could also play roles. We noticed that the surfaces of the hybrid active layers are quite rough from the atomic force microscopy (AFM) topographic images (Figure 6.8). It is likely that the surface of the active layer cannot be fully covered by the deposition of

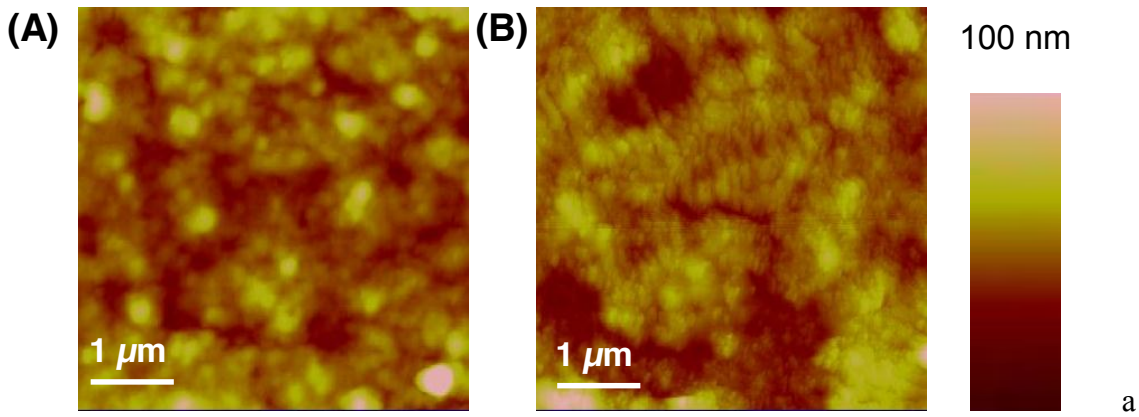

Figure 5.10 AFM images of 85 wt% (A) and 80 wt% (B) CdSe QDs:P3HT films on ZnO coated ITO glass.

10 nm MoO_3 layer, which could create direct contact points between the active layer and the anode. In contrast, the spin-coated 40 nm PEDOT:PSS layer alleviates these defects and reduces the shorts between the active layer and the anode. Therefore, devices with the dual HTLs containing PEDOT:PSS and MoO_3 show the best device performance.

We also calculated the series resistance (R_s) and shunt resistance (R_{sh}) to quantitatively understand the effect of different HTLs on the device performance. The J-V curves of the fabricated devices were measured in the dark and fitted to calculate R_s and R_{sh}. Because the difference in electron mobility (1.1×10^{-3} $cm^2(V \cdot s)^{-1}$) and hole mobility (1.8×10^{-6} $cm^2(V \cdot s)^{-1}$) exceeds two orders of magnitude, photocurrent reaches the fundamental space-charge limit.[223] An improved Shockley model using space-charge approach[224] was used to fit the dark J-V curves (Eqn. 6.5 and 6.6). Typical semilog scale dark J-V plots of these solar cells are displayed in Figure 6.9. The dark current at forward bias can be divided into three regions based on the voltage at the inflection points of the dark J-V curves (Figure 6.9). The J-V characteristics at regions Ⅰ and Ⅲ are primarily determined by R_{sh} and R_s, respectively, and that at region Ⅱ is governed by diode parameters J_0 and n that are in the improved Shockley model using space-charge approach.[225]

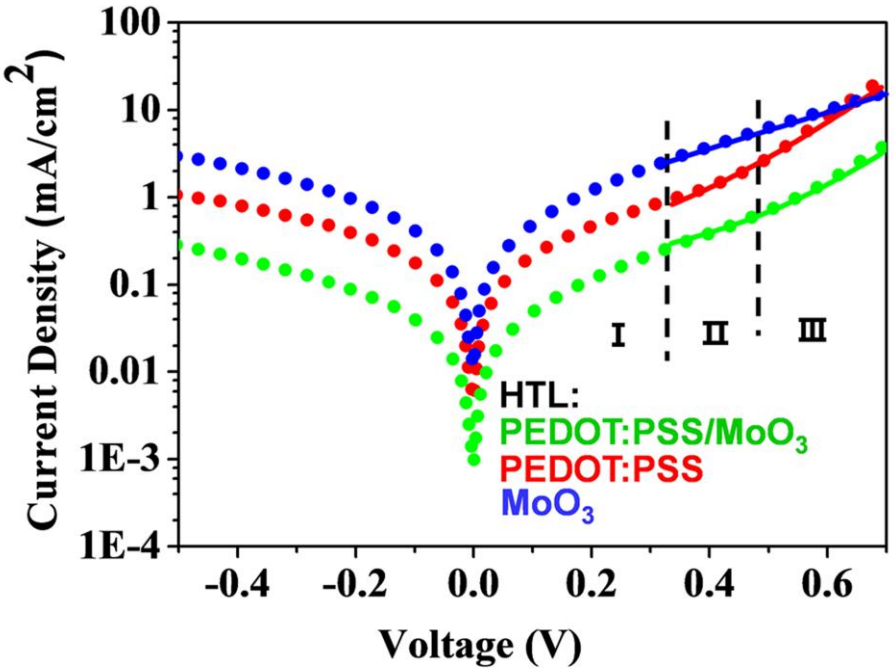

Figure 5.11 Typical semilog scale J-V plots of inverted CdSe QDs:P3HT solar cells in the dark. Devices were fabricated with a structure of ITO/ZnO/85 wt% CdSe QDs:P3HT/HTL/Ag. A MoO_3 only, a PEDOT:PSS only, or a PEDOT:PSS/MoO_3 were used as the HTLs. The thickness of PEDOT:PSS and MoO_3 are 40 and 10 nm, respectively.

The calculated R_{sh} and R_s of the corresponding devices are listed in Table 6.1. Devices with MoO_3 as the HTL present the smallest R_{sh} among three types of HTLs. A small R_{sh} is often the result of pinholes presented in the active layer or connected pathways between two electrodes[207] or the imperfect coverage of a HTL. Because all the devices were fabricated using the same active layer under the same conditions, the difference in R_{sh} should be predominately caused by the different HTLs. Imperfect coverage of MoO_3 could cause the small R_{sh}, which induces the current leaking through the circuit, and thus resulting in high dark current as shown in Figure 6.9. In addition, devices with small R_{sh} exhibit the characteristics of a small rectification and a steep slope under the reverse bias in the illuminated J-V curves (Figure 6.5C). Thus, a poor performance was observed in the devices with MoO_3 as the HTL. Using PEDOT:PSS as the HTL, the R_{sh} of the devices was increased about one order of magnitude. Comparing to the devices with MoO_3 as the HTL,

the devices using PEDOT:PSS as the HTL show lower dark currents (Figure 6.9). The lower dark current leads to the devices with higher V_{OC} by using MoO_3 as the HTL (Table 1) according to the relationship that V_{OC} is proportional to logarithmic ratio of photocurrent to dark current (Eq. 6.4)[226]. Moreover, the illuminated J-V becomes more flat under reverse bias and the rectification is increased (Figure 6.5C). All these indicate the PEDOT:PSS layer could provide a better coverage to the active layer and improve the leakage and recombination. Further improvement of R_{sh} was realized by evaporating a 10 nm layer of MoO_3 on the devices pre-coated with a 40 nm layer of PEDOT:PSS. Devices with the dual HTL show a higher R_s (3.45 Ω) than those with PEDOT:PSS (2.05 Ω) as the HTL. The R_s includes the bulk and the contact resistance.[227] The slight increase in the R_s of devices with a dual HTL is due to an increase in the contact resistance by the insertion of a MoO_3 layer between PEDOT:PSS and Ag because all the other parts of the devices are the same. As mentioned before, the introduction of a MoO_3 layer prevents the transfer of electrons from the active layer to the anode and reduces the chance of charge recombination. Devices with the dual HTL show a lower dark current (Fig. 4) and larger V_{OC} (Table 1) than those with PEDOT:PSS as the HTL. Thus, a large rectification and flat illuminated J-V curve under reverse bias are observed (Figure 6.5C). By adopting a dual HTL, both of the R_s and R_{sh} are increased. An improvement in the R_{sh} contributes the enhancement in the performance of the fabricated devices with a dual HTL since a dual HTL can best prevent the leakage current in the devices. As a result, the devices with a dual HTL exhibit the best performance among the devices using the same weight ratio of CdSe QDs.

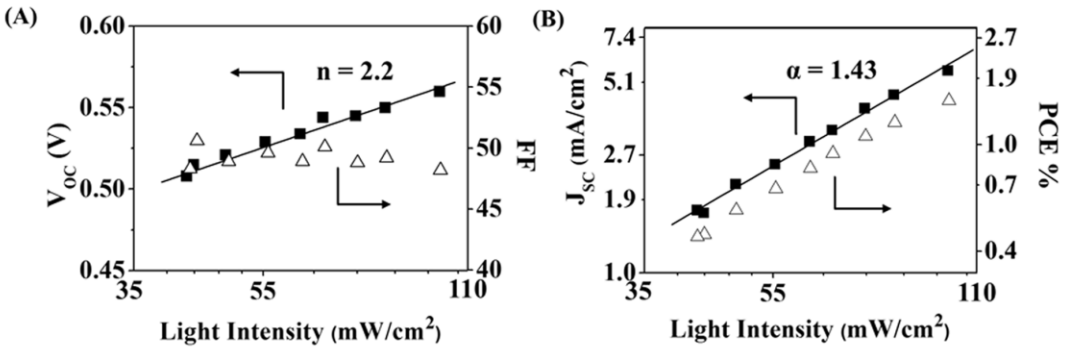

Figure 5.12 (A) V_{OC} and FF as a function of logarithmic scaled light intensity. A fit of V_{OC} and logarithmic light intensity to the simple Shockley equation is shown. Ideality factor (n) is determined to be 2.2. (B) J_{SC} and PCE as a function of light intensity in a double logarithmic scale. A fit of J_{SC} and light intensity (I) to the relationship of $J_{SC} \propto I^{\alpha}$ with α = 1.43 is shown. Devices were fabricated with a structure of ITO/ZnO/85 wt% CdSe QDs:P3HT/ PEDOT:PSS/MoO_3/Ag. The thickness of PEDOT:PSS and MoO_3 are 40 and 10 nm, respectively.

5.4.5 Dependence of Device Parameters on the Performance of Solar Cells

Photon induced charge carrier generation process strongly dependents on the intensity of the incidence light. Device parameters such as J_{SC}, V_{OC}, FF, and PCE were measured with a light intensity from 42 to 100 mW/cm^2 using the device with 85 wt% CdSe QDs in the BHJ layer and PEDOT:PSS/ MoO_3 as the HTL. The dependence of V_{OC} and FF on light intensity is shown in Figure 6.10A and the relationship of J_{SC} and PCE with light intensity is displayed in Figure 6.10B. V_{OC} increases linearly with the increase of the logarithmic light intensity while FF decreases slightly. When the V_{OC} equals to an applied voltage, the internal electrical field within the devices is reduce to zero. The field dependence of the photocurrent becomes insignificant. Simple Shockley model was used to fit the linear relationship between V_{OC} and logarithmic power. A slope of nkT/q was fitted and the ideality factor (n) was determined to be 2.2, which is greater than 2.0. An ideality factor equals to 2.0 means the recombination of charge carriers is full trap-assisted.[228, 229] A higher ideality factor observed, which is normal in CdSe:P3HT hybrid solar cells,[207] could be explained by the surface states of CdSe QDs at the p-n junction between P3HT and CdSe.[230] In a conventional CdSe:P3HT hybrid solar cells, a dramatic

decrease in FF at high intensity was observed,[224] which is a detrimental for solar cells working under high intensity such as solar conditions. Only a slight decrease in FF with the increase of the light intensity was observed in the inverted solar cells with a dual HTL. This indicates the resistive losses of CdSe QDs:P3HT hybrid system at high illumination power are effectively prevented by adopting the structure of the inverted configuration and the dual HTL. As can be seen in Figure 6.10B, J_{SC} and PCE increase linearly with the increase of the light intensity. J_{SC} is linear with illuminated light intensity, indicating there is no substantial space charge buildup by increasing the light intensity. Furthermore, a linear fit of the J_{SC} plot yields a scaling exponent $\alpha = 1.43$, according to the power-law relationship of $J_{SC} \propto P_{light}^{\alpha}$, where P_{light} is the light power (or intensity). The larger than unit value could be due to the small range of light intensity. Nonetheless, this means the charge carrier losses are dominated by monomolecular recombination via defects in the active layer[231, 232]. Bimolecular recombination of electrons and holes, which reflected by $\alpha = 0.5$ in the light intensity dependence of photocurrent, was not observed even at high light intensities in the inverted hybrid CdSe-polymer solar cells adopting PEDOT:PSS/MoO_3 as dual HTLs. An increase of V_{OC}, J_{SC} and slight decrease of FF result in the increase of PCE under increased light intensity.

5.4.6 Study of the CdSe QDs: PTB7-F20 Hybrid Films

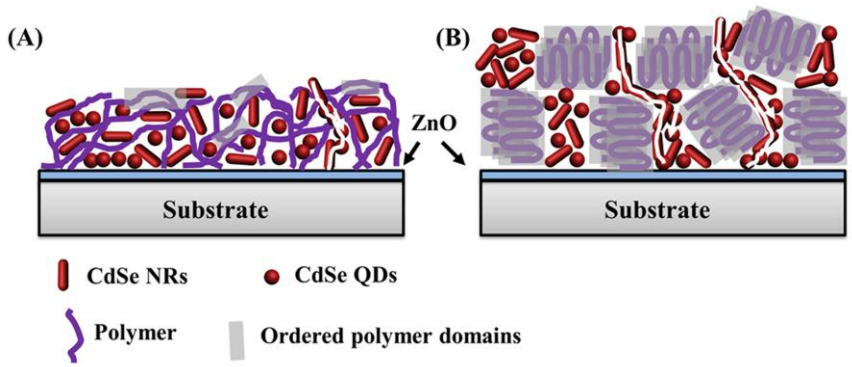

Scheme 5.1 An illustration of the morphology dependence of (A) CdSe QDs + CdSe NRs:PTB7-F20 film and (B) CdSe QDs + CdSe NRs:P3HT film on the substrate coated with ZnO layer. The percolation pathways were marked as white lines in the illustrations. Electrons were collected by the cathode through a ZnO layer.

PTB7 is one of the promising polymers with regularly alternating thienothiophene and benzodithiophene blocks in each repeating unit. BHJ solar cells fabricated with this polymer as the donor achieve > 8% PCEs.[96] Compared to P3HT, the intramolecular charge separation is more efficient along the polymer backbone of PTB7. PTB7 forms small domains in a BHJ solar cell (Scheme 6.1A), which facilitate the separation of electron and hole pair in a greater average distance. In contrast, P3HT crystalizes in large highly crystalline polymer domains (Scheme 6.1 B). Carriers are more likely to be trapped and recombine if no adjacent crystalline is available for them to hop to. Thus, BHJ devices fabricated using PTB7 as the electron donors consistently show better performance than those fabricated using P3HT as the donor. PTB7-F20 is a fluorinated thieno[3, 4-b] thiophene copolymer.[233] The thienothiophene unit

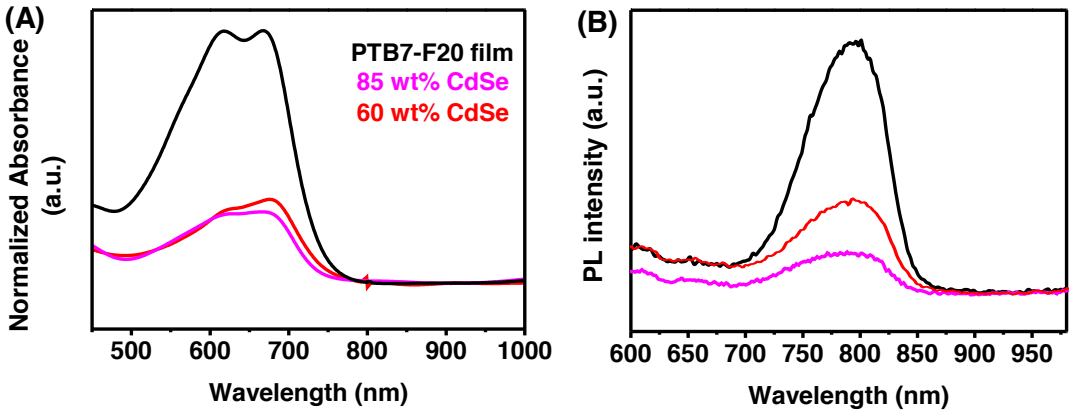

Figure 5.13 (A) UV-Vis absorption spectra and (B) PL spectra of pure PTB7-F20 film and the hybrid CdSe QDs:PTB7-F20 films with 60 wt% and 85 wt% of CdSe QDs. Blend films of almost similar thickness (ca. 100 nm) for all CdSe QDs:PTB7-F20 ratios were spin-coated on ITO coated glass with a 36 nm ZnO NPs layer to eliminate the influence of the film thickness.

with and without F was mixed with a ratio of 2:8 in PTB7-F20. PTB7-F20 thin film possesses a hole mobility of 9.0×10^{-4} $cm^2(V \cdot s)^{-1}$,[233] which is much larger than that of P3HT (1.8×10^{-6} $cm^2(V \cdot s)^{-1}$). A combination of CdSe QDs and CdSe NRs as the acceptor provides an efficient network for the electron transport.[189, 234] By adopting PTB7-F20 as

the donor and CdSe QDs and CdSe NRs as the acceptor, the charge recombination is expected to be suppressed due to the efficient transportation of both the electrons and holes.

The neat PTB7-F20 film exhibits two dominant absorption peaks at around 667 nm and around 615 nm (Figure 6.13A), respectively. Similar to P3HT and many other semiconducting polymers,[235] the presence of this resolvable vibronic progression in the UV-Vis absorption spectrum indicates the presence of J-like (head to tail) polymer aggregation[236] in PTB7-F20. The blend film with 80 wt% of CdSe QDs shows a maximum absorption at 681 nm with a shoulder around 619 nm. The change in the relative intensity of these two peaks indicates the polymer aggregation is reduced by the introduction of CdSe QDs. The peak at 681 nm is further suppressed and a platform is observed at from 614 to 675 nm by increasing the weight ratio of CdSe to 85 wt%. Similar to PL of hybrid CdSe QDs:P3HT films (Figure 6.3B), the PL of the films mainly come from the polymer part. The PL quenching becomes more efficient by increasing the amount of CdSe QDs. Up to 65% of the emission of the PTB7-F20 is quenched by the addition of 60 wt% of CdSe QDs. Further increase the weight ratio of CdSe QDs to 85 wt% in the hybrid film leads to an 85% PL quenching.

5.4.7 Inverted CdSe QDs + NRs: PTB7-F20 Hybrid Solar Cells

The architecture of a fabricated inverted hybrid CdSe:PTB7-F20 solar cell is similar to the one shown in Figure 6.5A. The ZnO layer with a thickness of 31.1±4.3 nm was used as the ETL and was deposited by a sol-gel reaction.[237] This layer was spin coated from a ZnO precursor at 4000 rpm followed by a static annealing at 200°C for 1 h. PTB7-F20 was used as the electron donor and 6.1 nm CdSe QDs or a blend of 6.1 nm CdSe QDs and CdSe NRs (aspect ratio: 1:10.5, weight ratio of QD:NR = 67:33) was used as the electron acceptor in the BHJ layer. The weight ratio of CdSe in the active layer was kept as 85% for all the devices fabricated. The active layer was spin coated at 1000 rpm and dried at room temperature. Dual HTLs composed by 40 nm, spin coated PEDOT:PSS and 10 nm, thermal evaporated MoO_3 were deposited sequentially on top of the active layer. Finally, the anode 100 nm Ag layer was thermally evaporated through a shadow mask to make sixteen electrodes each with an area of 3.14 mm^2. The background pressure was $<10^{-6}$ Torr during the deposition.

Typical J-V characteristics of devices were recorded and displayed in Figure 6.14. For the device containing 85 wt% CdSe QDs with the dual HTL, a J_{SC} of 3.9±0.2 mA/cm^2, a V_{OC} of 0.68±0.01 V and a FF of 51.5±2.2% were observed, which led to a PCE of 1.38±0.21%. Devices fabricated using PTB7-F20 as the donor consistently show higher V_{OC} and FF (Table 6.3) than those fabricated using P3HT (Table 6.1). This may be ascribed to the enhanced intramolecular charge separation and reduced charge recombination enabled by PTB7-F20. The device performance is improved by using a combination of CdSe QDs and CdSe NRs. The V_{OC} and FF were increased to 0.70±0.02 V and 52.9±1.1%, respectively. A dramatic increase in the J_{SC} from 3.9±0.2 to 5.5±0.3 mA/cm^2 led to an overall PCE of 2.03±0.33%. Higher J_{SC}'s and better PCEs in devices based on a combination of QDs + NRs were also observed by several other groups.[189, 234] The increase in the observed J_{SC} could be explained by the facile electron transport enabled by the percolation pathways network formed by interconnecting the parallel aligned NRs with QDs.

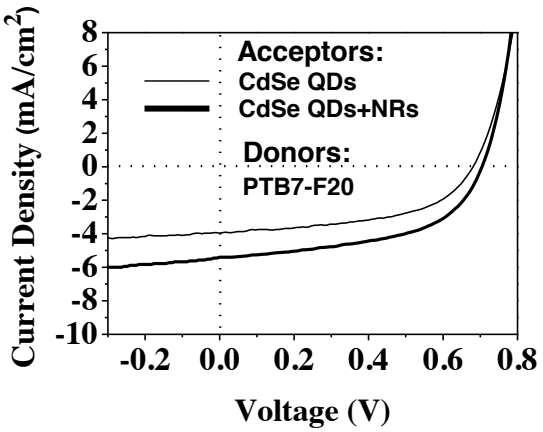

Figure 5.14 Typical J-V characteristics of the inverted CdSe:PTB7-F20 solar cells under AM 1.5G 1 sun illumination. Devices were fabricated with a structure of ITO/ZnO/85 wt% CdSe:PTB7-F20/PEDOT:PSS/MoO_3/Ag. CdSe QDs or a CdSe QDs + CdSe NRs (weight ratio = 2:1) were used as the acceptors. The thickness of PEDOT:PSS and MoO_3 are 40 and 10 nm, respectively.

Table 5.3 Summary of the performance parameters of inverted CdSe:PTB7-F20 solar cells under AM 1.5G 1 sun illumination. Devices were fabricated with a structure of ITO/ZnO/85 wt% CdSe:PTB7-F20/PEDOT:PSS/MoO_3/Ag. CdSe QDs or a CdSe QDs + CdSe NRs (weight ratio = 2:1) were used as the acceptors. The thickness of PEDOT:PSS and MoO_3 are 40 and 10 nm, respectively.

Acceptor	**Voc (V)**	**Jsc (mA/cm^2)**	**FF (%)**	**PCE (%)**	**PCE$_{max}$ (%)**
CdSe QDs	0.68±0.01	3.9±0.2	51.5±2.2	1.38±0.21	1.59
CdSe QDs+NRs	0.70±0.02	5.5±0.3	52.9±1.1	2.03±0.33	2.35

5.5 Conclusions

In summary, inverted hybrid CdSe-polymer solar cells with a dual HTL of PEDOT:PSS/MoO_3 showed a better performance than those with a single HTL of PEDOT:PSS or MoO_3. The better surface coverage provided by the PEDOT:PSS layer plus the improved hole extraction and enhanced electron blocking provided by the MoO_3 layer account for the improved device performance enabled by such a dual HTL. Study on the relationship of V_{OC}, J_{SC}, FF and PCE as a function of light intensity indicated that the resistive losses of CdSe QDs:P3HT hybrid system at high illumination power were effectively prevented by adopting the inverted structure and using the dual HTL. The further study showed that the dual HTL is applicable to hybrid CdSe:PTB7-F20 solar cells. An efficiency as high as 2.35% was reached by inverted hybrid CdSe-PTB7-F20 solar cells with a structure of ITO/ZnO/CdSe QDs + NRs:PTB7-F20/ PEDOT:PSS/MoO_3/Ag. The concept of a dual HTL could be applied to other organic and hybrid solar cell systems in order to achieve high device performance.

Chapter 6 SOLVENT VAPOR-ASSISTED THERMAL ANNEALING FOR THE HIGH-PERFORMANCE PLANAR CH3NH3SNXPB1-XI3 PEROVSKITE SOLAR CELLS

6.1 Introduction

In the previous chapters, we explored the charge generation and extraction processes in a conventional organic-inorganic hybrid solar cell. As we know, the size of an inorganic nanocrystals is from 10 to 100 nm and the size of a polymer chain is about several armstrongs. The charge separation happens between the interface of a polymer chain and the inorganic nanocrystal. The incomparable size will cause the insufficient charge separation at the interface. The fabricated organic-inorganic hybrid solar cells always show the efficiency below 10%. The exploration of an active layer using a molecular level organic-inorganic hybrid material is crucial to achieve a device with the efficiency above 10%. We explored the utilization of organic-inorganic hybrid perovskites for solar cell applications.

Since the first report of organolead halide perovskites ($CH_3NH_3PbI_3$ and $CH_3NH_3PbBr_3$) as visible-light sensitizers in photoelectrochemical cells,[104] great progresses have been made to use organometal halide perovkites for PV applications[36-38, 95, 105-108, 238] and the certified PCE has rocketed to 20.1%.[29] This is mainly due to the extraordinary electronic properties of the hybrid organic-inorganic halide perovskites including tunable bandgap,[95, 99] high panchromatic absorption,[100] long carrier diffusion length,[101, 102] and excellent ambipolar charge transport properties.[103] Organometal halide perovskite is a class of materials with the general chemical formula of AMX_3, where M is a small divalent metal ions (e.g., Pb^{2+}, Sn^{2+}, and Ge^{2+}), X is an anion from the halide series (F^-, Cl^-, Br^-, and I^-), and A is a large organic cation and typically restricted to MA ($CH_3NH_3^+$), EA ($CH_3CH_2NH_3^+$),[89, 90] TMA $(CH_3)_4N^+$),[91] and FA ($NH_2CH_2{=}NH_2^+$).[92-98] Among various organometal halide perovskites, Pb-based perovskites are the most widely studied and used for PV applications. Typically, $MAPbI_3$ perovskite materials adopt a tetragonal I4cm perovskite structure at room temperature and undergo a reversible structural phase transition to the cubic P4mm space group at elevated temperatures.[99] Lead is a toxic element and has potential harmful effects on human health.[239] The reduction of

lead usage without sacrificing the device performance is of crucial importance to push the feasibility of this technology in practical applications.

One promising strategy is to replace Pb with Sn. Both Sn and Pb are group 14 elements. Although Sn has a smaller ionic radius of 1.35 Å compared to that of Pb (1.49 Å),[240] partial substitution of Pb with Sn content up to 43% is within the structural tolerance.[241] The resultant crystals still maintain a tetragonal I4cm perovskite structure at room temperature. A transition from tetragonal I4cm to cubic P4mm perovskite structure occurs when the Sn content in the perovskite exceeds 50%.[99] In the meantime, partial or complete replacement of Pb with Sn alters the valence band maximum and conduction band minimum of perovskite materials, resulting in the band gaps of $CH_3NH_3Sn_xPb_{1-x}I_3$ from 1.55 to 1.17 eV by varying x from 0 to 0.75, i.e., from $CH_3NH_3PbI_3$ to $CH_3NH_3Sn_{0.75}Pb_{0.25}I_3$.[99] The absorption onset is able to reach as high as 1050 nm by using $CH_3NH_3Sn_{0.75}Pb_{0.25}I_3$.[99]

The early reported Sn-based perovskite solar cells adopted the device structure built upon mesoporous TiO_2 scaffold, which requires a high temperature (500°C) sintering process.[99, 242-244] The active layers were prepared by spin coating the anhydrous N, N-dimethylformamide (DMF) solutions of either the mixtures of a certain molar ratio of Sn halide to Pb halide compounds and methylammonium iodide (MAI)[242] or pre-synthesized perovskites (e.g., $CH_3NH_3Sn_xPb_{1-x}I_3$[99, 245] and $CH_3NH_3SnI_{3-x}Br_x$[244]) followed by thermal annealing. The best performance with a PCE of 7.37% was achieved from a device with the active layer made from pre-synthesized binary Pb-Sn perovskite with 25% Sn ($CH_3NH_3Sn_{0.25}Pb_{0.75}I_3$).[99] A record high PCE of 6.4% was demonstrated by a pure Sn perovskite ($CH_3NH_3SnI_3$) solar cell.[243] Very recently, Sn-based perovskite solar cells with a planar heterojunction configuration of ITO/PEDOT:PSS/$CH_3NH_3Sn_xPb_{1-x}I_{3-x}Cl_x$/$PC_{61}BM$/$C_{60}$-bis/Ag were fabricated by a low temperature solution procedure.[240] Sn was introduced to the lead perovskite with mixed halide. The $CH_3NH_3Sn_xPb_{1-x}I_{3-x}Cl_x$ layer was prepared by spin coating a DMF solution with a mixture of $SnCl_2$, $PbCl_2$, and CH_3NH_3I followed by thermal annealing. An average PCE of 9.77% and a maximum PCE of 10.10% were achieved for the solar cells with 15% Sn in the perovskite layer ($CH_3NH_3Sn_{0.15}Pb_{0.85}I_{3-x}Cl_x$).

Until now, all the Sn-based perovskite layers were fabricated by one-step solution spin coating process. The perovskite layers tend to form clusters with many pinholes, which

significantly affect device performance.[27,33] The process conditions have to be strictly controlled in order to obtain uniform and pinhole-free planar films.[240, 246] It has been reported that perovskite layers can also be fabricated via the interdiffusion of sequentially spin coated metal halide and MAI layers.[247-249] Nucleation and growth of perovskite crystalline grains becomes kinetically more controllable because nucleation and reaction rate between metal halide and MAI can be independently manipulated.[247-249] This eventually enables a better control over the pinhole-free perovskite film formation process. By carefully control the nucleation density on substrates, smooth, pinhole-free organolead triiodide perovskite films with large-aspect-ratio grains were successfully made and a high PCE of 18.3% was achieved.[250] There are two main issues associated with sequential deposition technique, one is the incomplete conversion of thick metal iodide or MAI film to perovskite film and the other one is the inconsistent degree of conversion resulting in polydispersed crystal size. Solvent annealing was also applied to promote grain growth and improve crystallinity of perovskite films.[248, 250-252] Solar cells with solvent annealed $CH_3NH_3PbI_3$ perovskite layers showed improved photocurrent and thus enhanced performance compared to those with only thermal annealing.[251]

In this chapter, we fabricated planar heterojunction binary Pb-Sn iodide perovskite solar cells and prepared the $CH_3NH_3Sn_xPb_{1-x}I_3$ active layers using a two-step solution-process method followed by only-thermal annealing and thermal annealing plus solvent vapor-assisted thermal annealing, respectively, as illustrated in Figure 1. Unlike one-step solution process that makes the binary Pb-Sn perovskite polycrystalline directly,[240] we grew the binary Pb-Sn iodide polycrystals first and showed that the crystalline structure of PbI_2 was retained for 10 and 25% Sn substitutions but the morphology, grain size, and grain orientation were significantly influenced by the amount of Sn substitutions. After spin casting the MAI layer, we annealed the films in three ways. The only-thermal annealing promoted the diffusion of MAI to the binary Pb-Sn iodide polycrystals and the binary Pb-Sn iodide perovskites with the tetragonal I4cm perovskite structure were formed. The devices containing the active layer of $CH_3NH_3Sn_{0.25}Pb_{0.75}I_3$ demonstrated the best performance with an average PCE of 8.45% and the maximum PCE of 8.83%, higher than the PCE of 7.37% with the same composition perovskite but different device structure and different perovskite film preparation method.[99] The other two annealing processes

involved the thermal annealing for 1 h followed by DMF or dimethyl sulfoxide (DMSO) vapor-assisted thermal annealing for another 1 h, respectively. Previous study showed that the perovskite phase was completely formed after 1 h thermal annealing.[251] Therefore, the DMF or DMSO vapor-assisted thermal annealing used here is different from that reported before,[251] in which DMF (and DMSO) solvent annealing was performed right after the spin coating of MAI without the formation of perovskite phase. Previous studies showed that DMF and DMSO have different affinity to PbI_2.[253, 254] One DMF coordinates to one Pb and needlelike PbI_2·DMF crystals can be formed with a layer of DMF on each side of the Pb-I-Pb sheet.[253] Two DMSO attach to one Pb and PbI_2·DMSO complex can be formed,[254] which even retards the crystallization of PbI_2.[248] There are no reports on the interactions of DMF and DMSO to perovskites. Our results clearly showed that both DMF and DMSO interact with perovskites, no matter pure Pb or Pb-Sn perovskites. DMSO has much pronounced effect than DMF to pure Pb perovskite, especially Pb-Sn provskites. EQE measurements showed that the absorption onset redshifts from 825 nm for pure Pb perovskite to 950 nm for 10% Sn and 1010 nm for 25% Sn binary Pb-Sn perovskites. Different annealing processes have no impact on the absorption onsets of each perovskites but significant redistribution of EQE over the wavelength range, indicating the possible rearrange and segregation of Pb and Sn in the films as well as the change of grain size resulting in different efficiency in photon absorption and carrier generation and transport in different wavelength regime. The solar cells containing 10% Sn ($CH_3NH_3Sn_{0.1}Pb_{0.9}I_3$) made via the thermal annealing plus DMSO vapor-assisted thermal annealing demonstrated an average PCE of 9.95% and the maximum PCE of 10.25%. To the best of our knowledge, this is the highest PCE reported for $CH_3NH_3Sn_xPb_{1-x}I_3$ solar cells. To be noticed, the thickness of the perovskite layers is ~210 nm for all the devices, thinner than the typical high PCE pervoskite solar cells reported.[95, 240, 249] With such a thin perovskite layer, the materials consumption and the potential hazardous caused by Pb is greatly reduced. Using solvent vapor-assisted thermal annealing process to control and manipulate film morphology, grain size, and especially the distribution of metal cations in binary metal perovskite layers open an avenue to grow desired property perovskite materials to enhance device performance.

6.2 Experimental Section

6.2.1 Materials and Synthesis of MAI

PbI_2 (99%), Bathocuproine (BCP, 99.99%), methylamine (CH_3NH_2) solution (33 wt. % in absolute ethanol), hydroiodic acid (HI, contains No stabilizer, distilled, 57 wt. % in H_2O, 99.99% trace metals basis), DMF (anhydrous, 99.8%), DMSO (anhydrous, ≥99.9%), 2-propanol (anhydrous, 99.5%), 1, 2-dichlorobenzene (DCB, anhydrous, 99%), CB (anhydrous, 99.8%), ethanol (200 proof, anhydrous, ≥99.5%), and Poly (methyl methacrylate) (PMMA, average Mw ~120,000 by GPC) were purchased from Sigma-Aldrich and used as received. $PC_{61}BM$ (99.5%) was purchased from Nano-C. PEDOT:PSS (Clevios™ P VP AI 4083) was obtained from H.C. Starck and filtered through a 0.45 μm nylon filter before use. Al pallets and ITO coated glass were obtained from R.D. Mathis and Colorado Concept Coatings LLC, respectively.

Methylammonium iodide (CH_3NH_2I) was synthesized as described previously.[37] In a typical procedure, 24 ml of a 33 wt% methylamine (CH_3NH_2) solution in anhydrous ethanol was charged with 100 mL ethanol in a 250 mL round bottom flask. The solution was stirred in an ice-water bath with the nitrogen protection. After that, 10 ml of 57 wt% hydroiodic acid (HI) in water was added dropwise to the methylamine solution in a time period of 30 min. The resultant mixture was stirred at 0°C for 1.5 h. The white precipitate was recovered by rotary evaporation at 40°C. The yellowish dried precipitate was dissolved in ethanol followed by sedimentation in diethyl ether by stirring the solution for 30 min. Then the mixture was washed three times with diethyl ether. The washed solid was then collected and dried at 50°C in a vacuum oven for 24 h.

6.2.2 Perovskite Film Fabrication and Characterization

The fabrication of perovskite film is displayed in Figure 7.1. The ITO coated glass substrates (sheet resistance = 10 Ω sq^{-1}) were first cut into 15 mm x 15 mm pieces. The substrates were cleaned by several ultrasonication steps in soapy DI water, millipore water, acetone, and isopropanol, each for 15 min. The cleaned substrates were treated with oxygen plasma for 30 s and spin-coated with filtered PEDOT:PSS solution at 3000 rpm for 60 s. After being baked in air at 105°C for 30 min to eliminate the solvent, the substrates were transferred to a nitrogen glovebox for the spin coating of metal iodide layer. To prepare the

solutions for making $Sn_xPb_{1-x}I_2$ films with x = 0, 0.1, 0.25, 0.5, 0.9, and 1, SnI_2 and PbI_2 powders were mixed with a molar ratio of 0:1, 0.1:0.9, 0.25:0.75, 0.5:0.5, 0.9:0.1, and 1:0, respectively. Each mixed powder was then dissolved in DMF to a concentration of 0.868 M. The solution was spin-coated onto the PEDOT:PSS substrate at 6000 rpm for 45 s followed by baking at 70°C for 20 min. A 70 uL of 0.314 M MAI 2-propanol solution was dropped onto the substrate, set for 5 s, and then spin-coated at 4000 rpm for 35 s. The substrates were dried at room temperature for 1 h followed by thermal annealing at 100°C for 2 h. For the perovskite films annealed with DMF or DMSO vapor-assisted thermal annealing, the perovskite films were first thermally annealed at 100°C for 1 h and then covered by a glass petri dish. A drop of 10 μL of DMF or DMSO was added onto the hotplate inside the petri dish to allow solvent vapor-assisted thermal annealing at 100°C for 1 h. For the perovskite films used for UV-Vis and 2-dimention X-ray diffraction (2D-XRD) characterizations, a PMMA layer was coated to protect the films by spin coating a 30 mg/ml PMMA CB solution at 2000 rpm for 60 s.

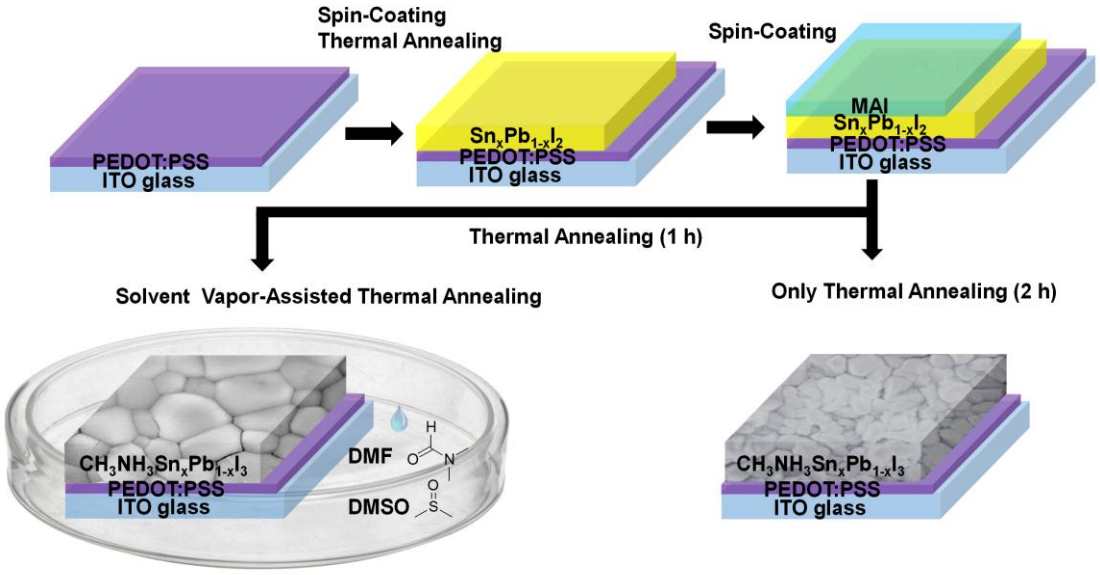

Figure 6.1 Schematics of a two-step solution-process method to prepare the $CH_3NH_3Sn_xPb_{1-x}I_3$ layers. The $CH_3NH_3Sn_xPb_{1-x}I_3$ polycrystalline films were obtained by only-thermal annealing or thermal annealing plus DMF or DMSO solvent vapor-assisted thermal annealing. The chemical structures of DMF and DMSO solvents are also shown.

The measurement of 2D-XRD was carried out on a Bruker GADDS D8 Discover diffractometer using Cu Kα radiation (λ = 1.5419 Å). Three frames with 160 s/frame were obtained for each sample. Scan angle 2θ begins at 25° with a frame width of 30°. During the scan, the samples oscillate along x and y axis with an amplitude of 1.0 mm. Data were processed using the EVA package provided by Bruker Axs. The morphology of the perovskite films were characterized using SEM (FEI Sirion SEM). UV-Vis-NIR optical absorption measurements of the samples were performed on a Varian Cary 5000 UV-Vis-NIR spectrophotometer (wavelength range 350-1200 nm).

6.2.3 Device Fabrication and PV Performance Measurement

Solar cells were fabricated with a structure of ITO/PEDOT:PSS/ $CH_3NH_3Sn_{1-x}Pb_xI_3$ (x = 0, 0.1, 0.5, 0.75, 0.9, and 1)/$PC_{61}BM$/C_{60}/BCP/Al. The ITO/PEDOT:PSS/$CH_3NH_3Sn_{1-x}Pb_xI_3$ (x = 0, 0.1, 0.5, 0.75, 0.9, and 1) films were fabricated as described above. To fabricate the $PC_{60}BM$ layer, $PC_{60}BM$ powder was dissolved in DCB to a concentration of 27.1 mg/ml. The as-prepared solution was stirred at 90°C for 2 h and filtered through a 0.45 μm PTFE filter. The filtered $PC_{60}BM$ solution was spin coated on the perovskite film at 3000 rpm for 60 s followed by annealing at 90°C for 1 h. A 20 nm C_{60} layer and an 8 nm BCP layer were thermally deposited in sequence. Finally, the cathode Al layer of 100 nm was thermally evaporated through a shadow mask to make 16 electrodes each with an area of 3.14 mm^2. The background pressure was $<1\times10^{-6}$ Torr during the thermal deposition.

The illuminated J-V curves were recorded in a glove box under nitrogen atmosphere using a Keithley 2400 Source Meter unit. The measurements were performed under AM1.5 illumination condition at an intensity of 100 mW/cm^2. The light intensity was calibrated to 100 mW/cm^2 using a calibrated silicon solar cell that had been previously standardized at the National Renewable Energy Laboratory. EQE spectra were gathered in air using an Oriel Xenon lamp (450 W) with an AM1.5 filter, a monochromator (Oriel Cornerstone 130 1/8 m), a chopper with a frequency of 100 Hz, a lock-in amplifier (SR830, Stanford Research Corp), and a Si-based diode (J115711-1-Si detector) for calibration.

6.3 Results and Discussions

6.3.1 Fabrication and Characterization of Metal Iodide ($Sn_xPb_{1-x}I_2$) Films

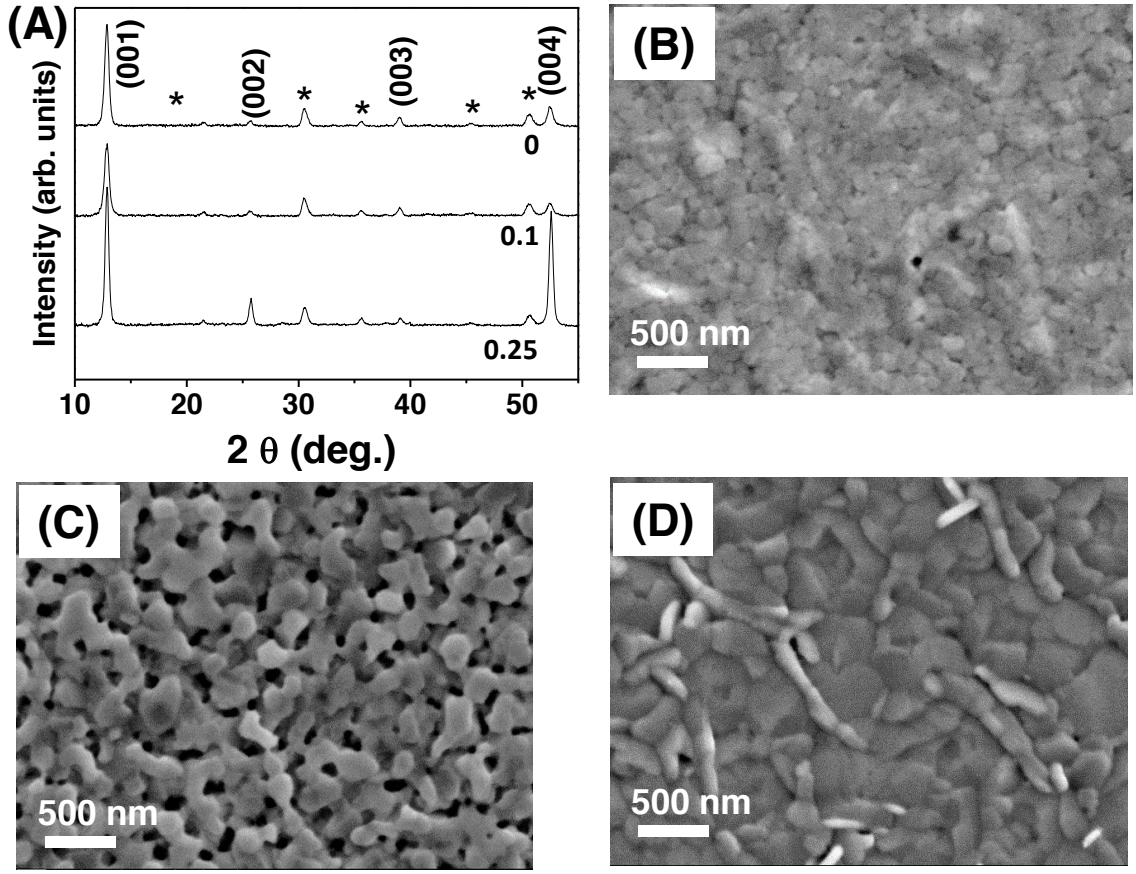

Figure 6.2 (A) XRD patterns of the PbI_2, $Sn_{0.1}Pb_{0.9}I_2$, and $Sn_{0.25}Pb_{0.75}I_2$ films. The peaks belong to ITO are labeled by asterisk. (B-D) SEM images of PbI_2, $Sn_{0.1}Pb_{0.9}I_2$, and $Sn_{0.25}Pb_{0.75}I_2$ films, respectively.

The metal iodide ($Sn_xPb_{1-x}I_2$) films were formed by spin casting the DMF solutions of pure PbI_2 or the mixtures of SnI_2 and PbI_2 followed by thermal annealing at 70°C for 20 min. The XRD patterns in Figure 7.2 are the results by merging the two frames of the 2D-XRD patterns via integrating χ. By excluding the peaks belonging to the ITO/PEDOT:PSS substrates and PMMA protection layer (labeled by asterisk), all peaks in Figure 7.2A for the pure PbI_2 film are ascribed to hematite PbI_2 with a space group of P-3m1 (164).[255]

There are no new peaks or peak shift for the $Sn_{0.1}Pb_{0.9}I_2$ and $Sn_{0.25}Pb_{0.75}I_2$ films compared to the pure PbI_2 film, indicating that Sn^{2+} substitutes Pb^{2+} in the PbI_2 crystal and the binary

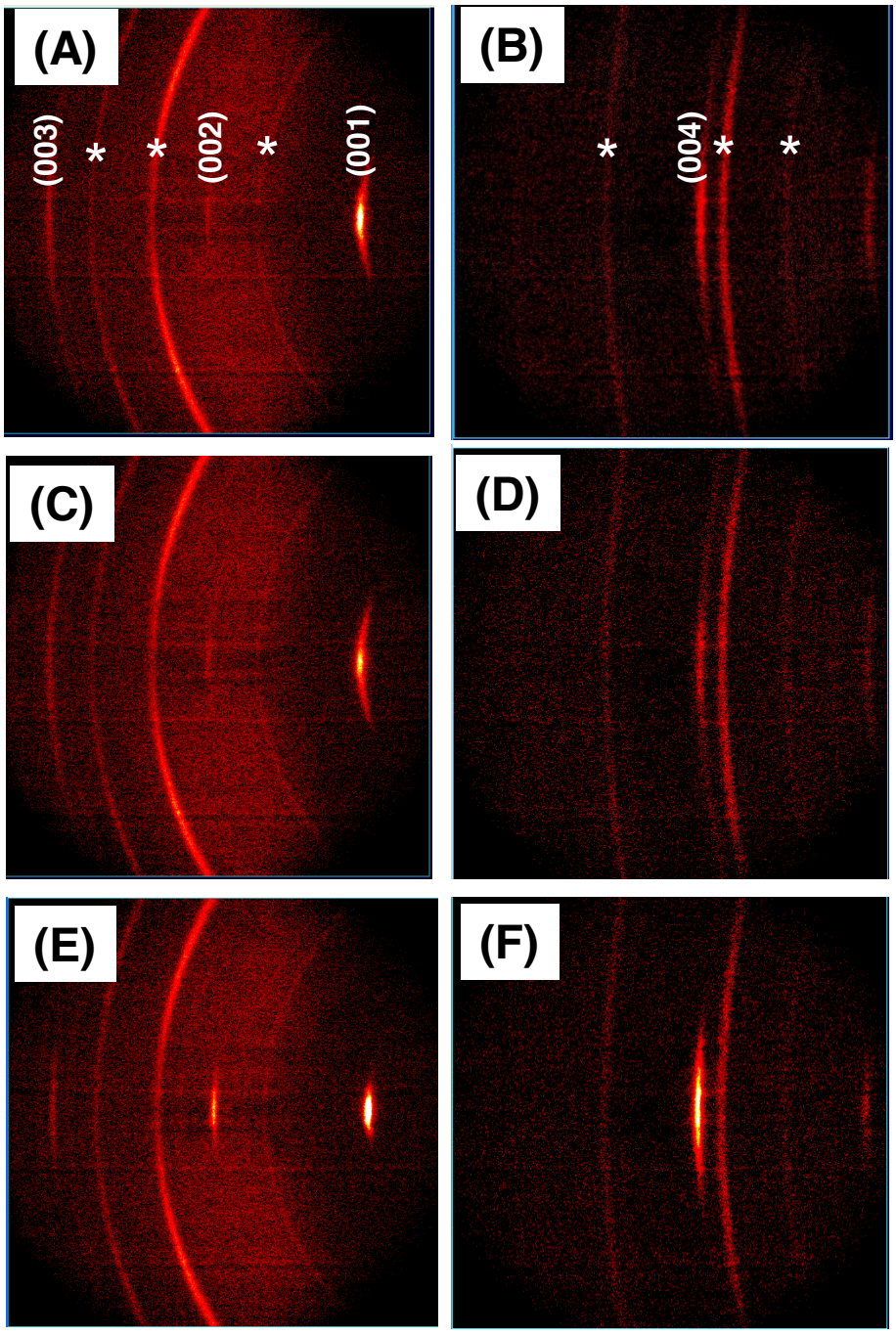

Figure 6.3 The first frame (2θ from 10° to 40°) and the second frame (2θ from 40° to 70°) of 2D X-ray diffraction patterns of the PbI_2 (A and B), $Sn_{0.1}Pb_{0.9}I_2$ (C and D), and $Sn_{0.25}Pb_{0.75}I_2$ (E and F) films. The scale of 2θ increases from right to left.

Pb-Sn iodide crystals retain the PbI_2 crystalline structure. A dramatic intensity increase in the peaks at 25.7° (002) and 52.6° (004) was observed in the XRD pattern of the $Sn_{0.25}Pb_{0.75}I_2$ film, which might be due to the change of grain orientation or increase in crystallinity. Figure 7.3 displays 2D-XRD patterns of PbI_2, $Sn_{0.1}Pb_{0.9}I_2$, and $Sn_{0.25}Pb_{0.75}I_2$ films. The diffraction rings corresponding to (001), (002), (003), and (004) plane show very obvious intensity distribution, indicating $Sn_{1-x}Pb_xI_2$ crystalline domains are highly oriented in the in-plane direction. The pattern corresponding to (001) plane of $Sn_{0.25}Pb_{0.75}I_2$ film shrinks to an elongated dot and the intensity of (002) and (004) plane dramatically increases (Figure 7.3E and 7.3F). This indicates the orientation is more pronounced in the $Sn_{0.25}Pb_{0.75}I_2$ film compared to the other two films. The SEM images of these three composition films were taken right after the films were made. Figure 7.2B shows that the PbI_2 film is composed by the 100-300 nm crystal grains with a smooth surface and few pin holes. The $Sn_{0.1}Pb_{0.9}I_2$ film has a porous, interconnected structure with the crystal grain size of 100- 500 nm and pore size of 100-200 nm (Figure 7.2C). The $Sn_{0.25}Pb_{0.75}I_2$ film is packed with dense flake-like crystals with the size 100-500 nm (Figure 7.2D). About half of the flakes are tilted or even perpendicular to the substrate surface. The SEM image confirms the XRD result that the reorientation of crystalline grains occurred in the $Sn_{0.25}Pb_{0.75}I_2$ film. Pure PbI_2 crystals were synthesized using a solvothermal method and hexagonal PbI_2 crystalline plates grown horizontally on lead foils in I_2 powder and ethanol systems were obtained.[255] The highly asymmetric hexagonal plates with an aspect ratio ~1/10 and the [001] direction of the plate thin direction indicates that growth rate along the [001] direction is much slower than that along the hexagonal plane perpendicular to the [001] direction. Here, PbI_2 and SnI_2 were dissolved in DMF and the pure PbI_2 or binary $Sn_xPb_{1-x}I_2$ recrystallized during the thermal annealing process, in which the coordinated DMF in PbI_2·DMF was released according to the previous thermogravimetric analysis of PbI_2·DMF.[253] Our XRD results showed no PbI_2·DMF phase after thermal annealing. The SEM images and XRD results showed in-plane orientation of PbI_2 and $Sn_{0.1}Pb_{0.9}I_2$ films while grain reorientation of $Sn_{0.25}Pb_{0.75}I_2$ film.

6.3.2 Fabrication and Characterization of $CH_3NH_3Sn_xPb_{1-x}I_3$ Films

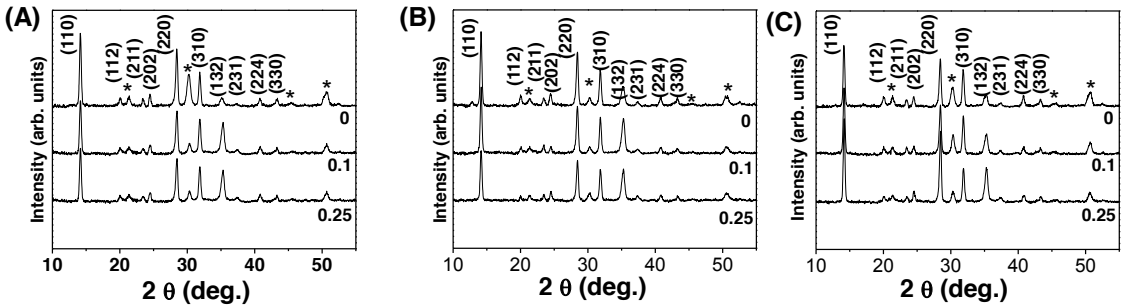

Figure 6.4 XRD patterns of the $CH_3NH_3PbI_3$, $CH_3NH_3Sn_{0.1}Pb_{0.9}I_3$, and $CH_3NH_3Sn_{0.25}Pb_{0.75}I_3$ films. The perovskite layers were prepared with the only-thermal annealing (A), or the thermal plus DMF (B) or DMSO (C) vapor-assisted thermal annealing.

The crystalline metal iodide films serve as templates to grow perovskite crystals. The PbI_6^{4-} octahedrons change from the edge connection in metal iodide crystals to the corner connection in perovskite crystals accompanied by the insertion of MA cations. We spin coated MAI 2-propanol solution over the metal iodide polycrystalline films and thermally annealed the films to enhance the growth of perovskite crystals. One set of films was thermally annealed at 100°C for 2 h and another two sets of films were thermally annealed at 100°C for 1 h and then a drop of DMF or DMSO was added to the hot plate and covered with a glass petri dish to continue annealing at the same temperature for another 1 h under the present of solvent vapor. Figure 7.3 shows the XRD patterns of the films containing pure Pb and 10 and 25% Sn of Pb-Sn prepared via three different annealing processes. The peaks for films containing pure Pb are ascribed to tetragonal perovskite crystal with a space group of I4cm, no matter they are prepared via only-thermal annealing or thermal annealing plus solvent vapor-assisted thermal annealing. The XRD patterns of films containing 10 and 25% Sn of Pb-Sn prepared by three annealing processes are almost identical to those containing pure Pb, indicating that the $CH_3NH_3Sn_{0.1}Pb_{0.9}I_3$ and $CH_3NH_3Sn_{0.25}Pb_{0.75}I_3$ perovskite crystals are in I4cm phase. The results are in agreement with the previous study that a transition from tetragonal I4cm to cubic P4mm perovskite structure occurs for greater than 50% Sn content in perovskites.[99] It is noticed that the $MAPb_{0.85}Sn_{0.15}I_{3-x}Cl_x$ film prepared via one-step solution method showed partial I4cm/P4mm phases that might be

due to the mixed halide (I and Cl).[240] The 2D-XRD patterns of $CH_3NH_3PbI_3$, $CH_3NH_3Sn_{0.1}Pb_{0.9}I_3$, and $CH_3NH_3Sn_{0.25}Pb_{0.75}I_3$ perovskite films are shown in Figure 7.5. The diffraction rings corresponding to (110) and (220) plane show noticeable intensity distribution for the $CH_3NH_3Sn_{0.25}Pb_{0.75}I_3$ film prepared by only-thermal annealing, indicating the highly oriented texture of the film. This texture may originate from the tilt/perpendicular orientated plates in the $Sn_{0.25}Pb_{0.75}I_2$ film.

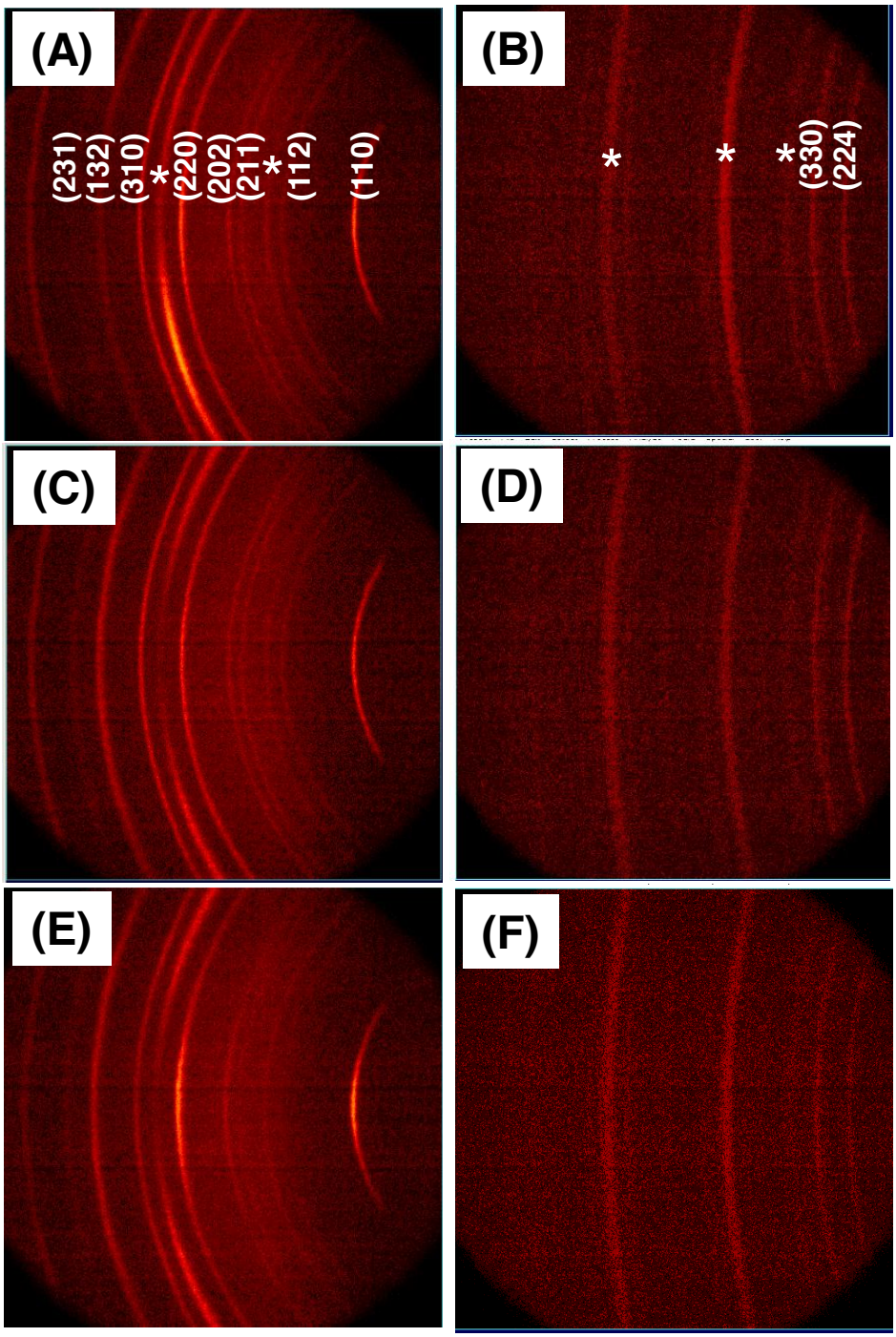

Figure 6.5 The first frame (2θ from 10° to 40°) and the second frame (2θ from 40° to 70°) of 2D X-ray diffraction patterns of the $CH_3NH_3PbI_3$ (A and B), $CH_3NH_3Sn_{0.1}Pb_{0.9}I_3$ (C and D), and $CH_3NH_3Sn_{0.25}Pb_{0.75}I_3$ (E and F) films prepared via only-thermal annealing. The scale of 2θ increases from right to left.

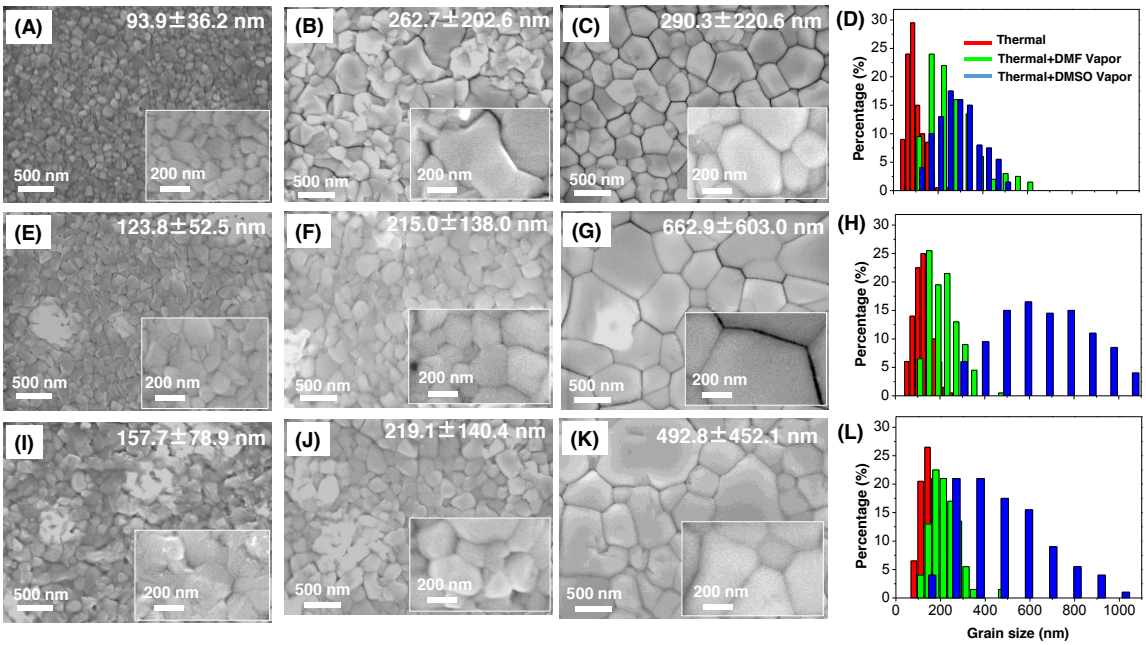

Figure 6.6 SEM images and grain size distributions of the $CH_3NH_3PbI_3$ (A, B, C, and D), $CH_3NH_3Sn_{0.1}Pb_{0.9}I_3$ (E, F, G, and H), and $CH_3NH_3Sn_{0.25}Pb_{0.75}I_3$ (I, J, K, and L) films. The perovskite layers were prepared with the only-thermal annealing, or thermal annealing plus DMF or DMSO vapor-assisted thermal annealing.

The morphology of all prepared $CH_3NH_3Sn_xPb_{1-x}I_3$ films were investigated using SEM on both top-view and cross-sectional view. Different annealing processes have significant impact to the morphology in terms of grain size and surface smoothness. Figure 7.6A, E, and I show the SEM images of the $CH_3NH_3PbI_3$, $CH_3NH_3Sn_{0.1}Pb_{0.9}I_3$, and $CH_3NH_3Sn_{0.25}Pb_{0.75}I_3$ perovskite films prepared via only-thermal annealing. All three films are densely packed with small grains without pinholes. The histogram of grain size distribution is summarized in Figure 7.6D, H, and L for pure Pb and 10 and 25% Sn content Pb-Sn provskites, respectively. Grain size is increased with the increasing of Sn content in perovskites from the average grain size of 93.9±36.2 nm for pure Pb to 123.8±52.5 nm for 10% Sn and 157.7±78.9 nm for 25% Sn. Among three only-thermal annealed perovskites, the $CH_3NH_3PbI_3$ film has relatively uniform grain size with a smaller standard deviation. After the thermal plus DMF solvent vapor-assisted thermal annealing, however, the grains of $CH_3NH_3PbI_3$ film grew larger with more irregular shapes and a very large standard deviation (Figure 7.6B and D). This annealing process also produced larger grains in the

$CH_3NH_3Sn_{0.1}Pb_{0.9}I_3$ and $CH_3NH_3Sn_{0.25}Pb_{0.75}I_3$ films but relative smaller standard deviations and more isotropically grown grains compared to the $CH_3NH_3PbI_3$ film (Figure 7.6F, J, H and L). The thermal plus DMSO solvent vapor-assisted thermal annealing changed the morphology of films dramatically. For the $CH_3NH_3PbI_3$ film, even though the average grain size and standard deviation do not change too much compared to the film with the thermal plus DMF vapor-assisted thermal annealing, the grains are in more regular shapes with straight sides and the surface are much smoother (Figure 7.6C and D). For the films containing Sn, the surfaces are even smoother and the grains as large as ~ 1 μm present. For the $CH_3NH_3Sn_{0.1}Pb_{0.9}I_3$ film, the top surface of each grain is completely flat, indicating a single crystalline plane termination (Figure 7.6G). The grain size is ranged from ~300 nm to slightly over ~ 1 μm with the average size about 660 nm (Fig 7.6H). For the $CH_3NH_3Sn_{0.25}Pb_{0.75}I_3$ film, the top surfaces of grains are smooth but in-lane defects are clearly shown (Figure 7.6K). The grain size has an even broader distribution from ~200 nm to slightly over ~ 1 μm with the average size about 590 nm (Fig 7.6L).

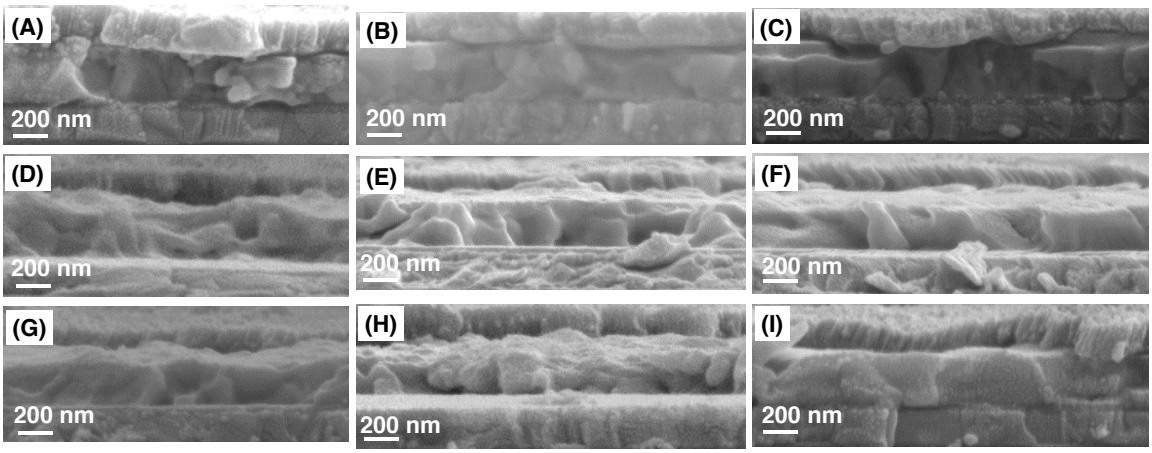

Figure 6.7 Cross-sectional SEM images of the $CH_3NH_3PbI_3$, $CH_3NH_3Sn_{0.1}Pb_{0.9}I_3$, and $CH_3NH_3Sn_{0.25}Pb_{0.75}I_3$ films. The perovskite layers were prepared with the only-thermal annealing (A, D, and G), or the DMF (B, E, and H) or DMSO (C, F, and I) vapor-assisted thermal annealing.

The cross-sectional view SEM images of the devices with the pure Pb and 10 and 25% Sn content perovskite films prepared under three different annealing processes are shown in Figure 7.7. All the films have a thickness about 200 nm and the annealing processes

have no impact to the film thickness. However, the number of grain boundaries across the vertical direction of the films is different due to the difference in grain size. For the films prepared under the only-thermal annealing process, the pure Pb (Figure 7.7A) and 10% Sn content (Figure 7.7D) films have many grain boundaries across the vertical direction of the films because of small grains as observed from the top-view SEM images in Figure 7.6A and E. The 25% Sn content film has more single grains throughout the entire film thickness presumably due to the larger grains. Figure 7.7B and E show that there are still many grains stacked across the vertical direction of films even after the thermal annealing plus DMF solvent vapor-assisted thermal annealing. Figure 7.7H shows even more grain boundaries across the film after the thermal plus DMF vapor-assisted thermal annealing for the film containing 25% Sn compared to the only-thermal annealed film. The films prepared under the thermal plus DMSO vapor-assisted thermal annealing show consistently more single grains across the entire film vertically (Figure 7.7C, F, and I). The different number of grain boundaries across the film thickness counts partially for the device performance discussed later.

The pure Pb perovskite ($CH_3NH_3PbI_3$) films were prepared using thermal annealing and DMF solvent annealing, respectively, and the resulted grain size as a function of film thickness were investigated.[251] All the films have a similar grain size (~200 nm) under the thermal annealing process regardless of the film thickness 250, 430, or 1015 nm. After DMF solvent annealing, the grain size was almost doubled for the 250 and 430 nm thick $CH_3NH_3PbI_3$ films. The grain size comparable to the film thickness was obtained for the 1015 nm thick $CH_3NH_3PbI_3$ film. It was mentioned that similar behaviors were observed for the $CH_3NH_3PbI_3$ films under DMSO solvent annealing. It has to be pointed out that the solvent annealing process reported[251] is different from the one we used here. A drop of DMF or DMSO was added to the hot plate right after the MAI was spin coated over the PbI_2 polycrystalline films. Both PbI_2 and MAI can be dissolved in DMF and DMSO, resulting in a large diffusion length of two precursors during the solvent annealing process. Here, a drop of DMF or DMSO was added after 1 h thermal annealing of the stacked MAI and polycrystalline metal iodide layers. Perovskite crystals are completely formed under this condition.[251] Therefore, the DMF or DMSO vapor-assisted thermal annealing here causes the morphology changes of perovskite crystals not the formation of large perovskite

grains from PbI_2 polycrystals and MAI. In other words, DMF or DMSO interacts with perovskite crystals not PbI_2 crystals.

The unique results associated with the thermal annealing plus DMF and DMSO solvent vapor-assisted thermal annealing processes of pure Pb and binary Pb-Sn perovksites and the possible explanations are discussed. (1) All the films show the crystalline structure of a tetragonal I4cm phase regardless annealing process. The dramatically different in film morphologies under DMF or DMSO vapor-assisted thermal annealing suggests that DMF and DMSO interact with perovskites by attaching to Pb and Sn. The almost identical XRD patterns indicate that no DMF or DMSO complex residuals in the polycrystalline perovskite films. (2) Unlike DMF or DMSO solvent annealing process causing no difference to the morphology of $CH_3NH_3PbI_3$ films,[251] the thermal annealing plus DMF or DMSO solvent vapor-assisted thermal annealing processes result in very different film morphologies of the $CH_3NH_3PbI_3$ films, indicating DMF and DMSO have different interaction with the perovskite $CH_3NH_3PbI_3$. Both DMF and DMSO are strong polar solvents that contain electronegative oxygen atom with the coordination ability. The coordination ratio between Pb in PbI_2 and the solvent is 1:1[253] and 1:2[254] for DMF and DMSO, respectively, indicating that DMSO has a stronger coordination ability with PbI_2 than that of DMF. DMSO vapor can easily attack Pb at the film surface and grain boundaries. The binding of DMSO to Pb at the grain boundaries lowers the surface energy of these boundaries. The merge of smaller crystalline grains to larger ones is more easily happen for the perovskite films under DMSO vapor annealing. In addition, DMSO has a low volatility due to its relatively high boiling point (189°C vs. 153°C for DMF) and low saturated vapor pressure (0.76 kPa at 60°C vs. 9.31 kPa for DMF), which can maintain a prolonged presence of DMSO to complete the merge of more small grains to larger ones. (3) For the perovskite films containing Sn, DMF and DMSO do not just simply help to merge small grains, they could also cause the rearrangement of Sn and Pb inside grains due to the different bond energies of Sn and Pb with iodide and oxygen. The bond energy increases in the order of Pb-I < Sn-I < Pb-O < Sn-O with the values of 194, 235, 374, and 528 kJ/mol, respectively.[240, 256] Although there is no report on the coordination ratio of Sn to DMF and DMSO, we assume a similar trend as that for Pb. DMSO (or DMF) could bind to Sn via forming a strong Sn-O bond, which even breaks the existing Sn-I bond. This

could also happen to Pb site but preferential to Sn. As illustrated in Figure 7.8, the DMSO attaching to Sn by breaking Sn-I bond creates different number of iodide dangling bond on each Pb centered iodide octahedrons, which allows those "unsaturated" octahedrons moving around to reform the "saturated" octahedrons. During this process, the rearrangement is driven by the reduction of surface energy of crystalline grains. The lower bond energy of Pb-I and Pb-O than Sn-I and Sn-O could lead to the segregation of Pb to grain surface to reduce the surface energy. The rich-Pb at the top layer of binary Pb-Sn perovskites were also observed. The flat grain surface could be the (110) plane of perovskites as shown the strong (110) and (220) plane peaks in the XRD patterns. It is noticed that there are more in-plane defects observed on the perovskite film containing 25% Sn. This could be the strain caused by more Pb^{2+} on surface due to the larger ionic radius of Pb^{2+} than that of Sn^{2+}. This effect is more pronounced when Sn content is high. The in-lane defects might also be caused by the merge of different orientated perovskite grains originated from the different orientated $Sn_{0.25}Pb_{0.75}I_2$ plates as observed in Figure 7.6D. For the 10% Sn content perovskite film, the $Sn_{0.10}Pb_{0.90}I_2$ polycrystalline grains are already orientated in the same direction, which facilitates the merge of small perovskite grains with the help of DMSO.

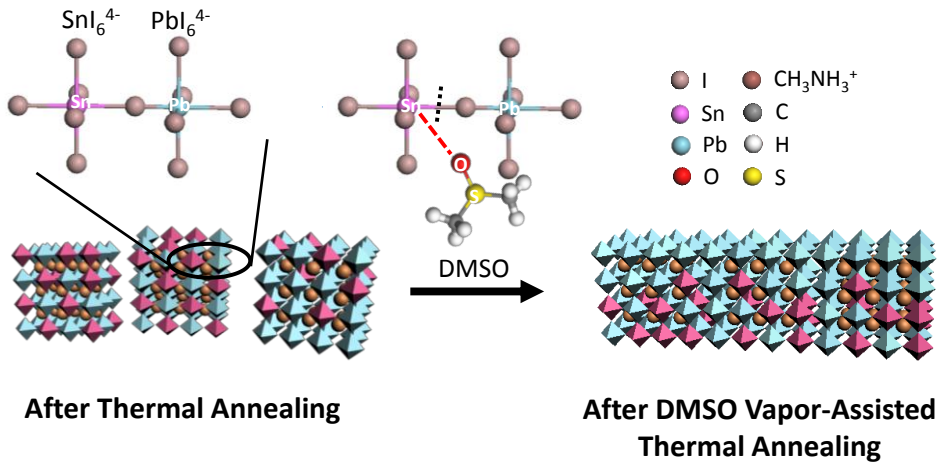

Figure 6.8 Schematics of the possible bond breaking of Sn-I (or Pb-I) in $CH_3NH_3Sn_xPb_{1-x}I_3$ perovskite grains via DMSO attacking during the thermal plus DMSO vapor-assisted thermal annealing process, leading to large, flat grains and the redistribution of Pb and Sn in grains.

6.3.3 Device Performance of $CH_3NH_3Sn_xPb_{1-x}I_3$ Solar Cells

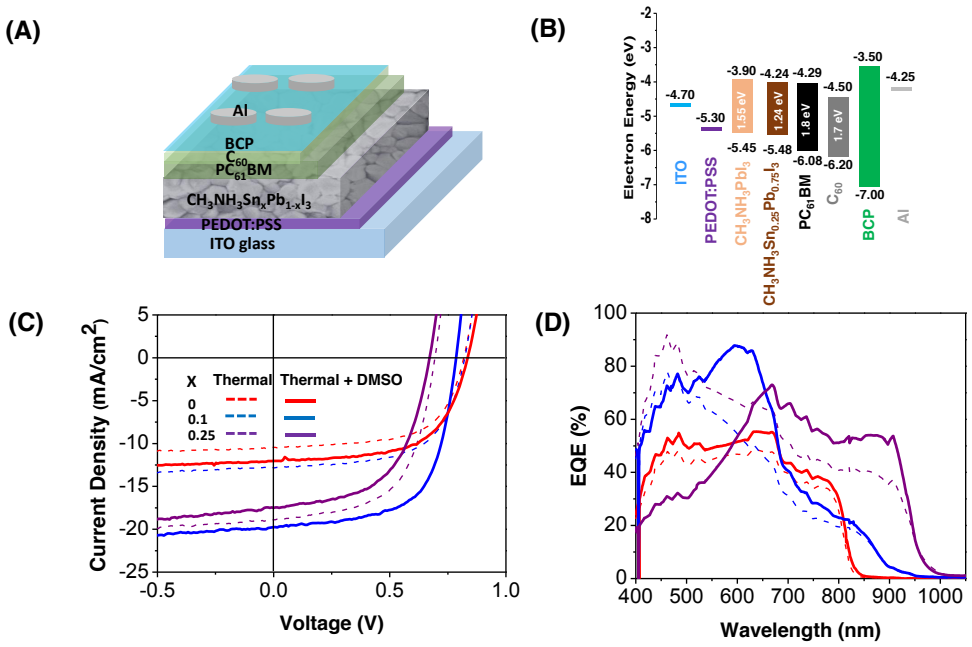

Figure 6.9 (A) Device configuration of a planar $CH_3NH_3Sn_xPb_{1-x}I_3$ perovskite solar cell. (B) Energy diagram for materials involved in the solar cells. (C) Typical J-V characteristics and (D) EQE spectra of $CH_3NH_3Sn_xPb_{1-x}I_3$ (X = 0, 0.1, and 0.25) perovskite solar cells under 1 sun AM 1.5G solar illumination with the perovskite layers prepared via only-thermal and thermal plus DMSO vapor-assisted annealing.

The perovskite layers prepared in different annealing processes were deployed in the solar cells with a planar heterojunction structure of ITO/PEDOT:PSS/$CH_3NH_3Sn_xPb_{1-x}I_3$/$PC_{61}BM$/C_{60}/BCP/Al (Figure 7.9A), where PEDOT:PSS acted as the hole transport layer, $PC_{61}BM$/C_{60} as the ETLs, and BCP as the exciton blocking layer. The energy diagram of the perovskites $CH_3NH_3Sn_xPb_{1-x}I_3$ (x = 0, 0.25) and materials involved in the devices are displayed in Figure 7.9B. While the valence band maxima are almost the same, the conduction band minimum is lower for $CH_3NH_3Sn_{0.25}Pb_{0.75}I_3$, resulting in a reduced band gap from 1.55 eV of $CH_3NH_3PbI_3$ to 1.24 eV of $CH_3NH_3Sn_{0.25}Pb_{0.75}I_3$.[99] Figure 7.9C shows the J-V characteristics of the solar cells with the perovskite layers prepared by the only-thermal annealing and the thermal plus DMSO vapor-assisted thermal annealing under 1 sun AM 1.5G solar illumination. Table 7.1 summarizes the J_{SC}, V_{OC}, fill-factor (FF), and

PCE derived from the J-V curves. For the solar cells with the only-thermal annealing prepared

Table 6.1 PV performance parameters of the $CH_3NH_3Sn_xPb_{1-x}I_3$ (x = 0, 0.1, and 0.25) perovskite solar cells under 1 sun AM 1.5G solar illumination. The $CH_3NH_3Sn_xPb_{1-x}I_3$ perovskite films were prepared via the only-thermal annealing or the thermal plus DMSO vapor-assisted thermal annealing.

	V_{OC} (V)	J_{SC} (mA/cm^2)	FF (%)	PCE (%)	PCE_{max} (%)
Only-thermal annealing					
$CH_3NH_3PbI_3$	0.81±0.05	11.1±0.9	62.6±0.8	5.61±0.43	6.10
$CH_3NH_3Sn_{0.1}Pb_{0.9}I_3$	0.82±0.07	13.9±0.6	53.4±3.9	6.10±0.41	6.57
$CH_3NH_3Sn_{0.25}Pb_{0.75}I_3$	0.77±0.08	20.3±0.9	56.7±4.8	8.45±0.59	8.83
Thermal + DMSO vapor-assisted thermal annealing					
$CH_3NH_3PbI_3$	0.81±0.01	12.1±1.1	63.9±5.7	6.20±0.03	6.23
$CH_3NH_3Sn_{0.1}Pb_{0.9}I_3$	0.78±0.02	19.0±0.8	67.1±0.3	9.95±0.51	10.25
$CH_3NH_3Sn_{0.25}Pb_{0.75}I_3$	0.70±0.02	17.7±0.5	56.3±2.0	6.98±0.68	7.76

perovskite layers, the partial substitution of Pb with Sn leads to a significant increase in J_{SC} from 11.1±0.9 to 13.9±0.6 to 20.3±0.9 mA/cm^2 for the $CH_3NH_3PbI_3$, $CH_3NH_3Sn_{0.1}Pb_{0.90}I_3$, and $CH_3NH_3Sn_{0.25}Pb_{0.75}I_3$ solar cells, respectively. The trend is in concord with a recent report even though the devices were fabricated with a configuration of FTO/TiO_2/$CH_3NH_3Sn_xPb_{1-x}I_3$/Spiro-OMeTAD/Au.[99] The combination of unchanged V_{OC}, increased $J_{SC,}$ and decreased FF led to a slightly increased average PCE of the $CH_3NH_3Sn_{0.1}Pb_{0.90}I_3$ solar cells compared to that of the $CH_3NH_3PbI_3$ solar cells. The significantly increased Jsc of the $CH_3NH_3Sn_{0.25}Pb_{0.75}I_3$ perovskite solar cells resulted in an

average PCE of 8.45±0.59% with a maximum PCE of 8.83% even though the V_{OC} and FF were decreased. The performance is higher than the PCE of 7.37% with the same composition perovskite but different device structure and different perovskite film preparation method.[99] While the improvement upon electronic properties resulting from the addition of Sn to $CH_3NH_3PbI_3$ perovskite,[99, 245] plays a role in the increase of J_{SC}, the larger grains of 10 and 25% Sn perovskite films also make contributions, especially for the 25% Sn perovskite film in which many single grains cross the entire film shown by the cross-sectional view SEM image (Figure 7.7I). The fewer grain boundaries across the film thickness reduce the charge carrier recombination at the grain boundary and therefore, results in higher J_{SC}'s.

The significant morphology changes of the $CH_3NH_3Sn_xPb_{1-x}I_3$ (x = 0, 0.1, and 0.25) perovskite films after the thermal plus DMSO vapor-assisted thermal annealing impact device performance. The $CH_3NH_3Sn_{0.1}Pb_{0.90}I_3$ solar cells exhibit an average J_{SC} of 19.0±0.8 mA/cm^2, V_{OC} of 0.78±0.2 V, and FF of 0.78±0.2%, yielding an average PCE of 9.95±0.51% and a maximum PCE of 10.25%. To the best of our knowledge, this is the best performance for the solar cells with binary Pb-Sn triiodide perovskites. Compared to the significantly enhanced device performance of the $CH_3NH_3Sn_{0.1}Pb_{0.90}I_3$ solar cells, the $CH_3NH_3PbI_3$ solar cells only have a 10.5% increase of the average PCE because of the slightly increased average J_{SC} and FF and unchanged V_{OC}. However, the $CH_3NH_3Sn_{0.25}Pb_{0.75}I_3$ solar cells display drops in the average V_{OC}, J_{SC} and FF by 9.1%, 12.8%, and 0.7%, respectively, leading to a 12.1% decrease of the average PCE. This might be due to the oxidation of Sn^{2+} to Sn^{4+} during the DMSO vapor-assisted thermal annealing, even though the anhydrous DMSO was used and the process was carried out in a N_2-filled glove box. The presence of Sn^{4+} could trap electrons and result in a degraded performance.[99, 245] The in-plane defects observed in the SEM image (Figure 7.7I) could also cause the recombination of carriers.

The EQE spectra of these solar cells are shown in Figure 7.9D. The solar cells containing the only-thermally annealed perovskites show a clear redshift of the absorption onset from 825 to 950 to 1010 nm for the $CH_3NH_3Sn_xPb_{1-x}I_3$ perovskites with x = 0, 0.1, and 0.25, respectively. The absorption onsets of $CH_3NH_3PbI_3$ and $CH_3NH_3Sn_{0.25}Pb_{0.75}I_3$ match the corresponding band gaps reported.[95, 99] No absorption onset or band gap has been reported for the $CH_3NH_3Sn_{0.1}Pb_{0.9}I_3$ perovskite. The absorption onset of 950 nm,

equivalent to the band gap of 1.31 eV, follows the trend of the absorption onset shift and band gap narrowing of $CH_3NH_3Sn_xPb_{1-x}I_3$ from x = 0 to 0.75.[99] The higher EQE in the range of 400-700 nm and the extra absorption between 850-950 nm for the only-thermal annealed $CH_3NH_3Sn_{0.1}Pb_{0.9}I_3$ solar cell compared to the only-thermal annealed $CH_3NH_3PbI_3$ solar cell lead to an increased $J_{SC.}$ The very high J_{SC} for the only-thermal annealed $CH_3NH_3Sn_{0.25}Pb_{0.75}I_3$ solar cells is truly because of the higher EQE over the entire wavelength range of 400-1010 nm. It is very interesting to observe that the different annealing processes do not vary the absorption onsets of each perovskite solar cell, but the spectral shapes change dramatically for the binary Pb-Sn perovskite solar cells while they are very similar for the pure Pb perovskite solar cells. The slightly increased EQE over the entire range of 400-825 nm for the thermal plus DMSO vapor-assisted thermally annealed pure Pb perovskite solar cell is consistent with the slight increase of J_{SC} observed. The similar shape indicates that the entire process from photon absorption to carrier extraction is similar for the pure Pb perovskite solar cells prepared under two annealing processes, although the film morphology is different. In contrast, the thermal plus DMSO vapor-assisted thermal annealed $CH_3NH_3Sn_{0.1}Pb_{0.90}I_3$ solar cells exhibit a significant increase of EQE in the range of 500-700 nm with a peak EQE close to 90%. Because peak sun light flux occurs in this range, a great increase of J_{SC} from 13.9 to 19.0 mA/cm^2 was obtained, leading to the best PCE of 10.25%. The thermal plus DMSO vapor-assisted thermal annealed $CH_3NH_3Sn_{0.25}Pb_{0.75}I_3$ solar cells exhibits a moderate increase of EQE in the long wavelength range of 650-950 nm but a great drop of EQE in the range of 400-650 nm, which eventually results in a decrease of J_{SC} from 20.3 to 17.7 mA/cm^2. The change of EQE in different wavelength ranges caused by different annealing processes suggests the possible rearrangement of Sn and Pb in the $CH_3NH_3Sn_xPb_{1-x}I_3$ perovskites films due to the movement of octahedrons during the DMSO vapor-assisted thermal annealing process, which induces the change of the efficiency from photon absorption to charge generation, transport, and collection. Clearly, DMSO vapor-assisted thermal annealing provides a new way to manipulate binary Pb-Sn perovskite films to yield desired properties.

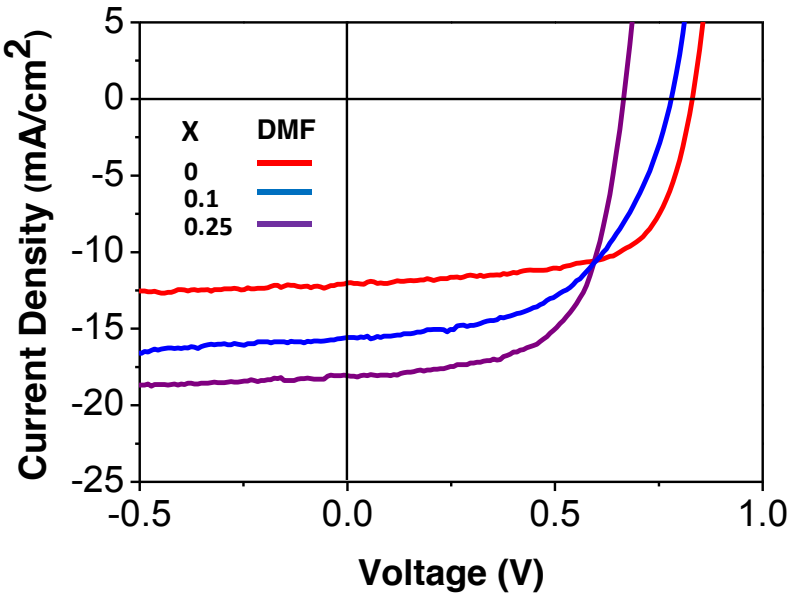

Figure 6.10 Typical J-V characteristics of $CH_3NH_3Sn_xPb_{1-x}I_3$ (x = 0, 0.10, and 0.25) perovskite solar cells under 1 sun AM 1.5G solar illumination. The perovskite layers were prepared with the thermal plus DMF vapor-assisted thermal annealing.

Table 6.2 PV performance parameters of the $CH_3NH_3Sn_xPb_{1-x}I_3$ (x = 0, 0.1, and 0.25) perovskite solar cells under 1 sun AM 1.5G solar illumination. The $CH_3NH_3Sn_xPb_{1-x}I_3$ perovskite films were prepared via the thermal plus DMF vapor-assisted thermal annealing.

	V_{OC} (V)	J_{SC} (mA/cm^2)	FF (%)	PCE (%)	PCE_{max} (%)
$CH_3NH_3PbI_3$	0.80±0.01	12.5±1.3	60.7±1.9	6.07±0.90	6.58
$CH_3NH_3Sn_{0.1}Pb_{0.9}I_3$	0.79±0.01	15.8±1.4	61.9±3.1	6.74±0.53	7.12
$CH_3NH_3Sn_{0.25}Pb_{0.75}I_3$	0.70±0.00	18.0±0.9	58.7±2.8	7.40±0.53	7.75

The device performance and the J-V curves of the thermal plus DMF vapor-assisted thermal annealed $CH_3NH_3Sn_xPb_{1-x}I_3$ (x = 0, 0.1, and 0.25) perovskite solar cells are shown in Table 7.2 and Figure 7.10. Compared to the only-thermal annealed perovskite solar cells,

the PCEs of the $CH_3NH_3Sn_xPb_{1-x}I_3$ (x = 0, 0.1) perovskite solar cells are increased by 8.2% and 10.5%, respectively, while the PCE of the $CH_3NH_3Sn_{0.25}Pb_{0.75}I_3$ solar cells is decreased by 12.4%. Although the grain size is increased slightly after the thermal plus DMF vapor-assisted thermal annealing, which increases J_{SC}, the still relatively rough surfaces may cause the reduction of FF. With the increase of Sn, more Sn^{4+} could be produced which degrades the device performance as observed for the devices made via the thermal plus DMSO vapor-assisted thermal annealing.

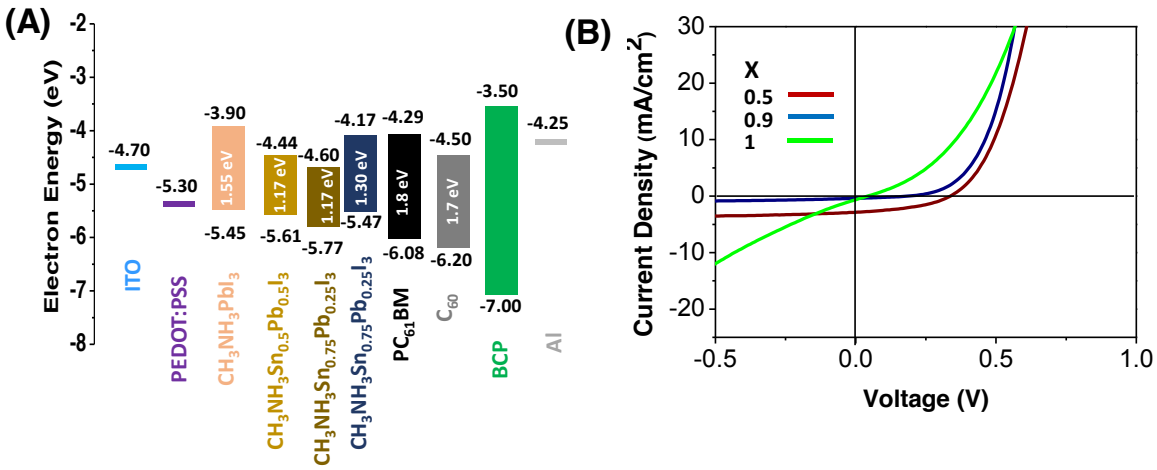

Figure 6.11 (A) Energy diagram for materials involved in the planar perovskite solar cells. (B) Typical J-V characteristics of $CH_3NH_3Sn_xPb_{1-x}I_3$ (x = 0.5, 0.9, and 1.0) perovskite solar cells under 1 sun AM 1.5G solar illumination. The perovskite layers were prepared via the only-thermal annealing.

Table 6.3 PV performance parameters of the $CH_3NH_3Sn_xPb_{1-x}I_3$ (x = 0.5, 0.9, and 1.0) perovskite solar cells under 1 sun AM 1.5G solar illumination. The $CH_3NH_3Sn_xPb_{1-x}I_3$ perovskite films were prepared via the only-thermal annealing process.

	V_{OC} (V)	J_{SC} (mA/cm^2)	FF (%)	PCE (%)	PCE_{max} (%)
$CH_3NH_3Sn_{0.5}Pb_{0.5}I_3$	0.41±0.04	3.1±0.7	57.5±8.5	0.72±0.36	0.76
$CH_3NH_3Sn_{0.9}Pb_{0.1}I_3$	0.17±0.03	1.2±0.4	39.3±1.7	0.08±0.22	0.09
$CH_3NH_3SnI_3$	0.04±0.01	1.8±0.5	25.7±0.9	0.02±0.00	0.02

We also fabricated planar heterojunction $CH_3NH_3Sn_xPb_{1-x}I_3$ perovskite solar cells with x = 0.5, 0.9, and 1.0. The binary Pb-Sn perovskite films were prepared via only-thermal annealing. The energy diagram of these Pb-Sn perovskites along with other materials in the devices and the J-V curves are shown in Figure 7.7A and B, respectively. The device performance parameters are summarized in Table 7.3. The $CH_3NH_3Sn_{0.5}Pb_{0.5}I_3$ perovskite solar cells show a J_{SC} of 3.1 mA/cm^2, V_{OC} of 0.41 V and FF of 57.5%, leading to a PCE of 0.76%. The $CH_3NH_3Sn_{0.9}Pb_{0.1}I_3$ and $CH_3NH_3SnI_3$ perovskite solar cells show almost no rectification behavior. The XRD patterns of these films are shown in Figure 7.12. The only-thermal annealed $CH_3NH_3Sn_{0.5}Pb_{0.5}I_3$ film remains in the pure perovskite phase. Additional peaks at 26.4°, and 32.2°, ascribed to the oxidized Sn^{4+} in the form of $(CH_3NH_3)_2SnI_6$,[245] appear in the XRD patterns of $CH_3NH_3Sn_{0.9}Pb_{0.1}I_3$ and $CH_3NH_3SnI_3$ perovskite films. Our XRD results are in concord with the previous report that the presence of more than 50% Pb in the perovskite is essential to retard the oxidation of Sn and to maintain the perovskite structure.[242] The significant drop of J_{SC} and $V_{OC,}$ as well as the eventual absence of rectification, were also observed in the binary Pb-Sn perovskite solar cells with the Sn content greater than 50%.[240] Apparently, it is crucial to rigorously reduce the water content in reagents and solvents and to control the environmental humidity and oxygen in order to make working perovskite solar cells with high Sn content.

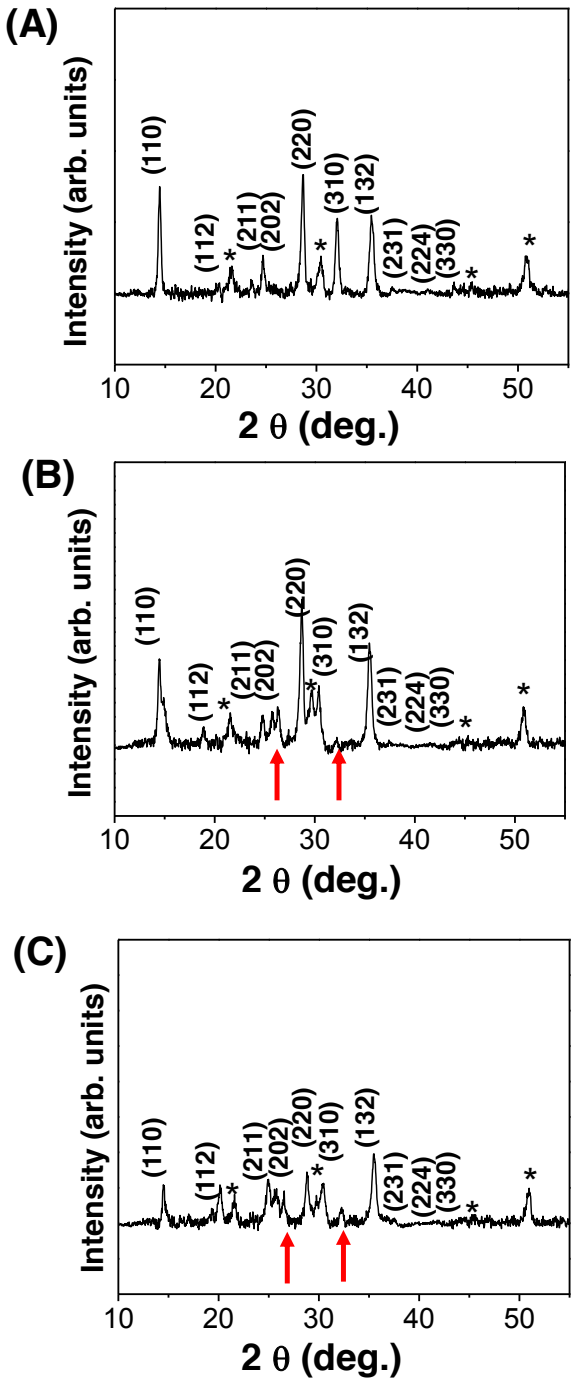

Figure 6.12 XRD patterns of the $CH_3NH_3Sn_{0.5}Pb_{0.5}I_3$ (A), $CH_3NH_3Sn_{0.75}Pb_{0.25}I_3$ (B), and $CH_3NH_3SnI_3$ (C) films prepared by the two-step solution-process followed by the only-thermal annealing. Additional peaks at 26.4° and 32.2° marked in red arrows are ascribed to the oxidized Sn^{4+} in the form of $(CH_3NH_3)_2SnI_6$ crystal.

6.4 Conclusion

In summary, we have demonstrated that the two-step solution process with the thermal plus solvent vapor-assisted thermal annealing is an effective method to make binary Pb-Sn triiodine perovskite polycrystalline films, to increase the grain size, and to manipulate the grain orientation, the surface termination, and the Pb and Sn distribution in grains. The Sn substitution in the $CH_3NH_3PbI_3$ perovskite resulted in the extension of absorption onset from 825 to 950 to 1010 nm for the $CH_3NH_3Sn_xPb_{1-x}I_3$ perovskites with x = 0, 0.1, and 0.25, respectively. Unlike organolead triiodine perovskite solar cells, the EQE of binary Pb-Sn triiodine perovskite solar cells was sensitive to the annealing processes. The highest PCE of 10.25% was achieved from the planar $CH_3NH_3Sn_{0.1}Pb_{0.9}I_3$ perovskite solar cell with the thermal plus DMSO vapor-assisted thermal annealing. Further enhanced performance of devices with a higher Sn content might be realized by rigorously reducing the exposure of water and oxygen during the device fabrication process. Because of the nature of an ionic crystal and the unique chemical structure of hybrid inorganic-organic perovskites, the solvent-assisted thermal annealing process could offer an easy yet effective way to manipulate material properties and to further increase perovskite solar cell performance.

Chapter 7 CONCLUSIONS AND OUTLOOK

7.1 Conclusions

This dissertation focuses on the development of next generation of organic-inorganic hybrid solar cells for the efficient sunlight harvest. The study starts from the basic inorganic material synthesis and property measurements to address the light absorption problem in solar cell research. During the fabrication of organic-inorganic hybrid solar cells, we realize the interfacial layer strongly affects the device performance. This problem was solved by adopting a dual HTL. In order to further improve the charge separation process of an organic-inorganic hybrid solar cells, a molecular level organic-inorganic hybrid system is developed.

Enhancing the light absorption is the first issue needs to be addressed in organic-inorganic hybrid solar cell research. We synthesized pyrite FeS_2 materials with high absorption coefficient and NIR absorption. In the pyrite FeS_2 synthesis, we are the first to synthesize pyrite hierarchical microparticles with well-defined {100} facetted cubic textures using a simple hydrothermal method with the presence of en and PVP. The roles of en and PVP on the phase and morphologies of the synthesized materials are clearly illustrated. The mechanisms discussed here may provide new insights to the synthesis of pyrite materials and help to better understand the formation of pyrite phase and the control of morphology.

By using a hot injection method, the size and morphology of the pyrite material are controlled down to the nanoscale. The morphology and phase purity of pyrite NCs were systematically studied. Two critical parameters were identified in the synthesis of phase pure pyrite materials, i.e. the molar ratio of iron to sulfur and the reaction temperature. The synthesized pyrite NCs have the absorption up to the NIR region and exhibit a larger indirect bandgap than that of bulk pyrite. Further study indicates the pyrite seeds generate from a mackinawite $FeS_{0.94}$ nanosheets template. The initial anisotropic growth of NCs follows OA mechanism. OR growth become obvious as time progress, resulting in faceted NCs. In accordance with the analysis of HRTEM images and surface free energies, we find that the attachment occurs between the opposite facets with high surface free energies including (210)-Fe and (210)-2S as well as (001)-Fe and (001)-2S. The phase and

morphology-controlled pyrite NCs make it possible to further study the optical and electronic properties of pyrite NCs and to develop pyrite NC based PV devices for sustainable energy. I collaborated with my labmate Beau J. Richardson and developed an inverted hybrid polymer solar cell with TOPO passivated pyrite NCs.[31] The inverted ternary hybrid solar cells show enhanced photocurrent and great stability with air exposure up to 28 days. The study presents pyrite NC as a low-cost, earth abundant, and non-toxic material for solar energy conversion.

During the fabrication of inverted organic-inorganic hybrid solar cells based on pyrite FeS_2 materials, we find the effective hole extraction at the active layer/anode interface as well as the prevention of leakage current are crucial for the solar cells with enhanced performance. By adopting the inverted structure and using the dual HTLs, the resistive losses of CdSe QDs:P3HT hybrid system at high illumination power are effectively prevented. Inverted CdSe QDs:P3HT OIHSCs with the PEDOT:PSS/MoO_3 dual HTLs show superior performance over those with a single HTL of PEDOT:PSS or MoO_3. The dual HTLs is applicable to the solar cells with CdSe QDs and NRs blended with PTB7-F20. An efficiency as high as 2.35% was achieved in OIHSCs with a structure of ITO/ZnO/CdSe QDs + NRs:PTB7-F20/ PEDOT:PSS/MoO_3/Ag.

The incomparable size of polymer and inorganic semiconductor leads to the insufficient interfacial area. This affects the charge separation and impedes the further performance improvement of hybrid organic-inorganic solar cells. Molecular level organic-inorganic hybrid $CH_3NH_3Sn_xPb_{1-x}I_3$ perovskites were used to fabricate solar cells. The Sn substitution in the $CH_3NH_3PbI_3$ perovskite resulted in the extension of absorption onset from 825 up to 1060 nm for the $CH_3NH_3Sn_{0.25}Pb_{0.75}I_3$ perovskite. The highest PCE of 10.25% was achieved from a planar $CH_3NH_3Sn_{0.1}Pb_{0.9}I_3$ perovskite solar cell with the thermal plus DMSO vapor-assisted thermal annealing.

7.2 Outlook

Organic-inorganic hybrid solar cells would still be the main topic for the researchers in PVs. The current studies present many interesting and exciting findings. There are still a lot of areas to explore.

Pyrite FeS_2 is an attractive materials for PV application. The future direction would be the control of shape and size uniformity of the synthesized materials. The current study indicates the growth of pyrite FeS_2 NCs follows OA mechanism at the early stage of growth. The exploration of new growth mechanisms would be crucial for the synthesis of uniform NCs. Studies based on DFT will be helpful to understand the growth of materials from theoretical aspects. In order to screen the best conditions for the synthesis, the new theoretical study should focus on the solvents, ligands, and temperature on the growth of pyrite FeS_2 NCs. The current study provides a way to passivate the pyrite FeS_2 NCs' surface using TOPO. There is little information of the crystalline information within the NCs. The removal of the defects within NCs by choosing advanced synthetic methods would further improve the performance of solar cells with pyrite FeS_2 NCs.

The dual HTLs is effective to improve the performance of the inverted organic-inorganic hybrid solar cells with the rough active layer. There are many parameters not optimized, such as the thickness of each HTL layer and choices of other combinations of HTLs. Besides the two systems discussed in this study, the application of dual HTLs to other inverted organic-inorganic hybrid solar cells would also be interesting.

Although organic-inorganic hybrid $CH_3NH_3Sn_xPb_{1-x}I_3$ perovskite solar cells were developed, the controlled $CH_3NH_3PbI_3$ perovskite solar cells with thermal annealing only show the efficiency as high as 5.61±0.43%. The improvement in the processing procedures or the choice of the materials with higher purity would further increase the efficiency of the fabricated control device. The oxidation of Sn in organic-inorganic hybrid $CH_3NH_3Sn_xPb_{1-x}I_3$ perovskite solar cells is still not fully prevented. Using reductive additives would be an effective way to address this problem.

A vertically aligned bilayer perovskite solar cell architecture with the objective to efficiently harvest sunlight up to the NIR region will be the future direction of research. The cell is composed by a first layer of pristine $CH_3NH_3PbI_3$ and a second layer of $CH_3NH_3Sn_{1-x}Pb_xI_3$ ($x\neq1$). In such a bilayer perovskite solar cell, high energy photons (>1.55 eV) are absorbed in $CH_3NH_3PbI_3$. Low energy photons (<1.55 eV) are allowed to pass through and absorbed in the $CH_3NH_3Sn_{1-x}Pb_xI_3$ layer with bandgaps < 1.55 eV. The generated electrons both in $CH_3NH_3PbI_3$ and $CH_3NH_3Sn_{1-x}Pb_xI_3$ flow through ETL and are collected by Al electrode. The holes transport through PEDOT:PSS layer and are

collected by ITO. By adopting a bilayer structure, the perovskite bilayer, with the ability to harvest the sunlight in the NIR region, maintains a high EQE from 400 nm to 650 nm. Thereby, a higher photocurrent is expected and less energy lost as heat.

Appendix A SOLVOTHERMAL SYNTHESIS AND CHARACTERIZATION OF IRON SULFIDE MATERIALS

A.1 Introduction

The best structure for an organic-inorganic solar cell is with vertically aligned one-dimensional inorganic nanostructures connected to the cathode. The long axis of the NRs provide continuous pathways for the electron transport, which is superior to QDs, where electron hopping between QDs is required.[3] In that case, generated electrons are effectively transported to the cathode with minimal recombination. Thus the synthesis of one-dimensional semiconductor is of great interest. Different from the hydrothermal method mentioned in Chapter 2, the usage of solvent other than water is more compatible for high temperature synthesis. The solvent also provides additional functions such as binding and coordination. Our synthesis of one-dimensional pyrite FeS_2 is based on the theoretical study conducted by Russo S.P. et al.[136, 137]: the preferential binding of en on {111} facet will promote the growth along <100> direction.

In the past decade, anisotropic semiconductor nanomaterials such as CdTe NRs,[257, 258] CdSe NRs,[3, 259] and CdSe tetrapods[190, 260] were synthesized and frequently used as an electron acceptor to form donor-acceptor type hybrid organic-inorganic solar cells. Power conversion efficiency as high as 3.64% is achieved by using a blend of CdSe QDs and NRs as the acceptor and poly (3-hexylthiophene) (P3HT) as the donor in a hybrid solar cell.[194] However, the use of toxic elements such as cadmium, selenium raises serious environmental concerns and is considered as a limitation for the mass production of these materials.[88,119] Recently, a low cost, non-toxic, and abundant semiconductor pyrite was proposed to use as the electron acceptor in organic-inorganic hybrid solar cells[33]. Pyrite is a material with an indirect energy transition at 0.95 eV, a direct transition at 1.03 eV, and an integrated absorption coefficient of 3.3×10^5 cm^{-1} for the energy spectrum of wavelength values (λ) between 300 and 750 nm.[125] Because of the high absorption coefficient from visible to near-infrared region, material consumption of pyrite is significantly reduced for solar cell applications.[261]

Originally, pyrite was prepared using several high temperature approaches including sulfurization of iron films,[72] sulfurization of iron oxide films,[73] reactive sputtering,[74] and

spray pyrolysis,[262] yet at elevated temperatures, the segregation of iron and sulfur species is unavoidable, which changes the stoichiometry and material phase of the deposited film. Thus, solution based hot injection methods[76-78] and hydro/solvothermal process were developed to synthesize pyrite materials with morphologies such as nanocubes,[77, 80] NRs,[128] and nanowires.[128] Hydro/solvothermal process is preferred over hot injection methods due to the ease of scale up production. Generally, pyrite particles with the size ranging from 100 nm to several micrometers were synthesized by hydro/solvothermal process.[67, 80-83] Cubic pyrite particles with the size ranging from 150 to 500 nm were obtained by thermally decomposing a single iron-sulfur complex via a hydrothermal process.[125, 126] Pyrite cubes with the {100} facets and octahedrons with the {111} facets were synthesized by using surfactants and controlling the pH value of the reaction solutions.[127, 128] Recently, it was also demonstrated that monodispersed pyrite microspherolites can be obtained via a microwave-assisted hydrothermal process in the presence of PVP.[124] Despite the recent advancement of hydro/solvothermal routes to the synthesis of pyrite FeS_2 materials, the synthesis of phase pure pyrite nanowires still remains as a challenge. Although the successful synthesis of one-dimensional nanostructures of pyrite FeS_2 in large quantities by solvothermal process was claimed by Chaudhuri S. et al.,[82, 263, 264] the results were not reliable since they didn't show the composition and crystallinity of the individual nanowires. The characterization of the phase purity only limited to techniques such as XRD and large area EDS, which cannot detect the amorphous impurities in the products. Contradictory to their results, magnetic iron sulfide nanowires with the form of $Fe_{1-x}S$ (x=0.08-0.1) were obtained and no pyrite phase was detected by using a similar solvothermal procedures, in which thioacetamide (CH_3CSNH_2) was used as the sulfur source and $FeCl_2$ was used as the iron source.[265] The experiments were carried out at 180°C with a Fe:S ratio of 1:2.

In this chapter, the synthesis of iron sulfide materials was performed under the same conditions as literature.[125] Only amorphous iron sulfide nanowires was obtained by using $Fe(NO_3)_3 \cdot 9H_2O$, $FeCl_3 \cdot 6H_2O$ and $FeCl_2 \cdot 4H_2O$ as the iron source. Thiourea and en were used as the sulfur source and solvent, respectively. The morphology of the synthesized materials was characterized by SEM and TEM. Concentration of the reactants, S:Fe ratio, types of iron source as well as reaction temperature control the morphology of the

synthesized products. The composition of nanowires, NRs, and plates was analyzed by EDS. XPS was used to determine the composition and chemical state of sulfur in the synthesized nanowires. The major products obtained were determined to be $Fe_{1-x}S$ (X=0.11-0.35). These nanowires were further annealed at 700°C for 30 min in order to obtain crystalline products. A possible route to obtain phase pure pyrite nanowires is proposed.

A.2 Experimental Section

A.2.1 Materials for the Synthesis of Iron Sulfide Materials

En (≥99.5%) was obtained from Fluka. $Fe(NO_3)_3 \cdot 9H_2O$ (≥99.999%), $FeCl_2 \cdot 4H_2O$ (99.99%), $FeSO_4 \cdot 7H_2O$ (≥99 %), and thiourea (≥99.0%) were purchased from Sigma-Aldrich. $FeCl_3 \cdot 6H_2O$ (ACS, 97.0-102.0%) was obtained from Alfa Aesar. Millipore water was self-made using a Millipore Simplicity Ultrapure Water System. All chemicals were used as received without further purification.

A.2.2 Solvothermal Synthesis of Iron Sulfide Materials

Table 7.1 Summary of the reaction conditions and morphology of the major products.

Product No.	Fe source	Fe:S (mol:mol)	Temperature (°C)	Concentration (mol/l of Fe source)	Morphology of major product
1	$Fe(NO_3)_3 \cdot 9H_2O$	1:4	180	0.005	nanowires, macrowires
2	$Fe(NO_3)_3 \cdot 9H_2O$	1:4	180	0.03	nanorods
3	$Fe(NO_3)_3 \cdot 9H_2O$	1:4	180	0.04	nanorods
4	$Fe(NO_3)_3 \cdot 9H_2O$	1:4	180	0.08	thin nanorods
5	$Fe(NO_3)_3 \cdot 9H_2O$	1:4	195	0.005	nanowires, macrowires, microplates
6	$Fe(NO_3)_3 \cdot 9H_2O$	1:4	210	0.005	microplates
7	$Fe(NO_3)_3 \cdot 9H_2O$	1:6	180	0.005	nanowires
8	$FeCl_3 \cdot 6H_2O$	1:4	180	0.08	plates
9	$FeCl_2 \cdot 4H_2O$	1:4	180	0.08	plates, wires

All synthesis conditions are listed in Table 3.1. Typically, the synthesis of sample-1 was performed as follows: 0.0297 g of $Fe(NO_3)_3 \cdot 9H_2O$ was mixed with 0.0056 g of thiourea in a mortar (molar ratio: Fe:S=1:4), to which 14.7 ml of en was added. The mixture was stirred vigorously with pestle. After the color of the mixture turned to brown, the mixture was transferred to a teflon-lined stainless steel autoclave with 85% filled. The autoclave was placed in a muffle oven and maintained at 180°C for 12 h. After that, the autoclave was taken out of the oven and cooled to room temperature naturally. The black precipitates were collected and washed with ethanol, followed by centrifugation at 4400 rpm for 18 min. Then, precipitates were re-dispersed in ethanol followed by centrifugation. Re-dispersion and centrifugation were repeated for three times in order to remove any residues and side products.

A.2.3 Characterizations of Iron Sulfide Materials

The morphology and elemental composition of the products were characterized using SEM and EDS (FEI Sirion SEM), respectively. SEM samples were prepared by dropping the particle solution on a silicon chip and being dried in air. TEM and scanning transmission electron microscopy (STEM) images were acquired using FEI Tecnai G2 F20 TEM operating at an accelerating voltage of 200 kV. Spot size 9 was applied for STEM measurement and a high angle annular dark field (HAADF) detector was used to collect images. The samples for TEM/STEM analysis were prepared by drop casting a dilute solution of materials in ethanol onto ultrathin carbon-coated copper grids. XRD measurement was carried out on a GADDS D8 Discover diffractometer (Bruker) using Cu Kα radiation (λ = 1.5419 Å). Three frames with 100 seconds/frame were obtained for each sample. Scan angle 2θ begins at 30 degrees with a frame width of 25 degrees. Data were processed using the EVA package provided by Bruker Axs. Samples for XRD measurements were prepared by dusting the vacuum dried samples on a double-sided tape attached to a glass slide. XPS composition data and high-resolution spectra were acquired on a Kratos AXIS Ultra DLD instrument equipped with a monochromatic Al Kα X-ray source. Binding energies (BEs) were referenced to the hydrocarbon C_{1s} peak at 285 eV. XPS samples were prepared by placing the vacuum dried samples on carbon conductive tape on the sample holder. Data analyses were performed with CasaXPS. TGA of samples was performed with a SDT 2960 Simultaneous DSC-TGA analyzer of TA instruments from 30 to 700°C with a temperature ramp of 40°C/min.

A.3 Results and Discussion

A.3.1 Concentration, S:Fe Ratio, and Iron Source on the Morphology of Iron Sulfide Materials

Wires with the length from 500 nm to 100 μm and diameter in the range of 100-200 nm (Figure 3.1) were synthesized by reacting $Fe(NO_3)_3 \cdot 9H_2O$ with thiourea at 180°C for 12 h in en. When the concentration of $Fe(NO_3)_3 \cdot 9H_2O$ was increased from 0.005 mol/l to 0.03 mol/l, the length of wires decreased to 3-6 μm and the diameter of wires increased to 200-500 nm. There is no obvious change in the morphology of the synthesized products using 0.04 mol/l $Fe(NO_3)_3 \cdot 9H_2O$ compared to those using 0.03 mol/l of $Fe(NO_3)_3 \cdot 9H_2O$.

Further increase of $Fe(NO_3)_3 \cdot 9H_2O$ concentration to 0.08 mol/l results in 50-100 nm thick NRs with the length of 3-6 μm and width of 200-500 nm. Based on these observations, high concentration of reactants leads to shorter and fatter structure. This could be explained by nucleation and growth[266, 267] of the materials. When the concentration of the reactants is increased, the number of nucleus generated in the reaction is also increased. Initially, there will be more NRs generated in the solution than that using lower concentration of reactants. The growth of NRs in the long axis is more like to be interrupted by the adjacent NRs due to an increase in the NRs concentration. Thus, short rods were the main product instead of nanowires by using a high concentration of reactants.

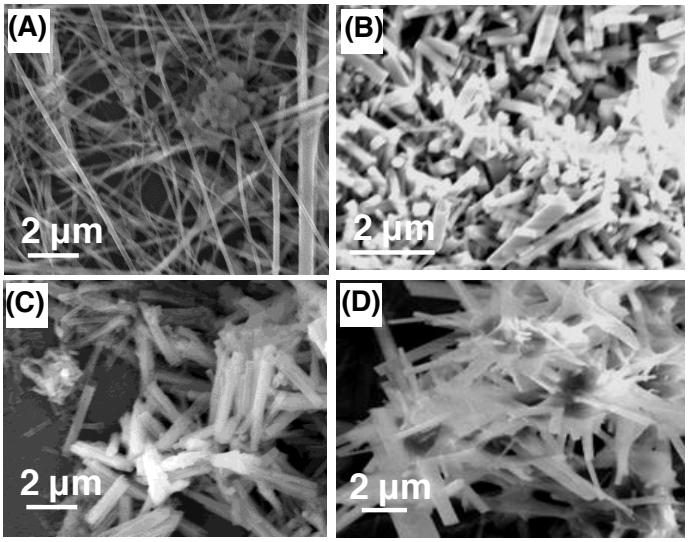

Figure 7.1 The SEM images of iron sulfide materials synthesized by reacting $Fe(NO_3)_3 \cdot 9H_2O$ with thiourea at 180°C for 12 h in en. The concentration of $Fe(NO_3)_3 \cdot 9H_2O$ in the reactor is (A) 0.005 mol/l, (B) 0.03 mol/l, (C) 0.04 mol/l, and (D) 0.08 mol/l. Fe:S ratio was kept as 1:4.

Fe:S ratio of the reactants determines the ratio of plates to wires in the final products. As can be seen from Figure 3.2, plates exist in the product synthesized with a Fe:S ratio of 1:4. Almost all the products synthesized using 1:6 molar ratio of Fe:S are wires. No obvious change in the morphology of products was observed when Fe:S ratio was further raised to 1:8. Thus, with a higher S:Fe ratio in reactants, more nanowires will be generated in the final products. The synthesized wires tend to assemble to form bundles after drying at room

temperature (Figure 3.2C). This indicates the synthesized wires could be used as a template to fabricate nanostructured devices.

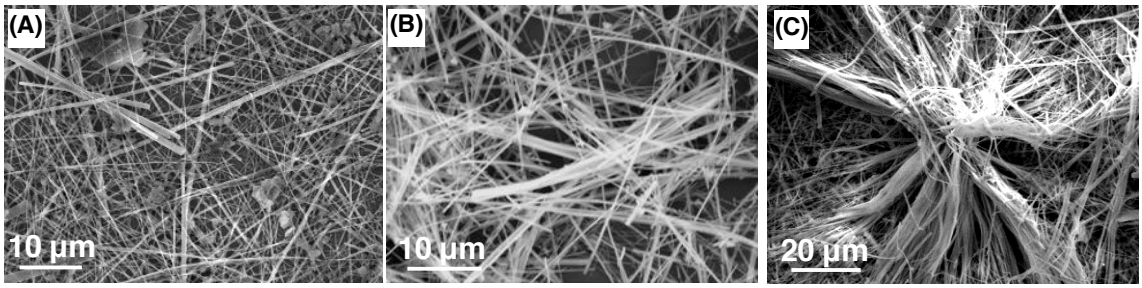

Figure 7.2 The SEM images of iron sulfide materials synthesized by reacting $Fe(NO_3)_3 \cdot 9H_2O$ with thiourea at 180°C for 12 h in en. The concentration of $Fe(NO_3)_3 \cdot 9H_2O$ in the reactor was kept as 0.005 mol/l. Fe:S ratio was (A) 1:4 and (B) 1:6, respectively. (C) Bundles were formed after drying sample-7 at room temperature.

The valence state of the iron and counter-ion play an important role in determining the morphology and phase of the final products. Generally, the products synthesized by using Fe source with chlorine contain more plates than those synthesized using $Fe(NO_3)_3 \cdot 9H_2O$. As can be seen from Figure 3.3A, only plates along with a few nanowires were observed under SEM when $FeCl_3 \cdot 6H_2O$ was used as the iron source. Compared to those using $FeCl_3 \cdot 6H_2O$, the products synthesized using $FeCl_2 \cdot 4H_2O$ contain more wires than those using $FeCl_3 \cdot 6H_2O$ as the iron source (Figure 3.3B). The generation of plates by using $FeCl_3 \cdot 6H_2O$ as the iron source instead of wires may be explained by the weak binding of Cl^- to the sidewalls of generated NR seeds compared to NO_3^-. Materials prone to grow into 2D structure with $FeCl_3 \cdot 6H_2O$ or $FeCl_2 \cdot 4H_2O$ as the iron source. Thus, 2D plates instead of 1D wires were obtained. From the SEM images with higher magnification, these wires and plates were observed to be in a layered structure (Figure 3.3C, D). EDS is employed to determine the composition of the synthesized materials. The Fe:S atomic ratio of the spots shown in Figure 3.4 is found to be 1:1.36, 1:1.53, and 1:1.12 for nanowires, NRs, and plates. Thus, the synthesized iron sulfide materials are $Fe_{1-x}S$ (X=0.11-0.35), regardless of the different morphologies observed.

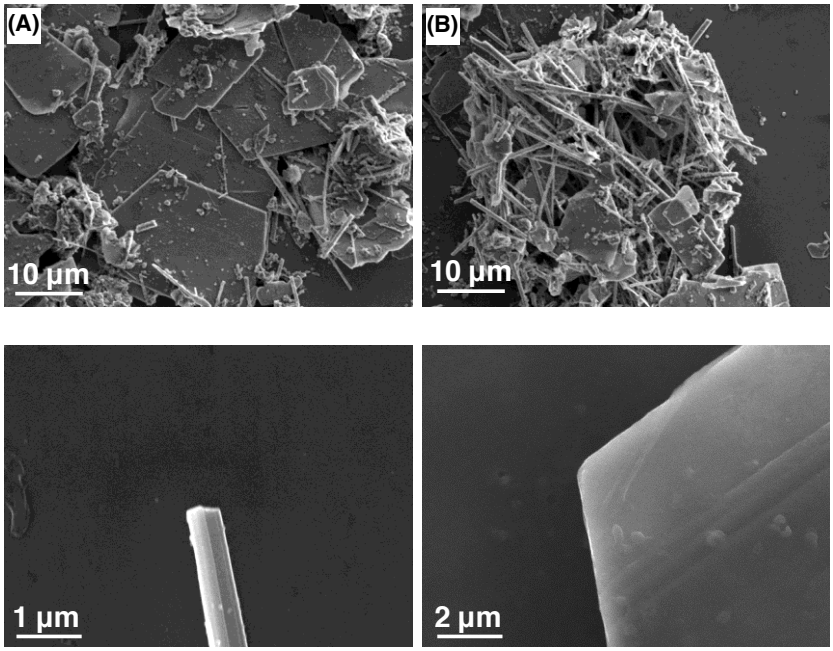

Figure 7.3 The SEM images of iron sulfide materials synthesized by reacting (A) $FeCl_3 \cdot 6H_2O$ or (B) $FeCl_2 \cdot 4H_2O$ with thiourea at 180°C for 12 h in en. The concentration of $FeCl_3 \cdot 6H_2O$ or $FeCl_2 \cdot 4H_2O$ in the reactor was kept as 0.005 mol/l. Fe:S ratio was 1:4. (C) and (D) are the typical SEM images for wire and plates. A layered structure was observed for both morphologies.

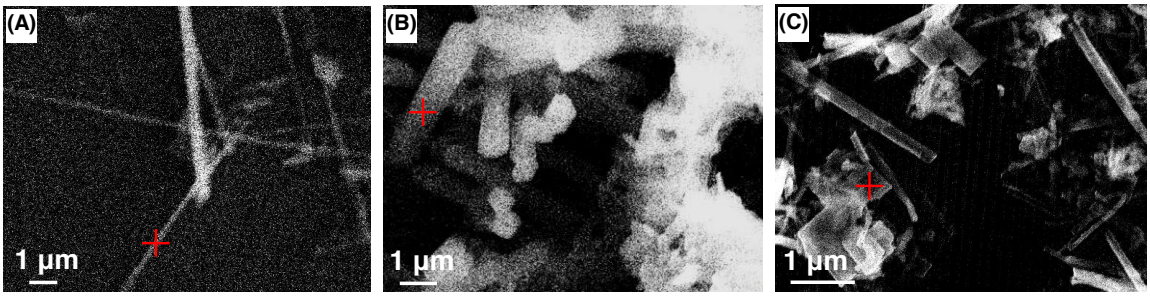

Figure 7.4 The SEM images of synthesized (A) wires, (B) rods and (C) plates. The red crosses indicate the spots where the EDS were performed. The Fe:S atomic ratio of the spot shown in figures is found to be 1:1.36, 1:1.53, and 1:1.12 for nanowires, NRs and plates.

A.3.2 Reaction Temperature on the Morphology of Iron Sulfide Materials

Temperature is an important factor in controlling the morphology of synthesized iron sulfur materials in the solvothermal synthesis. The products were mainly wires when the

reaction was performed at 180°C (Figure 3.5A). When the reaction was raised to 195°C, a mixture of microplates and wires was observed (Figure 3.5B). Microplates were the major product by reacting at 210°C (Figure 3.5C) for 12 h. At higher temperature, materials tend to grow into 2D structure instead of 1D wires. This may be due to 2D plates is a more thermodynamically stable form at higher temperature than 1D wires obtained at lower temperature.

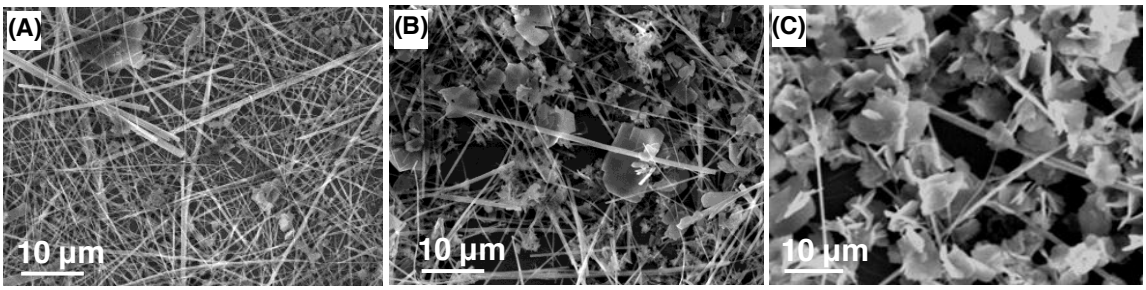

Figure 7.5 The SEM images of iron sulfide materials synthesized by reacting $Fe(NO_3)_3 \cdot 9H_2O$ with thiourea at (A) 180°C, (B) 195°C, and (C) 210°C for 12 h in en. The concentration of $Fe(NO_3)_3 \cdot 9H_2O$ in the reactor was kept as 0.005 mol/l. Fe:S ratio was 1:4.

A.3.3 Composition of Iron Sulfide Materials

XPS was also used to analyze the composition of synthesized materials. The synthesized materials mainly contain Fe, O, N, C, and S (Figure 3.6A). The Fe:S atomic ratio of sample-3 is determined to be 1:0.88 by using the area ratio of Fe_{2s} and S_{2p} peaks. There are four species of sulfur in sample-3 (Figure 3.6B). The composition of those four different sulfurs is: 53.9% (S^{2-} at 161.4 eV), 17.3% (S_n^{2-} at 164.3 eV), 24.9% ($S_2O_3^{2-}$ at 167.0 eV), and 3.9% (SO_4^{2-} at 168.4 eV). The oxidized sulfur $S_2O_3^{2-}$ and SO_4^{2-} may be introduced during the sample preparation for the XPS measurements. The major sulfur in the synthesized materials is in the form of S^{2-}. That means the chemical formular of the synthesized samples may be $Fe_{1-x}S$ or FeS_{1-x}. Combined with the EDS results, it is safe to conclude that the synthesized sample-3 is $Fe_{1-x}S$ (X=0.11-0.35). In contrast, the naturally occurring pyrite contains Fe, O, C, and S. C and O may come from the absorbed CO_2 and O_2 on the surface. The S_{2p} peak is fitted with four peaks which are at 161.4 eV (S^{2-}), 162.4 eV (S_2^{2-}), 164.3 eV (S_n^{2-}), and 168.4 eV (SO_4^{2-}), respectively. The composition is calculated to be 3.0% (S^{2-}), 43.6% (S_2^{2-}), 13.6% (S_n^{2-}), and 6.5% (SO_4^{2-}). Most of the sulfur is in the

form of S_2^{2-}. It also contains oxidized sulfur in the form of SO_4^{2-}. S^{2-} may come from cleaved surface which is commonly observed in naturally occurring pyrite. Fe:S atomic ratio of the naturally occurring pyrite is 1:0.64. The Fe:S (1:0.64) atomic ratio determined from XPS is smaller than the actual ratio in pyrite if we consider pyrite is in a form of FeS_2. This may be explained by the different ability for the electrons in Fe_{2p} and S_{2p} to escape from the surface. Electrons at 2p orbital of iron escape from the surface of the sample more easily than electrons at 2p orbital of iron due to the weak electrostatic force between electrons at 2p orbital and the nucleus of Fe. Thus, more electrons at 2p orbital of iron were collected by the detector than those at 2p orbital of sulfur, which results in larger area of Fe_{2p} than that of S_{2p}.

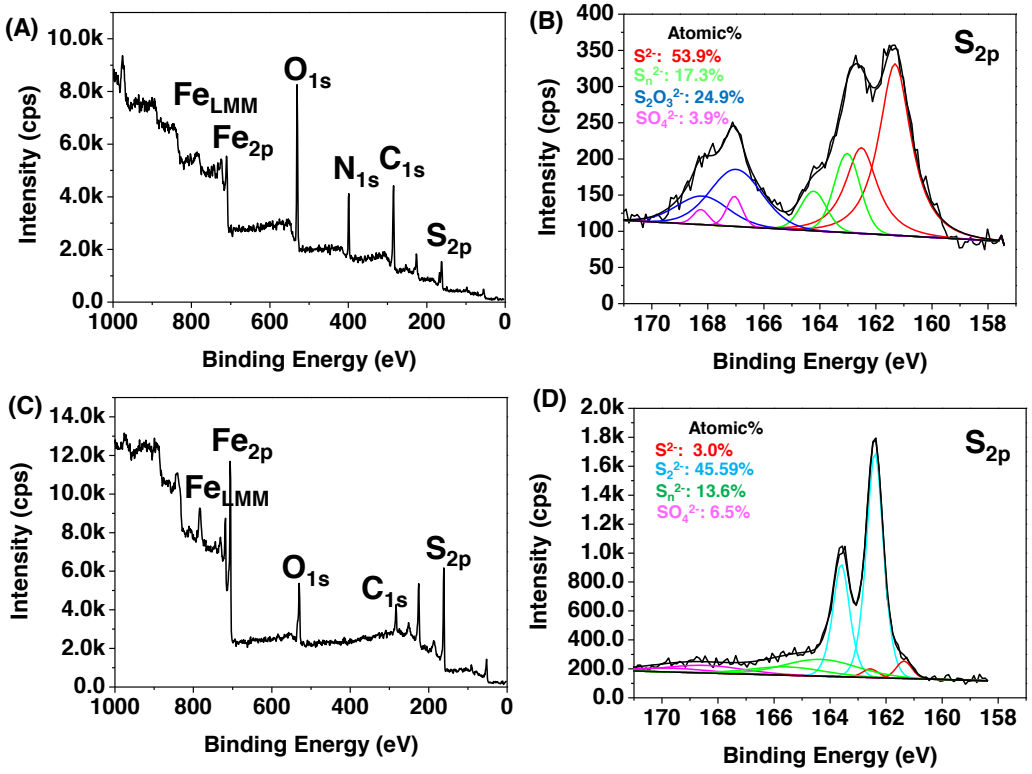

Figure 7.6 (A) Survey scan and (B) XPS S_{2p} spectrum of sample-3 synthesized by reacting $Fe(NO_3)_3 \cdot 9H_2O$ with thiourea at 180°C for 12 h in en. The concentration of $Fe(NO_3)_3 \cdot 9H_2O$ in the reactor is 0.04 mol/l and Fe:S ratio was kept as 1:4. (C) Survey scan and (D) XPS S_{2p} spectrum of a naturally occurring pyrite sample.

All these synthesized samples do not show any XRD peaks from 15 to 80 degree. To understand the structure of these materials, TEM experiments were performed and representative TEM images of nanowires, NRs and plates were displayed in Figure 3.7. There are a lot of defects such as dent and holes in the synthesized nanowires and NRs (Figure 3.7A, B). Plates were composed of four 3-4 μm plates and assembled in a certain angle (Figure 3.7C). Higher magnification TEM images were also taken. However, bubbles as indicated by the white arrows generated when we tried to focus the electron beam on the samples (Figure 3.7D, E). There was no crystalline phase observed when the magnification of TEM was further increased (Figure 3.7F). STEM was used to study the geometry of the nanowires. Sharp edges were observed in these wires (Figure 3.8A). Some of the wires have core-shell structure as revealed by the different contrast in the STEM image (Figure 3.8B). Since no XRD peaks were identified and no crystalline phase was observed under TEM. We infer the synthesized materials are mainly amorphous.

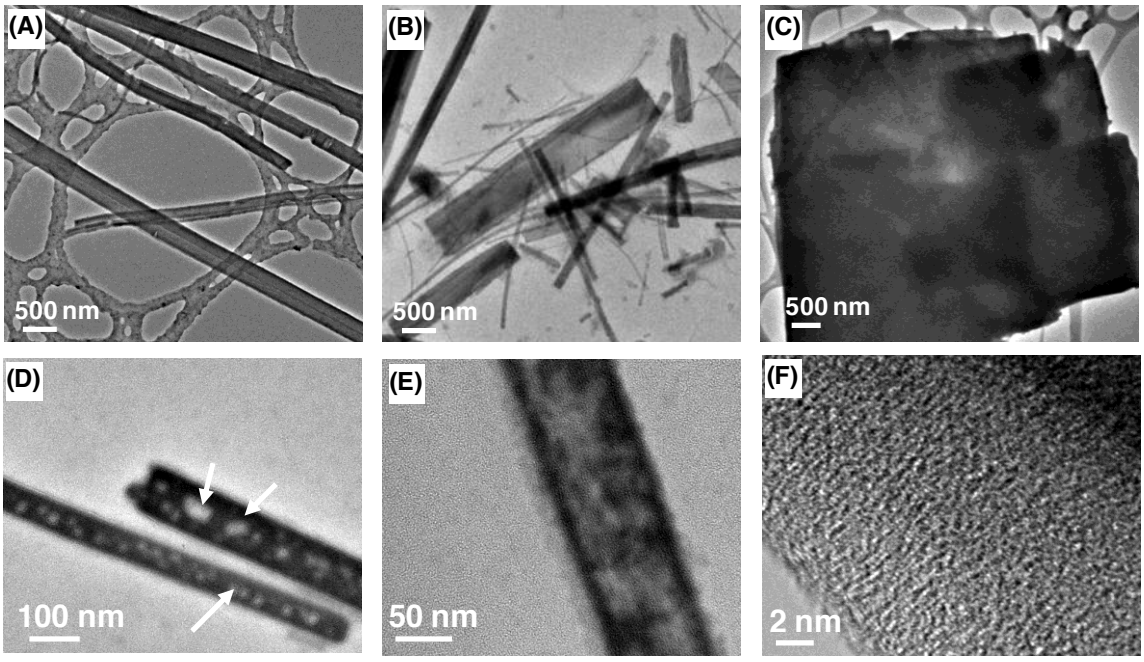

Figure 7.7 The TEM images of synthesized iron sulfide (A) wires, (B) rods and (C) plates.(D) Bubbles indicated by white arrows were generated when the electron beam is focused on the sample. (E) Voids were clearly observed in the samples heated with electron beams. (F) A HRTEM image shows the synthesized wires were amorphous.

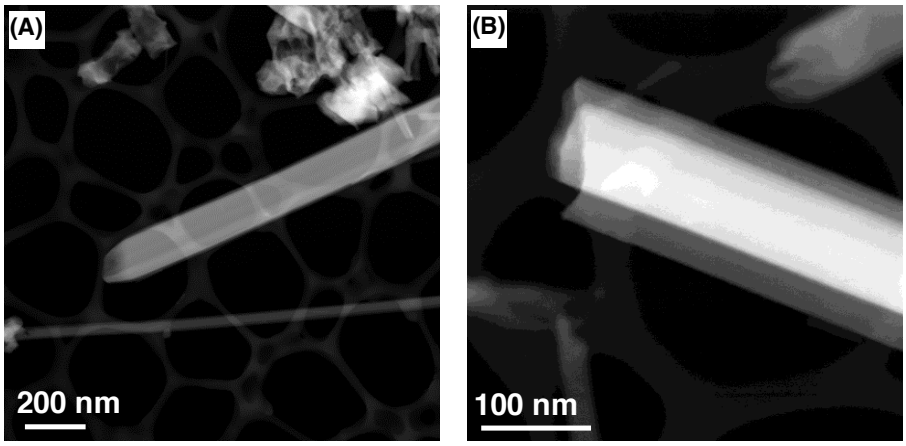

Figure 7.8 The STEM images of synthesized iron sulfide (A) wires with square cross section and (B) core-shell wires.

Because the substances in the nanowires and plates were easily evaporated by the heat generated from electron beam, we annealed the sample-3 and sample-8 at 700°C for 30 min under the protection of nitrogen. The annealed samples were studied by using SEM and XRD. As can be seen in Figure 3.9A, the surface of wires becomes very rough. Facets of crystals could be clearly observed. There are many holes present in the wire which is generated by losing volatile materials during annealing. Plate decomposes to connected microparticles with voids in it (Figure 3.9B). XRD results show the phase of both annealed samples is pyrrhotite $Fe_{0.96}S$ (Figure 3.9C). To understand the decomposition process of sample-3 and sample-8, TGA from 30-700°C with a ramp temperature of 40.00°C/min was performed. The results were shown in Figure 3.9D. The weight loss before 120°C is ascribed to the loss of water during sample preparation. Both of the samples start to dramatically lose weight at around 190°C until reach the temperature of 380°C. Only 5.5% and 4.97 % weight loss were observed from 380°C to 700°C for sample-3 and sample-8, respectively. Sample-3 and sample-8 lost 43.6 % and 36.52 % of their weight before 380°C. Unlike sample-3 and sample-8, the naturally occurring pyrite began to lose weight at 380°C. Only 24.2% weight was lost when the temperature was raised to 700°C. Although the synthesized materials are not pyrite, further transition from the pyrrhotite $Fe_{0.96}S$ to pyrite FeS_2 can be realized by the sulfurization of the existing samples according to the phase diagram of iron sulfide materials.[268]

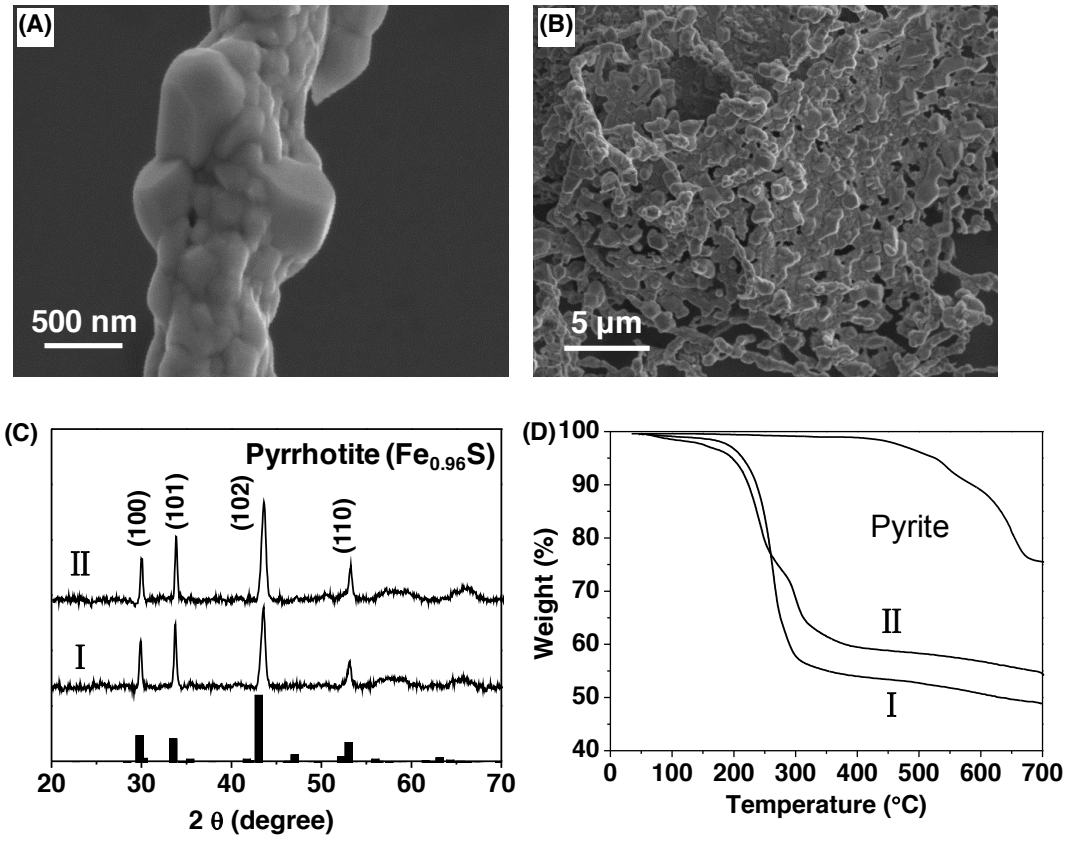

Figure 7.9 The SEM images of iron sulfide (A) wires and (B) plates annealed at 700°C for 30 min under the protection of nitrogen. (C) The XRD and (D) TGA results of sample-3(I) and sample-8 (II). TGA result of a naturally occurring pyrite sample was used as a contrast.

A.4 Conclusions

We synthesized iron sulfide nanowires through solvothermal method in an autoclave. Concentration of the reactants, S:Fe ratio, types of iron source as well as reaction temperature play an important role in controlling the morphology of the synthesized products. The synthesized materials were determined by XRD, TEM, and EDS to be amorphous $Fe_{1-x}S$ (X=0.11-0.35). The Fe:S atomic ratios are 1:1.36, 1:1.53, and 1:1.12 for nanowires, NRs, and plates, respectively. XPS results indicate the major form of sulfur in the synthesized product is S^{2-}. Our results are contradictory to a report[82] that one-dimensional nanostructures synthesized by solvothermal process are pyrite FeS_2. These amouphous iron sulfide materials were crystalized into pyrrhotite $Fe_{0.96}S$ by annealing at

700°C for 30 min. A transition of the annealed samples from the pyrrhotite $Fe_{0.96}S$ to pyrite FeS_2 through sulfurization could be a way to obtain pyrite FeS_2 nanowires.

References

1. M. He, D. Zheng, M. Wang, C. Lin and Z. Lin, *Journal of Materials Chemistry A*, 2014, **2**, 5994-6003.
2. A. Shah, P. Torres, R. Tscharner, N. Wyrsch and H. Keppner, *Science*, 1999, **285**, 692-698.
3. W. U. Huynh, J. J. Dittmer and A. P. Alivisatos, *Science*, 2002, **295**, 2425-2427.
4. G. Li, V. Shrotriya, J. S. Huang, Y. Yao, T. Moriarty, K. Emery and Y. Yang, *Nature Materials*, 2005, **4**, 864-868.
5. A. Hagfeldt, G. Boschloo, L. Sun, L. Kloo and H. Pettersson, *Chemical Reviews*, 2010, **110**, 6595-6663.
6. M. He, F. Qiu and Z. Lin, *The Journal of Physical Chemistry Letters*, 2013, **4**, 1788-1796.
7. C. J. Brabec and J. R. Durrant, *MRS Bulletin*, 2008, **33**, 670-675.
8. J. Zhao, A. Wang, M. A. Green and F. Ferrazza, *Applied Physics Letters*, 1998, **73**, 1991-1993.
9. A. Yella, H.-W. Lee, H. N. Tsao, C. Yi, A. K. Chandiran, M. K. Nazeeruddin, E. W.-G. Diau, C.-Y. Yeh, S. M. Zakeeruddin and M. Grätzel, *Science*, 2011, **334**, 629-634.
10. A. Ennaoui, S. Fiechter, C. Pettenkofer, N. Alonsovante, K. Buker, M. Bronold, C. Hopfner and H. Tributsch, *Solar Energy Materials and Solar Cells*, 1993, **29**, 289-370.
11. B. Bob, B. Lei, C. H. Chung, W. Yang, W. C. Hsu, H. S. Duan, W. W. J. Hou, S. H. Li and Y. Yang, *Advanced Energy Materials*, 2012, **2**, 504-522.
12. M. G. Panthani, V. Akhavan, B. Goodfellow, J. P. Schmidtke, L. Dunn, A. Dodabalapur, P. F. Barbara and B. A. Korgel, *Journal of the American Chemical Society*, 2008, **130**, 16770-16777.
13. P. Jackson, D. Hariskos, E. Lotter, S. Paetel, R. Wuerz, R. Menner, W. Wischmann and M. Powalla, *Progress in Photovoltaics: Research and Applications*, 2011, **19**, 894-897.
14. Q. Guo, G. M. Ford, W.-C. Yang, B. C. Walker, E. A. Stach, H. W. Hillhouse and R. Agrawal, *Journal of the American Chemical Society*, 2010, **132**, 17384-17386.
15. D. A. R. Barkhouse, O. Gunawan, T. Gokmen, T. K. Todorov and D. B. Mitzi, *Progress in Photovoltaics: Research and Applications*, 2012, **20**, 6-11.
16. J. Britt and C. Ferekides, *Applied Physics Letters*, 1993, **62**, 2851-2852.
17. T. Aramoto, S. Kumazawa, H. Higuchi, T. Arita, S. Shibutani, T. Nishio, J. Nakajima, M. Tsuji, A. Hanafusa and T. Hibino, *Japanese Journal of Applied Physics*, 1997, **36**, 6304-6305.
18. D. E. Carlson and C. R. Wronski, *Applied Physics Letters*, 2008, **28**, 671-673.
19. V. Fthenakis, *Renewable and Sustainable Energy Reviews*, 2009, **13**, 2746-2750.
20. G.-H. Kim, B. Walker, H.-B. Kim, J. Y. Kim, E. H. Sargent and J. Park, *Advanced Materials*, 2014, 3321-3327.
21. A. J. Nozik, *Physica E: Low-dimensional Systems and Nanostructures*, 2002, **14**, 115-120.
22. A. Martí, E. Antolín, C. R. Stanley, C. D. Farmer, N. López, P. Díaz, E. Cánovas, P. G. Linares and A. Luque, *Physical Review Letters*, 2006, **97**, 247701.

23. A. Martí, N. López, E. Antolín, E. Cánovas, A. Luque, C. R. Stanley, C. D. Farmer and P. Díaz, *Applied Physics Letters*, 2007, **90**, 233510.
24. M. C. Scharber, D. Mühlbacher, M. Koppe, P. Denk, C. Waldauf, A. J. Heeger and C. J. Brabec, *Advanced Materials*, 2006, **18**, 789-794.
25. S. H. Park, A. Roy, S. Beaupré, S. Cho, N. Coates, J. S. Moon, D. Moses, M. Leclerc, K. Lee and A. J. Heeger, *Nature Photonics*, 2009, **3**, 297-302.
26. J. Y. Kim, K. Lee, N. E. Coates, D. Moses, T.-Q. Nguyen, M. Dante and A. J. Heeger, *Science*, 2007, **317**, 222-225.
27. G. Dennler, M. C. Scharber, T. Ameri, P. Denk, K. Forberich, C. Waldauf and C. J. Brabec, *Advanced Materials*, 2008, **20**, 579-583.
28. J. B. Baxter and E. S. Aydil, *Applied Physics Letters*, 2005, **86**, 053114.
29. A. Mishra, M. K. Fischer and P. Bäuerle, *Angewandte Chemie International Edition*, 2009, **48**, 2474-2499.
30. B. Rezig, H. Dahman and M. Kenzari, *Renewable Energy*, 1992, **2**, 125-128.
31. B. J. Richardson, L. Zhu and Q. Yu, *Solar Energy Materials And Solar Cells*, 2013, **116**, 252-261.
32. C. W. Lin, D. Y. Wang, Y. T. Wang, C. C. Chen, Y. J. Yang and Y. F. Chen, *Solar Energy Materials and Solar Cells*, 2011, **95**, 1107-1110.
33. Y.-Y. Lin, D.-Y. Wang, H.-C. Yen, H.-L. Chen, C.-C. Chen, C.-M. Chen, C.-Y. Tang and C.-W. Chen, *Nanotechnology*, 2009, **20**, 405207.
34. C. Herzog, A. Belaidi, A. Ogacho and T. Dittrich, *Energy & Environmental Science*, 2009, **2**, 962-964.
35. D. Kieven, T. Dittrich, A. Belaidi, J. Tornow, K. Schwarzburg, N. Allsop and M. Lux-Steiner, *Applied Physics Letters*, 2008, **92**, -.
36. M. Liu, M. B. Johnston and H. J. Snaith, *Nature*, 2013, **501**, 395-398.
37. M. M. Lee, J. Teuscher, T. Miyasaka, T. N. Murakami and H. J. Snaith, *Science*, 2012, **338**, 643-647.
38. J. Burschka, N. Pellet, S.-J. Moon, R. Humphry-Baker, P. Gao, M. K. Nazeeruddin and M. Grätzel, *Nature*, 2013, **499**, 316-319.
39. NREL, Best Research Solar Cell Efficiencies, http://www.nrel.gov/ncpv/images/efficiency_chart.jpg.
40. M. A. Green, K. Emery, Y. Hishikawa, W. Warta and E. D. Dunlop, *Progress in Photovoltaics: Research and Applications*, 2014, **22**, 1-9.
41. P. M. Allemand, A. Koch, F. Wudl, Y. Rubin, F. Diederich, M. M. Alvarez, S. J. Anz and R. L. Whetten, *Journal of the American Chemical Society*, 1991, **113**, 1050-1051.
42. J. C. Hummelen, B. W. Knight, F. LePeq, F. Wudl, J. Yao and C. L. Wilkins, *The Journal of Organic Chemistry*, 1995, **60**, 532-538.
43. B. C. Thompson and J. M. J. Fréchet, *Angewandte Chemie International Edition*, 2008, **47**, 58-77.
44. T. B. Singh, N. Marjanović, G. J. Matt, S. Günes, N. S. Sariciftci, A. Montaigne Ramil, A. Andreev, H. Sitter, R. Schwödiauer and S. Bauer, *Organic Electronics*, 2005, **6**, 105-110.
45. W. J. Zeng, H. B. Wu, C. Zhang, F. Huang, J. B. Peng, W. Yang and Y. Cao, *Advanced Materials*, 2007, **19**, 810-814.
46. T. Yang, M. Wang, C. Duan, X. Hu, L. Huang, J. Peng, F. Huang and X. Gong,

Energy & Environmental Science, 2012, **5**, 8208-8214.
47. Y. Sun, S.-C. Chien, H.-L. Yip, Y. Zhang, K.-S. Chen, D. F. Zeigler, F.-C. Chen, B. Lin and A. K.-Y. Jen, *Chemistry Of Materials*, 2011, **23**, 5006-5015.
48. T. M. Brown, J. S. Kim, R. H. Friend, F. Cacialli, R. Daik and W. J. Feast, *Applied Physics Letters*, 1999, **75**, 1679-1681.
49. S. Kirchmeyer and K. Reuter, *Journal Of Materials Chemistry*, 2005, **15**, 2077-2088.
50. L. S. Pingree, B. A. MacLeod and D. S. Ginger, *The Journal of Physical Chemistry C*, 2008, **112**, 7922-7927.
51. S. K. Hau, H.-L. Yip, J. Zou and A. K.-Y. Jen, *Organic Electronics*, 2009, **10**, 1401-1407.
52. K. Norrman, M. V. Madsen, S. A. Gevorgyan and F. C. Krebs, *Journal of the American Chemical Society*, 2010, **132**, 16883-16892.
53. K. Wong, H. Yip, Y. Luo, K. Wong, W. Lau, K. Low, H. Chow, Z. Gao, W. Yeung and C. Chang, *Applied Physics Letters*, 2002, **80**, 2788-2790.
54. M. D. Irwin, D. B. Buchholz, A. W. Hains, R. P. Chang and T. J. Marks, *Proceedings of the National Academy of Sciences*, 2008, **105**, 2783-2787.
55. J. R. Manders, S.-W. Tsang, M. J. Hartel, T.-H. Lai, S. Chen, C. M. Amb, J. R. Reynolds and F. So, *Advanced Functional Materials*, 2013, **23**, 2993-3001.
56. J. Meyer, R. Khalandovsky, P. Görrn and A. Kahn, *Advanced Materials*, 2011, **23**, 70-73.
57. K. Zilberberg, S. Trost, H. Schmidt and T. Riedl, *Advanced Energy Materials*, 2011, **1**, 377-381.
58. J.-S. Huang, C.-Y. Chou, M.-Y. Liu, K.-H. Tsai, W.-H. Lin and C.-F. Lin, *Organic Electronics*, 2009, **10**, 1060-1065.
59. C. Tao, S. Ruan, G. Xie, X. Kong, L. Shen, F. Meng, C. Liu, X. Zhang, W. Dong and W. Chen, *Applied Physics Letters*, 2009, **94**, -.
60. T. Stubhan, T. Ameri, M. Salinas, J. Krantz, F. Machui, M. Halik and C. J. Brabec, *Applied Physics Letters*, 2011, **98**, -.
61. S. Tokito, K. Noda and Y. Taga, *Journal of Physics D: Applied Physics*, 1996, **29**, 2750.
62. Z. He, C. Zhong, S. Su, M. Xu, H. Wu and Y. Cao, *Nature Photonics*, 2012, **6**, 591-595.
63. S. Chen, K. R. Choudhury, J. Subbiah, C. M. Amb, J. R. Reynolds and F. So, *Advanced Energy Materials*, 2011, **1**, 963-969.
64. S. Chen, C. E. Small, C. M. Amb, J. Subbiah, T.-h. Lai, S.-W. Tsang, J. R. Manders, J. R. Reynolds and F. So, *Advanced Energy Materials*, 2012, **2**, 1333-1337.
65. B. Rezig, H. Dahman and M. Kenzari, *Renewable Energy*, 1992, **2**, 125-128.
66. C. Wadia, A. P. Alivisatos and D. M. Kammen, *Environmental Science & Technology*, 2009, **43**, 2072-2077.
67. C. Wadia, Y. Wu, S. Gul, S. K. Volkman, J. Guo and A. P. Alivisatos, *Chemistry Of Materials*, 2009, **21**, 2568-2570.
68. L. Yu, S. Lany, R. Kykyneshi, V. Jieratum, R. Ravichandran, B. Pelatt, E. Altschul, H. A. Platt, J. F. Wager and D. A. Keszler, *Advanced Energy Materials*, 2011, **1**, 748-753.
69. S. Nakamura and A. Yamamoto, *Solar Energy Materials and Solar Cells*, 2001, **65**,

79-85.
70. C. Steinhagen, T. B. Harvey, C. J. Stolle, J. Harris and B. A. Korgel, *The Journal of Physical Chemistry Letters*, 2012, **3**, 2352-2356.
71. L. Wei, D. Y. Wan, Y. T. Wang, B. Y. Wang, C. X. Ma and H. Sun, *Journal of Crystal Growth*, 2003, **253**, 230-238.
72. L. Wei, D. Y. Wan, B. Y. Wang, Y. T. Wang, H. Sun and R. G. Zhang, *Journal of Crystal Growth*, 2003, **257**, 286-292.
73. G. Smestad, A. Ennaoui, S. Fiechter, H. Tributsch, W. K. Hofmann, M. Birkholz and W. Kautek, *Solar Energy Materials*, 1990, **20**, 149-165.
74. M. Birkholz, D. Lichtenberger, C. Hopfner and S. Fiechter, *Solar Energy Materials and Solar Cells*, 1992, **27**, 243-251.
75. A. Yamamoto, M. Nakamura, A. Seki, E. L. Li, A. Hashimoto and S. Nakamura, *Solar Energy Materials and Solar Cells*, 2003, **75**, 451-456.
76. J. Puthussery, S. Seefeld, N. Berry, M. Gibbs and M. Law, *Journal of the American Chemical Society*, 2010, **133**, 716-719.
77. W. Li, M. Doblinger, A. Vaneski, A. L. Rogach, F. Jackel and J. Feldmann, *Journal Of Materials Chemistry*, 2011, **21**, 17946-17952.
78. Y. Bi, Y. Yuan, C. L. Exstrom, S. A. Darveau and J. Huang, *Nano Letters*, 2011, **11**, 4953-4957.
79. A. Kirkeminde and S. Ren, *Journal of Materials Chemistry A*, 2013, **1**, 49-54.
80. D. Wang, Q. Wang and T. Wang, *Crystengcomm*, 2010, **12**, 3797-3805.
81. D.-W. Wang, Q.-H. Wang and T.-M. Wang, *Crystengcomm*, 2010, **12**, 755-761.
82. S. Kar and S. Chaudhuri, *Chemical Physics Letters*, 2004, **398**, 22-26.
83. X. Chen, Z. Wang, X. Wang, J. Wan, J. Liu and Y. Qian, *Inorganic Chemistry*, 2005, **44**, 951-954.
84. C. Schliehe, B. H. Juarez, M. Pelletier, S. Jander, D. Greshnykh, M. Nagel, A. Meyer, S. Foerster, A. Kornowski and C. Klinke, *Science*, 2010, **329**, 550-553.
85. K.-S. Cho, D. V. Talapin, W. Gaschler and C. B. Murray, *Journal of the American Chemical Society*, 2005, **127**, 7140-7147.
86. A. Halder and N. Ravishankar, *Advanced Materials*, 2007, **19**, 1854-1858.
87. N. Pradhan, H. Xu and X. Peng, *Nano Letters*, 2006, **6**, 720-724.
88. D. Hapiuk, B. Masenelli, K. Masenelli-Varlot, D. Tainoff, O. Boisron, C. Albin and P. Melinon, *Journal of Physical Chemistry C*, 2013, **117**, 10220-10227.
89. M. Safdari, A. Fischer, B. Xu, L. Kloo and J. M. Gardner, *Journal of Materials Chemistry A*, 2015, **3**, 9201-9207.
90. J.-H. Im, J. Chung, S.-J. Kim and N.-G. Park, *Nanoscale Research Letters*, 2012, **7**, 1-7.
91. D. B. Mitzi, *Progress in Inorganic Chemistry, Volume 48*, 2007, 1-121.
92. A. Binek, F. C. Hanusch, P. Docampo and T. Bein, *The Journal of Physical Chemistry Letters*, 2015, **6**, 1249-1253.
93. D.-X. Yuan, A. Gorka, M.-F. Xu, Z.-K. Wang and L.-S. Liao, *Physical Chemistry Chemical Physics*, 2015, **17**, 19745-19750.
94. G. E. Eperon, D. Bryant, J. Troughton, S. D. Stranks, M. B. Johnston, T. Watson, D. A. Worsley and H. J. Snaith, *The Journal of Physical Chemistry Letters*, 2014, **6**, 129-138.
95. N. J. Jeon, J. H. Noh, W. S. Yang, Y. C. Kim, S. Ryu, J. Seo and S. I. Seok, *Nature*,

2015, **517**, 476-480.
96. J. M. Szarko, B. S. Rolczynski, S. J. Lou, T. Xu, J. Strzalka, T. J. Marks, L. Yu and L. X. Chen, *Advanced Functional Materials*, 2014, **24**, 10-26.
97. S. Pang, H. Hu, J. Zhang, S. Lv, Y. Yu, F. Wei, T. Qin, H. Xu, Z. Liu and G. Cui, *Chemistry Of Materials*, 2014, **26**, 1485-1491.
98. J. W. Lee, D. J. Seol, A. N. Cho and N. G. Park, *Advanced Materials*, 2014, **26**, 4991-4998.
99. F. Hao, C. C. Stoumpos, R. P. Chang and M. G. Kanatzidis, *Journal of the American Chemical Society*, 2014, **136**, 8094-8099.
100. S. Kazim, M. K. Nazeeruddin, M. Grätzel and S. Ahmad, *Angewandte Chemie International Edition*, 2014, **53**, 2812-2824.
101. S. D. Stranks, G. E. Eperon, G. Grancini, C. Menelaou, M. J. Alcocer, T. Leijtens, L. M. Herz, A. Petrozza and H. J. Snaith, *Science*, 2013, **342**, 341-344.
102. G. Xing, N. Mathews, S. Sun, S. S. Lim, Y. M. Lam, M. Grätzel, S. Mhaisalkar and T. C. Sum, *Science*, 2013, **342**, 344-347.
103. J. H. Heo, S. H. Im, J. H. Noh, T. N. Mandal, C.-S. Lim, J. A. Chang, Y. H. Lee, H.-j. Kim, A. Sarkar and M. K. Nazeeruddin, *Nature Photonics*, 2013, **7**, 486-491.
104. A. Kojima, K. Teshima, Y. Shirai and T. Miyasaka, *Journal of the American Chemical Society*, 2009, **131**, 6050-6051.
105. H. Zhou, Q. Chen, G. Li, S. Luo, T.-b. Song, H.-S. Duan, Z. Hong, J. You, Y. Liu and Y. Yang, *Science*, 2014, **345**, 542-546.
106. D. Liu and T. L. Kelly, *Nature Photonics*, 2014, **8**, 133-138.
107. N. J. Jeon, J. H. Noh, Y. C. Kim, W. S. Yang, S. Ryu and S. I. Seok, *Nature Materials*, 2014, 897-903.
108. O. Malinkiewicz, A. Yella, Y. H. Lee, G. M. Espallargas, M. Graetzel, M. K. Nazeeruddin and H. J. Bolink, *Nature Photonics*, 2014, **8**, 128-132.
109. H.-S. Kim, C.-R. Lee, J.-H. Im, K.-B. Lee, T. Moehl, A. Marchioro, S.-J. Moon, R. Humphry-Baker, J.-H. Yum and J. E. Moser, *Scientific reports*, 2012, **2**.
110. Q. Wang, Y. Shao, Q. Dong, Z. Xiao, Y. Yuan and J. Huang, *Energy & Environmental Science*, 2014.
111. Z. Xiao, C. Bi, Y. Shao, Q. Dong, Q. Wang, Y. Yuan, C. Wang, Y. Gao and J. Huang, *Energy & Environmental Science*, 2014, **7**, 2619-2623.
112. C. Bi, Y. Shao, Y. Yuan, Z. Xiao, C. Wang, Y. Gao and J. Huang, *Journal of Materials Chemistry A*, 2014, **2**, 18508-18514.
113. S. Sun, T. Salim, N. Mathews, M. Duchamp, C. Boothroyd, G. Xing, T. C. Sum and Y. M. Lam, *Energy & Environmental Science*, 2014, **7**, 399-407.
114. A. L. Abdelhady, M. Afzaal, M. A. Malik and P. O'Brien, *Journal Of Materials Chemistry*, 2011, **21**, 18768-18775.
115. C.-H. Lai, M.-Y. Lu and L.-J. Chen, *Journal Of Materials Chemistry*, 2012, **22**, 19-30.
116. A. Zhang, Q. Ma, M. Lu, G. Zhou, C. Li and Z. Wang, *The Journal of Physical Chemistry C*, 2009, **113**, 15492-15496.
117. D. Rickard and G. W. Luther, *Chemical Reviews*, 2007, **107**, 514-562.
118. L. Z. Zhang, Y. Hu, Z. Zheng, H. M. Jia and Y. W. Tang, *Journal of Physical Chemistry C*, 2008, **112**, 13037-13042.
119. C. N. R. Rao, M. Nath, A. Choudhury and A. Kundu, *Advanced Materials*, 2003,

15, 2098-2101.
120. H. H. Song, B. Wu, J. S. Zhou and X. H. Chen, *Chemical Communications*, 2011, **47**, 8653-8655.
121. X. M. He, X. Feng, W. H. Pu, C. Y. Jiang and C. R. Wan, *Ionics*, 2007, **13**, 375-377.
122. Q. C. Horn and Y. Shao-Horn, *Electrochimica Acta*, 2001, **46**, 2613-2621.
123. C. C. Chen, Y. Y. Lin, D. Y. Wang, H. C. Yen, H. L. Chen, C. M. Chen, C. Y. Tang and C. W. Chen, *Nanotechnology*, 2009, **20**, 405207.
124. Q. Z. Yao, M. L. Li, G. T. Zhou, X. F. Qu, C. F. Mu and S. Q. Fu, *Crystengcomm*, 2011, **13**, 5936-5942.
125. A. P. Alivisatos, C. Wadia, Y. Wu, S. Gul, S. K. Volkman and J. H. Guo, *Chemistry Of Materials*, 2009, **21**, 2568-2570.
126. Y. T. Qian, X. Y. Chen, Z. H. Wang, X. Wang, J. X. Wan and J. W. Liu, *Inorganic Chemistry*, 2005, **44**, 951-954.
127. Q. H. Wang, D. W. Wang and T. M. Wang, *Crystengcomm*, 2010, **12**, 3797-3805.
128. Q. H. Wang, D. W. Wang and T. M. Wang, *Crystengcomm*, 2010, **12**, 755-761.
129. A. Hung, I. Yarovsky and S. P. Russo, *Journal of Chemical Physics*, 2003, **118**, 6022-6029.
130. M. Rieder, J. C. Crelling, O. Sustai, M. Drabek, Z. Weiss and M. Klementova, *International Journal of Coal Geology*, 2007, **71**, 115-121.
131. H. Vogt, T. Chattopadhyay and H. J. Stolz, *Journal of Physics and Chemistry of Solids*, 1983, **44**, 869-873.
132. Y. Jianfeng, Z. Guisheng, H. Anming and Y. N. Zhou, *Journal Of Materials Chemistry*, 2011, **21**, 15981-15986.
133. Y. Sun, Y. Yin, B. T. Mayers, T. Herricks and Y. Xia, *Chemistry Of Materials*, 2002, **14**, 4736-4745.
134. U. K. Sen, B. M. Mandal and S. N. Bhattacharyya, *Journal of Polymer Science Part C-Polymer Letters*, 1981, **19**, 523-527.
135. C. R. Wilke, Chang, P., *A.I.Ch.E. J.*, 1995, **1**, 264.
136. A. S. Barnard and S. P. Russo, *The Journal of Physical Chemistry C*, 2007, **111**, 11742-11746.
137. A. S. Barnard and S. P. Russo, *Journal Of Materials Chemistry*, 2009, **19**, 3389-3394.
138. J. M. Guevremont, A. R. Elsetinow, D. R. Strongin, J. Bebie and M. A. A. Schoonen, *American Mineralogist*, 1998, **83**, 1353-1356.
139. S. H. Yu, S. L. Yang, H. B. Yao and M. R. Gao, *Crystengcomm*, 2009, **11**, 1383-1390.
140. R. E. Davis and H. F. Nakshbendi, *Journal of the American Chemical Society*, 1962, **84**, 2085-2090.
141. M. W. Chase, C. A. Davies, J. R. Downey, D. J. Frurip, R. A. McDonald and A. N. Syverud, *Journal of Physical and Chemical Reference Data*, 1985, **14**, 927-1856.
142. S.-H. Yu, J. Yang, Z.-H. Han, Y. Zhou, R.-Y. Yang, Y.-T. Qian and Y.-H. Zhang, *Journal Of Materials Chemistry*, 1999, **9**, 1283-1287.
143. Y. Y. Lin, D. Y. Wang, H. C. Yen, H. L. Chen, C. C. Chen, C. M. Chen, C. Y. Tang and C. W. Chen, *Nanotechnology*, 2009, **20**.
144. Y. Bi, Y. B. Yuan, C. L. Exstrom, S. A. Darveau and J. S. Huang, *Nano Letters*, 2011, **11**, 4953-4957.

145. Y. Bai, J. Yeom, M. Yang, S.-H. Cha, K. Sun and N. A. Kotov, *The Journal of Physical Chemistry C*, 2013, **117**, 2567-2573.
146. J. M. Lucas, C.-C. Tuan, S. D. Lounis, D. K. Britt, R. Qiao, W. Yang, A. Lanzara and A. P. Alivisatos, *Chemistry Of Materials*, 2013, **25**, 1615-1620.
147. H. A. Macpherson and C. R. Stoldt, *ACS Nano*, 2012.
148. C. Steinhagen, T. B. Harvey, C. J. Stolle, J. Harris and B. A. Korgel, *J. Phys. Chem. Lett.*, 2012, 2352-2356.
149. R. Sun, M. K. Y. Chan and G. Ceder, *Physical Review B*, 2011, **83**, 235311.
150. A. Sahu, A. Khare, D. D. Deng and D. J. Norris, *Chemical Communications*, 2012, **48**, 5458-5460.
151. P. P. Altermatt, T. Kiesewetter, K. Ellmer and H. Tributsch, *Solar Energy Materials and Solar Cells*, 2002, **71**, 181-195.
152. V. N. Antonov, L. P. Germash, A. P. Shpak and A. N. Yaresko, *physica status solidi (b)*, 2009, **246**, 411-416.
153. X. Peng, *Advanced Materials*, 2003, **15**, 459-463.
154. M. Gong, A. Kirkeminde and S. Ren, *Scientific reports*, 2013, **3**.
155. C. Bullen, J. van Embden, J. Jasieniak, J. E. Cosgriff, R. J. Mulder, E. Rizzardo, M. Gu and C. L. Raston, *Chemistry Of Materials*, 2010, **22**, 4135-4143.
156. Z. Li, Y. Ji, R. Xie, S. Y. Grisham and X. Peng, *Journal of the American Chemical Society*, 2011, **133**, 17248-17256.
157. A. G. Kanaras, C. Sönnichsen, H. Liu and A. P. Alivisatos, *Nano Letters*, 2005, **5**, 2164-2167.
158. D. R. Alfonso, *The Journal of Physical Chemistry C*, 2010, **114**, 8971-8980.
159. B. J. Richardson, L. Z. Zhu and Q. M. Yu, *Solar Energy Materials and Solar Cells*, 2013, **116**, 252-261.
160. M. Tokonami, Nishiguc.K and N. Morimoto, *American Mineralogist*, 1972, **57**, 1066-&.
161. H.-Y. Lai and C.-J. Chen, *Journal of Crystal Growth*, 2009, **311**, 4698-4703.
162. A. L. Abdelhady, M. A. Malik, P. O'Brien and F. Tuna, *The Journal of Physical Chemistry C*, 2011, **116**, 2253-2259.
163. W. Han and M. Gao, *Japanese Journal of Applied Physics*, 2008, **8**, 1023-1030.
164. K. Ramasamy, M. A. Malik, N. Revaprasadu and P. O'Brien, *Chemistry Of Materials*, 2013.
165. S. Mourdikoudis and L. M. Liz-Marzán, *Chemistry Of Materials*, 2013, **25**, 1465-1476.
166. J. H. Han, S. Lee and J. Cheon, *Chemical Society Reviews*, 2013, **42**, 2581-2591.
167. J. W. Thomson, K. Nagashima, P. M. Macdonald and G. A. Ozin, *Journal of the American Chemical Society*, 2011, **133**, 5036-5041.
168. V. I. Stenberg and P. G. Sweeny, *Industrial & Engineering Chemistry Fundamentals*, 1986, **25**, 735-741.
169. P. B. Hirsch, *Journal of Microscopy*, 1980, **118**, 3-12.
170. J. Arbiol, S. Estrade, J. D. Prades, A. Cirera, F. Furtmayr, C. Stark, A. Laufer, M. Stutzmann, M. Eickhoff, M. H. Gass, A. L. Bleloch, F. Peiro and J. R. Morante, *Nanotechnology*, 2009, **20**.
171. R. Schmechel and H. Werheit, *Journal Of Physics-condensed Matter*, 1999, **11**, 6803-6813.

172. X. Ben, P. Cao and H. S. Park, *The Journal of Physical Chemistry C*, 2013, **117**, 13738-13746.
173. Y. Li and P. J. Linchung, *Physical Review B*, 1987, **36**, 1130-1135.
174. S. B. Zhang, S. H. Wei and A. Zunger, *Physical Review B*, 2001, **63**, 075205.
175. M. A. El-Sayed, *Accounts of Chemical Research*, 2004, **37**, 326-333.
176. M. Gong, A. Kirkeminde and S. Ren, *Scientific reports*, 2013, **3**, 1-6.
177. M. Mullet, S. Boursiquot, M. Abdelmoula, J.-M. Génin and J.-J. Ehrhardt, *Geochimica et Cosmochimica Acta*, 2002, **66**, 829-836.
178. N. H. de Leeuw, S. C. Parker, H. M. Sithole and P. E. Ngoepe, *Journal Of Physical Chemistry B*, 2000, **104**, 7969-7976.
179. C. M. Eggleston and M. F. Hochella, *American Mineralogist*, 1992, **77**, 221-224.
180. J. M. Guevremont, D. R. Strongin and M. A. A. Schoonen, *American Mineralogist*, 1998, **83**, 1246-1255.
181. A. Hung, J. Muscat, I. Yarovsky and S. P. Russo, *Surface Science*, 2002, **513**, 511-524.
182. R. L. Penn and J. F. Banfield, *Science*, 1998, **281**, 969-971.
183. J. H. Yu, J. Joo, H. M. Park, S.-I. Baik, Y. W. Kim, S. C. Kim and T. Hyeon, *Journal of the American Chemical Society*, 2005, **127**, 5662-5670.
184. S. Mourdikoudis and L. M. Liz-Marzan, *Chemistry Of Materials*, 2013, **25**, 1465-1476.
185. L.-S. Li, J. Hu, W. Yang and A. P. Alivisatos, *Nano Letters*, 2001, **1**, 349-351.
186. G. Dennler, M. C. Scharber and C. J. Brabec, *Advanced Materials*, 2009, **21**, 1323-1338.
187. S. Roy, A. Aguirre, D. A. Higgins and V. Chikan, *The Journal of Physical Chemistry C*, 2012, **116**, 3153-3160.
188. R. Zhou, Y. Zheng, L. Qian, Y. Yang, P. H. Holloway and J. Xue, *Nanoscale*, 2012, **4**, 3507-3514.
189. K. F. Jeltsch, M. Schädel, J. B. Bonekamp, P. Niyamakom, F. Rauscher, H. W. Lademann, I. Dumsch, S. Allard, U. Scherf and K. Meerholz, *Advanced Functional Materials*, 2012, **22**, 397-404.
190. S. Dayal, N. Kopidakis, D. C. Olson, D. S. Ginley and G. Rumbles, *Nano Letters*, 2009, **10**, 239-242.
191. L. Han, D. Qin, X. Jiang, Y. Liu, L. Wang, J. Chen and Y. Cao, *Nanotechnology*, 2006, **17**, 4736.
192. J. Liu, T. Tanaka, K. Sivula, A. P. Alivisatos and J. M. Fréchet, *Journal of the American Chemical Society*, 2004, **126**, 6550-6551.
193. M. Wright and A. Uddin, *Solar Energy Materials and Solar Cells*, 2012, **107**, 87-111.
194. K. F. Jeltsch, M. Schädel, J.-B. Bonekamp, P. Niyamakom, F. Rauscher, H. W. A. Lademann, I. Dumsch, S. Allard, U. Scherf and K. Meerholz, *Advanced Functional Materials*, 2012, **22**, 397-404.
195. S. Dowland, T. Lutz, A. Ward, S. P. King, A. Sudlow, M. S. Hill, K. C. Molloy and S. A. Haque, *Advanced Materials*, 2011, **23**, 2739-2744.
196. S. Ren, L.-Y. Chang, S.-K. Lim, J. Zhao, M. Smith, N. Zhao, V. Bulović, M. Bawendi and S. Gradečak, *Nano Letters*, 2011, **11**, 3998-4002.
197. A. A. Watt, D. Blake, J. H. Warner, E. A. Thomsen, E. L. Tavenner, H. Rubinsztein-

Dunlop and P. Meredith, *Journal of Physics D: Applied Physics*, 2005, **38**, 2006.
198. J. Halls, C. Walsh, N. Greenham, E. Marseglia, R. Friend, S. Moratti and A. Holmes, *Nature*, 1995, **376**, 498-500.
199. M. P. de Jong, L. J. van IJzendoorn and M. J. A. de Voigt, *Applied Physics Letters*, 2000, **77**, 2255-2257.
200. S. K. Hau, H.-L. Yip, N. S. Baek, J. Zou, K. O'Malley and A. K.-Y. Jen, *Applied Physics Letters*, 2008, **92**, 253301.
201. R. Lazzaroni, M. Lögdlund, A. Calderone, J. L. Brédas, P. Dannetun, C. Fauquet, C. Fredriksson, S. Stafström and W. R. Salaneck, *Synthetic Metals*, 1995, **71**, 2159-2162.
202. P. Dannetun, M. Boman, S. Stafström, W. R. Salaneck, R. Lazzaroni, C. Fredriksson, J. L. Brédas, R. Zamboni and C. Taliani, *The Journal of Chemical Physics*, 1993, **99**, 664-672.
203. M. Schierhorn, S. W. Boettcher, J. H. Peet, E. Matioli, G. C. Bazan, G. D. Stucky and M. Moskovits, *ACS Nano*, 2010, **4**, 6132-6136.
204. B. J. Richardson, L. Zhu and Q. Yu, *Solar Energy Materials And Solar Cells*, 2013, **116**, 252-261.
205. C. Liu, J. Li, X. Zhang, Y. He, Z. Li, H. Li, W. Guo, L. Shen and S. Ruan, *Physical Chemistry Chemical Physics*, 2015, **17**, 7960-7965.
206. Y. Wang, Q. Luo, N. Wu, Q. Wang, H. Zhu, L. Chen, Y.-Q. Li, L. Luo and C.-Q. Ma, *ACS Applied Materials & Interfaces*, 2015, **7**, 7170-7179.
207. J. Y. Lek, Y. M. Lam, J. Niziol and M. Marzec, *Nanotechnology*, 2012, **23**, 315401.
208. P. Murgatroyd, *Journal of Physics D: Applied Physics*, 1970, **3**, 151.
209. J. Yang, A. Tang, R. Zhou and J. Xue, *Solar Energy Materials And Solar Cells*, 2011, **95**, 476-482.
210. L. Qian, J. Yang, R. Zhou, A. Tang, Y. Zheng, T.-K. Tseng, D. Bera, J. Xue and P. H. Holloway, *J. Mater. Chem.*, 2011, **21**, 3814-3817.
211. W. W. Yu, L. Qu, W. Guo and X. Peng, *Chemistry Of Materials*, 2003, **15**, 2854-2860.
212. P. Vanlaeke, A. Swinnen, I. Haeldermans, G. Vanhoyland, T. Aernouts, D. Cheyns, C. Deibel, J. D'Haen, P. Heremans, J. Poortmans and J. V. Manca, *Solar Energy Materials and Solar Cells*, 2006, **90**, 2150-2158.
213. H. Hintz, H. J. Egelhaaf, H. Peisert and T. Chassé, *Polymer Degradation and Stability*, 2010, **95**, 818-825.
214. M. J. Winokur, D. Spiegel, Y. Kim, S. Hotta and A. J. Heeger, *Synthetic Metals*, 1989, **28**, 419-426.
215. K. Kumari, S. Chand, V. Vankar and V. Kumar, *Applied Physics Letters*, 2009, **94**, 213503.
216. W. Fu, Y. Shi, W. Qiu, L. Wang, Y. Nan, M. Shi, H. Li and H. Chen, *Physical Chemistry Chemical Physics*, 2012, **14**, 12094-12098.
217. E. Talgorn, R. D. Abellon, P. J. Kooyman, J. Piris, T. J. Savenije, A. Goossens, A. J. Houtepen and L. D. Siebbeles, *ACS Nano*, 2010, **4**, 1723-1731.
218. M. J. Greaney, S. Das, D. H. Webber, S. E. Bradforth and R. L. Brutchey, *ACS Nano*, 2012, **6**, 4222-4230.
219. Y. Zhou, F. S. Riehle, Y. Yuan, H.-F. Schleiermacher, M. Niggemann, G. A. Urban and M. Krüger, *Applied Physics Letters*, 2010, **96**, 013304.

220. N. C. Greenham, X. Peng and A. P. Alivisatos, *Physical Review B*, 1996, **54**, 17628-17637.
221. L. Zhu, B. J. Richardson and Q. Yu, *Nanoscale*, 2014, **6**, 1029-1037.
222. L. Brus, *The Journal of Physical Chemistry*, 1986, **90**, 2555-2560.
223. V. Mihailetchi, J. Wildeman and P. Blom, *Physical Review Letters*, 2005, **94**, 126602.
224. W. U. Huynh, J. J. Dittmer, N. Teclemariam, D. J. Milliron, A. P. Alivisatos and K. W. Barnham, *Physical Review B*, 2003, **67**, 115326.
225. J. D. Servaites, M. A. Ratner and T. J. Marks, *Energy & Environmental Science*, 2011, **4**, 4410-4422.
226. N. Li, B. E. Lassiter, R. R. Lunt, G. Wei and S. R. Forrest, *Applied Physics Letters*, 2009, **94**, 023307.
227. D. Chirvase, J. Parisi, J. C. Hummelen and V. Dyakonov, *Nanotechnology*, 2004, **15**, 1317.
228. G. A. H. Wetzelaer, M. Kuik, H. T. Nicolai and P. W. M. Blom, *Physical Review B*, 2011, **83**, 165204.
229. M. Kuik, H. T. Nicolai, M. Lenes, G.-J. A. H. Wetzelaer, M. Lu and P. W. M. Blom, *Applied Physics Letters*, 2011, **98**, 093301.
230. A. Jain and A. Kapoor, *Solar Energy Materials And Solar Cells*, 2005, **85**, 391-396.
231. I. Riedel, J. Parisi, V. Dyakonov, L. Lutsen, D. Vanderzande and J. C. Hummelen, *Advanced Functional Materials*, 2004, **14**, 38-44.
232. I. Riedel and V. Dyakonov, *physica status solidi (a)*, 2004, **201**, 1332-1341.
233. H. Wang, X. Yu, C. Yi, H. Ren, C. Liu, Y. Yang, S. Xiao, J. Zheng, A. Karim and S. Z. Cheng, *The Journal of Physical Chemistry C*, 2013, **117**, 4358-4363.
234. Y. Zhou, M. Eck, C. Men, F. Rauscher, P. Niyamakom, S. Yilmaz, I. Dumsch, S. Allard, U. Scherf and M. Krüger, *Solar Energy Materials And Solar Cells*, 2011, **95**, 3227-3232.
235. J. Clark, J.-F. Chang, F. C. Spano, R. H. Friend and C. Silva, *Applied Physics Letters*, 2009, **94**, 163306.
236. M. Baghgar, J. A. Labastide, F. Bokel, R. C. Hayward and M. D. Barnes, *The Journal of Physical Chemistry C*, 2014, **118**, 2229-2235.
237. Y. Sun, J. H. Seo, C. J. Takacs, J. Seifter and A. J. Heeger, *Advanced Materials*, 2011, **23**, 1679-1683.
238. H.-S. Kim, C.-R. Lee, J.-H. Im, K.-B. Lee, T. Moehl, A. Marchioro, S.-J. Moon, R. Humphry-Baker, J.-H. Yum, J. E. Moser, M. Grätzel and N.-G. Park, *Scientific reports*, 2012, **2**, 591-598.
239. P.-Y. Chen, J. Qi, M. T. Klug, X. Dang, P. T. Hammond and A. M. Belcher, *Energy Environ. Sci.*, 2014, **7**, 3659-3665.
240. F. Zuo, S. T. Williams, P. W. Liang, C. C. Chueh, C. Y. Liao and A. K. Y. Jen, *Advanced Materials*, 2014, **26**, 6454-6460.
241. W.-J. Yin, J.-H. Yang, J. Kang, Y. Yan and S.-H. Wei, *Journal of Materials Chemistry A*, 2015, **3**, 8926-8942.
242. Y. Ogomi, A. Morita, S. Tsukamoto, T. Saitho, N. Fujikawa, Q. Shen, T. Toyoda, K. Yoshino, S. S. Pandey and T. Ma, *The Journal of Physical Chemistry Letters*, 2014, **5**, 1004-1011.
243. N. K. Noel, S. D. Stranks, A. Abate, C. Wehrenfennig, S. Guarnera, A.-A.

Haghighirad, A. Sadhanala, G. E. Eperon, S. K. Pathak and M. B. Johnston, *Energy & Environmental Science*, 2014, **7**, 3061-3068.
244. F. Hao, C. C. Stoumpos, D. H. Cao, R. P. Chang and M. G. Kanatzidis, *Nature Photonics*, 2014, **8**, 489-494.
245. C. C. Stoumpos, C. D. Malliakas and M. G. Kanatzidis, *Inorganic Chemistry*, 2013, **52**, 9019-9038.
246. G. E. Eperon, V. M. Burlakov, P. Docampo, A. Goriely and H. J. Snaith, *Advanced Functional Materials*, 2014, **24**, 151-157.
247. A. H. Ip, L. N. Quan, M. M. Adachi, J. J. McDowell, J. Xu, D. H. Kim and E. H. Sargent, *Applied Physics Letters*, 2015, **106**, 143902.
248. C.-H. Chiang, Z.-L. Tseng and C.-G. Wu, *Journal of Materials Chemistry A*, 2014, **2**, 15897-15903.
249. Z. Xiao, C. Bi, Y. Shao, Q. Dong, Q. Wang, Y. Yuan, C. Wang, Y. Gao and J. Huang, *Energy & Environmental Science*, 2014, **7**, 2619-2623.
250. C. Bi, Q. Wang, Y. Shao, Y. Yuan, Z. Xiao and J. Huang, *Nature communications*, 2015, **6**, 7747.
251. Z. Xiao, Q. Dong, C. Bi, Y. Shao, Y. Yuan and J. Huang, *Advanced Materials*, 2014, **26**, 6503-6509.
252. J. Lian, Q. Wang, Y. Yuan, Y. Shao and J. Huang, *Journal of Materials Chemistry A*, 2015, **3**, 9146-9151.
253. A. Wakamiya, M. Endo, T. Sasamori, N. Tokitoh, Y. Ogomi, S. Hayase and Y. Murata, *Chemistry Letters*, 2014, **43**, 711-713.
254. H. Miyamae, Y. Numahata and M. Nagata, *Chemistry Letters*, 1980, **6**, 663-664.
255. W. MingáLau, *Journal Of Materials Chemistry*, 2005, **15**, 4555-4559.
256. Y.-R. Luo, *Comprehensive handbook of chemical bond energies*, CRC press, 2007.
257. L. Wang, Y. Liu, X. Jiang, D. Qin and Y. Cao, *The Journal of Physical Chemistry C*, 2007, **111**, 9538-9542.
258. Y. Kang and D. Kim, *Solar Energy Materials and Solar Cells*, 2006, **90**, 166-174.
259. W. U. Huynh, J. J. Dittmer, W. C. Libby, G. L. Whiting and A. P. Alivisatos, *Advanced Functional Materials*, 2003, **13**, 73-79.
260. B. Sun, E. Marx and N. C. Greenham, *Nano Letters*, 2003, **3**, 961-963.
261. A. Ennaoui and H. Tributsch, *Solar Cells*, 1984, **13**, 197-200.
262. A. Yamamoto, M. Nakamura, A. Seki, E. L. Li, A. Hashimoto and S. Nakamura, *Solar Energy Materials and Solar Cells*, 2003, **75**, 451-456.
263. S. Kar, S. Chaudhuri and P. Nambissan, *Journal of applied physics*, 2004, **97**, 014301.
264. S. Kar and S. Chaudhuri, *Materials Letters*, 2005, **59**, 289-292.
265. M. Nath, A. Choudhury, A. Kundu and C. N. R. Rao, *Advanced Materials*, 2003, **15**, 2098-2101.
266. Z. A. Peng and X. Peng, *Journal of the American Chemical Society*, 2002, **124**, 3343-3353.
267. D. Aastuen, N. Clark, L. Cotter and B. J. Ackerson, *Physical Review Letters*, 1986, **57**, 1733.
268. A. Ennaoui, S. Fiechter, C. Pettenkofer, N. Alonso-Vante, K. Büker, M. Bronold, C. Höpfner and H. Tributsch, *Solar Energy Materials and Solar Cells*, 1993, **29**, 289-370.

Appendix B ABBREVIATION

2D-XRD 2-dimention X-ray diffraction

BCP bathocuproine

BHJ bulk heterojunction

CB chlorobenzene

CIGS copper indium gallium selenide

CZTSSe copper zinc tin sulfide selenide

DCB 1, 2-dichlorobenzene

DFT density functional theory

DI deionized

Diol 1, 2-hexadecanediol

DLS dynamic light scattering

DMF dimethylforamide

DMSO dimethyl sulfoxide

DPE diphenyl ether

DSSC dye-sensitized solar cells

EA ethylammonium

EDS energy-dispersive X-ray spectroscopy

EDX energy dispersive X-ray spectrometer

En/en ethylenediamine

EQE external quantum efficiency

ETL electron transport layer

FA formamidinium

FF fill factor

FFT fast fourier transform

FWHM full width at half maximum

HAADF high angle annular dark field

HOMO highest occupied molecular orbital

HRTEM high resolution transmission electron microscopy

HTL hole tansport layer

ITO indium tin oxide

Jsc short-circuit current density

J-V current density-voltage

LEP lone electron pair

LUMO lowest unoccupied molecular orbital

MA methylammonium

MAI methylammonium iodide

MEH-PPV poly [2-methoxy-5-(2-ethylhexyloxy)-1, 4-phenylenevinylene]

NC nanocrystal

NR nanorod

NREL National Renewable Energy Laboratory

OA oriented attachment

ODA octadecylamine

ODE 1-octadecence

OIHSCs Organic-inorganic hybrid solar cells

OLA oleyamine

OR Ostwald ripening

P3HT poly (3-hexylthiophene)

$PC_{61}BM$ [6, 6]-phenyl C_{61}-butyric acid methyl ester

$PC_{71}BM$ [6, 6]-phenyl C_{71}-butyric acid methyl ester

PCE power conversion efficiency

PCPDTBT poly [2, 6-(4, 4-bis (2-ethylhexyl)-4H-cyclopenta[2, 1-b:3, 4-b0]-dithiophene)-alt-4, 7-(2, 1, 3-benzothiadiazole)]

PDI polydispersity index

PEDOT:PSS poly (3, 4-ethylenedioxythiophene)-poly(styrenesulfonate)

PL Photoluminescence

P_{max} peak power

PMMA poly (methyl methacrylate)

PSC polymer solar cell

PTB7 poly({4, 8-bis[(2-ethylhexyl)oxy]benzo[1, 2-b:4, 5-b′]dithiophene-2, 6-diyl}{3-fluoro-2-[(2-ethylhexyl)carbonyl]thieno[3, 4-b]thiophenediyl})

PTB7-F20 poly (thienothiophene-co-benzodithiophenes)7-F20

PV photovoltaic

PVP polyvinylpyrrolidone

TEM transmission electron microscopy

TDPA n-tetradecylphosphonic acid

TGA thermal gravimetric analysis

TMA tetramethylammonium

TOP trioctylphosphine

TOPO trioctylphosphine oxide

QD quantum dot

SAED selected area electron diffraction

SCLC space charge limited current

SEM scanning electron microscopy

Spiro-OMeTAD 2, 2', 7, 7'-tetrakis-(N, N-di-p-methoxyphenylamine) 9, 9'-spirobifluorene

V$_{OC}$ open-circuit voltage

XPS X-ray photoelectron spectroscopy

XRD powder X-ray diffraction

CURRICULUM VITAE

EDUCATION

University of Washington, Seattle, WA

Ph.D., Chemical Engineering — Fall, 2015

Zhejiang University, Hangzhou, ZJ

M.S., Polymer Materials — Mar., 2010

B.S., Polymer Science and Engineering — July, 2007

EXPERIENCE

Graduate Research Assistant — June, 2010-Present

University of Washington, Seattle, WA — Advisor: Prof. Qiuming Yu

Graduate Research Assistant — Sept., 2007-Mar., 2010

Zhejiang University, Hangzhou, ZJ — Advisor: Prof. Jian Ji

PUBLICATIONS

1. **Leize Zhu**, Beau J. Richardson, and Qiuming Yu*, Inverted Hybrid CdSe-Polymer Solar Cells Adopting PEDOT:PSS/MoO_3 as Dual Hole Transport Layers, In Revision, Physical Chemistry Chemical Physics, 2015.
2. **Leize Zhu**, Brian Yuh, Stefan Schoen, Xinpei Li, Mohammed Aldighaithir, Beau J. Richardson, Ahmed Alamer, and Qiuming Yu*, Solvent Vapor-Assisted Thermal Annealing for the High-Performance Planar $CH_3NH_3Sn_xPb_{1-x}I_3$ Perovskite Solar Cells, In Revision, 2015.
3. **Leize Zhu**, Beau J. Richardson, and Qiuming Yu*, Anisotropic Growth of Iron Pyrite FeS_2 Nanocrystals via Oriented Attachment, Chemistry of Materials, 2015, 27, 3516.
4. Beau J. Richardson, **Leize Zhu**, and Qiuming Yu*, Inverted Hybrid Solar Cells Based on Pyrite FeS_2 Nanocrystals in P3HT: PCBM with Enhanced Photocurrent and Air-Stability, Solar Energy Materials and Solar Cells, 2013, 116, 252.
5. **Leize Zhu**, Beau J. Richardson, and Qiuming Yu*, Controlled Colloidal Synthesis of Iron Pyrite FeS_2 Nanorods and Quasi-Cubic Nanocrystal Agglomerations, Nanoscale, 2014, 6, 1029.
6. **Leize Zhu**, Beau Richardson, Jessica Tanumihardja, and Qiuming Yu*, Controlling Morphology and Phase of Pyrite FeS_2 Hierarchical Particles via the

Combination of Structure-Direction and Chelating Agents, CrystEngComm, 2012, 14, 4188.

7. **Leize Zhu**, Yonggang Shangguan, Yixin Sun, Jian Ji*, and Qiang Zheng, Rheological Properties of Redox-responsive, Associative Ferrocene-Modified Branched Poly(ethylene imine) and Its Modulation by β-cyclodextrin And Hydrogen Peroxide, Soft Matter, 2010, 6, 5541.
8. **Leize Zhu**, Wenbo Zhou, and Jian Ji*, Ferrocenyl Branched Poly (ethylene imine) Micelles as Reductive Templates for the Preparation of Silver Nanoparticles, Journal of Nanoparticle Research, 2010, 12, 2179.
9. **Leize Zhu**, Qiao Jin, Jianping Xu, Jian Ji*, and Jiacong Shen, Poly (2-(Methacryloyloxy) Ethyl Phosphorylcholine)-Functionalized Multi-walled Carbon Nanotubes: Preparation, Characterization, Solubility, and Effects on Blood Coagulation, Journal of Applied Polymer Science, 2009, 113, 351.

CONFERENCE PRESENTATIONS

1. **Leize Zhu**, Beau J Richardson, and Qiuming Yu*, Anisotropic Growth of Iron Pyrite FeS_2 Nanocrystals via Oriented Attachment, Oral, MRS, Session SS5, 2014, Spring, San Francisco, CA
2. **Leize Zhu**, Beau J Richardson, and Qiuming Yu*, Double Hole Transport Layers for Optimizing Inverted CdSe:P3HT Hybrid Bulk Heterojunction Solar Cells, Poster, MRS, 2014, Spring, San Francisco, CA
3. Beau J. Richardson, **Leize Zhu**, and Qiuming Yu*, Inverted Hybrid Photovoltaic Devices Utilizing Pyrite FeS_2 Nanocrystals, Poster, MRS, 2013, Spring, San Francisco, CA
4. **Leize Zhu**, Beau J. Richardson, and Qiuming Yu*, Shape Controlled Synthesis of Pyrite Nanocrystals for Photovoltaic Applications, Poster, MRS, 2012, Fall, Boston, CA
5. **Leize Zhu**, Jessica Tanumihardja, and Qiuming Yu*, Solvothermal Route to the Synthesis of Iron Sulfide Nanomaterials, Oral, AIChE, 2011, Fall, Minneapolis, MN